

Tomáš Haniš

Full Authority Vehicle Control Systems

CZECH TECHNICAL UNIVERSITY IN PRAGUE
FACULTY OF ELECTRICAL ENGINEERING



Habilitation thesis

Full Authority Vehicle Control Systems

Praha, 2019

Tomáš Haniš

Copyright

The works in the presented habilitation thesis are protected by copyright by Elsevier, IEEE, Springer International Publishing Switzerland and EDP Sciences. They are presented and reprinted in accordance with the copyright agreements with the respective publishers. Further copying or reprinting can be done exclusively with the permission of the respective publishers.

© *Tomáš Haniš 2019*

© *Springer International Publishing Switzerland 2015*

© *EDP Sciences, 2013*

© *Elsevier 2012, 2015, 2016*

© *IEEE 2019*

Abstract

This habilitation thesis is focused on Full-time Full-authority vehicle (motion) control system design methodologies and their applications, mainly in the automotive domain. The technology is well known in aerospace and especially in the Flight Control System community. It is however for some obscure reason completely ignored by the automotive community and therefore missing in vehicles. Furthermore, the development of complex control system architectures, fulfilling multi-domain and often contradicting objectives of rigid body motion control requirements versus constraining requirements (coming from structural loading objective, crew and passengers comfort requirements, etc.) is of interest of this thesis.

Anotace

Předkládaná habilitace pojednává o vývoji metodologie řídicích systémů s plnou kontrolou nad manévry dopravního prostředku a její aplikací v oblasti automobilového průmyslu. Tato technologie je velmi dobře známá v leteckém a kosmickém průmyslu a komunitě zabývající se návrhem řídicích systémů pro letadla, nicméně naprosto opomíjená automobilovou komunitou. Předkládaná habilitační práce se dále soustředí na návrh řídicích systémů respektující často protichůdné požadavky na provedení samotného manévru a požadavky na strukturální zatížení, případně komfort posádky/řidiče nebo pasažérů.

Acknowledgements

My thanks come here to my colleagues and friends who directly and significantly contributed to particular papers collected in this habilitation thesis.

- Martin Hromčík, associate professor at the Faculty of Electrical Engineering, CTU in Prague, is the co-author of most of presented papers. Martin has always been excellent colleague and challenging partner for mutual discussions.
- Andreas Wildshek, Alexander Schirrer, Martin Kozek and Felix Stroscher, my colleagues from ACFA 2020 project, for inspiring cooperation.
- Marin. A. Eder, Federico. Belloni a, Angelo. Tesauro, my colleagues from Danish Technical University for extensive cooperation in truly inspiring and multi-disciplinary collective.
- Denis Efremov, Vit Cibulka, David Vošahlík, Alam Mushfiqul, my PhD students and colleagues from CTU in Prague.

I am aware of the fact that I missed to name many people who helped me substantially in my career on the way to this habilitation, and they all fully deserve and have my deep gratitude and respect. I apologize to all of you, my dear colleagues and friends, for not mentioning you explicitly at this place, and I beg for your understanding.

The research presented in this habilitation thesis has been supported by the following grants.

- ACFA 2020 - Active Control for Flexible 2020 Aircraft, projekt 7. RP EU, AAT-2007-RTD-1, 2008-2011
- AKTION - Structural Vibration Control, vědecká spolupráce v rámci dvoustranných a mnohostranných mezinárodních dohod, 51p4, 2008-2009
- Aktivní tlumení pro mobilní prostředky, program MŠMT KONTAKT, ME10094, 2010-2012

Contents

Copyright.....	1
Abstract.....	3
Anotace.....	3
Acknowledgements.....	5
Contents.....	7
1 Introduction	9
2 State of the Art.....	11
2.1 Current fundamental vehicle control concepts	11
2.2 Related current research projects	12
2.3 Advancements in related technologies	12
2.4 Relationship to Autonomous Driving.....	12
3 Multi-domain objectives tradeoff & multi-layer control law architectures	13
4 Actuator and sensor optimization	13
5 Flight Control Systems with multi-objective problem definition.....	14
5.1 Feed-forward Control law design	15
5.2 Feedback Control law design	15
6 Drive Control Systems.....	17
6.1 Traction control.....	17
6.2 Driving envelope definition.....	18
7 System Verification	19
8 Comments on Selected Publications.....	21
8.1 Paper 1: Optimal sensors placement and spillover suppression	21
8.2 Paper 2: Linf optimal Feed-Forward Gust Load Alleviation Design for a Large Blended Wing Body Airliner	21
8.3 Paper 3: Active gust load alleviation system for flexible aircraft: Mixed feedforward/feedback approach.....	22
8.4 Section in book: Modeling and Control for a Blended Wing Body Aircraft	22
8.5 Paper 4: Vehicle longitudinal dynamics control based on LQ.....	22
8.6 Paper 5: Introduction of Driving Envelope and Full-Time-Full-Authority Control for Vehicle Stabilization Systems	22
8.7 Paper 6: A multi-frequency fatigue testing method for wind turbine rotor blades	22
9 Conclusion.....	23
9.1 Summary	23
References	24

1 Introduction

The autopilot term, so often used by autonomous driving community, is well established at the aerospace community, as is the role and importance of flight controls experts and their advanced methodologies for control laws design. The autopilot concept is functionally supported and relies on complex hierarchy of control system layers like Stability and Control Augmentation Systems (SAS, CAS) to provide aircraft or missile stabilization, damping, angular velocities tracking, attitude holds, and finally navigation and path tracking. This methodology is a result of costly and lengthy development process driven by the space-race in the 1950s, moon race in the 1960s, and military air-force technological boom during cold war. This need for advance control solutions gave rise to inherently unstable vehicle configurations, the fly-by-wire concept, over-actuated systems and advanced multivariable control theory methodologies like H2 optimal control and filtering (e.g. LQR and Kalman filter), robust control system design (Hinf) and more. All this knowledge is nowadays out there, publically available, and tempting to be used in related contexts.

High motivation for aerospace to automotive technology transfer are almost shocking similarities and analogies found by comparison of non-linear mathematical models of flight mechanics and vehicle dynamics, types of non-linearities and characteristics of governing forces and torques acting upon the aerospace vessels and automotive vehicles. For instance, the single-track vehicle lateral dynamics and the aircraft short period approximation models are structurally identical, with the pitching moment curve displaying nearly suspicious similarities to the tire slip curve. Therefore, the advanced full-authority vehicle control is a clear candidate for such research.

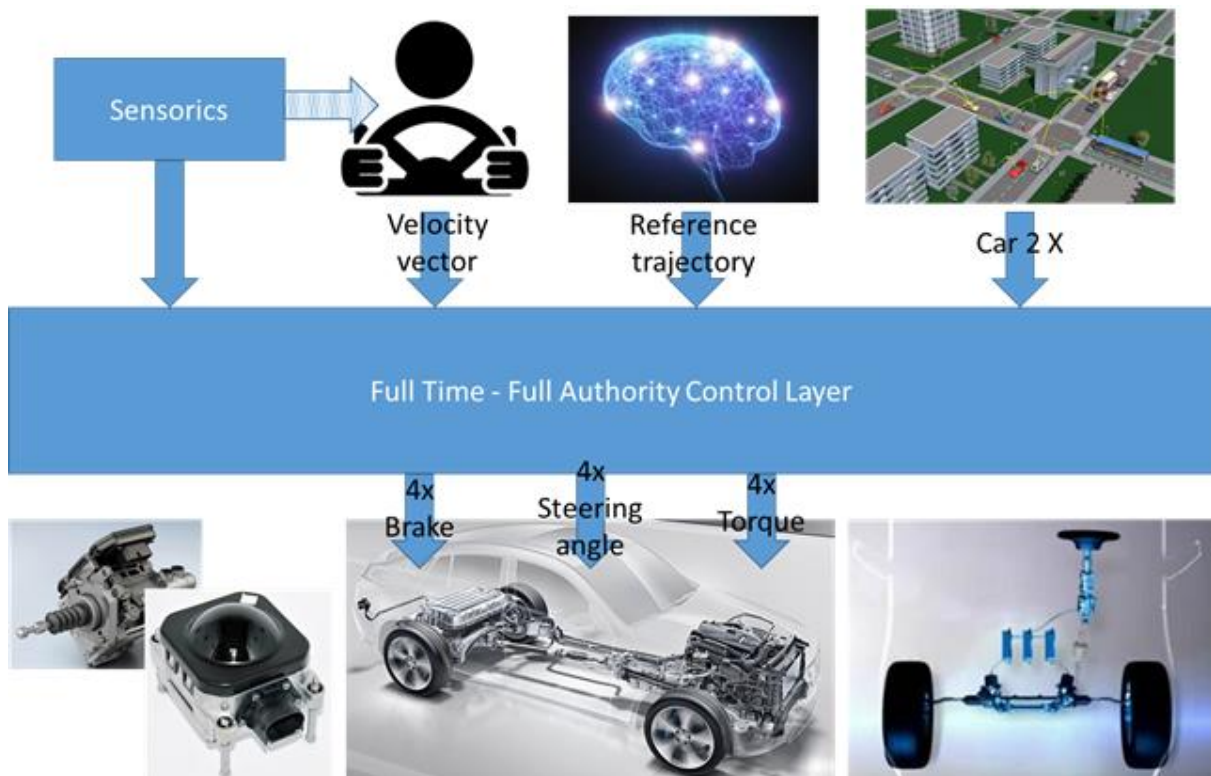


Figure 1: FAVeC layer.

The Full Authority Vehicle Control (FAVeC) research delivers a control system layer providing full separation (both full-time and full-authority) of driver/autonomous driving algorithms from the vehicle in tedious and routine tasks dealing with vehicle dynamics (namely stabilization, damping, and reference trajectory tracking). Such setup is heavily inspired by aerospace, both military and civil applications, where human pilot capabilities are not sufficient in response time, amount of information needed to be processed, and force needed for actuation. The existing drive by wire

solutions are commonly mistaken with task of mechanical parts substitution by non-intelligent mechatronics sub-systems, where incredible amount of energy is invested in emulation of force feedback for driver in order to provide same driving feeling experience like in the mechanical link case. This half way solution inherits all disadvantages of mechatronics system (lower reliability compared to mechanical solution, higher complexity, higher cost, demanding tuning and often resulting in "artificial feeling" to driver) and drops all desirable benefits (augmentation of driver sensorics, higher bandwidth, higher resolution and precision, possibility to exploit over-actuated vehicle's full potential). The proposed FAVeC layer provides this functionality and human driver will take a role of mission planning. The precise, reliable and repeatable maneuver execution will be assured by a smart drive-by-wire system (FAVeC layer, see Figure 1). This solution will serve as a technology enabler for new concepts and autonomous driving solutions themselves. Namely the functionality of "autopilot", also inspired and well known from aerospace, providing so desired functionality of vehicle autonomous operation is just the tip of the iceberg from control system point of view. Such functionality is based on and heavily dependent on control system hierarchical structure, assuring functionality of stabilization, damping, angular speeds tracking, orientation control and finally path tracking. Yet current development in autonomous technologies for automotive applications is mainly focused on this tip of the ice berg, omitting well proven and justified role of "flight control system" and methodology for such system design in systematic manner.

2 State of the Art

The FAVeC research objective is to develop effective and systematic control design methodologies for emerging active vehicle stabilization and control systems, commonly denoted as “the drive-by-wire” technology. In contrast to current and previous isolated attempts, the FAVeC has the ambition to fully exploit the complex mechatronic system of an over-actuated chassis; with independent all-wheel-steer and all-wheel drive possibilities and with integrated full-time full-authority multivariable feedback control laws; providing driver with similar functionalities and levels of safety and protection as the fly-by-wire systems [1]-[4] of modern civil aircraft.

2.1 Current fundamental vehicle control concepts

The current automotive industry fundamental principle is the driver full authority; for more than one whole century. Based on this principle and, more important, limited by this assumption, development of any new vehicle platform is dominated by the objectives of driver handling and inherent mechanical stability on one hand, and electronic assistance systems on the other hand, as if these were two independent and separated problems.

In general, any existing assistance system belongs to one of following three categories:

1. Emergency assistance: such system would "kick in" only at the verge of critical situations and serves as a last resource attempt (ABS, ESP, Emergency braking, emergency obstacle avoidance, etc.).
2. Active driving comfort enhancement by Advance Driver Assistance Systems (ADAS): such systems take over tedious and routine tasks that driver would otherwise have to face (Adaptive Cruise Control, Lane Keeping Assistant, Trailer Parking Assistant, etc.). Unfortunately, the fundamental principle, “driver is in charge”, still holds and in case of any non-standard situation the vehicle control is handed over to the driver, often in the most unfortunate way.
3. Indication based ADAS: such systems inform drivers about possibly dangerous situations and prevent the driver initial action (Cross-traffic assistance, Crossroad assistance, City assistance, etc.), but again - based on the fundamental rule that the driver can overpower any system in the vehicle.

The same rule also severely limits development and deployment of mechatronic solutions like the steer by wire and brake by wire systems in the automotive industry. In spite of this fact though, several attempts of such systems commercial deployment were done in recent years, proving feasibility and compliance with automotive standards and processes, but still bounded by the one fundamental rule of driver's full authority. This leads to halfway solutions, with research and development efforts focused on the arguably less important issues of driver feedback experience rather than the principal augmentation of the driver capabilities [5].

Vehicle dynamics is traditionally fine-tuned by purely mechanical chassis configurations and adjustments, and the dynamical properties of the car are thus hardcoded into the vehicle platform [6][7]. This hardcoded and fixed setup has to, however, provide sufficient and robust performance over tremendous variety of vehicle configurations (number of passengers, cargo, tires selection), driving scenarios (all year operation, slow nimble traffic in cities, high speed maneuvers on highways, off-roading). One fixed and purely mechanical solution fulfilling so demanding and broad requirements needs to be necessary sub-optimal.

In contrast, the Full-time Full-authority Vehicle Control concept (the “FAVeC layer”) provides technical means for on-demand chassis geometry reconfigurations in real time and in a dynamic manner, determining the chassis characteristics on-line. The chassis mechanical/mechatronics reconfiguration will follow control law objectives in range from small anti-symmetrical manipulation of single axle wheels (toe-in, increasing vehicle stability in braking, to toe-out, increasing vehicle agility in cornering),

middle range adjustments of wheels on axle level (contra steering of rear axle in order to virtually change vehicle length). The vehicle dynamics shall be modified and adjusted by the continuously working feedback control loops of the FAVeC layer, which can be interpreted for instance as virtual CG position modification or virtual tires exchange.

2.2 Related current research projects

In contrast to the current status in automotive industry, where the innovative potential of new actuation possibilities and the full time full authority vehicle feedback control is not fully exploited due to essentially administrative and formal reasons, there are several laboratories at famous universities and research institutes [14]-[15] that are much further with their results, towards the ideas of the FAVeC layer proposed in this project. Vehicle dynamics is governed and limited by tires forces utilization. Over-actuated vehicle concept gives rise to various means of system actuation in Multiple-Input Multiple-Output (MIMO) sense. Traditionally, vehicle controller strategies are based on anti-symmetrical braking/traction moment distribution and optimal traction moment allocation ([8] and [9]). More advanced concepts use steering action in combination with torque vectoring ([10], [11], [12] and [13]) in order to introduce closed loop stability and meet control objectives using optimization based control system development framework.

2.3 Advancements in related technologies

The torque vectoring and torque distribution is the starting point how to introduce an actuator, enabling vehicle dynamics modification, via feedback, without compromising driver full authority in the steering channel. Such systems have already left significant footprints, especially in the high performance cars department. Progressive start-up companies (like Rimac automotive [16] and Nio [17]) declare their car (see Figure 1 right) handling qualities being augmented by full torque vectoring systems, leading to significant achievements in benchmarks, such as the Nürburgring Nordschleife road-legal cars lap times.



Figure 2: Technology demonstration platforms (from left Stanford Dynamic Design Lab [14], DLR Institute of Robotics and Mechatronics [15] and Rimac automotive [16]).

The steer-by-wire technology, the essential instrumentation element for the FAVeC layer, has been recently introduced to commercial market by Nissan within their luxury brand line Infinity [18]. Significant market penetration in steer-by-wire commercial applications is the rear axle steering, where luxury cars (Audi, Porsche and higher trims of VW brand) are benefiting from this feature. The full scale demonstrators (see Figure 1 left and middle) were developed at the Stanford Dynamic Design Lab [14] and at the DLR [15] fully replacing the steering mechanical link, thus relaxing the driver full-authority demand over front axle steering. This gives possibility to fully explore the over-actuated vehicle capabilities in sense of vehicle dynamics modification by wheel force manipulation and allocation.

2.4 Relationship to Autonomous Driving

Today, autonomous driving solutions based on neural networks and Artificial Intelligence (AI) are often presented as the optimal and complete approach to the autonomous vehicle problem (the “end-to-end” approach), where nuances of the vehicle dynamics are bluntly ignored. The research area of

FAVeC solution would therefore constitute the control system “low-level” layer, with all robust stability and robust performance guarantees; and leaving the AI approaches for the “higher-level” functionalities related to image processing and trajectory planning, where these methodologies are appropriate.

3 Multi-domain objectives tradeoff & multi-layer control law architectures

Another connecting point of vehicle control systems development throughout various application fields (from aerospace to automotive and wind energy) are multi-domain objectives criteria for controller performance. There is commonly tradeoff rises between rigid body motion control objectives and "secondary", one could say constraining factors as machine operation limits are approached and exploited. On one hand the performance goals set by never ending hunger for more speed, more agility, nimbleness and precision of operation leading to more powerful and lighter machines. On other hand the structural constrains, endurance and life expectancy requirements, safe and reliable operation demands, and often crew comfort requirements. Such demanding and often conflicting set of requirements call either for complex hierarchical controller design, or employment of optimization based control law approaches, where the systematic control architecture development can be conveniently expressed in the form of a multi-objective criterion and the tedious, hard work is passed to an optimization tool. Such approach, in combination with machine iterative design, leads to new, unorthodox and usually unstable vehicle configurations, relying on control system to provide demanded stability and overall (closed loop) dynamics. Something well known to Flight Control Systems community, especially in military applications. The common control system development methodology can be divided into subtasks of actuator and sensor selection, control system design, and finally the verification. The controller design methodology considered in this thesis is further divided based on application area (aerospace and automotive) and controller structure (Feed-forward and Feedback control system). Following sections discuss these subtasks.

4 Actuator and sensor optimization

The process of actuation/sensor system design, in sense of selection of suitable physical variable for manipulation (in case of actuators) or for measurement (in case on sensors), is essential for any consequential control system development. The employment of optimization techniques in such selection process is essential especially for complex system, where placement of actuators and sensors is not intuitive or it is too demanding. On top of that the optimization criterion can be easily augmented to accommodate spatial filtration functionality. The ability to filter out unwanted signals simply by clever sensor location selection is a complementary functionality to frequency based filtration. The spatial filtration is introduced in Paper 1 of this theses.

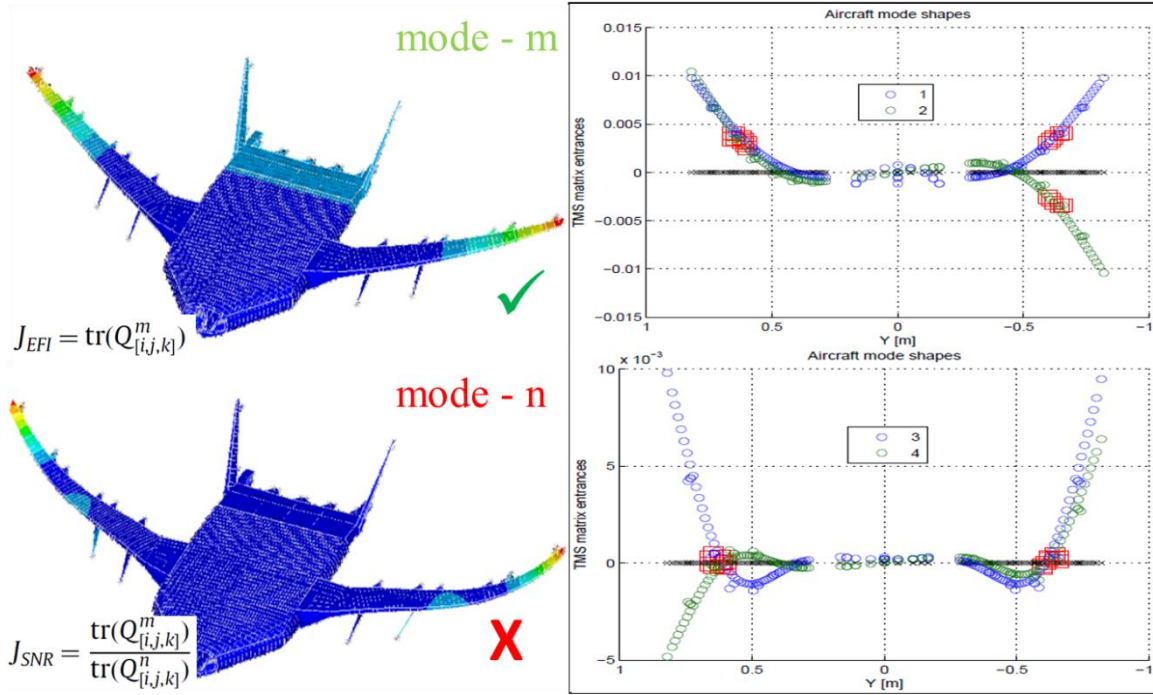


Figure 3: Aircraft symmetric wing bending mode shapes (first sym. wing bending model – left top; second sym. Wing bending mode – left bottom). Resulting sensors locations to maximize reading of required modes (right top) and minimize reading of unwanted modes (right bottom).

A new approach to optimal placement of sensors (OSP) in mechanical structures is presented. In contrast to existing methods, the presented procedure enables a designer to seek for a trade-off between the presence of desirable modes in captured measurements and the elimination of influence of those mode shapes that are not of interest in a given situation. An efficient numerical algorithm is presented, developed from an existing routine based on the Fischer information matrix analysis. We consider two requirements in the optimal sensor placement procedure. On top of the classical EFI approach, the sensors configuration should also minimize spillover of unwanted higher modes. We use the information approach to OSP, based on the effective independent method (EFI), and modify the underlying criterion to meet both of our requirements—to maximize useful signals and minimize spillover of unwanted modes at the same time, Figure 3. Performance of our approach is demonstrated by means of examples, and a flexible Blended Wing Body (BWB) aircraft case study related to a running European-level FP7 research project ‘ACFA 2020—Active Control for Flexible Aircraft’.

5 Flight Control Systems with multi-objective problem definition

The Stability Augmentation Systems (SAS) and Control/Command Augmentation Systems (CAS) are essential part of complex Flight Control Systems usually with hierarchical structure to reduce development process complexity even for rigid body control requirements. Once the set of requirements include also structural loading constraints (ultimate loading and fatigue loading), comfort requirements and safety objectives, employment of optimization based framework enabling introduction of mixed objective criterion to accommodate all these aspects is necessary. The methodology for development of CAS, taking into account both Rigid Body, as well as structural performance requirements and system uncertainty, was developed during ACFA 2020 aerospace project and is presented in Paper 2, 3 and the Book Section of this thesis.

5.1 Feed-forward Control law design

The main advantage of feed-forward control is its ability to response to measurable disturbances and commands directly, therefore with greater speed, since the lag introduced by system dynamics is not present. The fast response is important especially in case of measurable/detectable disturbance suppression. The convex synthesis technique was used in connection with L_∞ optimization in order to define mixed objective cost function respecting rigid body motion objectives, minimize structural loading and nonlinear constraints in form of actuators rate limit and saturation. Such technique was developed during ACFA 2020 project and it is introduced in Paper 2 of this thesis.

The potential advantages of Blended Wing Body (BWB) aircraft in terms of fuel efficiency are opposed by technical challenges such as the alleviation of gust loads. Due to the low wing, loading gusts, generally, have a more severe impact on BWB aircraft than on conventional aircraft. This work presents the design and optimization of a Gust Load Alleviation System (GLAS), see Figure 4 for a large BWB airliner. Numerical simulations are performed with an aeroelastic model of the aircraft including GLAS in order to compute time series of modal displacements for deriving equivalent static load cases which are used for the resizing of the aircraft structure.

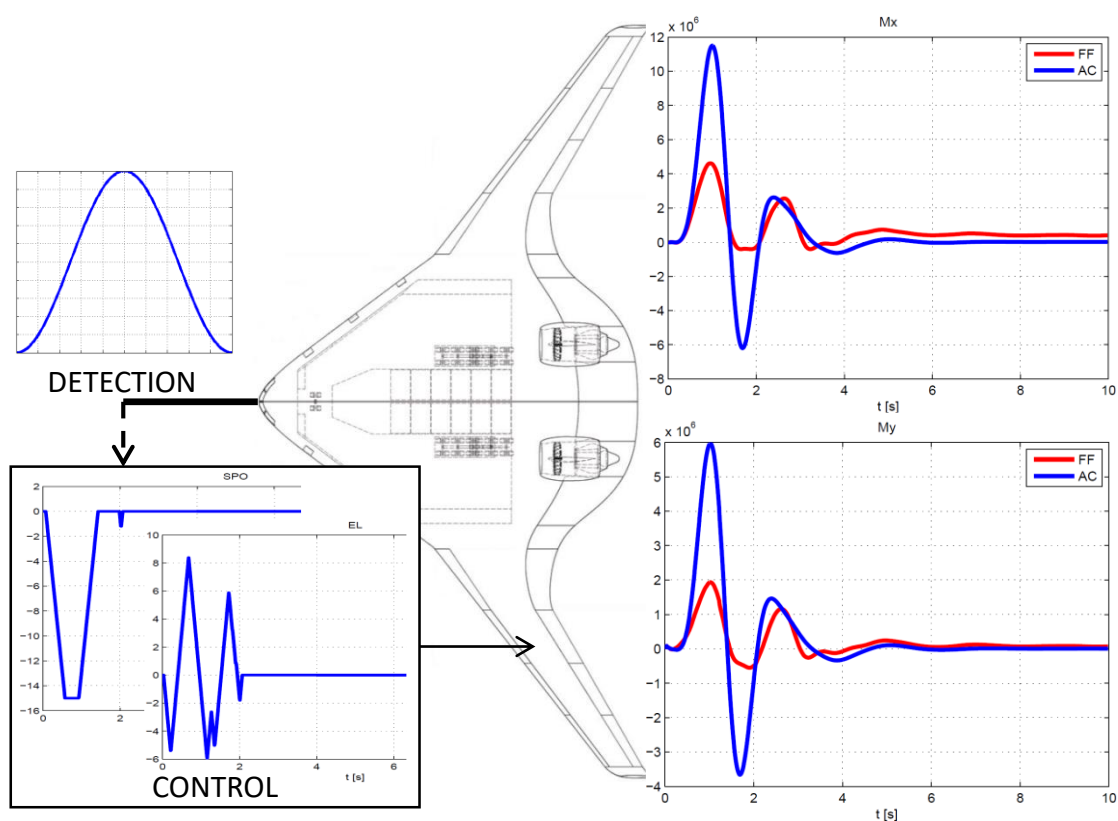


Figure 4: Setup of feed-forward Gust Load Alleviation System.

5.2 Feedback Control law design

The main drawback of feed-forward control techniques is lack of robustness. Therefore, a feedback control system is necessary as an augmentation of feed-forward controller providing demanded robustness with respect to system uncertainty and detected uncertainty deviation. Such feedback controller based on H_∞ optimization technique was developed and it is presented in Paper 3 of this thesis.

Lightweight flexible blended-wing-body (BWB) aircraft concept seems as a highly promising configuration for future high capacity airliners which suffers from reduced stiffness for disturbance

loads such as gusts. A robust feedforward gust load alleviation system (GLAS) was developed to alleviate the gust loading. This work focuses on designing a feedback controller which would improve the robust performance of the feedforward controller in reducing the peaks in wing root moments at very short gust lengths. The simulation results show that when the new feedback compensator is engaged with the feedforward controller, the performance of the GLAS system is improved significantly in terms of reduction in wing root moments for shorter as well as for longer gusts. This reduction in the wing root moment's peak provides potential structural benefits and weight savings

Finally, pure feedback and 2 Degrees of Freedom CAS based both on H_2 and H_∞ optimization techniques were developed during ACFA 2020 aerospace project. These control systems are developed following same multi-variable optimization criterion with objectives in rigid body domain as well as structural loading and passenger comfort domain, Figure 5. On top of that the embedded friendly solution (control structure low complexity approach, sometime called robust tuning) was taken into account, see Figure 6. Develop methodology was presented in the Book Section of this thesis.

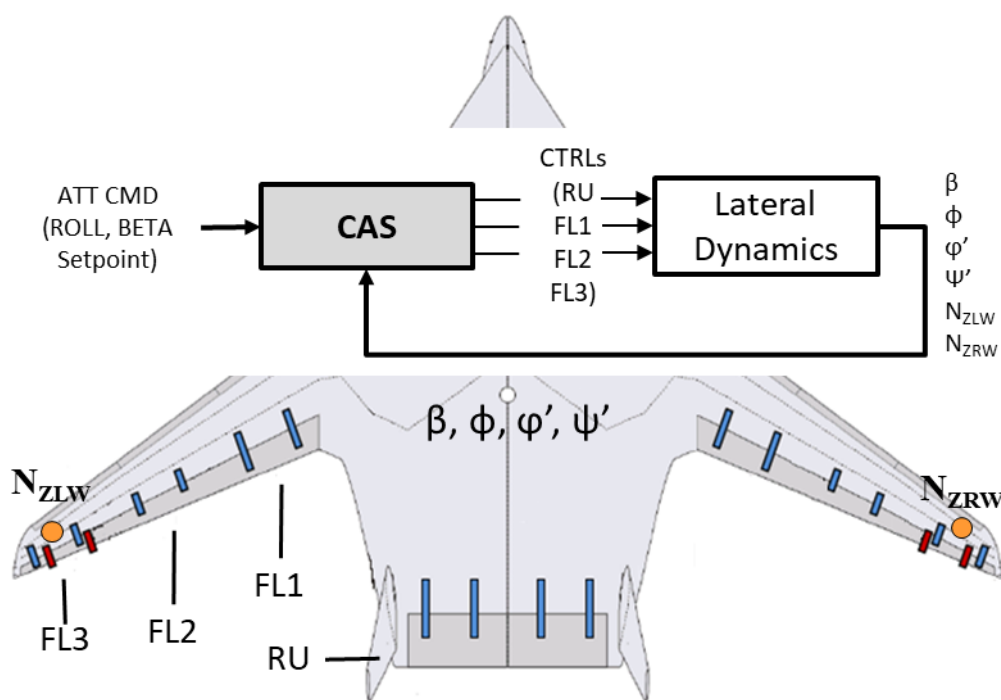


Figure 5: Setup of 2DoF Command Augmentation System (CAS) design by fixed order optimization with respect to rigid body requirements and flexible structure requirements.

Two different design approaches for design of lateral control augmentation system (CAS) for large BWB aircraft with flexible structure are elaborated and assessed in this section. The most challenging design issues are related to coupling of rigid-body (RB) mechanics and flexible dynamics. First, a classical approach is employed giving rise to separate flight dynamics controller (H_2 -optimal, with sufficient roll-off at higher frequencies to avoid spillover) and an active damper for most prominent lateral flexible modes on top of that (mixed-sensitivity H_∞ design). This approach proves successful and has obvious advantages related to the design process complexity and to implementation/verification/testing. On the other hand, there is always a risk of potentially significant performance loss compared to a fully integrated design. For this reason, a fully integrated design is also presented in the form of a fixed-order multi-input multi-output (MIMO) H_∞ -optimal flight control system (FCS) controller, obtained by means of direct non-convex non-smooth optimization using the dedicated software package HIFOO. Performance of both approaches is discussed. This design is carried out for the lateral motion of the NACRE BWB 750-passenger aircraft redesign model.

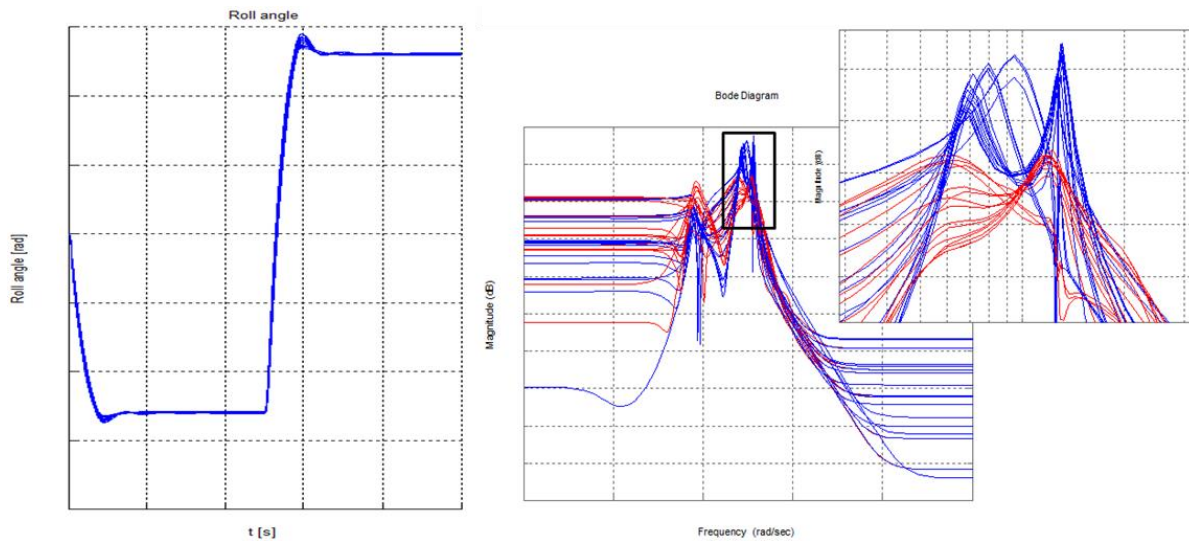


Figure 6: Roll angle response (CAS closed loop) to doublet reference signal (left). Frequency response of pure aircraft (right – blue line) and CAS closed loop (right – red line) showing increased damping of first and second structural mode.

6 Drive Control Systems

Development of SAS and CAS like control design methodology with application in automotive domain is the main objective of Full-Authority Vehicle Control system research and this thesis. Two results in form of conference papers, dealing with aerospace commonly used techniques, are presented in Paper 4 and 5.

6.1 Traction control

The full-time full-authority traction control system based on H_2 optimization approach was introduced. The driver to vehicle interface is redefined in drive-by-wire fashion, where the driver no longer commands directly the traction moment (regardless of tire to road interface conditions and wheel slip/ration or wheel spin), but rather provides reference for available traction force, which can be interpreted as the longitudinal acceleration reference. The CAS provides the driver with operation safety guarantees in form of tire to road interface preservation. The methodology is presented in Paper 4 of this thesis.

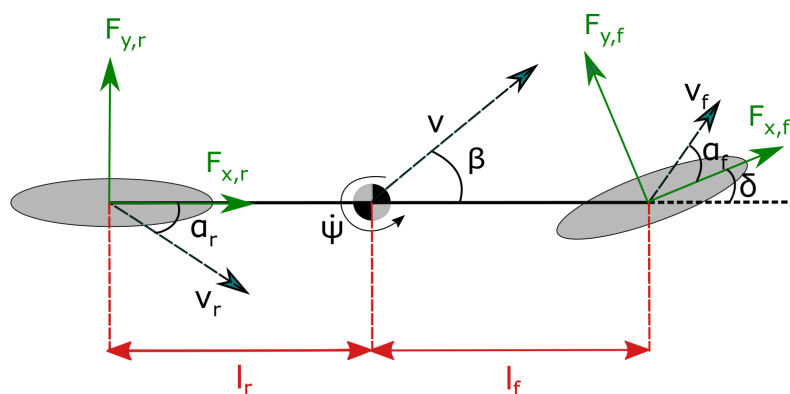


Figure 7: Vehicle single track model.

Trend of autonomous vehicles and e-mobility is in favor of an advanced control system development and deployment. Vehicle dynamics level control systems providing safety limits and high performance response, especially during high dynamics maneuvers, are necessary. This work provides solution for vehicle longitudinal dynamics (vehicle acceleration) considering physical limits given by road, tire and

vehicle dynamics respectively. The goal is to maximize vehicle longitudinal acceleration by controlling each wheel longitudinal slip ratio. Considered mathematical model is non-linear single track model, see Figure 7, incorporating non-linear Pacejka magic formula as a tire model. Design model for control system is derived as a linearized state-space model at constant acceleration operation point. Therefore, the common linearization approach, at system equilibrium, is not possible and the linearization along system trajectory is used. Such solution results in involvement of LPV techniques, as vehicle velocity is state variable. Finally, the LQ optimal control framework is employed to deliver control algorithms providing constant vehicle acceleration trajectory tracing. This is accomplished by longitudinal slip ratio control for each wheel, see Figure 8.

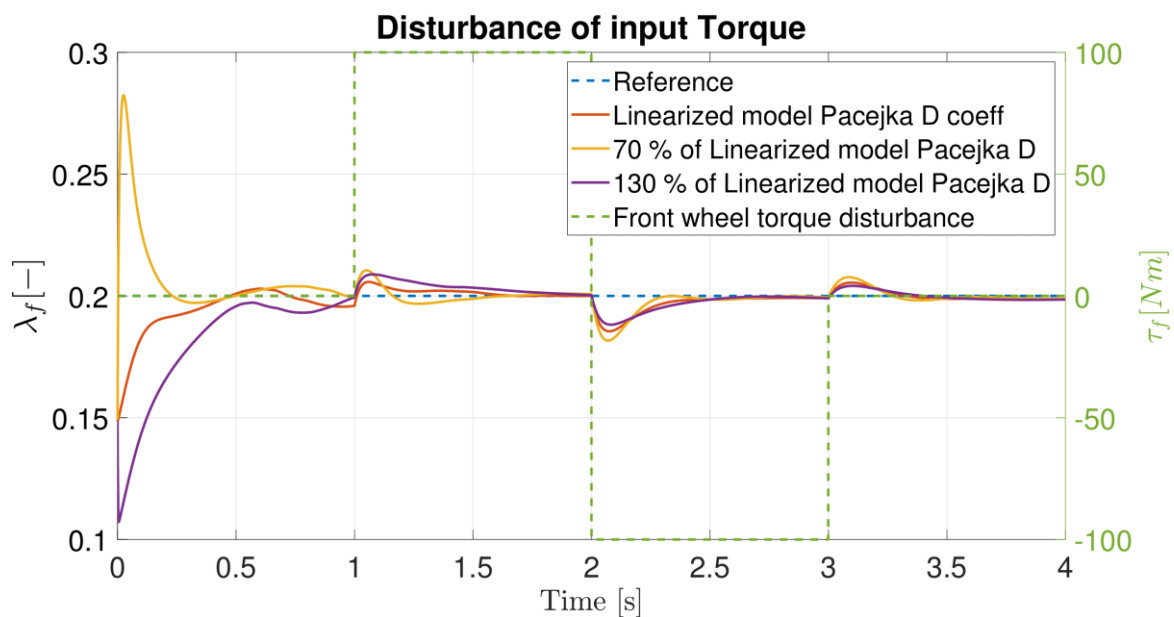


Figure 8: Response of front wheel longitudinal slip ratio (λ_f) to traction force disturbance. Robustness with respect to tire to road interface is represented by considering range of Pacejka D values (defining slip curve maximal value).

6.2 Driving envelope definition

The flight envelope concept equivalent for automotive industry, so called driving envelope, was introduced in order to define safety operation limits for road vehicles. The driving envelope concept, and more importantly the means of its protection, is an essential part for any multi-variable control system design. Such concept was introduced in Paper 5 of this thesis.

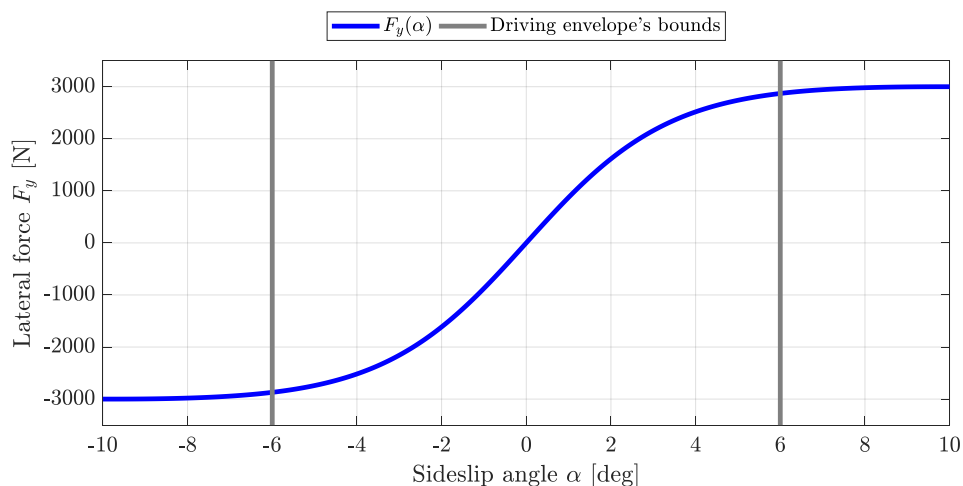


Figure 9: Front wheel lateral slip curve with limits of operation/slipping.

This paper introduces the idea of the full-time-full authority control, known from the flight control field, for the automotive industry. Also, it provides a derivation of a nonlinear single-track vehicle model for an over-actuated car and introduces the vehicle states feasibility set, called here driving envelope, inspired by aircraft flight envelope, providing safe operation zone limits for a vehicle, see Figure 9 and Figure 10. As an addition, authors show proof based on vehicle dynamic physics, what practical pros can bring the usage of the steered rear axle together with the front axle.

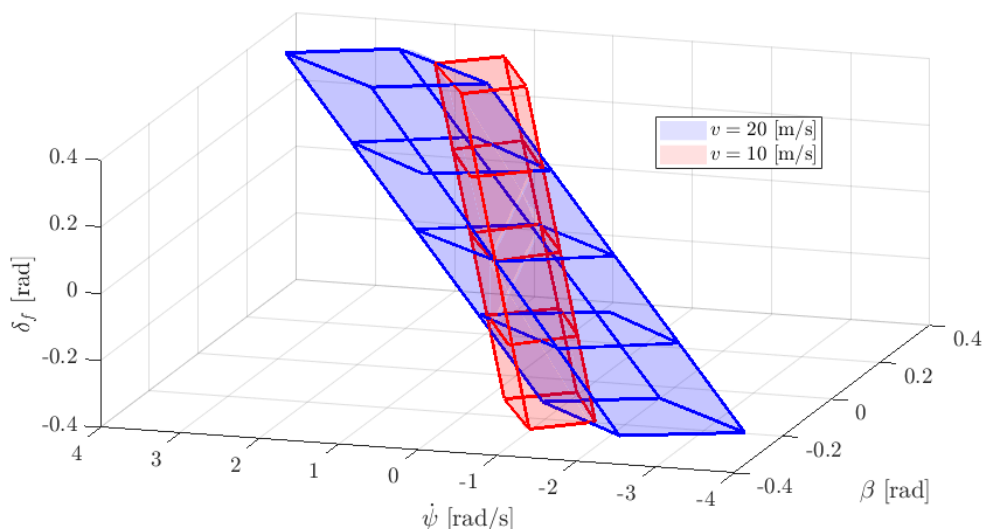


Figure 10: Front wheel driving envelope definition based on front wheel lateral slip curve limits and different cruising speed.

7 System Verification

The final step of control system development is the verification process. The foremost outcome of verification process is an examination of safety and consistent functionality of operation, reliability studies and robustness & endurance studies (in sense of all operation conditions coverage, lifetime expectancy, etc.). With technology advancements and increased system complexity it is important to come up with sophisticated means of (control) system design verification to ensure sufficient coverage of “test” scenarios and to reduce verification process time/cost. The optimization-based verification by means of testing with focus on lifetime is presented in Paper 6 of this theses. The proposed approach managed to reduce testing time be almost 50%, see Figure 12, and provided better match of structural strain distribution, see Figure 13.

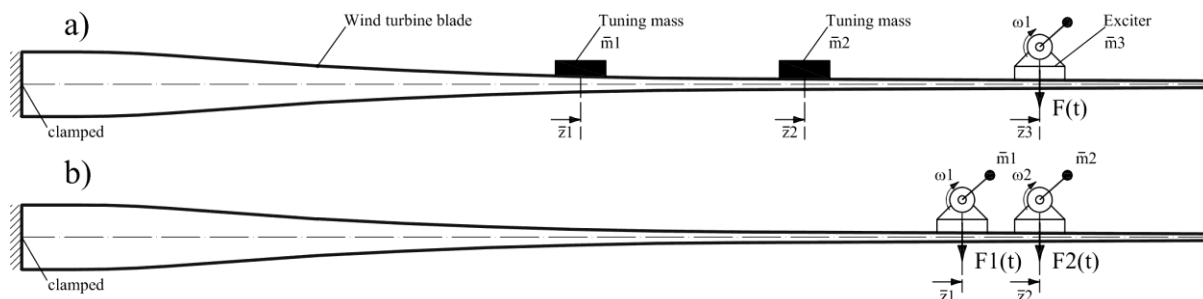


Figure 11: Wind turbine blade fatigue test setup. The conventional approach with tuning masses (to modify first flap-wise bending mode) and single frequency exciter (top). Proposed approach based on multi-mode control with two frequency exciters (bottom).

Rotor blades are among the most delicate components of modern wind turbines. Reliability is a crucial aspect, since blades shall ideally remain free of failure under ultra-high cycle loading conditions

throughout their designated lifetime of 20–25 years. Full-scale blade tests are the most accurate means to experimentally simulate damage evolution under operating conditions, and are therefore used to demonstrate that a blade type fulfils the reliability requirements to an acceptable degree of confidence. The state-of-the-art testing method for rotor blades in industry is based on resonance excitation where typically a rotating mass excites the blade close to its first natural frequency, see Figure 11. During operation the blade response due to external forcing is governed by a weighted combination of its eigenmodes. Current test methodologies which only utilize the lowest eigenfrequency induce a fictitious damage where additional tuning masses are required to recover the desired damage distribution. Even with the commonly adopted amplitude upscaling technique fatigue tests remain a time-consuming and costly endeavor. The application of tuning masses increases the complexity of the problem by lowering the natural frequency of the blade and therefore increasing the testing time. The novel method presented in this paper aims at shortening the duration of the state-of-the-art fatigue testing method by simultaneously exciting the blade with a combination of two or more eigenfrequencies. Taking advantage of the different shapes of the excited eigenmodes, the actual spatial damage distribution can be more realistically simulated in the tests by tuning the excitation force amplitudes rather than adding tuning masses. This implies that in portions of the blade the lowest mode is governing the damage whereas in others higher modes contribute more significantly due to their higher cycle count. A numerical feasibility study based on a publicly available large utility rotor blade is used to demonstrate the ability of the proposed approach to outperform the state-of-the-art testing method without compromising fatigue test requirements. It will be shown that the novel method shortens the testing time and renders the damage evolution with a higher degree of fidelity.

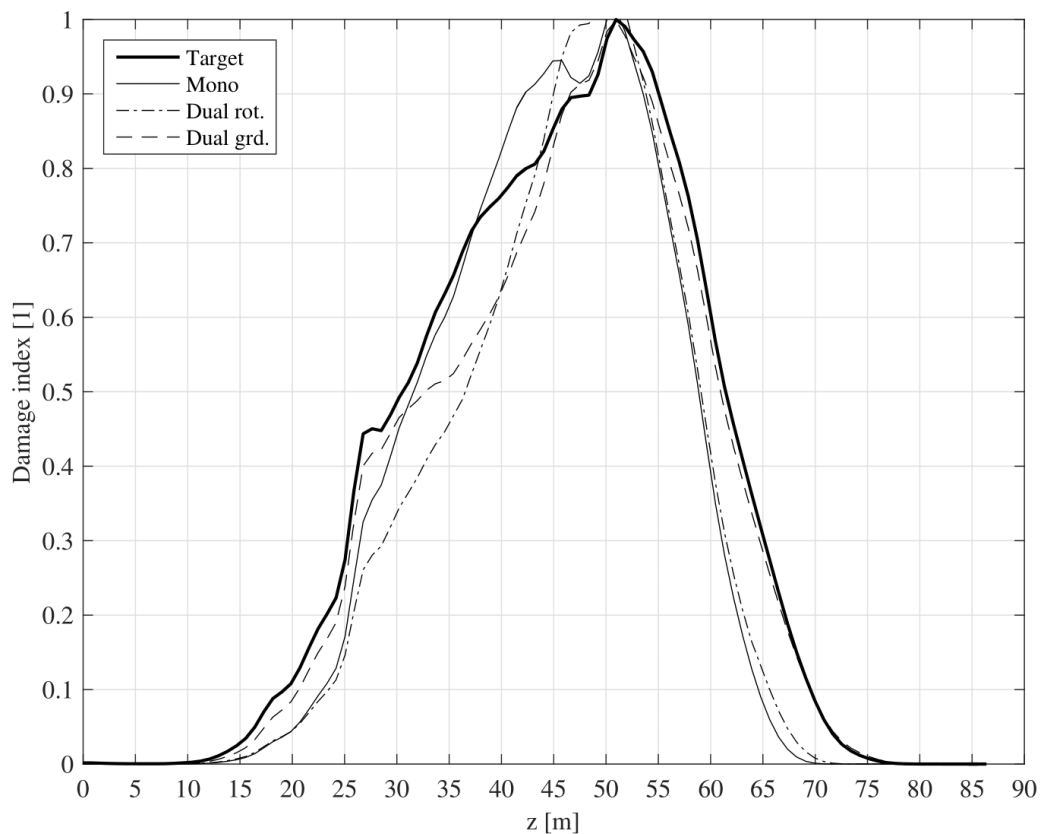


Figure 12: Fatigue damage distribution over wind turbine span.

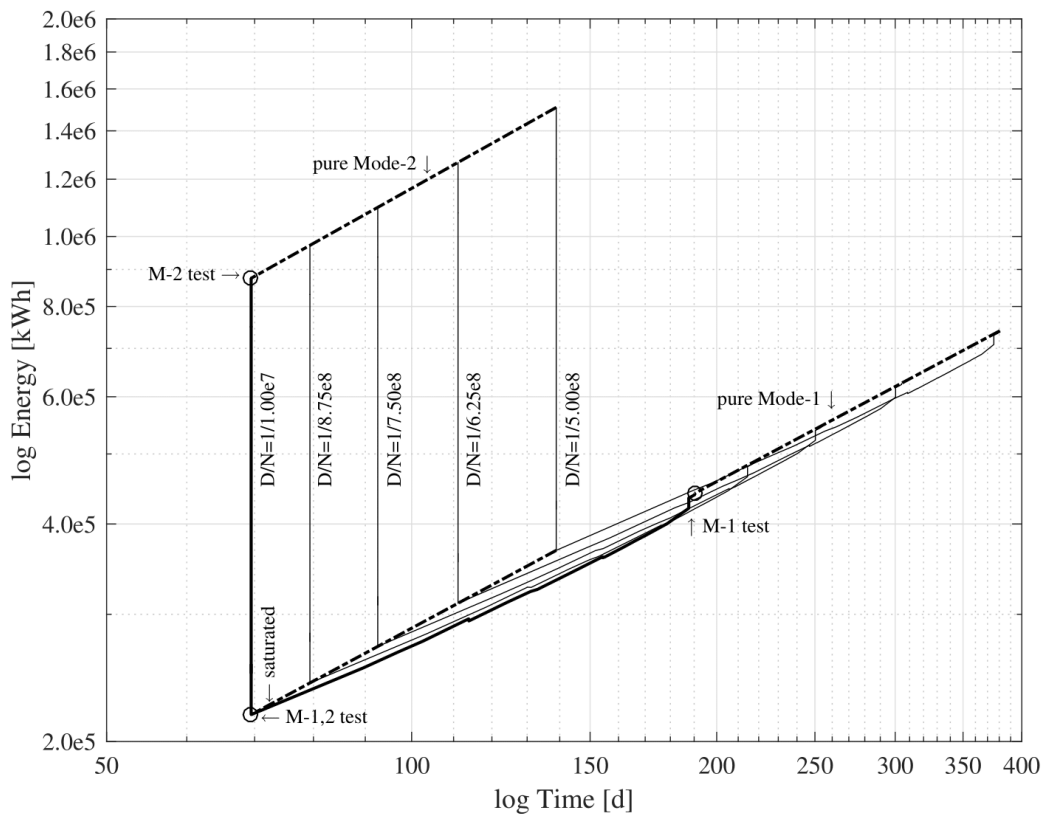


Figure 13: Energy vs. time cost of wind turbine blade fatigue test.

8 Selected Publications

The presented habilitation thesis takes the form of a collection of selected SCI Expanded journal papers, section in book and selected conference papers published by the applicant in recent ten years. The main area of interest is motion control systems development with multi-domain objectives, where the tradeoff between rigid body requirements and secondary limiting objectives (structural requirements, maneuver physical limitation, crew comfort, etc.) is critical. Such tasks are well suited for employment of optimization-based control law design framework, where the criterion can easily accommodate such complex and commonly contradicting requirements.

8.1 Paper 1: Optimal sensors placement and spillover suppression

Reference:

Haniš T. and Hromčík M.; *Optimal sensors placement and spillover suppression, Mechanical Systems and Signal Processing, 28 (2012) 367–378.*

8.2 Paper 2: Linf optimal Feed-Forward Gust Load Alleviation Design for a Large Blended Wing Body Airliner

Reference:

Hanis T., Wildschek A. and Stroscher F.; *L_∞-Optimal Feed-forward Gust Load Alleviation Design for a large Blended Wing Body Airliner. In: 4th European Conference for Aerospace Sciences. 4th European Conference for Aerospace Sciences. Saint Petersburg, 04.07.2011 - 08.07.2011. Paříž: Eucass. 2011.*

8.3 Paper 3: Active gust load alleviation system for flexible aircraft: Mixed feedforward/feedback approach

Reference:

Alam, M.; Hromčík, M.; Haniš, T.; Active Gust Load Alleviation System for Flexible Aircraft: Mixed Feedforward/Feedback Approach Aerospace science and technology. 2015, 41(1), 122-133. ISSN 1270-9638.

8.4 Section in book: Modeling and Control for a Blended Wing Body Aircraft

Reference:

edited by Martin Kozek, Alexander Schirrer; Modeling and Control for a Blended Wing Body Aircraft: A Case Study, Springer, Oct 27, 2014 - Technology & Engineering, ISBN 3319107925, 9783319107929.

8.5 Paper 4: Vehicle longitudinal dynamics control based on LQ

Reference:

Vosahlik D., Hanis T. and Hromcik H.; Vehicle longitudinal dynamics control based on LQ, 22nd International Conference on Process Control, June 11–14, 2019, Štrbské Pleso, Slovakia.

8.6 Paper 5: Introduction of Driving Envelope and Full-Time-Full-Authority Control for Vehicle Stabilization Systems

Reference:

Efremov D., Hanis T. and Hromcik H.; Introduction of Driving Envelope and Full-Time-Full-Authority Control for Vehicle Stabilization Systems, 22nd International Conference on Process Control, June 11–14, 2019, Štrbské Pleso, Slovakia.

8.7 Paper 6: A multi-frequency fatigue testing method for wind turbine rotor blades

Reference:

M. A. Eder, F. Belloni, A. Tesauro, T. Hanis; A multi-frequency fatigue testing method for wind turbine rotor blades; Journal of Sound and Vibration, Available online 2nd November 2016.

9 Conclusion

9.1 Summary

The full-time full-authority vehicle control systems are well known and for long time accepted in the aerospace industry and Flight Control Systems community. The nature of the Flight Control Systems enables control tasks decomposition, leading to hierarchically structured design and development of complex control systems in iterative manner. Such approach was used since 1940's, however once the multi-objective controller performance criteria were considered, engagement of more sophisticated approaches is necessary. Multi-variable optimization techniques were employed to fulfill demanding and often contradicting performance requirements for overall Flight Control Systems functionality (rigid body dynamics versus flexible structure requirements, vehicle motion control versus safety of operation combined with passengers' comfort demands, etc.).

The common drawback of modern (optimization based) control design techniques is the pronounced complexity of resulting controller (high order), which makes the possible implementation complicated, if feasible at all. Therefore, special attention was paid to reduction of resulting controller complexity. The fixed structure H_∞ controller optimization techniques, also known as robust tuning techniques, were employed to deliver embedded implementation friendly solutions.

Finally, the development of "Flight Control Systems" for on road vehicles is considered by application of the same principles and methodology of full-time and full-authority control structure, which was developed for aerospace case studies.

References

- [1] Nelson R., Flight stability and automatic control, Springer, 2003, ISBN: 978-0070462731.
- [2] Pratt R., Flight Control Systems: Practical Issues in Design and Implementation, IET, 2000, ISBN 0852967667
- [3] Bryson A., Control of Spacecraft and Aircraft, Princeton University Press, 1994, ISBN 0691087822
- [4] Blakelock J., Automatic Control of Aircraft and Missiles, John Wiley & Sons, Jan 18, 199, ISBN 9780471506515
- [5] Balachandran A., Application of force feedback steering for steer-by-wire vehicles with active steering, Dissertation thesis, Stanford University, 2015
- [6] Schramm D., Hiller M., Bardini R., Vehicle Dynamics, modeling and simulations, Springer, 2014, ISBN 978-3-662-54482-2
- [7] Kiencke U., Nielsen L., Automotive Control Systems: For Engine, Driveline, and Vehicle, Springer Science & Business Media, 2005, ISBN 9783540264842
- [8] Park H., Optimal tire force allocation for autonomous trajectory tracking, Dissertation thesis, 2017, Stanford University
- [9] De Novellis L., Sorniotti A., and Gruber P. Wheel torque distribution criteria for electric vehicles with torque-vectoring differentials. IEEE Transactions on Vehicular Technology, 2014.
- [10] De Cairano S., Tseng H., Bernardini D., and Bemporad A., Vehicle Yaw Stability Control by Coordinated Active Front Steering and Differential Braking in the Tire Sideslip Angles Domain. IEEE Transactions on Control Systems Technology, 2013.
- [11] Dai Y., Luo Y., Chu W., and Li K., Optimum tyre force distribution for four-wheel-independent drive electric vehicle with active front steering. International Journal of Vehicle Design, 2014.
- [12] Falcone P., Borrelli F., Asgari J., Tseng H., and Hrovat D., A model predictive control approach for combined braking and steering in autonomous vehicles. In 2007 Mediterranean Conference on Control & Automation, 2007.
- [13] Katriniok A., Maschuw J., Christen F., Eckstein L., and Abel D., Optimal Vehicle Dynamics Control for Combined Longitudinal and Lateral Autonomous Vehicle Guidance. In Control Conference (ECC), 2013 European.

Organizations and companies:

- [14] Stanford Dynamic Design Lab; <https://ddl.stanford.edu/>
- [15] DLR Institute for System Dynamics and Control; www.dlr.de
- [16] RIMAC Automotive; www.rimac-automobili.com
- [17] Nio; www.nio.io
- [18] Infiniti; www.infiniti.com

Paper 1

Haniš T. and Hromčík M.; Optimal sensors placement and spillover suppression, Mechanical Systems and Signal Processing, 28 (2012) 367–378.



Contents lists available at SciVerse ScienceDirect

Mechanical Systems and Signal Processing

journal homepage: www.elsevier.com/locate/ymssp

Optimal sensors placement and spillover suppression

Tomas Hanis^{a,*}, Martin Hromcik^b^a Department of Control Engineering, Czech Technical University in Prague, Faculty of Electrical Engineering, Technicka 2, 166 27 Prague, Czech Republic^b Center for Applied Cybernetics, Czech Technical University in Prague, Faculty of Electrical Engineering, Karlovo namesti 13-G, 121 35 Prague, Czech Republic

ARTICLE INFO

Article history:

Received 20 July 2010

Received in revised form

8 September 2011

Accepted 1 December 2011

Available online 9 January 2012

Keywords:

Optimal sensor placement

Effective independence (EFI)

Spillover suppression

ABSTRACT

A new approach to optimal placement of sensors (OSP) in mechanical structures is presented. In contrast to existing methods, the presented procedure enables a designer to seek for a trade-off between the presence of desirable modes in captured measurements and the elimination of influence of those mode shapes that are not of interest in a given situation. An efficient numerical algorithm is presented, developed from an existing routine based on the Fischer information matrix analysis. We consider two requirements in the optimal sensor placement procedure. On top of the classical EFI approach, the sensors configuration should also minimize spillover of unwanted higher modes. We use the information approach to OSP, based on the effective independent method (EFI), and modify the underlying criterion to meet both of our requirements—to maximize useful signals and minimize spillover of unwanted modes at the same time. Performance of our approach is demonstrated by means of examples, and a flexible Blended Wing Body (BWB) aircraft case study related to a running European-level FP7 research project ‘ACFA 2020—Active Control for Flexible Aircraft’.

© 2011 Elsevier Ltd. All rights reserved.

1. Introduction

Optimal sensor placement (OSP) in mechanical systems and structures has become a popular and frequently discussed research topic during last 10 years. Applications cover modeling, identification, fault detection, and active control of such systems as bridges [9,8], rail wagons [14], large space structures [15]. The goal is to tell the designers of the whole mechanical system where displacement, force, inertial acceleration, or other sensors are to be installed so that they are as informative as possible.

Various approaches have been developed. We will mention two in brief. The former, information based approach, is based on the analysis of the output shape matrix. An iterative elimination algorithm, denoted as EFI (for “Effective Independence”) has been developed that repeatedly deletes the lines of the initial, full output shape matrix with lowest amount of information, measured by either the trace or determinant of an underlying Fischer information matrix. See [4] for more detailed treatments and [9,8,15] for some case studies.

An alternative approach is based on the idea of maximizing the energy of the underlying modes in the optimally placed sensors. Related procedures lead to optimization problems over output Gramians of the system [16].

Both these approaches are applied on pre-selected modes of interest. For instance, in an active damping application for a transport vehicle, see a recent report [14], the bandwidth and thus implied modes are defined according to some comfort standards and considerations regarding impact of particular modes on the loads induced in the structure. Typically, a few

* Corresponding author. Tel.: +420 2 2435 7612; fax: +420 224 918 646.

E-mail addresses: han.tom@seznam.cz, hanistom@fel.cvut.cz (T. Hanis), xhromcik@control.felk.cvut.cz (M. Hromcik).

lower modes are selected as a result of such analysis. Resulting optimal sensors selection is subsequently called, with only those pre-selected modes in mind.

However, also those not-considered, typically mid- or high-frequency modes are still present in the process and, if excited by disturbances or the control action, they can influence the active damping system behavior in an unexpected manner. This phenomenon, denoted as spillover, cannot be captured directly by the two existing approaches mentioned above. Although some procedures have been developed that address these issues, see e.g. [17], they are based on advanced signal processing (filtering) of the measured signals and do not suggest how to modify the sensor positions themselves accordingly.

And it is exactly the problem that this paper is focused on. The aforementioned information approach is taken as the starting point. The underlying criterion is modified so that the influence of desirable modes is maximized, and those unwanted modes are minimized in the observations at the same time, see Section 2. The result is a compromise where suitably chosen simple weights serve as a tuning knob for the designer. A related numerical procedure is then developed, based on the EFI approach, in Section 3. Two examples are presented in Section 4 where one can appreciate the intuitively expected placements and study the influence of tuning. Further, a case study related to a large flexible BWB aircraft and its active vibration control system is presented in Section 5. Conclusions and suggestions for further research then follow in Section 6.

2. The effective independence method (EFI)

Optimal sensors placement techniques are extensively discussed in papers [2–9]. A short overview of the EFI method follows in this section, adopted from [9,8].

The aim of the EFI method is to select measurement positions that make the mode shapes readings of interest as linearly independent as possible. The method originates from the estimation theory and is based on maximization of related Fisher information matrix, measured by its determinant or trace. That is in fact equivalent to minimization of the condition number of the information matrix related to selected sensors. The number of sensors is iteratively reduced from an initially large candidate set by removing those sensors which contribute least of all the candidate position to the linear independence of the target mode readings. In the end, the remaining sensors are delivered as the optimal sensor set. As a useful guideline to stop the iterative removing process, the determinant of the Fisher information matrix can be plotted with respect to the number of sensors; if a considerable drop is identified, further reduction should be considered with care.

2.1. Structural model

The sensor placement problem can be investigated from uncoupled modal coordinates of governing structural equations as follows:

$$\ddot{q}_i + M_i^{-1} \cdot C_i \cdot \dot{q}_i + M_i^{-1} \cdot K_i \cdot q_i = M_i^{-1} \cdot \Phi_i^T \cdot B_0 \cdot u \quad (1)$$

$$y = \Phi \cdot q + \epsilon = \sum_{i=1}^N q_i \cdot \Phi_i + \epsilon \quad (2)$$

where q_i is the i th modal coordinate and is also the i th element of the vector, q , in the 2nd equation, M_i , K_i and C_i are the corresponding i th modal mass, stiffness and damping matrix, respectively, Φ is the mode shape matrix with its i th column as the i th mass-normalized mode shape, B_0 is simply a location matrix formed by ones (corresponding to actuators) and zeros (no load), specifying the positions of the force vector u . y is a measurement column vector indicating which positions of the structure are measured, and ϵ is a stationary Gaussian white noise with zero mean and a variance of σ^2 .

2.2. Method principle

From the output measurement, the EFI algorithm analyzes the covariance matrix of the estimate error for an efficient unbiased estimate of the modal coordinates as follows [5,6,2,3,7,9]:

$$E[(q-\hat{q}) \cdot (q-\hat{q})^T] = \left[\left(\frac{\partial y}{\partial q} \right)^T \cdot [\sigma^2]^{-1} \cdot \left(\frac{\partial y}{\partial q} \right) \right]^{-1} = Q^{-1} \quad (3)$$

where Q is the Fisher information matrix, σ^2 represents the variance of the stationary Gaussian measurement white noise ϵ in (2), E denote the mean value, and \hat{q} is the efficient unbiased estimate of q . Maximizing Q over all sensor positions will result in the best state estimate of q . Ψ denotes the eigenvectors matrix of Q and λ is related diagonal eigenvalue matrix. The EFI coefficients of the candidate sensors are computed by the following formula:

$$E_D = [\Phi \cdot \Psi] \otimes [\Phi \cdot \Psi] \cdot \lambda^{-1} \cdot \mathbf{1} \quad (4)$$

where \otimes represents a term-by-term matrix multiplication, and $\mathbf{1}$ is an $n \times 1$ column vector with all elements of $\mathbf{1}$. E_D 's entries are the EFI indices, which evaluate the contribution of all candidate sensor locations to the linear independence of

the target modes measurement. Simple selection procedure is then employed to sort the elements of the E_D vector, and to remove its smallest entry at a time and also related candidate sensor, giving rise to a reduced mode shape matrix Φ . The E_D coefficients are then updated according to the new modal shape matrix, and the process is repeated iteratively until the number of remaining sensors equals a preset value. The remaining lines of the Φ matrix (or related EFI indices) define the optimal measurement locations.

3. The effective independence method with modified criterion

The main result of the paper is presented in this section. We develop a numerical scheme for OSP, based on the EFI method, such that the spillover [10–13] of unwanted higher modes is minimized.

3.1. Method principle

The modified criterion is based on the EFI reasoning presented above. Main task of the pure EFI is just to maximize information on desired modes through optimal configuration of sensors (measurements) expressed by the Fisher information matrix (FIM), or its trace or determinant respectively. The modified criterion we propose reads

$$J_{MEFI} = \alpha J_{EFI} + (1 - \alpha) J_{SNR} \tag{5}$$

with optimum

$$J_{MEFI}^*(\alpha_0) = \max_{\substack{[i,j,k] \in \Omega \\ \alpha = \alpha_0}} [\alpha J_{EFI} + (1 - \alpha) J_{SNR}] \tag{6}$$

where

$$J_{EFI} = \text{tr}(Q_{[i,j,k]}^m) \tag{7}$$

with optimum

$$J_{EFI}^* = \max_{[i,j,k] \in \Omega} \text{tr}(Q_{[i,j,k]}^m) \tag{8}$$

stands for the standard EFI part (maximize the information content for those desirable modes), and

$$J_{SNR} = \frac{\text{tr}(Q_{[i,j,k]}^m)}{\text{tr}(Q_{[i,j,k]}^n)} \tag{9}$$

with optimum

$$J_{SNR}^* = \max_{[i,j,k] \in \Omega} \left[\frac{\text{tr}(Q_{[i,j,k]}^m)}{\text{tr}(Q_{[i,j,k]}^n)} \right] \tag{10}$$

is a newly added term to penalize the unwanted mode shapes in sensor readings. Ω is the set of all candidate triples of sensors (we are considering three sensors to be selected to simplify indexing). $Q_{[i,j,k]}^m$ is the Fisher information matrix (see (3)) for m th modes (those to be captured), where $Q_{[i,j,k]}^n$ is the Fisher information matrix for the unwanted modes. Note that maximizing (9) increases information about the desirable modes in the measurements (maximizing numerator of (9) and simultaneously suppresses the unwanted modes influence (minimizing denominator of (9)).

The coefficient $\alpha \in (0, 1)$ serves as a tuning parameter and defines the relative importance of each part of the criterion. Selection of the parameter α is problem-dependent. However, although it is not possible to give a generally valid value for α , its influence for particular data can be investigated by means of related SNR-plots as explained in Example 1 in detail, see Section 4).

The ratio part in J_{SNR} however becomes problematic as both terms in $\text{tr}(Q_{[i,j,k]}^m)/\text{tr}(Q_{[i,j,k]}^n)$ approach zero (near the nodes of both desirable and unwanted mode shapes) which leads to irrelevant results. This unintended behavior is suppressed by applying a suitable mapping function on $\text{tr}(Q_{[i,j,k]}^m)$ and $\text{tr}(Q_{[i,j,k]}^n)$ to assure for reasonably high information content (those degenerated, almost 0 candidates, are effectively discriminated). A suitable mapping function can take the following form, for example (see also Fig. 1):

$$f(t) = \sqrt[n]{1 + t^n} \tag{11}$$

3.2. Modified EFI algorithm

Now we have an accordingly modified criterion. Next task is to modify the EFI heuristic in a very similar manner, to arrive at a tractable numerical scheme for the problem. Critical part of EFI method is in evaluation of E_D vector (see (4)), so the modified evaluation takes the following shape:

$$E_{DM}(\alpha) = \alpha E_D + (1 - \alpha) E_{DSNR}$$

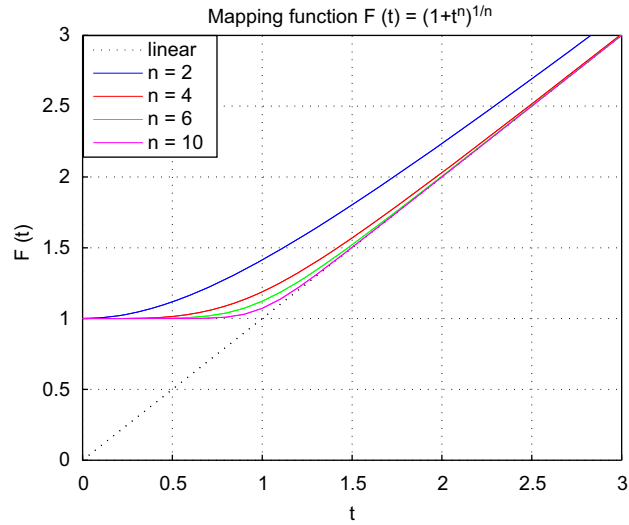


Fig. 1. Mapping function.

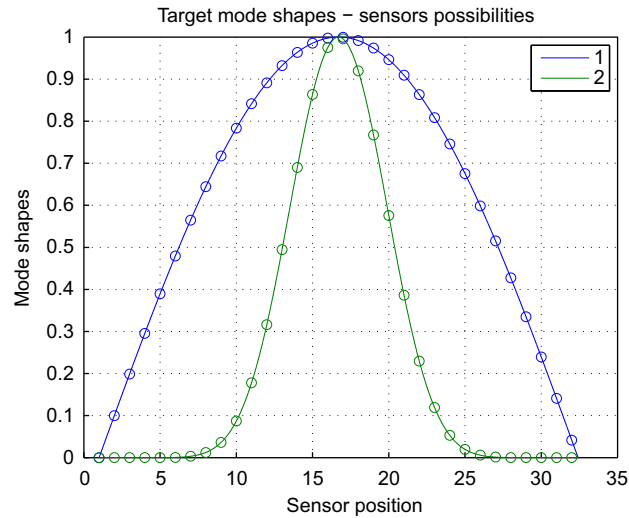


Fig. 2. Mode shapes and candidate sensor positions.

$$E_D = [\Phi \cdot \Psi] \otimes [\Phi \cdot \Psi] \cdot \lambda^{-1} \cdot 1$$

$$E_{DSNR} = \frac{[\Phi^m \cdot \Psi^m] \otimes [\Phi^m \cdot \Psi^m] \cdot \lambda^{m-1} \cdot 1}{[\Phi^n \cdot \Psi^n] \otimes [\Phi^n \cdot \Psi^n] \cdot \lambda^{n-1} \cdot 1} \tag{12}$$

Note that potential numerical issues near the node points are covered by the mapping function (11) applied on E_D and E_{DSNR} vector.

4. Example

Let us consider a flexible system with two modes of interest depicted in Fig. 2. Its structural equations read

$$\begin{bmatrix} 1 & 0 \\ 0 & 1 \end{bmatrix} \cdot \ddot{q} + \begin{bmatrix} 0.1 & 0 \\ 0 & 0.1 \end{bmatrix} \cdot \dot{q} + \begin{bmatrix} 0.1 & 0 \\ 0 & 0.1 \end{bmatrix} \cdot q = \Phi^T \cdot I_{33 \times 33} \cdot u \tag{13}$$

$$y = \Phi \cdot q \tag{14}$$

$$\Phi^T = \begin{bmatrix} 0 & 0.0998 & 0.1987 & 0.2955 & 0.3894 & 0.4794 & 0.5646 & 0.6442 & \dots \\ 0 & 0.0000 & 0.0000 & 0.0000 & 0.0001 & 0.0006 & 0.0033 & 0.0123 & \dots \\ 0.7174 & 0.7833 & 0.8415 & 0.8912 & 0.9320 & 0.9636 & 0.9854 & 0.9975 & \dots \\ 0.0361 & 0.0870 & 0.1780 & 0.3161 & 0.4947 & 0.6899 & 0.8637 & 0.9752 & \dots \\ 0.9996 & 0.9917 & 0.9738 & 0.9463 & 0.9093 & 0.8632 & 0.8085 & 0.7457 & \dots \\ 0.9957 & 0.9197 & 0.7672 & 0.5758 & 0.3864 & 0.2297 & 0.1193 & 0.0532 & \dots \\ 0.6755 & 0.5985 & 0.5155 & 0.4274 & 0.3350 & 0.2392 & 0.1411 & 0.0416 & \\ 0.0198 & 0.0059 & 0.0013 & 0.0002 & 0.0000 & 0.0000 & 0.0000 & 0.0000 & \end{bmatrix}$$

In this case it is fairly intuitive to decide by common sense where sensors should be placed if we want to maximize measurement of the first mode and reduce the second one. One can see results of the classical EFI approach in Fig. 6, related to the EFI criterion (7). It is clear that the EFI approach gives rise to sensors configuration optimal to fit the desired mode (first one), but spillover of the second one is huge. Measured energy of both modes (required E_{RQ} and not required E_{NOTRQ}) is printed in upward (Fig. 6). The signal to noise ratio coefficient (defined in dB units) was evaluated to represent

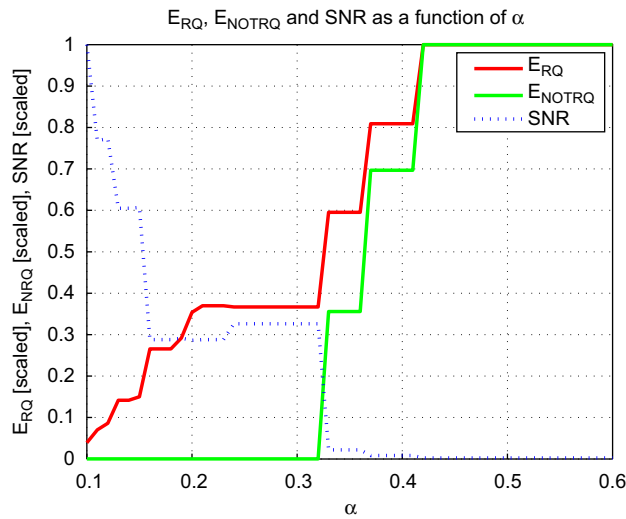


Fig. 3. The α -dependency of SNR coefficient, captured energy of required (J_{RQ}) and not required (J_{NOTRQ}) modes.

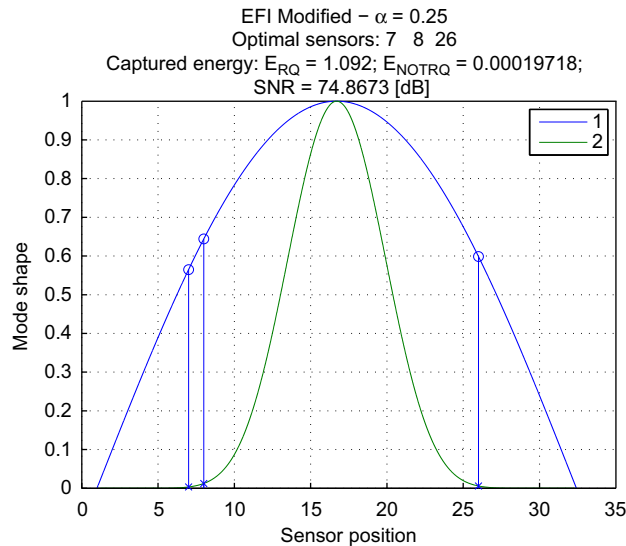


Fig. 4. OSP by the modified EFI algorithm.

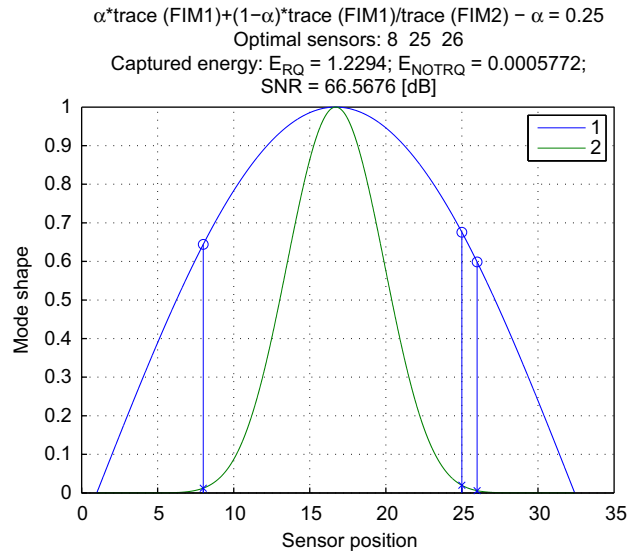


Fig. 5. OSP by direct maximization of J_{MEFI} .

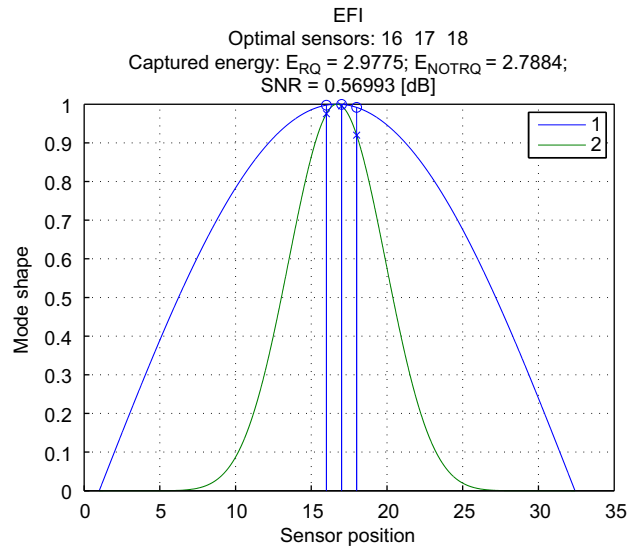


Fig. 6. OSP by classical EFI.



Fig. 7. BWB visualization.

spillover. SNR is defined by the following form:

$$SNR = 20 \cdot \log_{10} \left(\frac{E_{RQ}}{E_{NOTRQ}} \right) \tag{15}$$

Spillover reduction of the unwanted mode can be achieved by our modified criterion (see (5)). First, one has to select the α -value properly in the modified criterion (5). The dependencies of the captured energy of wanted modes (E_{RQ}) and of the captured energy of unwanted modes (E_{NOTRQ}) on α are depicted in Fig. 3. The optimal selection of the α value is at the point where E_{RQ} is large and E_{NOTRQ} is still sufficiently small. In our case, the suitable range for α is apparently the 0.2–0.3 interval, and the value of 0.25 is therefore selected.

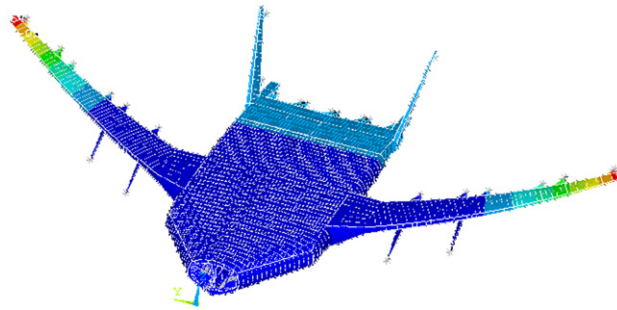


Fig. 8. Shape of first mode.

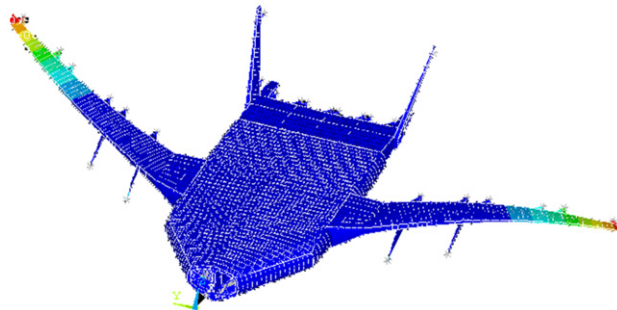


Fig. 9. Shape of second mode.

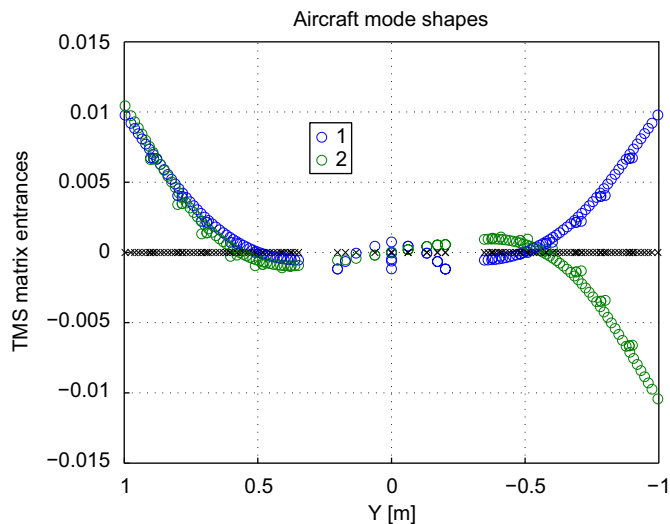


Fig. 10. Shape of first (blue o) and second (green o) modes and sensors reference positions with zero deflection (black x). (For interpretation of the references to color in this figure legend, the reader is referred to the web version of this article.)

Having α , we can proceed with the modified criterion (5) and related modified EFI algorithm of Section 3.2. Results are presented in Fig. 4. One can see that spillover of the second mode with respect to the first mode is reduced if the sensors are selected according to the proposed criterion (5), and that the measurement of the useful mode is still at a good level. In addition, the suggested modified EFI algorithm appears to be an efficient approach to solve the problem (5)—mind the modes symmetry and compare (4) (modified EFI algorithm) and Fig. 5 (optimum of (5) found by “brute force”—in this particular very simple case it is feasible to exploit all the sensors combinations and select the true optimum, at the cost of high computational burden though).

For completeness, the standard EFI approach results for three sensors are given in Fig. 6. Obviously, first mode is captured very well (which is good), nevertheless, the second mode is not attenuated at all (it is not a part of the problem formulation for the standard EFI approach).

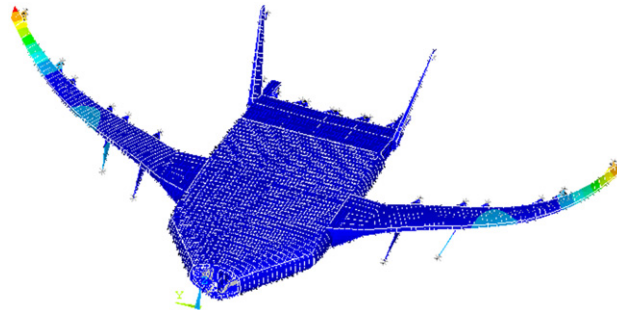


Fig. 11. Shape of third mode.

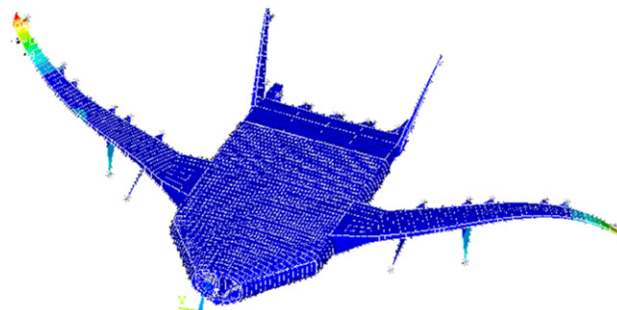


Fig. 12. Shape of fourth mode.

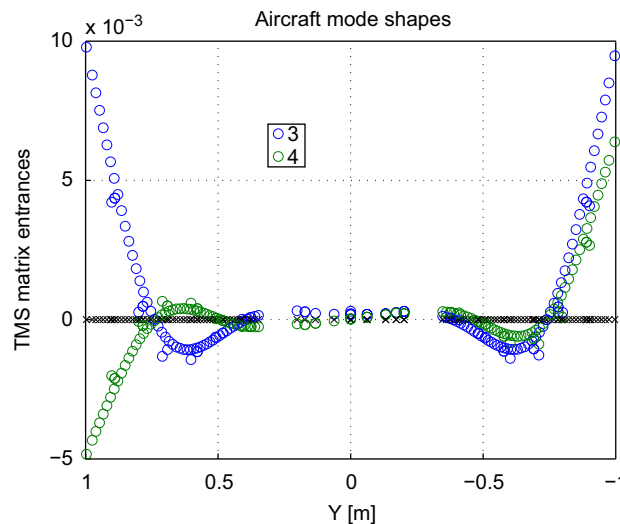


Fig. 13. Shape of third and fourth modes and sensors reference positions with zero deflection (black x).

5. Case study

ACFA 2020 is a collaborative research project funded by the European Commission under the seventh research framework programme (FP7). The project deals with innovative active control concepts for ultra efficient 2020 aircraft configurations like the blended wing body (BWB) aircraft (see Fig. 7). The Advisory Council for Aeronautics Research in Europe (ACARE) formulated the “ACARE vision 2020”, which aims for 50% reduced fuel consumption and related CO₂ emissions per passenger-kilometer and reduction of external noise. To meet these goals is very important to minimize the environmental impact of air traffic but also of vital interest for the aircraft industry to enable future growth. Blended Wing Body type aircraft configurations are seen as the most promising future concept to fulfill the ACARE vision 2020 goals because aircraft efficiency can be dramatically increased through minimization of the wetted area and reducing of structural load and vibration by active damping in an integrated control law design (adopted from [1]).

The ability to distinguish between particular modes in measurement simply by optimization of appropriate sensor configuration is critical in this application due to the presence of more flexible modes in a narrow frequency range of 0–10 Hz. We cannot therefore rely on signal processing (filtering), and we have to think of a smart sensors configuration instead.

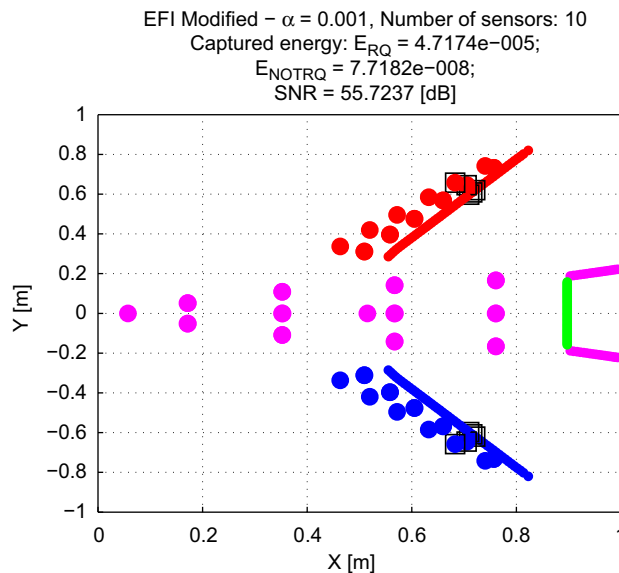


Fig. 14. Optimal sensor positions.

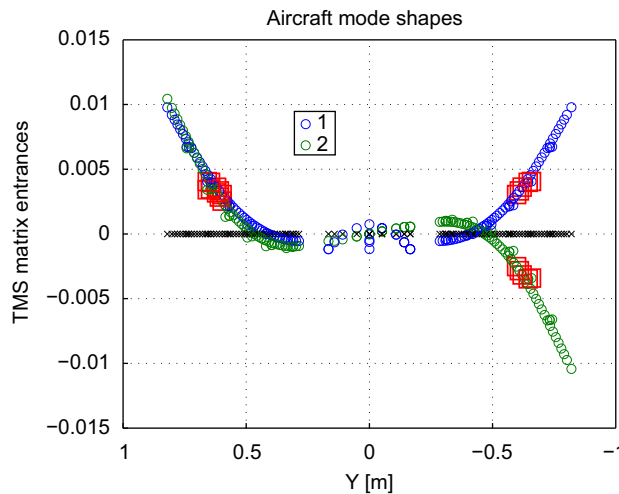


Fig. 15. Optimal sensor positions (red squares) plotted in required modes shapes (first mode shape—blue o and second mode shape—green o) and sensors reference positions with zero deflection (black x). (For interpretation of the references to color in this figure legend, the reader is referred to the web version of this article.)

The most significant modes of the aircraft are first symmetrical and anti-symmetrical wing bending modes (in frequency first and second modes). Shape of the first and second aircraft mode modeled in ANSYS can be seen from Figs. 8 and 9. The target mode shapes of these modes are plotted in Fig. 10. For all next considerations we will assume these modes to be controlled and then we need to maximize information content of these modes in measurement.

The second symmetrical and anti-symmetrical modes, also called engine modes (in frequency third and fourth modes) are considered as a non-controlled modes and we need to minimize information content of these modes in measurement. Shape of the third and fourth aircraft modes modeled in ANSYS can be seen from Figs. 11 and 12 and the target mode shapes are plotted in Fig. 13.

Results of optimization for case of first and second modes as required versus third and fourth modes to be rejected are plotted in Fig. 14. One can see that information content of required modes captured by this configuration of sensors is thousand times higher than information content of not-required modes (SNR approach 56 dB).

Selected sensors are superimposed into target mode shapes. One can see from Fig. 15 that higher deflections of wings during first symmetrical and anti-symmetrical bending modes are at more outboard positions. On the other hand, the nodes (zero deflection of wings due to particular mode) of the second symmetrical and anti-symmetrical wing bending modes are situated in the second third of wing lengths as can be seen from Fig. 16. Sensors location optimization therefore results in positions near the most outboard nodes of the not-required modes.

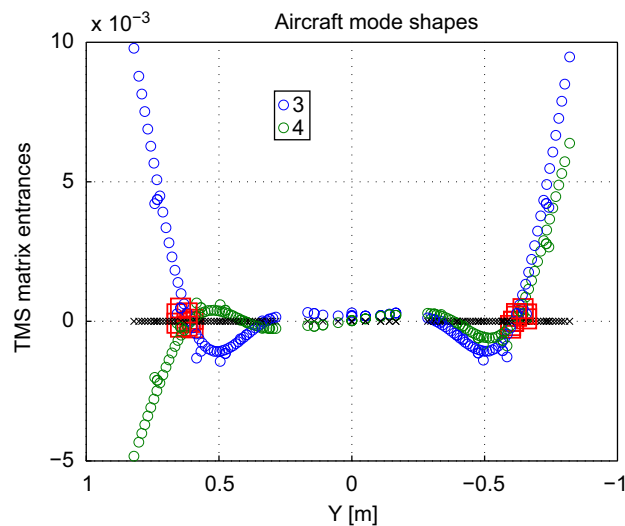


Fig. 16. Optimal sensor positions (red squares) plotted in not-required modes shapes (third mode shape—blue o and fourth mode shape—green o) and sensors reference positions with zero deflection (black x). (For interpretation of the references to color in this figure legend, the reader is referred to the web version of this article.)

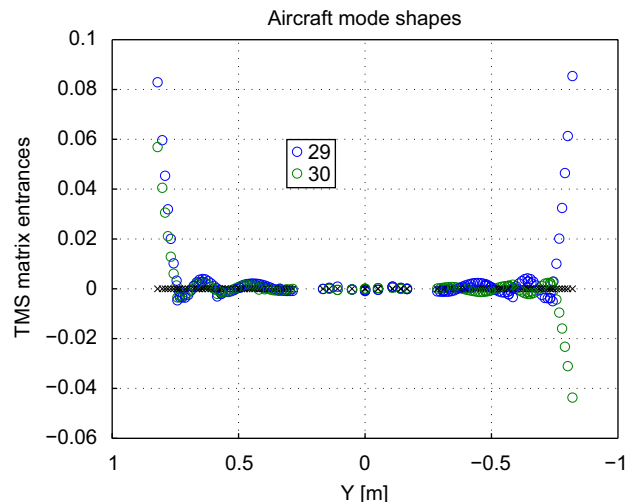


Fig. 17. Shape of 29th (blue o) and 30th (green o) modes and sensors reference positions with zero deflection (black x). (For interpretation of the references to color in this figure legend, the reader is referred to the web version of this article.)

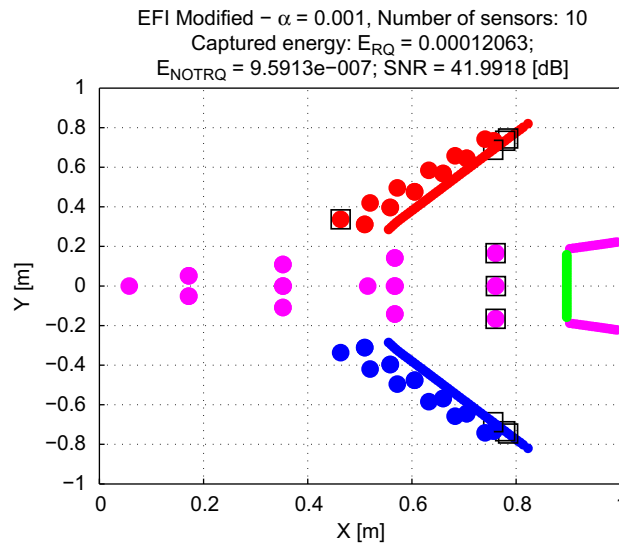


Fig. 18. Optimal sensor positions.

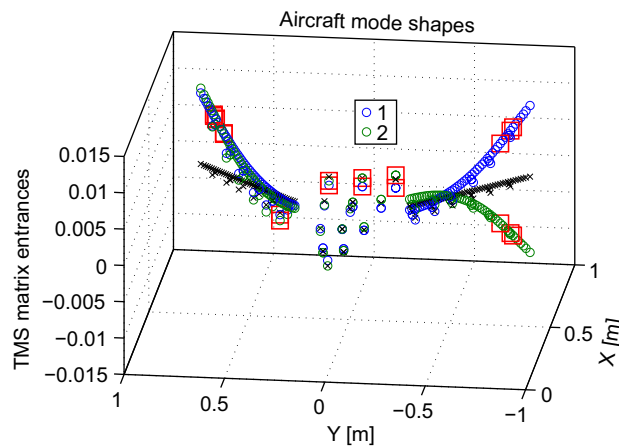


Fig. 19. Optimal sensor positions (red squares) plotted in required mode shapes (first mode shape—blue o and second mode shape—green o) and sensors reference positions with zero deflection (black x). (For interpretation of the references to color in this figure legend, the reader is referred to the web version of this article.)

The case of two highest modeled modes to be rejected is considered next. Last two modes in this case can be considered as a “high frequency noise” with defined spatial distribution to be filtered out by our OSP method. The 29th and 30th target mode shapes are plotted in Fig. 17.

Optimal sensors placement for the case of first symmetrical and anti-symmetrical modes versus last two symmetrical and anti-symmetrical modes is plotted in Fig. 18. Similarly as in the previous case, the most outboard sensors are involved due to nodes of not-required modes, but now also sensors in rear fuselage are selected. This behavior can be explained by comparison of target mode shapes plotted in Figs. 10 and 17. One can see a diving aircraft tail in case of first symmetrical wing bending mode and the fuselage rotation along longitudinal axis in the case of first anti-symmetrical wing bending mode (Fig. 10). On the other hand no deflection of fuselage occurs in 29th and 30th symmetrical and anti-symmetrical wing bending modes. This can also be seen from comparison of selected sensor sets superimposed into target mode shapes of required modes (Fig. 19) and undesirable modes (Fig. 20).

6. Conclusions

Novel approach to optimal sensors placement which takes into account the spillover issues has been presented in this paper. The information based approach was adapted, and a related effective algorithm was developed from the standard EFI procedure. Performance of the algorithm was assessed by means of a simple example and a Blended-Wing-Body aircraft case study.

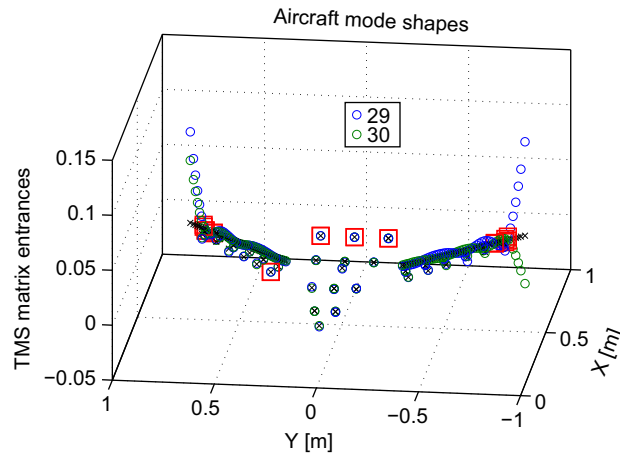


Fig. 20. Optimal sensors positions (red squares) plotted in undesirable modes shapes (29th mode shape—blue o and 30th mode shape—green o) and sensors reference position with zero deflection (black x). (For interpretation of the references to color in this figure legend, the reader is referred to the web version of this article.)

Acknowledgments

The work of M. Hromcik was supported by the Ministry of Education of the Czech Republic (MSMT) under contract No. 1M0567. The work of T. Hanis was supported by the EC project ACFA 2020—Active Control for Flexible 2020 Aircraft under No. 213321.

References

- [1] <<http://www.acfa2020.eu/>>.
- [2] D.C. Kammer, M.L. Tinker, Optimal placement of triaxial accelerometers for modal vibration tests, *Mech. Syst. Signal Process.* 18 (2004) 29–41.
- [3] D.C. Kammer, Sensor set expansion for modal vibration testing, *Mech. Syst. Signal Process.* 19 (2005) 700–713.
- [4] D.C. Kammer, Sensor placement for on-orbit modal identification and correlation of large space structures, *J. Guidance Control Dyn.* 14 (1991) 251–259.
- [5] D.C. Kammer, Optimal sensor placement for modal identification using system-realization methods, *J. Guidance Control Dyn.* 19 (3) (1995).
- [6] D.C. Kammer, Effect of model error on sensor placement for on-orbit modal identification of large space structures, *J. Guidance Control Dyn.* 15 (2) (1992).
- [7] W.L. Poston, R.H. Tolson, Maximizing the determinant of the information matrix with the effective independence method, *J. Guidance Control Dyn.* 15 (6) (1992).
- [8] D.S. Li, H.N. Li, C.P. Fritzen, The connection between effective independence and modal kinetic energy methods for sensor placement, *J. Sound Vib.* 305 (2007) 945–955.
- [9] M. Meo, G. Zumpano, On the optimal sensor placement techniques for a bridge structure, *Eng. Struct.* 27 (2005) 1488–1497.
- [10] W. Liu, Z. Hou, M.A. Demetriou, A computational scheme for the optimal sensor/actuator placement of flexible structures using spatial H2 measures, *Mech. Syst. Signal Process.* 20 (4) (2006) 881–895.
- [11] J.W. Choi, U.S. Park, Spillover suppression via eigenstructure assignment in large flexible structures, *J. Guidance Control Dyn.* 25 (3) (2001).
- [12] Y. Chait, C.J. Radcliffet, Control of flexible structures with spillover using an augmented observer, *J. Guidance Control Dyn.* 12 (2) (1989).
- [13] J.W. Choi, U.S. Park, Spillover stabilization of large space structures, *J. Guidance Control Dyn.* 13 (6) (1989).
- [14] Ch. Benatzky, M. Kozek, A. Schirrer, A. Stribersky, Vibration damping of a flexible car body structure using Piezo-Stack actuators, in: 17th IFAC World Congress, Seoul, Korea, 2008.
- [15] L. Yao, W.A. Sethares, D.C. Kammer, Sensor placement for on-orbit modal identification of large spacestructure via a genetic algorithm, in: IEEE International Conference on Systems Engineering, 1992, Kobe, Japan, 1992, pp. 332–335.
- [16] W.K. Gawronski, *Advanced Structural Dynamics and Active Control of Structures*, Springer-Verlag, New York, 2004.
- [17] M.-H. Kim, D.J. Inman, Reduction of observation spillover in vibration suppression using a sliding mode observer, *J. Vib. Control* 7 (2001) 1087–1105.

Paper 2

Hanis T., Wildschek A. and Stroscher F.; L_∞ -Optimal Feed-forward Gust Load Alleviation Design for a large Blended Wing Body Airliner. In: 4th European Conference for Aerospace Sciences. 4th European Conference for Aerospace Sciences. Saint Petersburg, 04.07.2011 - 08.07.2011. Paříž: Eucass. 2011.

L_{∞} -OPTIMAL FEEDFORWARD GUST LOAD ALLEVIATION DESIGN FOR A LARGE BLENDED WING BODY AIRLINER

A. Wildschek¹, T. Haniš², and F. Stroscher³

¹EADS Innovation Works
Munich 81663, Germany

²Czech Technical University in Prague
Prague 16627, Czech Republic

³Technische Universität München
Garching 85747, Germany

The potential advantages of Blended Wing Body (BWB) aircraft in terms of fuel efficiency are opposed by technical challenges such as the alleviation of gust loads. Due to the low wing, loading gusts, generally, have a more severe impact on BWB aircraft than on conventional aircraft. This paper presents the design and optimization of a Gust Load Alleviation System (GLAS) for a large BWB airliner. Numerical simulations are performed with an aeroelastic model of the aircraft including GLAS in order to compute time series of modal displacements for deriving equivalent static load cases which are used for the resizing of the aircraft structure.

1 INTRODUCTION

For a significant fuel efficiency improvement on long-range transport aircraft, the transition to BWB configurations offers a promising long-term solution. The advantage of higher lift-to-drag ratio is opposed by technical challenges such as the design of a flat pressurized cabin, specific demands on the control system due to the high coupling between flap deflections and aircraft movements in all three axes, handling asymmetric engine failure without tail as discussed in [1] as well as handling gust loads. Due to the low wing loading, BWB aircraft are generally more sensitive to gust loads than conventional wing tube aircraft. The investigations in this paper are based on the ACFA BWB (Active Control for Flexible BWB Aircraft), a 450-passenger configuration with two rear-mounted

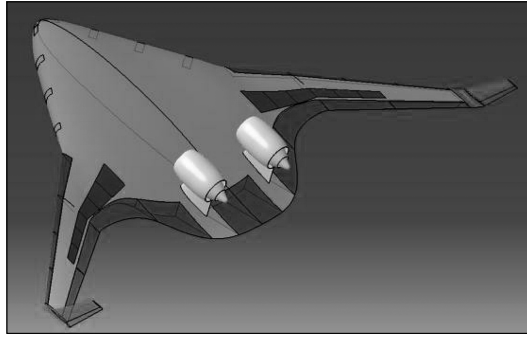


Figure 1 Control surface setting of the ACFA BWB

turbofan engines, which originates from the European project ACFA2020 (Active Control of Flexible 2020 Aircraft) (Fig. 1).

The structural concept is based on gust and manoeuvre load computations. For some fuel configurations, the BWB airliner is statically unstable, thus requiring active stabilization. The coupled aeroelastic/flight mechanic BWB model used for this investigation is parameterized in Mach, dynamic pressure, fuel mass, and center of gravity (CG) position. Three discrete CG positions are considered. The CG variation is achieved by fuel redistribution which is important on a BWB airplane for trim without too large control surface deflections in order to achieve optimum cruise performance [2]. The other three model parameters are defined on a much finer grid.

In this investigation, the BWB airliner is controlled using 12 trailing edge flaps and 12 spoilers on the upper side of the wings. Reasonable nonlinear actuators are modeled for actuation of said control surfaces. On each wing, three inner spoilers are actuated simultaneously and three outer spoilers are actuated simultaneously. Artificial pitch stiffness is basically achieved by feedback of the incremental vertical CG load factor Δn_z to 4 elevators. In order to achieve similar characteristics as for an aircraft with neutral stability, this feedback is done via a proportional-integral controller [3]. A pitch damper (i. e., feedback from pitch rate q to the elevators) allows placement of the poles of the angle of attack mode. In order to additionally damp the first symmetric wing bending mode, modal wing bending accelerations are measured for dynamic actuation of the outer wing trailing edge flaps [4]. The commands of the feedforward gust load alleviation system are just added to the commands of this flight control law. Taking into account manoeuvre load alleviation [5], gust loads become the dominant sizing factor. For efficient gust load alleviation, the weighted L_∞ norm of the responses of wing bending and torsion moment as well as shear force need to be minimized for gusts of different scale lengths throughout the whole flight

envelope while not exceeding maximum and minimum load factor. Section 2 will provide an optimization procedure for such GLAS considering these constraints.

2 GUST LOAD ALLEVIATION DESIGN

Lead time information about the gust is acquired at the aircraft nose by the alpha probe. The alpha probe measures $\alpha_{\text{air}}(t)$, a signal which contains a share due to gust as well as a share due to motion of the flexible aircraft. For the GLAS, however, $\alpha_{\text{wind}}(t)$ is required, i. e., only the share due to gust. According to [6], the computation of $\alpha_{\text{wind}}(t)$ is done by the following algorithm:

$$\alpha_{\text{wind}}(t) = \cos(\Phi(t)) \left[\arcsin\left(\frac{\dot{H}(t)}{V_{\text{TAS}}(t)}\right) - \Theta(t) \right. \\ \left. + \cos(\Phi(t)) \left(\alpha_{\text{air}}(t) + \frac{q(t)r_{\text{AoA}}}{V_{\text{TAS}}(t)} \right) + \sin(\Phi(t)) \left(\beta - \frac{r(t)r_{\text{AoS}}}{V_{\text{TAS}}(t)} \right) \right]. \quad (1)$$

Thereby, $\Phi(t)$ is the bank angle in radians; $\dot{H}(t)$ is the aircraft's inertial vertical speed in m/s; $V_{\text{TAS}}(t)$ is the flight velocity of the aircraft in m/s with respect to the surrounding air; $\Theta(t)$ is the pitch angle in radians; $\beta(t)$ is the sideslip angle in radians; $r(t)$ is the yaw rate in rad/s; and r_{AoA} and r_{AoS} are the distances in meters from the CG to the alpha and to the beta sensor, respectively. Since, e. g., the vertical speed is computed by the inertia measurement unit by complementary filtering, this signal is delayed more than the other signals, which can be directly measured, such as the angle of attack of the alpha probe. In [6], it is suggested to artificially delay also the other signals; so, the equation for computation of alpha wind is mathematically correct. However, this introduces a delay on the reference signal required for feedforward gust load alleviation which is bad for reaction time of the GLAS. It was found that vertical speed does not need to be delayed because it changes very slowly anyhow. The GLAS control setup is similar to the one described in [7–9] and shown in Fig. 2 for the physical aircraft. Solid lines illustrate actual signals whereas dashed lines illustrate effects propagating through the atmosphere.

Exogenous disturbance in terms of (time dependent) vertical airflow stochastically distributed in space $w(t, x, y, z)$ excites the flexible aircraft. The share in the error signal vector $\vec{e}(t)$ coming from said disturbance is denoted disturbance signal vector $\vec{d}(t)$. Exogenous disturbance also excites the alpha probe which measures $\alpha_{\text{air}}(t)$. The signal $\alpha_{\text{wind}}(t)$ is high passed in order to get rid of constant components which cannot be accurately cancelled by Eq. (1). Resulting signal is shaped by Finite Impulse Response (FIR) filters with vector of transfer functions $\vec{H}(s)$ (i. e., one FIR filter per actuated control surface pair) in order to

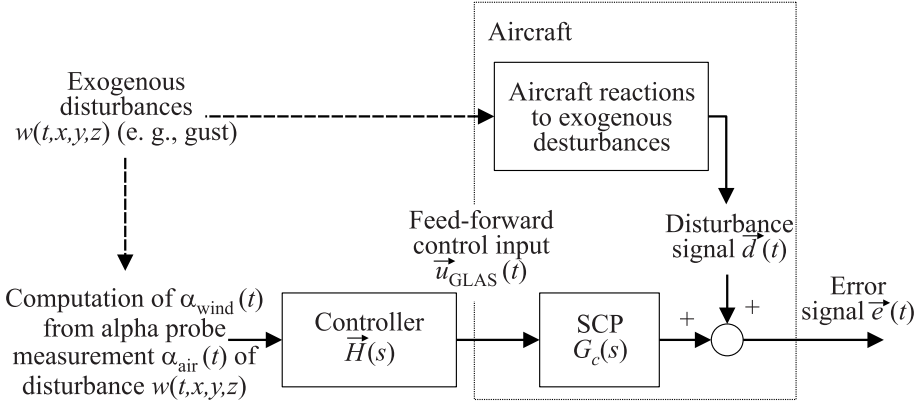


Figure 2 GLAS control setup

generate the control commands $\vec{u}_{\text{GLAS}}(t)$ for different control surface pairs (e. g., symmetrically driven ailerons or spoilers or elevators). The effect of $\vec{u}_{\text{GLAS}}(t)$ on $\vec{e}(t)$ is obtained by filtering $\vec{u}_{\text{GLAS}}(t)$ by the so-called Secondary Control Path (SCP). Considering a mathematical model of the aircraft's equations of motion linearized in a certain trim point, the error signal $\vec{e}(t)$ is just the sum of $\vec{d}(t)$ and $\vec{u}_{\text{GLAS}}(t)$, filtered by the matrix of transfer functions of the SCP, denoted $G_c(s)$. On the real aircraft, the error signal vector $\vec{e}(t)$ contains only physical signals (e. g., the incremental load factor $\Delta n_z(t)$) which can be used for in-flight monitoring of GLAS performance.

For GLAS optimization based on some model of the airplane, $\vec{e}(t)$ can also contain unphysical signals such as incremental wing bending and torsion moments as well as shear force at different wing cuts. The design objective is to adjust $\vec{H}(s)$ in order to minimize the L_∞ -norm of a criteria based on forces and moments as will be explained later, keep $\Delta n_z(t)$ within certain limits (for passenger safety) and at the same time, do not exceed certain limits for the L_∞ -norms of $\vec{u}_{\text{GLAS}}(t)$, i. e., considering saturations of control surfaces. In this investigation, the GLAS uses 4 pairs of control surfaces: elevators, inner spoilers, outer spoilers, and symmetrically driven ailerons. The vector of control commands $\vec{u}_{\text{GLAS}}(t)$ thus can be written as

$$\vec{u}_{\text{GLAS}}(t) = (u_{\text{el GLAS}}(t), u_{\text{spoiler1 GLAS}}(t), u_{\text{spoiler2 GLAS}}(t), u_{\text{ai GLAS}}(t))^{\text{T}}.$$

The superscript T denotes transposition; $u_{\text{el GLAS}}(t)$ denotes the GLAS command to elevators; $u_{\text{spoiler1 GLAS}}(t)$ denotes the GLAS command to the inner spoilers; $u_{\text{spoiler2 GLAS}}(t)$ denotes the GLAS command to the outer spoilers; and $u_{\text{ai GLAS}}(t)$ denotes the GLAS command to ailerons. The discrete time control command for, e. g., elevators is generated by filtering a sampled version of high

passed signal $\alpha_{\text{wind}}(n)$ by an FIR filter with filter length N . Thus, in the following, all continuous time signals are used in discrete time with T_s denoting the sampling period, and n denoting the time step. With z denoting the z -transform variable and z^{-1} , therefore, denoting a one sample delay, the z -transfer function of the FIR controller for, e. g., the elevators $H_{\text{el}}(z)$ can be written as:

$$H_{\text{el}}(z) = h_{0\text{el}} + h_{1\text{el}}z^{-1} + h_{2\text{el}}z^{-2} + \dots + h_{N-1\text{el}}z^{-N+1}.$$

The discrete time command to, e. g., the elevator at time step n is

$$u_{\text{elGLAS}}(n) = \vec{h}_{\text{el}}^T \vec{\alpha}(n) = \vec{\alpha}^T(n) \vec{h}_{\text{el}}$$

with

$$\vec{h}_{\text{el}} = [h_{0\text{el}}, h_{1\text{el}}, h_{2\text{el}}, \dots, h_{N-1\text{el}}]^T$$

denoting the vector of FIR coefficients, and $\vec{\alpha}(n)$ denoting the vector of the sampled reference signal at time step n :

$$\vec{\alpha}(n) = [\alpha(n), \alpha(n-1), \dots, \alpha(n-N+1)]^T.$$

The discrete time signal $\alpha(n)$ is obtained by high pass filtering of $\alpha_{\text{wind}}(n)$ and feeding this signal through a threshold switch. Since in opposition to turbulence, a 1-cosine gust is a finite event of duration of $2H/V_{\text{TAS}}$, the discrete time sequence of $u_{\text{elGLAS}}(n)$ due to a gust measured by the alpha probe and after conditioning and sampling being fed through the FIR filter can be written as

$$\begin{pmatrix} u_{\text{elGLAS}}(n=0) \\ u_{\text{elGLAS}}(n=1) \\ \dots \\ u_{\text{elGLAS}}(n) \\ \dots \\ u_{\text{elGLAS}}\left(n = F_s \frac{2H}{V_{\text{TAS}}} + N - 2\right) \\ u_{\text{elGLAS}}\left(n = F_s \frac{2H}{V_{\text{TAS}}} + N - 1\right) \\ 0 \\ \dots \end{pmatrix}$$

$$= \begin{pmatrix} \alpha(n=0) & 0 & \cdots & 0 & 0 \\ \alpha(n=1) & \alpha(n=0) & \cdots & 0 & 0 \\ \cdots & \cdots & \cdots & \cdots & \cdots \\ \alpha(n) & \alpha(n-1) & \cdots & \alpha(n-N+2) & \alpha(n-N+1) \\ \cdots & \cdots & \cdots & \cdots & \cdots \\ 0 & 0 & \cdots & \alpha\left(n = F_s \frac{2H}{V_{TAS}}\right) & \alpha\left(n = F_s \frac{2H}{V_{TAS}} - 1\right) \\ 0 & 0 & \cdots & 0 & \alpha\left(n = F_s \frac{2H}{V_{TAS}}\right) \\ 0 & 0 & \cdots & 0 & 0 \\ \cdots & \cdots & \cdots & \cdots & \cdots \end{pmatrix} \times \begin{pmatrix} h_{0\text{el}} \\ h_{1\text{el}} \\ \cdots \\ h_{N-2\text{el}} \\ h_{N-1\text{el}} \end{pmatrix}. \quad (2)$$

Here, H denotes the gust gradient distance and V_{TAS} is the true airspeed which is considered constant for the gust definition.

2.1 Formulation of the Optimization Problem

In the following, the constraints for optimization of the 4 FIR filters for control commands for elevators, inner spoilers, outer spoilers, and symmetrically driven ailerons are formulated. With sizing gusts of different lengths from 30 to 500 ft starting at time $t = 0$, it was sufficient to fulfill the following constraints within a time interval $[0; t_{\text{end}}]$ of 10 s since oscillations excited by gust are diminished after that amount of time. On the one hand, the maximum and minimum control surface deflections need to be bounded by:

$$\left. \begin{aligned} u_{\text{el GLAS}}(n) &\leq u_{\text{el max}} \quad \forall n \in [0; t_{\text{end}}F_s]; \\ u_{\text{el GLAS}}(n) &\geq u_{\text{el min}} \quad \forall n \in [0; t_{\text{end}}F_s]; \end{aligned} \right\} \quad (3)$$

$$\left. \begin{aligned} u_{\text{spoiler1 GLAS}}(n) &\leq u_{\text{spoiler1 max}} \quad \forall n \in [0; t_{\text{end}}F_s]; \\ u_{\text{spoiler1 GLAS}}(n) &\geq u_{\text{spoiler1 min}} \quad \forall n \in [0; t_{\text{end}}F_s]; \\ u_{\text{spoiler2 GLAS}}(n) &\leq u_{\text{spoiler2 max}} \quad \forall n \in [0; t_{\text{end}}F_s]; \\ u_{\text{spoiler2 GLAS}}(n) &\geq u_{\text{spoiler2 min}} \quad \forall n \in [0; t_{\text{end}}F_s]; \\ u_{\text{ai GLAS}}(n) &\leq u_{\text{ai max}} \quad \forall n \in [0; t_{\text{end}}F_s]; \\ u_{\text{ai GLAS}}(n) &\geq u_{\text{ai min}} \quad \forall n \in [0; t_{\text{end}}F_s] \end{aligned} \right\} \quad (4)$$

with subscript ‘max’ denoting maximum allowed deflection of the respective control surface, and subscript ‘min’ denoting prescribed minimum allowed deflection of the respective control surface. On the other hand, the deflection rates \dot{u} need to be limited because the available actuators’ energy is finite. Thereby, F_s is the sampling frequency, and $T_s = 1/F_s$ denotes the sampling time of the discrete controller:

$$\left. \begin{aligned} \frac{u_{\text{el GLAS}}(n) - u_{\text{el GLAS}}(n-1)}{T_s} &\leq \dot{u}_{\text{el max}} \quad \forall n \in [1; t_{\text{end}}F_s]; \\ \frac{u_{\text{el GLAS}}(n) - u_{\text{el GLAS}}(n-1)}{T_s} &\geq \dot{u}_{\text{el min}} \quad \forall n \in [1; t_{\text{end}}F_s]; \end{aligned} \right\} \quad (5)$$

$$\left. \begin{aligned} \frac{u_{\text{spoiler1 GLAS}}(n) - u_{\text{spoiler1 GLAS}}(n-1)}{T_s} &\leq \dot{u}_{\text{spoiler1 max}} \quad \forall n \in [1; t_{\text{end}}F_s]; \\ \frac{u_{\text{spoiler1 GLAS}}(n) - u_{\text{spoiler1 GLAS}}(n-1)}{T_s} &\geq \dot{u}_{\text{spoiler1 min}} \quad \forall n \in [1; t_{\text{end}}F_s]; \\ \frac{u_{\text{spoiler2 GLAS}}(n) - u_{\text{spoiler2 GLAS}}(n-1)}{T_s} &\leq \dot{u}_{\text{spoiler2 max}} \quad \forall n \in [1; t_{\text{end}}F_s]; \\ \frac{u_{\text{spoiler2 GLAS}}(n) - u_{\text{spoiler2 GLAS}}(n-1)}{T_s} &\geq \dot{u}_{\text{spoiler2 min}} \quad \forall n \in [1; t_{\text{end}}F_s]; \\ \frac{u_{\text{ai GLAS}}(n) - u_{\text{ai GLAS}}(n-1)}{T_s} &\leq \dot{u}_{\text{ai max}} \quad \forall n \in [1; t_{\text{end}}F_s]; \\ \frac{u_{\text{ai GLAS}}(n) - u_{\text{ai GLAS}}(n-1)}{T_s} &\geq \dot{u}_{\text{ai min}} \quad \forall n \in [1; t_{\text{end}}F_s]. \end{aligned} \right\} \quad (6)$$

For passenger safety, the maximum and the minimum load factors need to be bounded too:

$$n_z(n) \leq 2.5 \quad \forall n \in [0; t_{\text{end}}F_s]; \quad n_z(n) \geq 0 \quad \forall n \in [0; t_{\text{end}}F_s]. \quad (7)$$

The cost function J is defined as a function of the vector of control commands $\vec{u}_{\text{GLAS}}(n)$ with tuning paramaters a_1 , a_2 , and a_3 and b_1 , b_2 , and b_3 . Considering that positive as well as negative peak force and moment, the cost function J needs to be reduced for one sizing gust and one fuel case can be written as:

$$J = \max_n \left[a_1 \left(F_{z_0} + \sum_{i=0}^{t_{\text{end}}F_s} f_{z_{\text{Gust}}}(i)w(n-i) + \sum_{i=0}^{t_{\text{end}}F_s} f_{z_{\text{el}}}(i)u_{\text{el GLAS}}(n-i) \right. \right. \\ \left. \left. + \sum_{i=0}^{t_{\text{end}}F_s} f_{z_{\text{spoilers1}}}(i)u_{\text{spoilers1 GLAS}}(n-i) \right) \right]$$

$$\begin{aligned}
 & + \sum_{i=0}^{t_{\text{end}} F_s} f_{z_{\text{spoilers2}}}(i) u_{\text{spoilers2 GLAS}}(n-i) + \sum_{i=0}^{t_{\text{end}} F_s} f_{z_{\text{ai}}}(i) u_{\text{ai GLAS}}(n-i) \\
 & + a_2 \left(M_{x_0} + \sum_{i=0}^{t_{\text{end}} F_s} m_{x_{\text{Gust}}}(i) w(n-i) + \sum_{i=0}^{t_{\text{end}} F_s} m_{x_{\text{el}}}(i) u_{\text{el GLAS}}(n-i) \right. \\
 & \quad \left. + \sum_{i=0}^{t_{\text{end}} F_s} m_{x_{\text{spoilers1}}}(i) u_{\text{spoilers1 GLAS}}(n-i) \right. \\
 & + \sum_{i=0}^{t_{\text{end}} F_s} m_{x_{\text{spoilers2}}}(i) u_{\text{spoilers2 GLAS}}(n-i) + \sum_{i=0}^{t_{\text{end}} F_s} m_{x_{\text{ai}}}(i) u_{\text{ai GLAS}}(n-i) \\
 & + a_3 \left(M_{y_0} + \sum_{i=0}^{t_{\text{end}} F_s} m_{y_{\text{Gust}}}(i) w(n-i) + \sum_{i=0}^{t_{\text{end}} F_s} m_{y_{\text{el}}}(i) u_{\text{el GLAS}}(n-i) \right. \\
 & \quad \left. + \sum_{i=0}^{t_{\text{end}} F_s} m_{y_{\text{spoilers1}}}(i) u_{\text{spoilers1 GLAS}}(n-i) \right. \\
 & + \sum_{i=0}^{t_{\text{end}} F_s} m_{y_{\text{spoilers2}}}(i) u_{\text{spoilers2 GLAS}}(n-i) + \sum_{i=0}^{t_{\text{end}} F_s} m_{y_{\text{ai}}}(i) u_{\text{ai GLAS}}(n-i) \left. \right] \\
 & - \min_n \left[b_1 \left(F_{z_0} + \sum_{i=0}^{t_{\text{end}} F_s} f_{z_{\text{Gust}}}(i) w(n-i) + \sum_{i=0}^{t_{\text{end}} F_s} f_{z_{\text{el}}}(i) u_{\text{el GLAS}}(n-i) \right. \right. \\
 & \quad \left. \left. + \sum_{i=0}^{t_{\text{end}} F_s} f_{z_{\text{spoilers1}}}(i) u_{\text{spoilers1 GLAS}}(n-i) \right. \right. \\
 & + \sum_{i=0}^{t_{\text{end}} F_s} f_{z_{\text{spoilers2}}}(i) u_{\text{spoilers2 GLAS}}(n-i) + \sum_{i=0}^{t_{\text{end}} F_s} f_{z_{\text{ai}}}(i) u_{\text{ai GLAS}}(n-i) \\
 & + b_2 \left(M_{x_0} + \sum_{i=0}^{t_{\text{end}} F_s} m_{x_{\text{Gust}}}(i) w(n-i) + \sum_{i=0}^{t_{\text{end}} F_s} m_{x_{\text{el}}}(i) u_{\text{el GLAS}}(n-i) \right. \\
 & \quad \left. + \sum_{i=0}^{t_{\text{end}} F_s} m_{x_{\text{spoilers1}}}(i) u_{\text{spoilers1 GLAS}}(n-i) \right. \\
 & + \sum_{i=0}^{t_{\text{end}} F_s} m_{x_{\text{spoilers2}}}(i) u_{\text{spoilers2 GLAS}}(n-i) + \sum_{i=0}^{t_{\text{end}} F_s} m_{x_{\text{ai}}}(i) u_{\text{ai GLAS}}(n-i) \\
 & \quad \left. + b_3 \left(M_{y_0} + \sum_{i=0}^{t_{\text{end}} F_s} m_{y_{\text{Gust}}}(i) w(n-i) + \sum_{i=0}^{t_{\text{end}} F_s} m_{y_{\text{el}}}(i) u_{\text{el GLAS}}(n-i) \right) \right)
 \end{aligned}$$

$$\begin{aligned}
 & + \sum_{i=0}^{t_{\text{end}} F_s} m_{y_{\text{spoilers1}}}(i) u_{\text{spoilers1 GLAS}}(n-i) \\
 & + \sum_{i=0}^{t_{\text{end}} F_s} m_{y_{\text{spoilers2}}}(i) u_{\text{spoilers2 GLAS}}(n-i) + \sum_{i=0}^{t_{\text{end}} F_s} m_{y_{\text{ai}}}(i) u_{\text{ai GLAS}}(n-i) \Bigg]. \quad (8)
 \end{aligned}$$

For consideration of several sizing gusts and several fuel cases, Eq. (8) is extended by similar additional terms, which is not formulated here for the sake of clearness of this subsection. The GLAS is robustly optimized for several gust lengths between 30 and 500 ft and for 22 fuel configurations. Static shear force, torsion moment, and bending moment for 1g level flight are denoted F_{z_0} , M_{x_0} , and M_{y_0} ; $w(n)$ is the discrete time gust excitation; and $f_{z_{\text{Gust}}}(i)$, $f_{z_{\text{el}}}(i)$, $f_{z_{\text{spoilers1}}}(i)$, $f_{z_{\text{spoilers2}}}(i)$, and $f_{z_{\text{ai}}}(i)$ denote the i th samples of shear force impulse responses of the linearized aircraft model to: gust excitation, elevators input, inner spoilers input, outer spoilers input, and ailerons input. At the same wing cut, respective impulse responses for torsion moment are denoted $m_{x_{\text{Gust}}}(i)$, $m_{x_{\text{el}}}(i)$, $m_{x_{\text{spoilers1}}}(i)$, $m_{x_{\text{spoilers2}}}(i)$, and $m_{x_{\text{ai}}}(i)$, and for bending moment $m_{y_{\text{Gust}}}(i)$, $m_{y_{\text{el}}}(i)$, $m_{y_{\text{spoilers1}}}(i)$, $m_{y_{\text{spoilers2}}}(i)$, and $m_{y_{\text{ai}}}(i)$. The optimization problem can thus be formulated as:

$$\min_{\vec{u}_{\text{GLAS}}} [J]. \quad (9)$$

Subject to: Eqs. (3)–(7).

2.2 Solution of the Optimization Problem

Numerical optimization was performed using linear longitudinal plant models for various fuel variants (with linear approximations of sensors and actuators) including phugoid, short period mode, 6 flexible modes and several lag states, and basic flight control system (FCS) [5] (Fig. 3).

For simplicity, the gusts are considered one-dimensional in this investigation, i. e., the exogenous disturbance $w(n)$ is still time dependent but not space dependent anymore. The interconnection of above aircraft model with the GLAS feedforward control is shown in Fig. 4.

The optimization problem defined by Eq. (9) can be reformulated as the following linear program (LP):

$$\begin{cases} \min \vec{\gamma}; \\ \vec{u}_{\text{GLAS}} \\ A\vec{x} \leq \vec{b}; \\ D\vec{u}_{\text{GLAS}}(n) \leq \vec{c}. \end{cases} \quad (10)$$

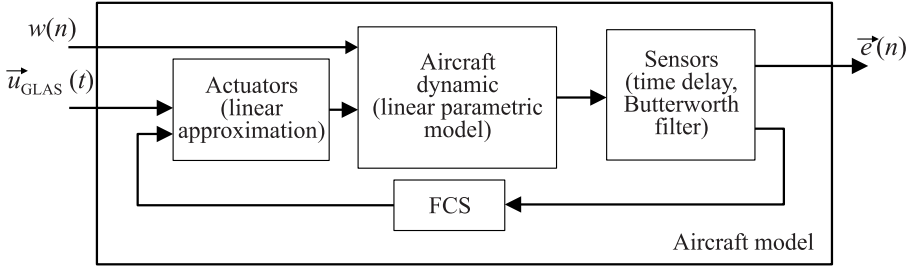


Figure 3 The GLAS design model

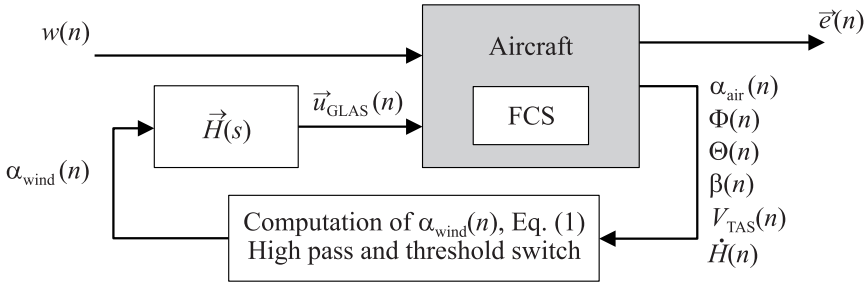


Figure 4 Feedforward control law interconnection

Here, according to Eq. (8), the objective function $\vec{\gamma}$ is defined by

$$\vec{\gamma} = [a_1, a_2, a_3, b_1, b_2, b_3] \cdot \begin{bmatrix} \gamma_1 \\ \gamma_2 \\ \gamma_3 \\ \gamma_4 \\ \gamma_5 \\ \gamma_6 \end{bmatrix} .$$

The decision variables $u_{GLAS}(n)$ are the discrete time responses of the FIR controllers $H(z)$ to a measured 1-cosine gust, i. e., the left side of Eq. (2) extended to consider all 4 pairs of control surfaces. Note that in (10), the controller $\vec{H}(z)$ is implicitly contained in $\vec{u}_{GLAS}(n)$. Therefore, the minimizer of the LP defined by (10) provides the L_∞ optimal control law. The optimization task is now defined as a linear program in a form directly suitable for some LMI parser which calls a linear solver.

In accordance with Eq. (8), in (10), the variable \vec{x} is defined as

$$\vec{x} = \begin{bmatrix} 1 \\ u_{el\text{GLAS}}(0) \\ \vdots \\ u_{el\text{GLAS}}(N-1) \\ u_{spoiler1\text{GLAS}}(0) \\ \vdots \\ u_{spoiler1\text{GLAS}}(N-1) \\ u_{spoiler2\text{GLAS}}(0) \\ \vdots \\ u_{spoiler2\text{GLAS}}(N-1) \\ u_{ai\text{GLAS}}(0) \\ \vdots \\ u_{ai\text{GLAS}}(N-1) \end{bmatrix} ;$$

the variable \vec{b} is defined as

$$\vec{b} = \begin{bmatrix} 1 \\ \left. \begin{matrix} \gamma_1 \cdot \\ \vdots \\ 1 \end{matrix} \right\} t_{\text{end}} F_s \\ 1 \\ \left. \begin{matrix} \gamma_3 \cdot \\ \vdots \\ 1 \end{matrix} \right\} t_{\text{end}} F_s \\ 1 \\ \left. \begin{matrix} 2.5 \cdot \\ \vdots \\ 1 \end{matrix} \right\} t_{\text{end}} F_s \\ 1 \\ \left. \begin{matrix} -\gamma_4 \cdot \\ \vdots \\ 1 \end{matrix} \right\} t_{\text{end}} F_s \\ 1 \\ \left. \begin{matrix} -\gamma_6 \cdot \\ \vdots \\ 1 \end{matrix} \right\} t_{\text{end}} F_s \\ 1 \\ \left. \begin{matrix} 0 \cdot \\ \vdots \\ 1 \end{matrix} \right\} t_{\text{end}} F_s \\ 1 \end{bmatrix} ; \tag{11}$$

and the variable A is defined as

$$A = \begin{bmatrix} A_1 \\ -A_1 \end{bmatrix}$$

where

$$A_1 = \begin{bmatrix} F_{z_0} + f_{z_{\text{Gust}(0)}} & f_{z_{\text{el}(0)}} & 0 & \cdots \\ \vdots & \vdots & f_{z_{\text{el}(0)}} & \cdots \\ \vdots & \vdots & \vdots & \cdots \\ \vdots & \vdots & \vdots & \cdots \\ \vdots & \vdots & \vdots & \cdots \\ F_{z_0} + f_{z_{\text{Gust}(t_{\text{end}} F_s)}} & f_{z_{\text{el}(t_{\text{end}} F_s)}} & f_{z_{\text{el}(t_{\text{end}} F_s - 1)}} & \cdots \\ M_{x_0} + m_{x_{\text{Gust}(0)}} & m_{x_{\text{el}(0)}} & 0 & \cdots \\ \vdots & \vdots & m_{x_{\text{el}(0)}} & \cdots \\ \vdots & \vdots & \vdots & \cdots \\ \vdots & \vdots & \vdots & \cdots \\ \vdots & \vdots & \vdots & \cdots \\ M_{x_0} + m_{x_{\text{Gust}(t_{\text{end}} F_s)}} & m_{x_{\text{el}(t_{\text{end}} F_s)}} & m_{x_{\text{el}(t_{\text{end}} F_s - 1)}} & \cdots \\ M_{y_0} + m_{y_{\text{Gust}(0)}} & m_{y_{\text{el}(0)}} & 0 & \cdots \\ \vdots & \vdots & m_{y_{\text{el}(0)}} & \cdots \\ \vdots & \vdots & \vdots & \cdots \\ \vdots & \vdots & \vdots & \cdots \\ \vdots & \vdots & \vdots & \cdots \\ M_{y_0} + m_{y_{\text{Gust}(t_{\text{end}} F_s)}} & m_{y_{\text{el}(t_{\text{end}} F_s)}} & m_{y_{\text{el}(t_{\text{end}} F_s - 1)}} & \cdots \\ n_{z_{\text{Gust}(0)}} & n_{z_{\text{el}(0)}} & 0 & \cdots \\ \vdots & \vdots & n_{z_{\text{el}(0)}} & \vdots \\ \vdots & \vdots & \vdots & \cdots \\ \vdots & \vdots & \vdots & \cdots \\ \vdots & \vdots & \vdots & \cdots \\ n_{z_{\text{Gust}(t_{\text{end}} F_s)}} & n_{z_{\text{el}(t_{\text{end}} F_s)}} & n_{z_{\text{el}(t_{\text{end}} F_s - 1)}} & \cdots \end{bmatrix}$$

$$\begin{array}{cccccc}
 \cdots & 0 & \cdots & f_{z_{ai}(0)} & \cdots & 0 \\
 \cdots & \vdots & \cdots & \vdots & \cdots & \vdots \\
 \cdots & 0 & \cdots & \vdots & \cdots & 0 \\
 \cdots & f_{z_{el}(0)} & \cdots & \vdots & \cdots & f_{z_{ai}(0)} \\
 \cdots & \vdots & \cdots & \vdots & \cdots & \vdots \\
 \cdots & f_{z_{el}(t_{end} F_s - N)} & \cdots & f_{z_{ai}(t_{end} F_s)} & \cdots & f_{z_{el}(t_{end} F_s - N)} \\
 \cdots & 0 & \cdots & m_{x_{ai}(0)} & \cdots & 0 \\
 \cdots & \vdots & \cdots & \vdots & \cdots & \vdots \\
 \cdots & 0 & \cdots & \vdots & \cdots & 0 \\
 \cdots & m_{x_{el}(0)} & \cdots & \vdots & \cdots & m_{x_{ai}(0)} \\
 \cdots & \vdots & \cdots & \vdots & \cdots & \vdots \\
 \cdots & m_{x_{el}(t_{end} F_s - N)} & \cdots & m_{x_{ai}(t_{end} F_s)} & \cdots & m_{x_{ai}(t_{end} F_s - N)} \\
 \cdots & 0 & \cdots & m_{y_{ai}(0)} & \cdots & 0 \\
 \cdots & \vdots & \cdots & \vdots & \cdots & \vdots \\
 \cdots & 0 & \cdots & \vdots & \cdots & 0 \\
 \cdots & m_{y_{el}(0)} & \cdots & \vdots & \cdots & m_{y_{ai}(0)} \\
 \cdots & \vdots & \cdots & \vdots & \cdots & \vdots \\
 \cdots & m_{y_{el}(t_{end} F_s - N)} & \cdots & m_{y_{ai}(t_{end} F_s)} & \cdots & m_{y_{ai}(t_{end} F_s - N)} \\
 \cdots & 0 & \cdots & n_{z_{ai}(0)} & \cdots & 0 \\
 \vdots & \vdots & \vdots & \vdots & \cdots & \vdots \\
 \cdots & 0 & \cdots & \vdots & \cdots & 0 \\
 \cdots & n_{z_{el}(0)} & \cdots & \vdots & \cdots & n_{z_{ai}(0)} \\
 \cdots & \vdots & \cdots & \vdots & \cdots & \vdots \\
 \cdots & n_{z_{el}(t_{end} F_s - N)} & \cdots & n_{z_{ai}(t_{end} F_s)} & \cdots & n_{z_{ai}(t_{end} F_s - N)}
 \end{array} ; \quad (12)$$

The computational effort with respect to memory demands can grow really fast, as it is a function of the number of variables, i.e., the number of used control surfaces, the time horizon of optimization, the time horizon of control, the number of considered operation points, and the sampling period. Thus, one option for the reduction of said memory burden is to evaluate the criterion in sparse points only, iteratively adding points whenever constraints are violated.

Note that the constraint in Eq. (7) is considered in Eqs. (11) and (12). In accordance with Eqs. (3)–(6), the D variable is defined as

$$D = \begin{bmatrix} D_1 \\ -D_1 \\ D_2 \\ -D_2 \end{bmatrix}; \quad D_1 = \begin{bmatrix} I_{N \times N} & 0 & 0 & 0 \\ 0 & I_{N \times N} & 0 & 0 \\ 0 & 0 & I_{N \times N} & 0 \\ 0 & 0 & 0 & I_{N \times N} \end{bmatrix}; \quad D_2 = \begin{bmatrix} I_D & 0 & 0 & 0 \\ 0 & I_D & 0 & 0 \\ 0 & 0 & I_D & 0 \\ 0 & 0 & 0 & I_D \end{bmatrix}$$

where the finite differences for approximation of the discrete derivative in Eqs. (5) and (6) are contained in:

$$I_D = \begin{bmatrix} -1 & 1 & 0 & \cdots & 0 \\ 0 & \ddots & \ddots & \ddots & \vdots \\ \vdots & \ddots & \ddots & \ddots & 0 \\ 0 & \cdots & 0 & -1 & 1 \end{bmatrix}_{(N-1) \times N}$$

The variable \vec{c} is defined as $\vec{c} = \begin{bmatrix} \vec{c}_1 \\ \vec{c}_2 \end{bmatrix}$ where \vec{c}_1 is determined in accordance with Eqs. (3) and (4) and \vec{c}_2 in accordance with Eqs. (5) and (6):

$$\vec{c}_1 = \begin{bmatrix} \left. \begin{matrix} u_{el} \max \cdot \\ \vdots \\ 1 \end{matrix} \right\} N \\ \left. \begin{matrix} u_{spoiler1} \max \cdot \\ \vdots \\ 1 \end{matrix} \right\} N \\ \left. \begin{matrix} u_{spoiler2} \max \cdot \\ \vdots \\ 1 \end{matrix} \right\} N \\ \left. \begin{matrix} u_{ai} \max \cdot \\ \vdots \\ 1 \end{matrix} \right\} N \\ \left. \begin{matrix} u_{el} \min \cdot \\ \vdots \\ 1 \end{matrix} \right\} N \\ \left. \begin{matrix} u_{spoiler1} \min \cdot \\ \vdots \\ 1 \end{matrix} \right\} N \\ \left. \begin{matrix} u_{spoiler2} \min \cdot \\ \vdots \\ 1 \end{matrix} \right\} N \\ \left. \begin{matrix} u_{ai} \min \cdot \\ \vdots \\ 1 \end{matrix} \right\} N \end{bmatrix}; \quad \vec{c}_2 = \begin{bmatrix} \left. \begin{matrix} T_s \dot{u}_{el} \max \cdot \\ \vdots \\ 1 \end{matrix} \right\} N - 1 \\ \left. \begin{matrix} T_s \dot{u}_{spoiler1} \max \cdot \\ \vdots \\ 1 \end{matrix} \right\} N - 1 \\ \left. \begin{matrix} T_s \dot{u}_{spoiler2} \max \cdot \\ \vdots \\ 1 \end{matrix} \right\} N - 1 \\ \left. \begin{matrix} T_s \dot{u}_{ai} \max \cdot \\ \vdots \\ 1 \end{matrix} \right\} N - 1 \\ \left. \begin{matrix} T_s \dot{u}_{el} \min \cdot \\ \vdots \\ 1 \end{matrix} \right\} N - 1 \\ \left. \begin{matrix} T_s \dot{u}_{spoiler1} \min \cdot \\ \vdots \\ 1 \end{matrix} \right\} N - 1 \\ \left. \begin{matrix} T_s \dot{u}_{spoiler2} \min \cdot \\ \vdots \\ 1 \end{matrix} \right\} N - 1 \\ \left. \begin{matrix} T_s \dot{u}_{ai} \min \cdot \\ \vdots \\ 1 \end{matrix} \right\} N - 1 \end{bmatrix}$$

2.3 Results of Numeric Optimization

As expected, the most restrictive constraint is Eq. (16) since due to the low wing loading, sizing updraft gusts can cause vertical load factors of $3g$ and more on the ACFA BWB aircraft (Fig. 5). Unless elevator constraints as defined by Eqs. (3) and (5) are set to unrealistically high values, no solution was found for $\vec{u}_{\text{GLAS}}(n)$ which would fulfill Eq. (7). The reduction of load factor was only possible by rapid elevator deflection which pitches the aircraft into the gust. Deflection of spoilers is shown to be an efficient measure for reduction of wing loads, but causes a high pitch-up moment which in fact increases the angle of attack and, thus, the vertical load factor. This behavior is mainly due to the fact that the ACFA BWB is a high wing configuration and, thus, the spoilers drag force has a high lever arm with respect to the CG. Figure 5 illustrates total bending moment $M_x(n)$ (i. e., multiplier of a_3 in Eq. (8)) at a representative wing cut (Fig. 5a) and vertical acceleration at CG $N_z(n)$ (Fig. 5b) for 11 fuel cases resulting from an optimization run with relaxed constraints on rate limitation

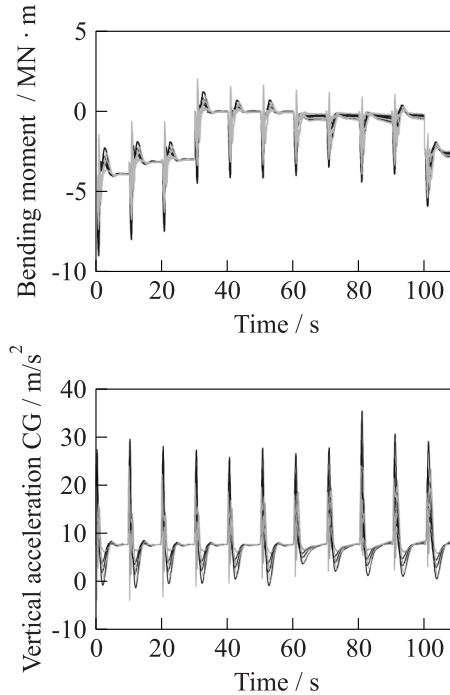


Figure 5 Responses of $M_x(n)$ and $N_z(n)$ with relaxed constraints on elevators' rate limit (black — without GLAS; and grey — with GLAS)

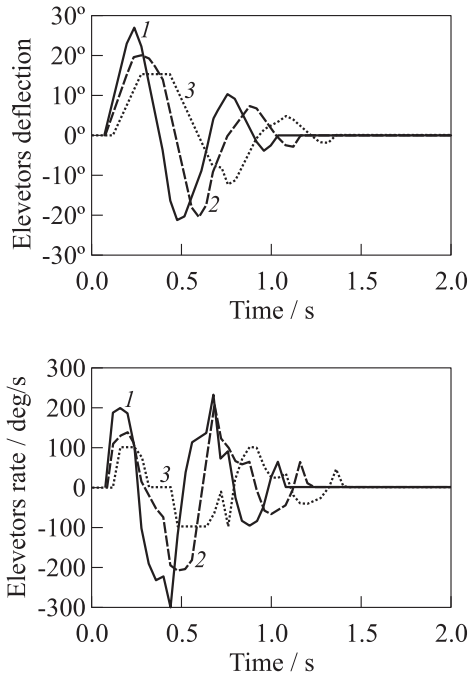


Figure 6 Required elevators’ deflection $u_{el\text{GLAS}}(n)$ and respective rate for three different sizing gusts: 1 — elevators response to a sizing 250-foot gust; 2 — 350-foot gust; and 3 — elevators response to a sizing 500-foot gust

for $u_{el\text{GLAS}}(n)$ for maximum operating Mach number at an altitude of 28,743 ft. The responses for each of the 11 fuel cases are consecutively plotted for 10 s resulting in overall 110 s for the X-axis. The results for three different gust gradient distances H are plotted on top of each other. It can be seen that the maximum bending moment is reduced by almost 20% while constraints on $N_z(n)$ are fulfilled.

As illustrated by Fig. 6, the elevators’ deflection $u_{el\text{GLAS}}(n)$ was limited to $\pm 15^\circ$ and the respective rate was at least limited to ± 10 deg/s for encounter of a 500-foot sizing gust (3). For smaller gust gradient distances the resulting deflections and rates are accordingly higher due to the frequency content of the excitation. Note that loads and load factor due to the 500-foot gust are much higher than for the 250- and 350-foot gust. Thus, the huge deflections and deflection rates resulting for the 250- and 350-foot gust can be neglected for the following discussion, since they are just a result of the GLAS control law being aggressively optimized for the 500-foot gust. Since the deflections required to satisfy Eq. (7) are fairly large even for the 500-foot gust, a reduction

of elevators' size would not be a reasonable means for increasing the elevators' bandwidth using the same actuators. Actuators that would be able to deflect the huge elevators of the ACFA BWB at the rates of 100 deg/s and more are most probably too heavy and too energy-consuming for efficient use on a commercial transport aircraft.

3 NUMERIC SIMULATIONS OF THE GUST LOAD ALLEVIATION SYSTEM

Numeric simulations with and without GLAS are performed with a flexible aircraft model linearized at various representative trim points. The simulation model includes nonlinear fourth-order actuators for the trailing edge control surfaces and spoilers, sensor delays, and flight control laws. Encounter of sizing gusts of different gust gradient distances are simulated in accordance with Federal Aviation Regulations [10]. Figure 7 illustrates $M_x(t)$ and $N_z(t)$ resulting from simulations at maximum operating Mach number and altitudes ranging

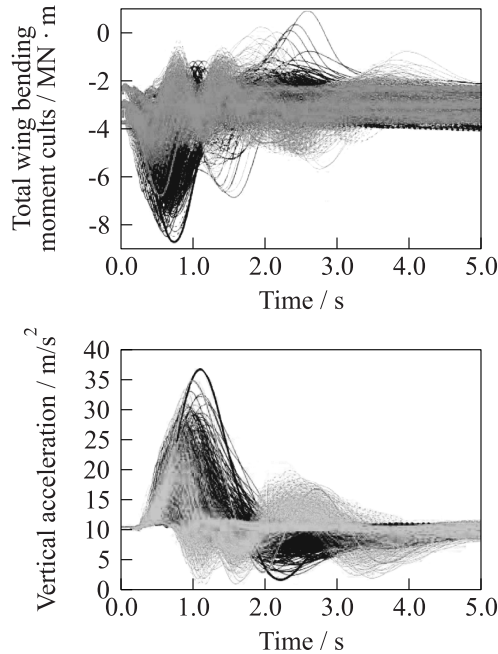


Figure 7 Simulated $M_x(t)$ and $N_z(t)$ for sizing gust encounters considering nonlinear actuator models (black — without GLAS; and grey — with GLAS)

from 28,743 to 38,638 ft. The GLAS used in this simulation was designed robust with respect to different fuel cases and gust gradient distances considering reasonable constraints for maximum elevators' deflection rates. The total bending moment is still reduced by 20%. The vertical acceleration $N_z(t)$, however, cannot be reduced using the nonlinear actuators, i. e., considering limitations on available actuators' energy.

4 STRUCTURAL RESIZING OF THE BLENDED WING BODY AIRCRAFT

The impact of load alleviation on fuel efficiency may reasonably be assessed by means of potential structural weight savings. A complete balance of additional weight, required by the load alleviation system, as well as weight savings with regards to the load bearing structure may lead to a conclusion in the early concept phase. The latter will be identified by resizing in terms of structural optimization. In a first design step, the structural optimization routine is applied to achieve a structural design considering sizing gusts and manoeuvres without active load alleviation. This design serves as a reference for the assessment of load alleviation performance. The second design step provides a structural design fulfilling the same requirements as the reference, but best possibly exploiting the control concepts for active load alleviation.

4.1 Model Setup

The structural optimization routine employs the finite-element model of the BWB aircraft, which has been applied in aeroelastic modelling before. All load bearing parts of the wing structure are assigned to design regions distributed over the wingspan (Fig. 8a).

The stringer stiffened skin is represented by composite elements with smeared stringers. The stiffness and mass properties of the panels are computed from design variables for stringer thickness t_{str} and skin thickness t_{sk} for each design zone, as shown in Fig. 8b. For structural optimization, the gradient-based solver MSC Nastran SOL200 [11] is applied. The objective of the optimization task is the minimization of overall mass. Constraints are applied for composite strains, as well as for analytic buckling criteria for the skin panels. In initial structural design of the wing, flutter speed was a critical design driver. Thus, a flutter speed check is implemented as constraint, as this value is influenced by the wingbox structural design.

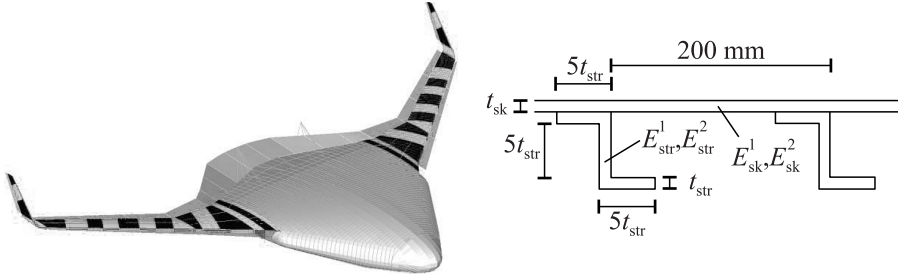


Figure 8 Design regions of the BWB wing (a) and stringer/panel design variables (b)

4.2 Load Cases

All load scenarios to be applied in structural resizing are derived from results of time-domain simulations of the BWB model. Longitudinal and lateral transient manoeuvres as well as discrete gust loads are considered. The so-called Mode Displacement Method (MDM) [12] is applied here for deriving equivalent static load cases from the modal displacement time histories η_e derived from numeric simulations of, e. g., gust encounter as described in section 3. With known modal matrix Φ_{ge} and stiffness matrix K_{gg} of same finite-element model applied in aeroelastic modeling, equivalent static load cases can be computed by

$$\begin{Bmatrix} \{F\}_i \\ \{M\}_i \end{Bmatrix} = [K_{gg}] [\Phi_{ge}] \{\eta_e\}.$$

The MDM leads to a very large number of load cases, if applied for all time steps in simulation. However, the MSC Nastran SOL200 solver is programmed to automatically identify critical load cases for further consideration in the following optimization cycles. This method dramatically reduces the computational costs and makes the analysis of manifold loadcases feasible. Further, critical timesteps to be applied for loads analysis, are identified from simulation history via bending moments and displacement signals.

4.3 Structural Optimization

The optimization problem is formulated as mass minimization with afore mentioned design variables and constraints. The optimization results are shown in terms of wing panel and stringer thicknesses of the design zones over wing span in Fig. 9. Figure 9a shows the resulting thicknesses for structural optimization without load alleviation, whereas Fig. 9b shows the results for the design

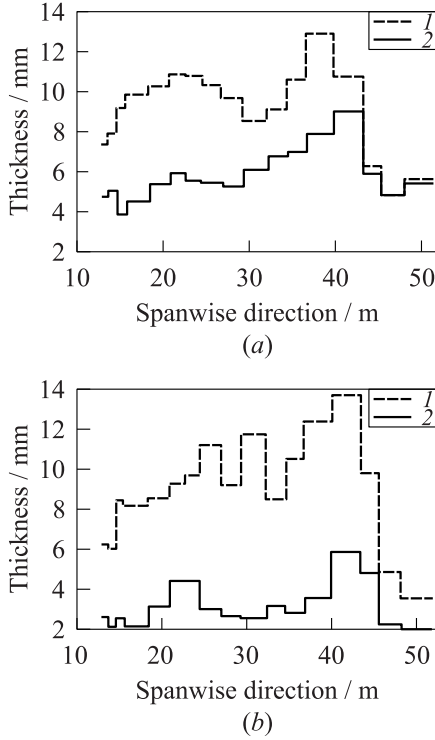


Figure 9 Optimized thicknesses of panels (1) and stringers (2) over wingspan (including winglet span)

with load alleviation considered. Independently from load alleviation, it can be seen that the outboard panels and stringers are remarkably reinforced by the optimization program. By observation of the active flutter constraint and its sensitivities, it was concluded that the outboard thickness increase is the most effective measure for flutter prevention, considering given optimization problem. The main effect of load alleviation on structural design is that the stringer thickness over the whole wing span can be decreased significantly. The total mass saving of the full aircraft due to load alleviation was found to be about 2 metric tons, or 0.5% of the aircraft’s maximum take-off weight.

5 CONCLUDING REMARKS

This paper presents the design and optimization of a GLAS for a large BWB airliner. Structural loads are shown to be effectively reduced by the GLAS with

the available actuators which allows for a resizing of the aircraft's wing structure resulting in significant mass savings. Buckling as well as flutter constraints are considered in the structural optimization. Vertical accelerations during gust encounter, however, are huge and cannot be reduced unless much more powerful actuators are provided for the elevators in order to be able to rapidly pitch the BWB aircraft into a gust and, thus, reduce the additional angle of attack. However, size, mass, and power consumption of such actuators is most probably too large for reasonable use on an efficiency-driven aircraft design. Future research should, thus, be dedicated to investigating other unconventional devices which can pitch the BWB aircraft into a gust using less control power. Another field of research is considering GLAS certification requirements in the optimization process for overall aircraft mass minimization.

ACKNOWLEDGMENTS

The authors would like to thank the European Commission for funding the ACFA2020 project within the 7th Research Framework Programme as well as all ACFA2020 partners.

REFERENCES

1. Wildschek, A., T. Havar, and K. Plötner. 2009. An all-composite, all-electric, morphing trailing edge device for flight control on a blended-wing-body airliner. *Proc. IMechE, Part G: J. Aerospace Eng.* 224(G1):1–9.
2. Wildschek, A., F. Stroscher, T. Haniš, and T. Belschner. 2013. Fuel management system for cruise performance optimization on a large blended wing body airliner. In: *Progress in flight dynamics, guidance, navigation, control, fault detection, and avionics*. Eds. Ch. Vallet, D. Choukroun, Ch. Philippe, G. Balas, A. Nebylov, and O. Yanova. EUCASS advances in aerospace sciences book ser. Moscow: TORUS PRESS. 6:651–70.
3. Brockhaus, R. 2001. *Flugregelung. 2. Auflage*. Berlin: Springer. 655–59.
4. Wildschek, A., F. Stroscher, T. H. Klimmek, Z. Šika, T. Vampola, M. Valášek, D. Gangsaas, N. Aversa, and A. Berard. 2010. Gust load alleviation on a large blended wing body airliner. *ICAS2010 — 27th Congress of the International Council of the Aeronautical Sciences*. Nice, France.
5. Westermayer, C., A. Schirrer, M. Hemedi, and M. Kozek. 2013. An \mathcal{H}_∞ full information approach for the feedforward controller design of a large blended wing body flexible aircraft. In: *Progress in flight dynamics, guidance, navigation, control, fault detection, and avionics*. Eds. Ch. Vallet, D. Choukroun, Ch. Philippe, G. Balas, A. Nebylov, and O. Yanova. EUCASS advances in aerospace sciences book ser. Moscow: TORUS PRESS. 6:685–706.

6. Hahn, K.-U. 2007. Apparatus and method for reducing the impact of turbulence and gusts on aircraft. European Patent EP 1 854 717 A1.
7. Wildschek, A., R. Maier, F. Hoffmann, M. Jeanneau, and N. Aversa. 2009. Minimizing dynamic structural loads of an aircraft. U.S. Patent US 2009/0084908.
8. Wildschek, A. 2009. An adaptive feed-forward controller for active wing bending vibration alleviation on large transport aircraft. Dissertation. München: Technische Universität.
9. Wildschek A., R. Maier, K.-U. Hahn, D. Leißling, M. Preß, and A. Zach. 2009. Flight test with an adaptive feed-forward controller for alleviation of turbulence excited wing bending vibrations. *AIAA Guidance, Navigation, and Control Conference and Exhibit*. Chicago, IL.
10. Federal Aviation Regulations. 1980. Part 25 — Airworthiness standards: Transport category airplanes. U.S. Department of Transportation, Federal Aviation Administration. Also: Code of Federal Regulations, title 14, aeronautics and space, Part 25 — Airworthiness standards: Transport category airplanes.
11. 2010. MD/MSC Nastran 2010 Design Sensitivity and Optimization User's Guide. MSC Software Corporation.
12. Kier, T., and G. Looye. 2009. Unifying manoeuvre and gust loads analysis models. *Forum (International) of Aeroelasticity and Structural Dynamics*.

Paper 3

Alam, M.; Hromčík, M.; Haniš, T.; Active Gust Load Alleviation System for Flexible Aircraft: Mixed Feedforward/Feedback Approach Aerospace science and technology. 2015, 41(1), 122-133. ISSN 1270-9638.



Short communication

Active gust load alleviation system for flexible aircraft: Mixed feedforward/feedback approach

Mushfiqul Alam^{a,*}, Martin Hromcik^b, Tomas Hanis^c^a Department of Measurement, Faculty of Electrical Engineering, Technicka 2, Czech Technical University in Prague, Czech Republic^b Department of Control Engineering, Faculty of Electrical Engineering, Karlovo Namesti 13, Czech Technical University in Prague, Czech Republic^c Department of Wind Energy, Building 114, Technical University of Denmark, DK

ARTICLE INFO

Article history:

Received 14 July 2014

Received in revised form 10 November 2014

Accepted 21 December 2014

Available online 6 January 2015

Keywords:

Gust load alleviation system

Feedforward control

Blended wing body

Flexible aircraft structure

ABSTRACT

Lightweight flexible blended-wing-body (BWB) aircraft concept seems as a highly promising configuration for future high capacity airliners which suffers from reduced stiffness for disturbance loads such as gusts. A robust feedforward gust load alleviation system (GLAS) was developed to alleviate the gust loading. This paper focuses on designing a feedback controller which would improve the robust performance of the feedforward controller in reducing the peaks in wing root moments at very short gust lengths. The simulation results show that when the new feedback compensator is engaged with the feedforward controller, the performance of the GLAS system is improved significantly in terms of reduction in wing root moments for shorter as well as for longer gusts. This reduction in the wing root moment's peak provides potential structural benefits and weight savings.

© 2015 Elsevier Masson SAS. All rights reserved.

1. Introduction

Current state-of-the-art aircraft such as Airbus A380 and Boeing 787 Dreamliner have pushed the limits of efficient conventional tube-wing configuration. As a result the aircraft designers investigate now alternative aircraft configurations such as the Blended Wing Body (BWB) concept. Several projects were undertaken in the European research programmes content such as ACFA (Active Control for Flexible Aircraft) 2020, NACRE (New Aircraft Concepts Research), VELA (Very Efficient Light Aircraft) and ROSAS (Research on Silent Aircraft Concepts) [2,18,15,7].

The transport aircraft BWB research and design efforts can be traced back to the 1980s. A comprehensive documentation of the US research efforts on the design of BWB subsonic transport aircraft, corresponding design issues and constraints, advantages and drawbacks existing with such configurations, as well as results from wind tunnel tests are presented in [17]. The research progress is demonstrated starting from a preliminary design study in 1988 for novel configurations up to the highly efficient Boeing BWB-450 baseline aircraft. Basically, three generations of BWB configurations are documented which were successively improved.

The European VELA project aimed at the development of skills, capabilities and methodologies required for the design and opti-

mization of civil flying wing aircraft. Within VELA two baseline flying wing BWB configurations were developed [24]. The project was focused on development of aerodynamic and control derivatives and their impact on flight stability. In addition low speed tunnel tests were performed while comparing the results from the experiment with the predictions made using CAD and CFD software tools. Special setup of dynamic tests was dedicated to the validation of the effects of deflecting control surfaces and other dynamic characteristics of flying wing configurations. Optimization techniques were then applied to maximize the efficiency of these configurations, varying parameters such as chord length, twist angle and airfoil section shape [8].

Later on NACRE project was undertaken to drive the development of the key capabilities required for the improvement of the novel aircraft concepts from the experience gained in VELA. The NACRE project was broken down to mainly four work packages; first, novel aircraft concept; second, novel lifting surfaces; third, novel power plant installation and fourth, novel fuselage. The key technical achievements can be classified in two key areas: (1) Multidisciplinary Design and Analysis Capabilities for Components, which includes, (a) Open Rotor propulsion integration for noise shielding; (b) Powered Tail innovative integrated design & analysis; (c) Natural Laminar Flow wing design and transition prediction and (d) Flying wing configuration design and multidisciplinary assessment [14]. (2) Experimental Validation & Testing Techniques, which includes, (a) Rear engine integration (Aerodynamics & Noise improvement); (b) High-Energy absorption; (c) Fly-

* Corresponding author.

E-mail address: mushfala@fel.cvut.cz (M. Alam).URL: <http://measure.feld.cvut.cz/en/malam> (M. Alam).

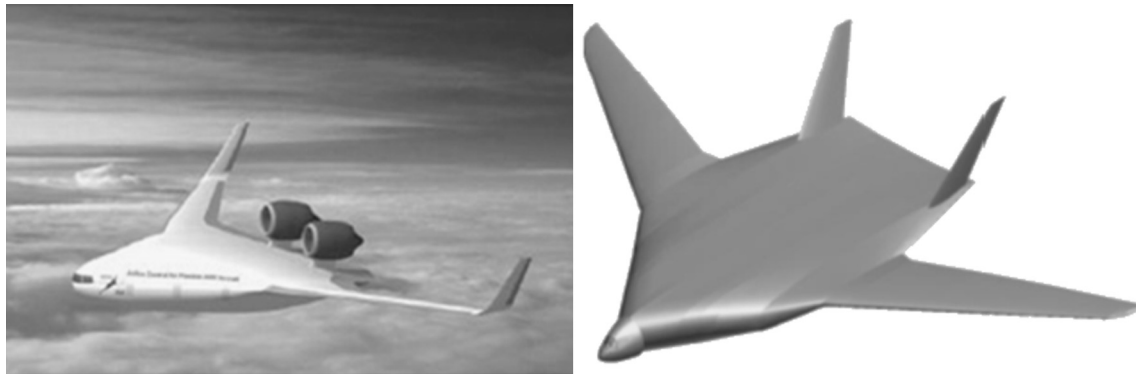


Fig. 1. Visualization of two selected BWB concepts ACFA2020 (left) [2] and NACRE (right) [3].

ing Wing cabin evacuation; (d) Innovative evaluation platform development [3,10,1].

Finally, within the ACFA2020 the predesign of a 450 passenger BWB aircraft is finalized achieving the major aircraft efficiency objectives regarding reduced fuel consumption and external noise. The project further studied robust as well as adaptive multi-channel control architectures for loads alleviation and improvement of ride comfort and handling qualities of BWB type aircraft. One of the main goals of the project, however, was to investigate the system's aeroelastic properties with respect to modern control design methodologies. Thereby, the potential in structural load reduction, improving of ride comfort and attainable handling qualities were main drivers [9].

The dynamical models of the finalized BWB aircraft were developed for carrying out the controller design. The models were generated based on a refined Finite Element Model (FEM) and aerodynamic data [2]. Fig. 1 shows the two above mentioned finalized BWB concepts within the European projects.

For future high capacity airliners, the BWB concept appears to be highly promising. The aircraft configuration presents a compact lifting body with significantly increased lift-to-drag ratio with obvious environmental (lower noise level and CO₂ emissions) and economic (lower fuel consumption, reduced operational expenses) consequences [17,20,23,21]. The lightweight BWB structure suffers however from reduced stiffness compared to the classical tube-wing configuration.

This aspect of reduced stiffness is further emphasized if thin lifting surfaces and the use of composite materials for aircraft structures are considered, leading to light weight flexible structures. When this type of aircraft passes through the turbulent atmosphere, it develops significant structural vibrations. Aircraft motion of this kind results in reduction of structural lifetime due to large dynamic loads and the consequent level of stresses. The amplitude of the aircraft's structural response, caused by gust excitation depends upon two factors. First, the amount of energy transferred from the gust disturbance to the structural modes; and second, the dissipation of any energy absorbed from gust by active structural damping. In addition, when the amplitude of the response of the elastic motions is comparable to that of the rigid body motion, an interaction or coupling of the rigid body energy and the elastic energy can appear leading to detriment of the flying qualities of the aircraft [19,22].

Current Gust Load Alleviation systems work primarily on the error feedback principle [5,30,33]. The first peak in the wing root moments (induces maximum load in the construction) determines the required sizing of the wing root joint reinforcement. Potential weight savings can be realized if the reduction in wing root moments is achieved. What is of special concern is therefore the 1st peak's reduction in the wing root moments, which is regarded as non-achievable by purely feedback solution [27]. Therefore com-

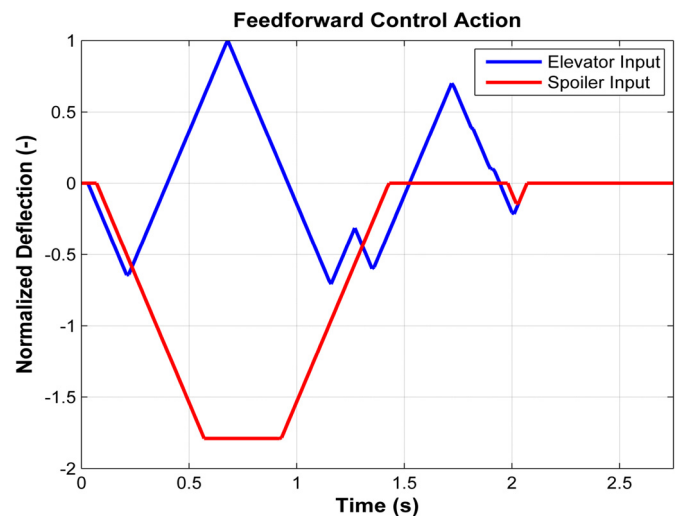


Fig. 2. Normalized feedforward control inputs [29].

bined feedforward plus feedback control can significantly minimize structural deflection due to air turbulence such as gusts [31,28]. If the sensors are placed smartly they could measure the r.m.s. (root mean square) vertical acceleration (along z-axis) at a number of locations on the aircraft. In order to precisely determine the effects of the wing bending relative to the center of gravity (CG) of the aircraft sensors are to be placed at the CG, wingtip right node and wingtip left node in principle. A related detailed treatment on optimal placement of sensors for this problematic issue is outlined in [12,16,25]. The acceleration of the wing relative to the CG is defined as η_z law (see Section 3.1) which actually gives the measure of wing bending, induced by a gust for instance.

To alleviate this gust loading, a triggered feedforward (FF) control strategy, see Fig. 2, was elaborated at EADS Innovation Works, Munich. Fig. 2 shows the normalized control signal with respect to the maximum elevator deflection. A pre-computed control sequence for ailerons and spoilers is triggered once the aircraft hits a gust, which is detected by an alpha-probe (angle-of-attack probe) placed at the node of the aircraft [29]. The pre-defined FF control sequence was designed to be robust with respect to different aircraft mass cases, altitudes, Mach numbers and gust lengths.

This FF control approach appears very efficient, according to high-fidelity simulations [29] for alleviation of the wing root bending and torsional moments for long gusts especially, which are the "sizing gusts" in fact – they produce largest impacts on the construction. However, a price paid for this are slightly increased wing root moments for shorter gusts, compared to the non-controlled

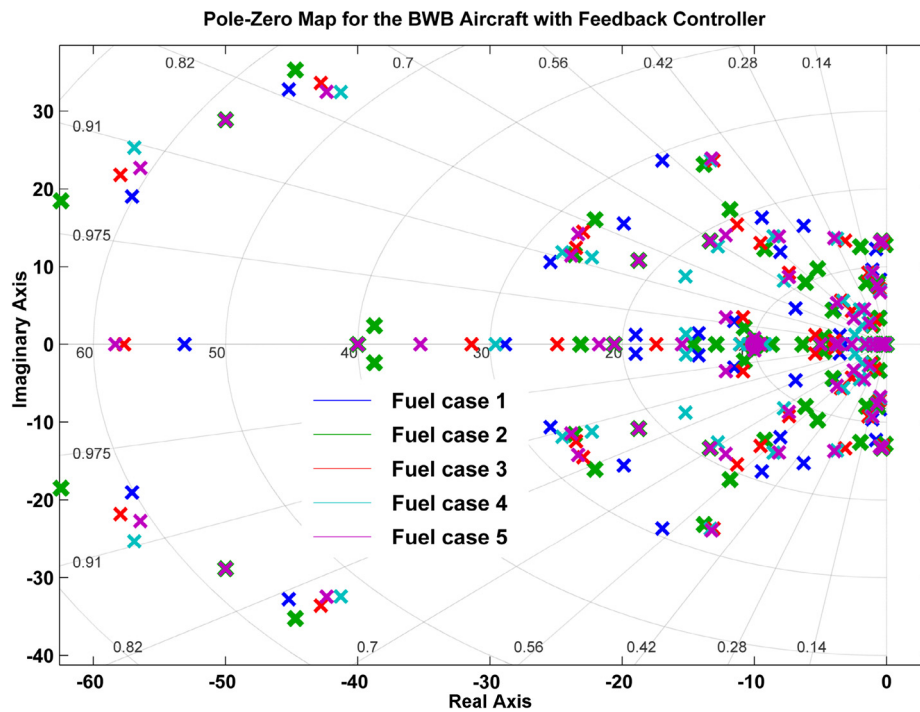


Fig. 3. Pole-zero plots of the original BWB aircraft with the stabilizing \mathcal{H}_∞ feedback controller [33].

case (bear in mind that the control sequence is pre-calculated and fixed for any gust length). These short gust cases are not the sizing ones, and the overall first-peak value throughout the gust length cases is significantly reduced, still this effect can be regarded as undesirable and disturbing.

Earlier attempts were made in [4] to improve the performance of the GLAS using linear quadratic regulators (LQR). The controller design and simulation showed promising improvement by reducing the wing root moments. However this type of controller was constrained by the difficulties of state estimation. Generally BWB aircraft are large systems with significantly high number of unmeasurable flexible states and, as a result it is difficult to implement full-order optimal controllers in this case.

Therefore a different concept is proposed in this paper. It is suggested to use additional simple feedback loops that would work along with the triggered FF GLAS system which would improve the FF control sequence performance over shorter gust lengths and further improve the performance for “sizing gusts”. The classical SISO control design methods were investigated.

The paper is organized in the following order. Section 2 presents a discussion on the development and generation of the aircraft’s dynamic model. Section 3 describes the detailed design of the control law. Section 4 provides a detailed comparative analysis on the improved results. Section 5 contains final concluding remarks.

2. Dynamic modeling

2.1. Aircraft model

The aircraft model used for loads analysis and design and validation of the GLAS is based on aerodynamic and structural data of the BWB configuration NACRE developed in the European project NACRE and modified in ACFA2020 [33]. The aircraft model was not originally developed for dynamic analysis. Necessary modifications were made so that the dynamic analysis could be performed. Components such as cockpit, elevator and wing’s leading edge, engine pylons and structures were added as concentrated

Table 1
Mass variation cases.

No. of cases	Fuel (as a fraction of full load)
1	1/16th
2	1/8th
3	1/4th
4	1/2nd
5	3/4th
6	1

point masses [33]. Non-structural masses of systems and equipment as well as operational masses were integrated into the structural model. Finally, various passenger/payload and fuel configurations were modeled with concentrated masses and also integrated into the structural model of the NACRE configuration. Aerodynamic polars, damping derivatives, and control surface derivatives were provided by the NACRE project for various mass cases and cruise speeds. For the gust load analysis six different varying fuel mass cases were considered as shown in Table 1.

The phugoid mode of the aircraft is not considered, the analysis is focused on short period model only. The considered aircraft, NACRE aircraft, was statically unstable in large regions of mass and flight envelope. Therefore, the flight control system required artificial pitch stabilization. The original aircraft model was stabilized by a robust (with respect to fuel/mass cases, altitude, and velocity) feedback \mathcal{H}_∞ controller [13,26,32]. Artificial pitch stiffness is achieved by feedback of the vertical CG load factor η_z to the elevator. In order to achieve neutral pitch stability this feedback is done via a PI controller [19,6]. An additional pitch damper (i.e. feedback from pitch rate q to the elevators) allows placement of the poles of the short period mode [33]. The original NACRE short period model has 20 states which include the rigid body short period mode and a number of flexible modes. By adding the stabilizing \mathcal{H}_∞ controller, the overall state count increased to sixty. The pole-zero map of the stabilized aircraft is shown in Fig. 3.

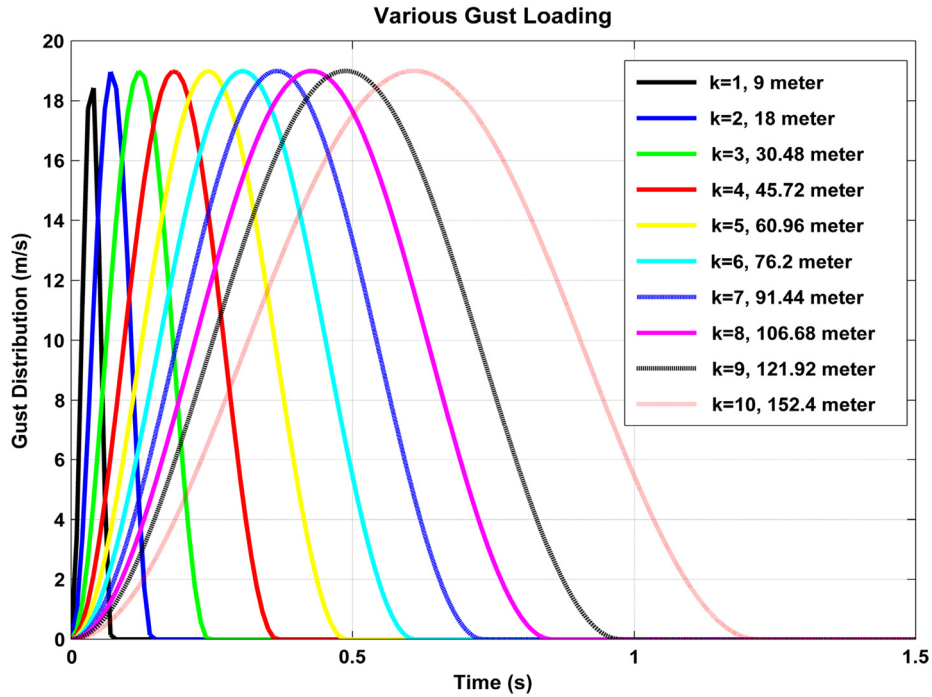


Fig. 4. Gust distribution of various gust lengths.

2.2. Gust modeling

Vertical wind gusts are traditionally modeled as a function of $(1 - \cos \beta)$ defined by the equation

$$x_g(t) = \frac{a}{T} (1 - \cos(2\pi/T)t) \quad (1)$$

where “ T ” is the duration of the gust, which is defined by

$$T = k/U_o \quad (2)$$

“ k ” is the gust length and U_o is the aircraft cruise speed. 10 different gust lengths were chosen for the simulation as shown in Fig. 4.

3. Control law design

3.1. η_z law

The wing bending of the flexible aircraft was assessed by attaching sensors that measure the r.m.s. values of vertical acceleration at a number of locations on the aircraft. For precise determination of the effects of wing bending, the sensors should be placed at the (CG), wingtip node right and wingtip node left. Details description for the placement of the sensors can be found in [12]. The acceleration of the wing relative to the CG is defined as η_z law, and it is calculated by:

$$\eta_{z_{law}} = \frac{1}{2} \eta_{z_{wingtip}}^{left\ node} + \frac{1}{2} \eta_{z_{wingtip}}^{right\ node} - \eta_{z_{CG}} \quad (3)$$

3.2. Control design

Fig. 5 shows the primary control surfaces of the NACRE aircraft. The non-linear models of the actuators were approximated by 2nd order linear model. The sensor delays were estimated by 2nd order Pade approximations. The FF control sequence works simultaneously with Spoiler 1 and 2 and Elevator 1 and 2.

In case of a gust disturbance, the proposed concept was to feedback the η_z law to the Flap 1 (inner aileron) and Flap 2 (center aileron), which would work together with the FF controller. Fig. 6 shows the control block diagram for the new control strategy.

In such a way, a two-stage feedback control law is devised; a separate control augmentation system (CAS) taking care of the flight dynamics primarily and the feedback active damping system (the newly designed SISO controllers) taking care – jointly with the triggered FF GLAS system – of the gust performance improvement. Such control structure has obvious advantages. First regarding tuning the controllers (both parts can be designed/tuned independently). Second, in the flight testing the newly designed controller can be turned on/off while keeping the aircraft under full control. Third, the point of flight safety is important, loss of such an add-on simple feedback controller is not a critical failure and would not take the aircraft out of control.

Flap 1 controller design

The first wind bending mode from $\eta_{z_{law}}$ to Flap 1 (inner aileron) lies between 2–3 Hz. $\eta_{z_{law}}$ controller was designed using the root locus method in MATLAB [11]. Eq. (4) shows the Flap 1 controller transfer function. In frequency domain the channel from Flap 1 to $\eta_{z_{law}}$ was already damped by 5–7 dB by the stabilizing \mathcal{H}_∞ controller [26]. While designing the controller using root locus method it was ensured that the lower frequency of the aircraft is not affected.

$$\eta_{z_{law}} \text{ to Flap 1} = \frac{6}{s^2 + 12s + 20} \quad (4)$$

The designed controller is a lowpass filter with approximately 1 Hz bandwidth (Fig. 7).

Flap 2 controller design

The first wind bending mode from $\eta_{z_{law}}$ to Flap 2 (center aileron) lies between 6–10 Hz. $\eta_{z_{law}}$ controller was designed using the root locus method. Eq. (5) shows the transfer function of the designed $\eta_{z_{law}}$ controller.

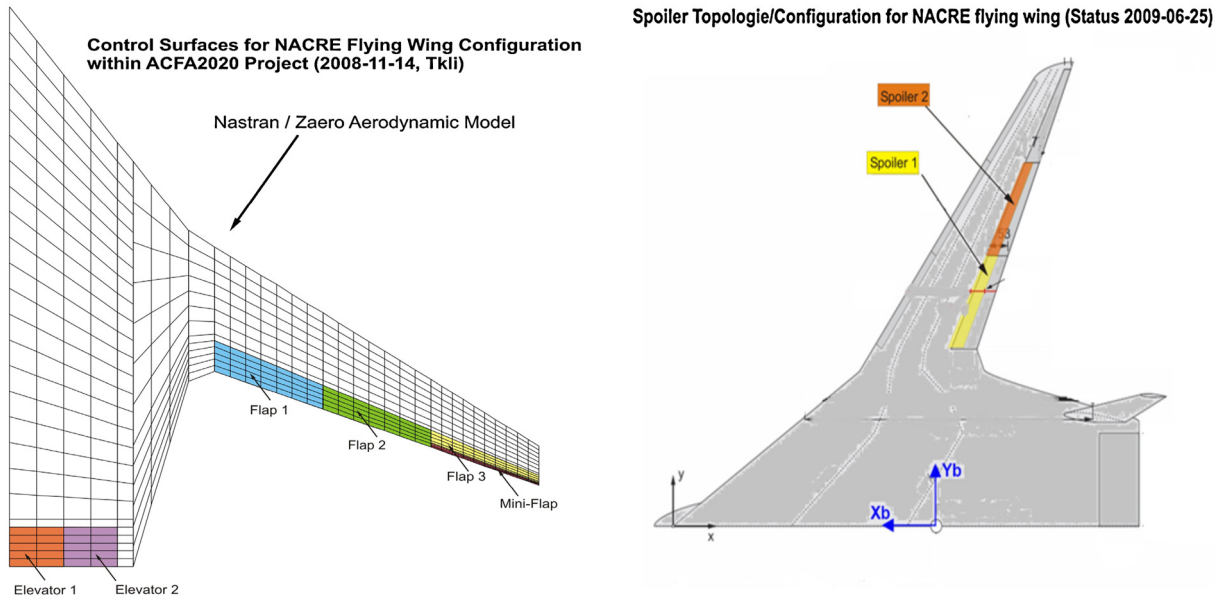
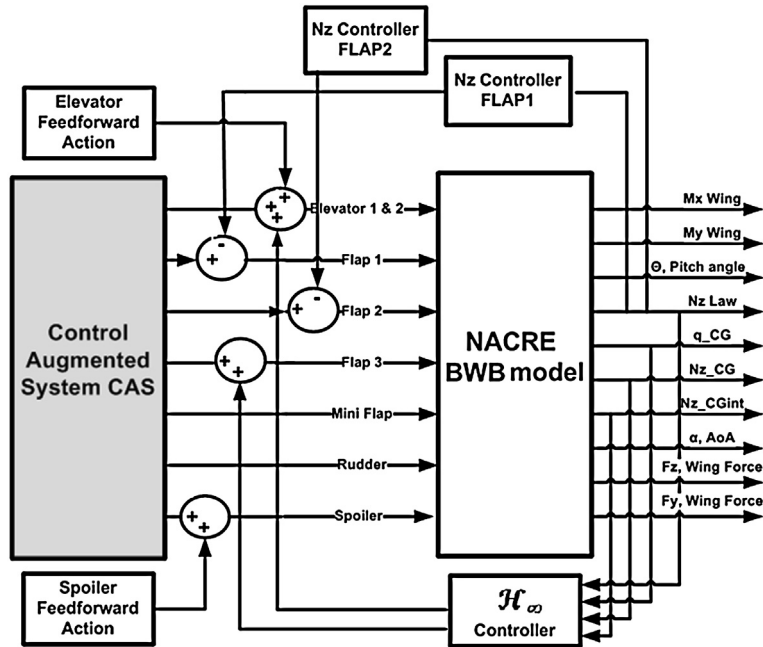


Fig. 5. Control surfaces of NACRE aircraft.

Fig. 6. New SISO control strategy by feeding back η_z law to Flap 1 and Flap 2.

$$\eta_{z_{law}} \text{ to Flap 2} = \frac{0.1s + 1}{s + 1} \quad (5)$$

A design requirement again is that the low frequency region is left untouched. Fig. 8 shows the frequency response of the $\eta_{z_{law}}$ controller over different mass cases. The designed controller is a first order filter with one zero and one pole.

4. Simulation results

Different mass cases (6 mass cases) were considered along with the gust lengths (10 gust lengths). The rate limiters and the saturation point of Flap 1 and 2 were also taken into account during the simulation. Flap 1 and Flap 2 were constrained by rate limiter at ± 40 deg/s and saturation point at $\pm 25^\circ$. The gust was used as an exogenous disturbance input signal to the flight dynamics model (to the angle of attack channel, more precisely).

M_x is defined as the wing root bending moment and M_y is defined as the wing root torsional moment. Fig. 9 to Fig. 11 show the response of the wing root moments M_x and M_y for the gust cases $k = 1, 5$ and 10 (other gust cases are shown in Appendix A). Simulations were done using SIMULINK [11]. All other gust cases had similar responses. The wing root moment values were normalized with respect to the maximum value of M_x & M_y which occurs at the longest gust case ($k = 10$). The cyan line corresponds to the original aircraft with only stabilizing \mathcal{H}_∞ controller engaged; blue line corresponds to aircraft with stabilizing \mathcal{H}_∞ controller engaged with only FF control action; finally the red line corresponds to the aircraft with stabilizing \mathcal{H}_∞ controller engaged with FF control action and newly designed $\eta_{z_{law}}$ controller to Flap 1 and 2 with \mathcal{H}_∞ controller engaged.

Observing Fig. 9, comparing the cyan and blue lines, the triggered FF action at short gust lengths ($k = 1$) artificially gives rise

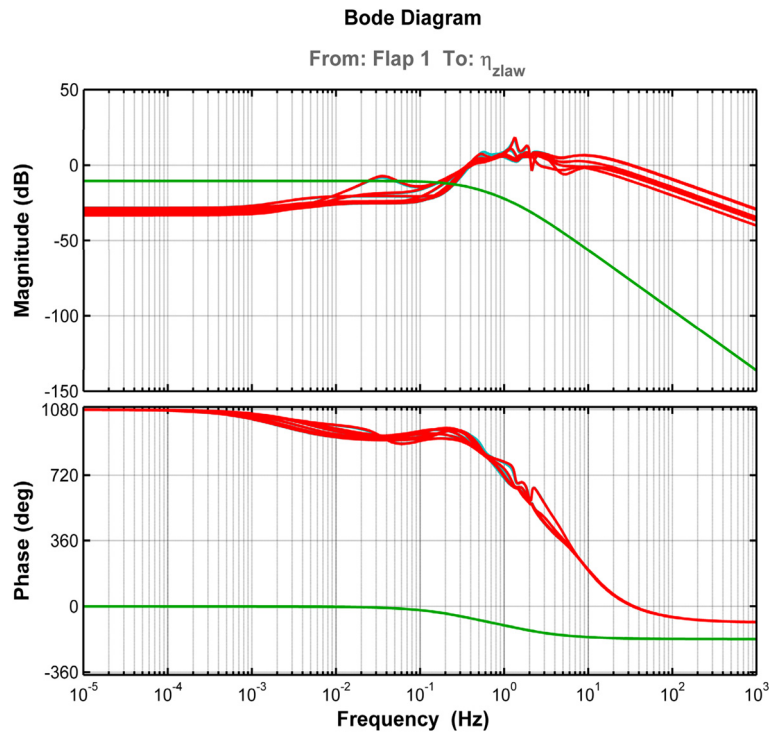


Fig. 7. Frequency response for different mass cases for (1 to 6) using η_{zlow} to Flap 1. Cyan shows the response of original aircraft with stabilizing \mathcal{H}_∞ controller engaged. Red shows the response with new Flap 1 controller engaged. Green shows the controller frequency response. (For interpretation of the references to color in this figure legend, the reader is referred to the web version of this article.)

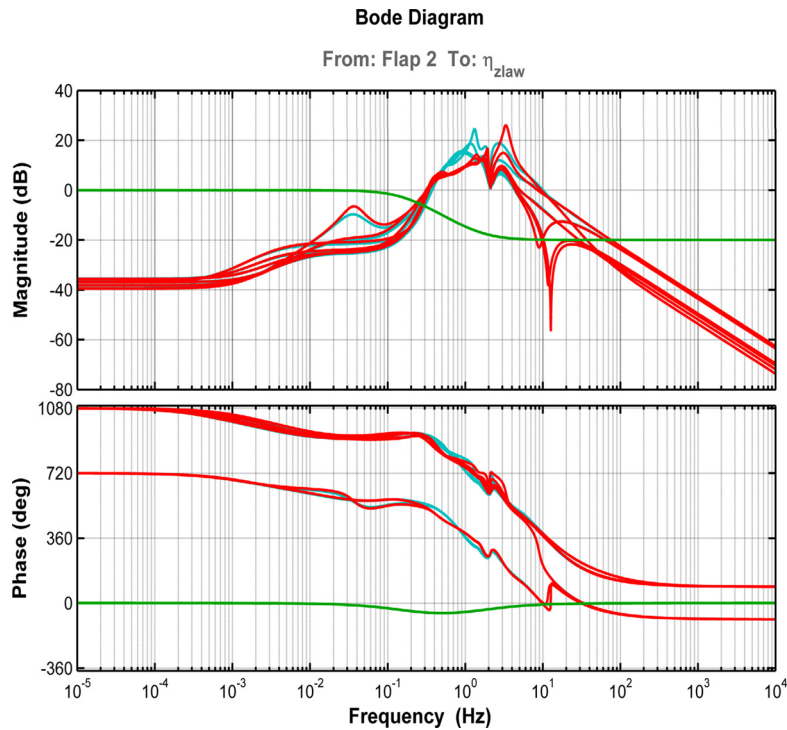


Fig. 8. Frequency response for different mass cases for (1 to 6) using η_{zlow} to Flap 2. Cyan shows the response of original aircraft with stabilizing \mathcal{H}_∞ controller engaged. Red shows the response with new Flap 2 controller engaged. Green shows the controller frequency response. (For interpretation of the references to color in this figure legend, the reader is referred to the web version of this article.)

to first peak in wing bending and torsional moments compared to free, uncontrolled aircraft (FF control action disengaged). This is the undesired effect of the FF control sequence at short gusts. Fig. 10 and Fig. 11 show that the triggered FF action at longer gust lengths $k \geq 5$, for the “sizing gusts”, significantly reduces the

first peak in wing bending and torsional moments, compared to the original aircraft. It is the key feature of the triggered FF GLAS system to reduce the 1st peak in the wing root moments.

The reduced performance of the FF control at shorter gust lengths can be attributed to the spoiler deflections. Now being

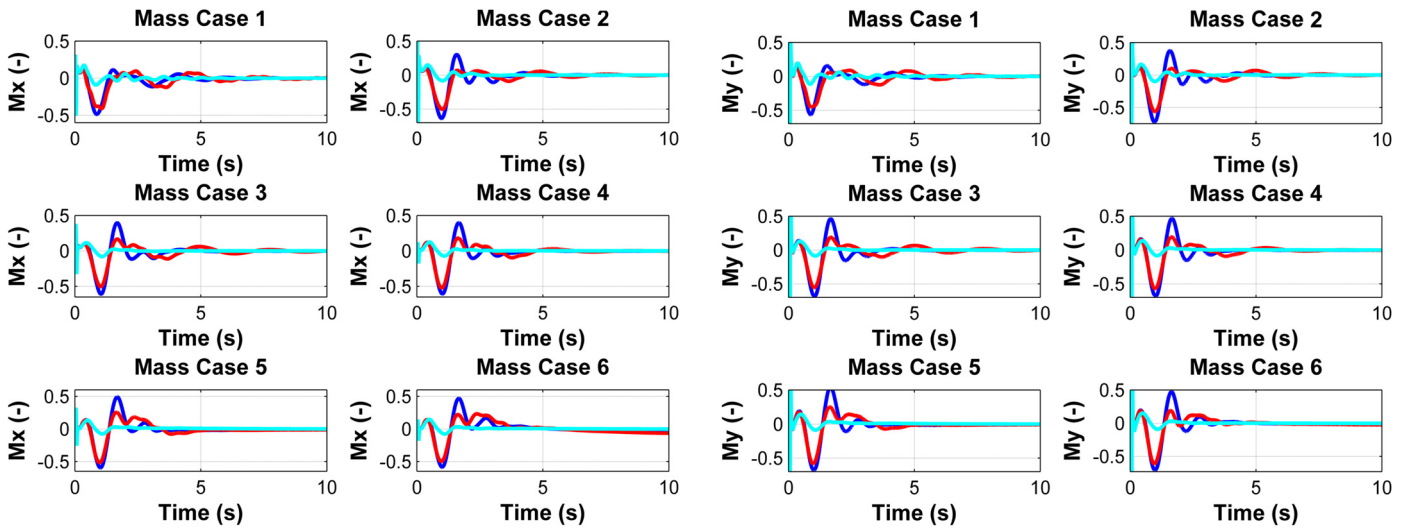


Fig. 9. Normalized wing root moment, M_x and M_y at gust length 9 m ($k=1$) for different mass cases using SISO controller. (For interpretation of the references to color in this figure legend, the reader is referred to the web version of this article.)

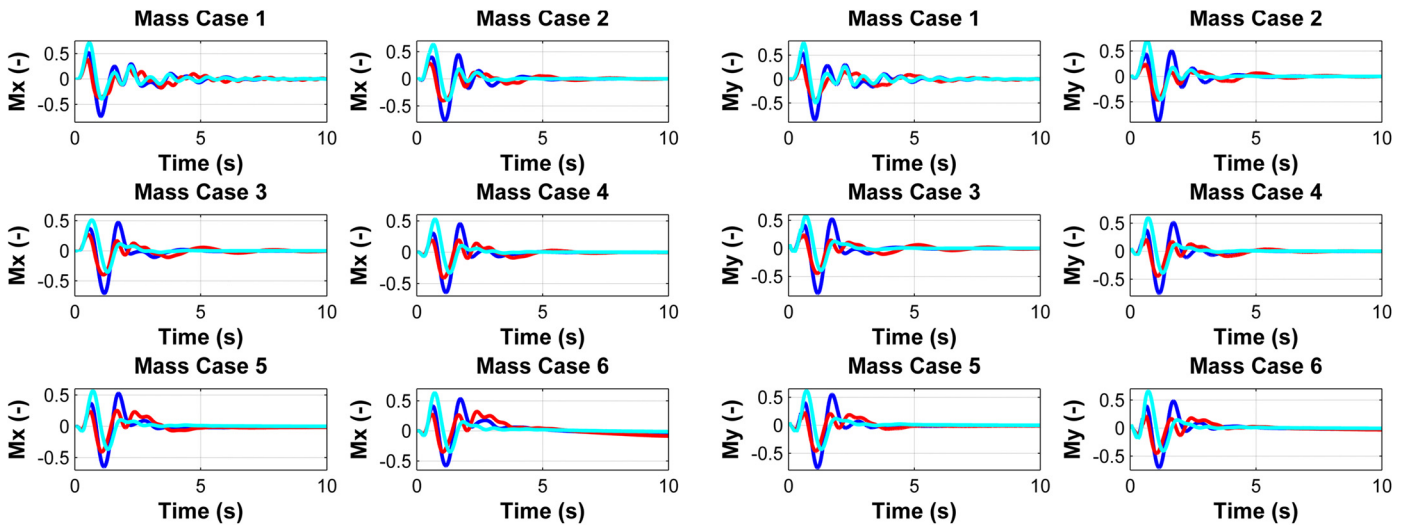


Fig. 10. Normalized wing root moment, M_x and M_y at gust length 60.96 m ($k=5$) for different mass cases using SISO controller. (For interpretation of the references to color in this figure legend, the reader is referred to the web version of this article.)

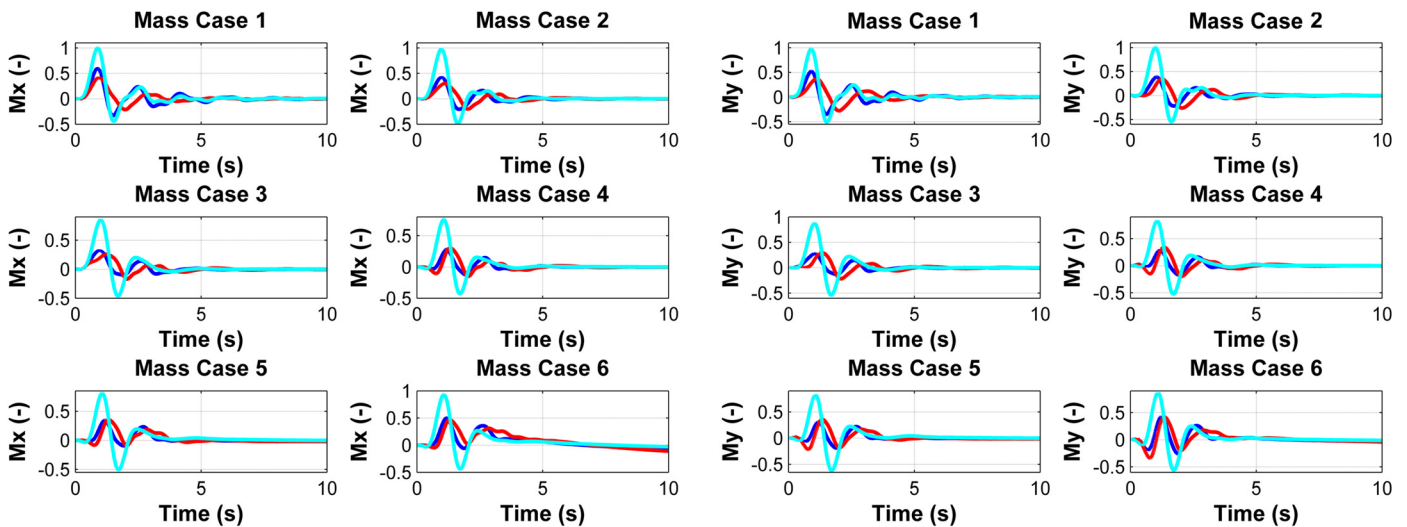


Fig. 11. Normalized wing root moment, M_x and M_y at gust length 152.4 m ($k=10$) for different mass cases using SISO controller. (For interpretation of the references to color in this figure legend, the reader is referred to the web version of this article.)

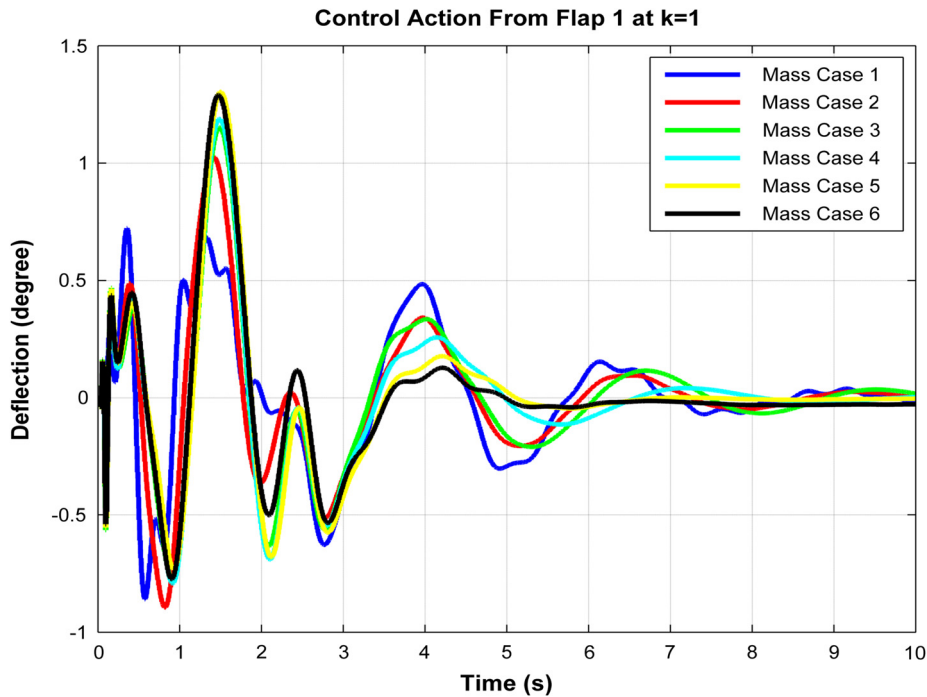


Fig. 12. Flap 1 control action at gust length $k = 1$.

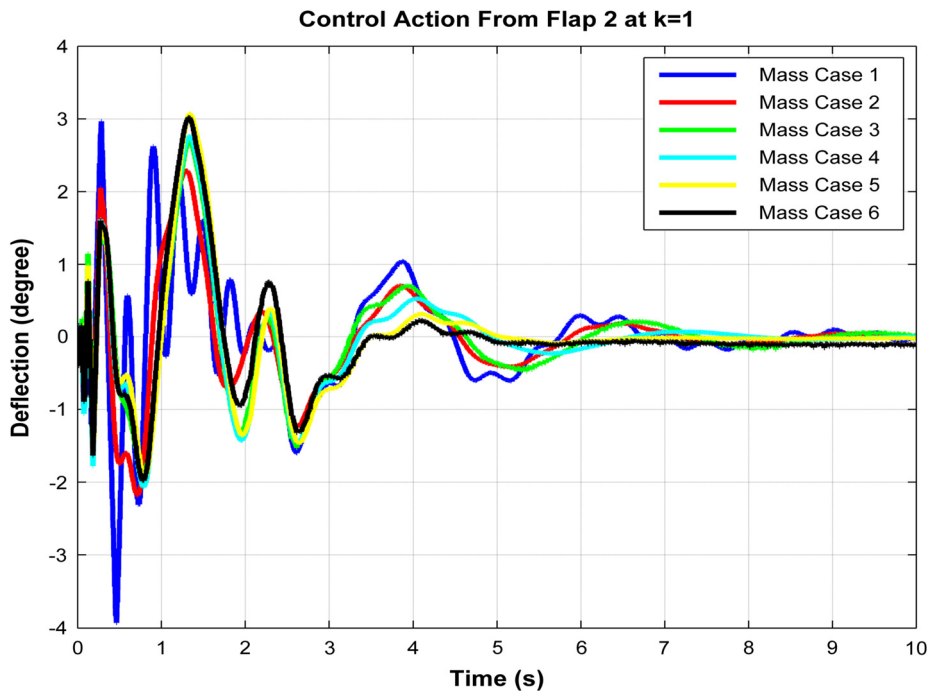


Fig. 13. Flap 2 control action at gust length $k = 1$.

Flap 1 and Flap 2 positioned right below Spoiler 1 and 2, it makes these control surfaces most effective to improve the performance. If Fig. 2 is considered for FF control deflection, it can be seen that Spoilers 1 and 2 deflect with a negative angle (which means the spoilers deflect upward) this produces a downward force on the wing. This downward force on the wing gave rise to wing root bending moment, M_x , and wing root torsional moment, M_y .

Of course the deflection of the spoilers and elevators and flaps during the flight is aerodynamically inefficient due to increased drag. However the deflections are made for a very short period of

time therefore the trade-off between drag and reduction of wing root moment is always beneficial.

When the newly designed feedback controller is engaged jointly with the FF triggered GLAS compensator, the simulation results show significant improvements in reducing the first peak in wing root bending moment and wing root torsional moments. From Fig. 9 to Fig. 11 (blue and red line), it can be appreciated that the new controller improves the FF control performance by reducing the 1st peak at low gust lengths $k = 1$ which was the primary design goal. In Fig. 10 and Fig. 11 it can be observed however that even for longer gust lengths $k \geq 5$ the newly designed controller

enhances the FF controller's performance by further reducing the wing root moments. Tables B.1 and B.2 (in Appendix B) provide detailed values regarding this improvement in the performance.

Fig. 12 and Fig. 13 show the resulting control deflection of Flap 1 and Flap 2. It can be seen that both the flap deflections start with a negative deflection and slowly move to higher positive values (which means the flaps deflect down), this produces a counter upward force on the wing which eventually reduces the wing root bending moment M_x and wing root torsional moment, M_y . The figures show the situation for the shortest gust load, the control action for other gust cases are similar.

One other important fact to consider is that the performance of the controller gets better from mass case 6 to 1. This means the performance of the newly designed controller gets better from high-mass case to low-mass case. This is practically beneficial due to the fact that during the flight the aircraft gradually loses weight due to the fuel burn.

The simulation results from Fig. 9 to Fig. 11 show therefore that by adding a feedback controller to the feedforward GLAS system, significantly improved performance is achieved in terms of reduction in wing root moments at shorter gust lengths as well as longer gust lengths. The feedforward controller gives a significant reduction in the wing root moments for gusts longer than 60.9 m (the sizing ones), while the additional feedback controller with Flap 1 and Flap 2 targets primarily the shorter gusts and has marginal positive effect on long gusts as well. On an average by adding the newly designed feedback controller the performance of the FF GLAS was improved by 39% in case of wing root bending moment M_x and 36% in case of wing root torsional moment M_y .

The 1st peak of wing root moments indicates the maximum load in the wing root constructions which provides the required sizing of the reinforcement needed at the wing root joints. Therefore the proposed improved GLAS system indicates a potential possibility in structural weight savings, in other words cost reduction and economic benefits.

5. Conclusions

The newly proposed control method improves the robustness performance of a previously developed feedforward gust load alleviation system. The proposed SISO controller provides a significant performance improvement to the feedforward controller at short gust lengths especially. While designing the controller via the root

locus method, frequency domain requirements were taken into account so that the low frequency dynamics of the aircraft was not affected. The first peak in the wing root moments was attenuated significantly which provides a potential possibility for structural weight savings for wing root joint reinforcement or increase in predicted life time of structure. In this research work only wing root moments were analyzed. The future works should carefully investigate and verify the moment distribution along the wing span.

Conflict of interest statement

None declared.

Acknowledgement

The authors would like to thank EADS Innovation Works, Munich, and all partners in the ACFA 2020 consortium (www.acfa2020.eu) for developing and providing the aircraft model. The work of M. Alam was partially supported by the Erasmus Mundus scholarship awarded by the European Commission, EACEA (Education, Audiovisual and Culture Executive Agency) and by the Czech Technical University in Prague under internal grant No. SGS13/144/OHK3/2T/13. The work of M. Hromcik was supported by the Czech Science Foundation (GACR) under grant No. GA13-06894S.

Appendix A

Fig. A.1 and Fig. A.2 show the aircraft's wing root moment at gust cases $k = 2, 9$.

Appendix B

The reductions in the peaks of the system are summarized in Tables B.1 and B.2. The 1st column of the first peak represents the percentage improvement in the performance using feedforward controller compared to the original aircraft response without the FF controller engaged. And it is calculated by

$$\% \text{Improvement using FF controller} = \frac{\text{peak of original aircraft} - \text{peak } i \text{ using FF}}{\text{peak of original aircraft}} * 100 \quad (\text{B.1})$$

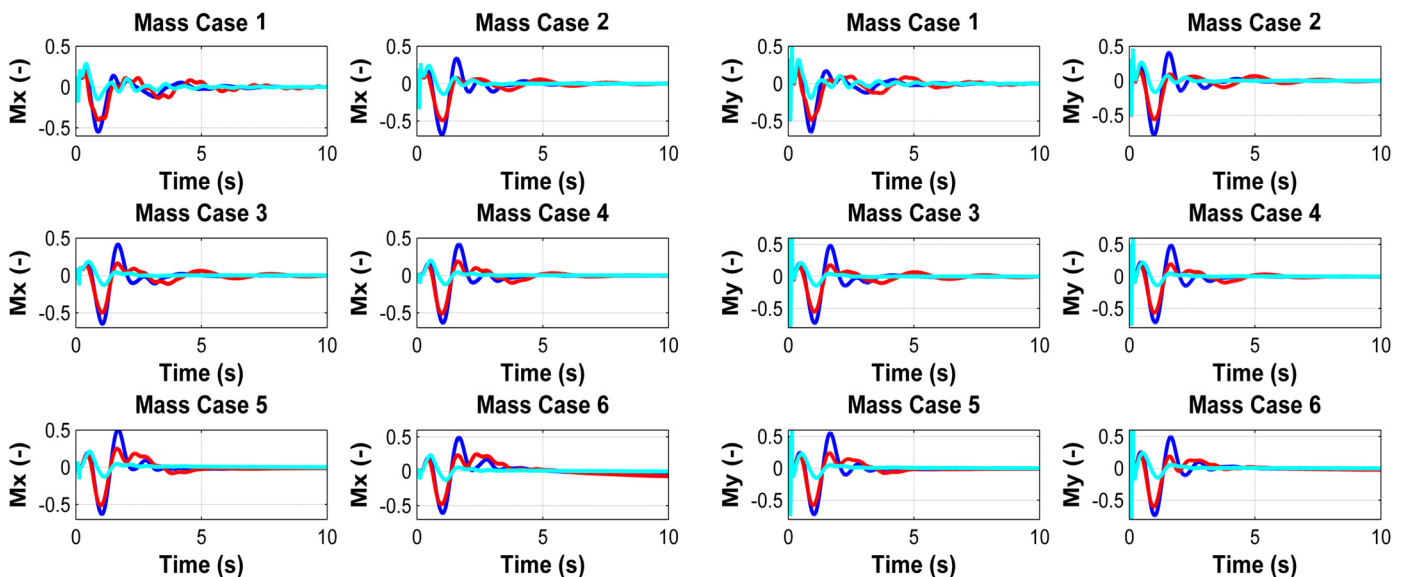


Fig. A.1. Normalized wing root moment, M_x and M_y at gust length 18 m ($k = 2$) for different mass cases using SISO controller.

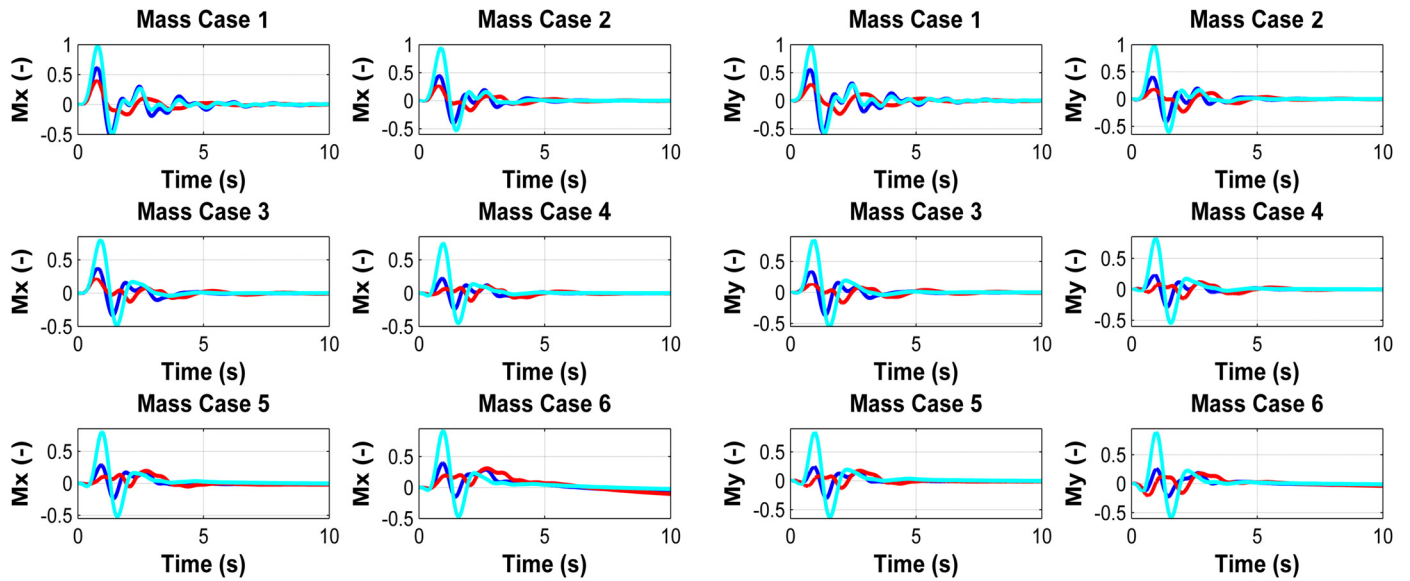


Fig. A.2. Normalized wing root moment, M_x and M_y at gust length 121.92 m ($k=9$) for different mass cases using SISO controller.

Table B.1

Comparison of peak reduction in wing root moment M_x between original aircraft, using feedforward action and feedforward action with SISO controllers.

Mass case	K = 1				K = 2				K = 3			
	1st peak		2nd peak		1st peak		2nd peak		1st peak		2nd peak	
	FF (%)	SISO (%)										
1	32.49	2.82	-434.51	21.54	25.40	16.82	-268.15	24.90	25.63	15.29	-178.64	31.13
2	43.91	6.42	-700.65	21.06	29.73	27.15	-397.74	27.90	31.68	14.43	-240.02	34.45
3	2.22	27.90	-678.94	17.14	20.81	10.23	-418.63	23.01	17.84	10.28	-254.08	28.32
4	18.56	-0.15	-779.63	13.79	6.46	32.98	-428.14	18.71	27.29	15.20	-262.97	23.65
5	-1.49	0.45	-680.15	12.86	6.22	10.89	-411.20	18.39	19.32	13.11	-228.26	23.36
6	2.64	2.93	-669.94	14.79	12.88	17.88	-375.07	20.50	21.70	10.49	-222.89	25.72

Mass case	K = 4				K = 5				K = 6			
	1st peak		2nd peak		1st peak		2nd peak		1st peak		2nd peak	
	FF (%)	SISO (%)										
1	26.10	22.86	-120.12	34.58	27.55	23.61	-87.39	49.82	28.97	30.25	-63.79	59.96
2	33.42	27.88	-146.97	39.79	36.99	24.33	-95.27	47.38	37.53	31.10	-58.83	55.29
3	22.65	25.57	-154.54	37.18	28.33	25.59	-99.58	43.80	32.71	29.16	-60.75	51.17
4	34.56	27.29	-154.87	29.78	42.53	36.44	-94.74	36.31	50.82	44.01	-51.84	155.56
5	27.21	21.02	-131.44	30.07	35.65	30.71	-76.40	36.92	44.17	37.22	-36.57	46.15
6	27.66	17.63	-122.55	32.09	34.83	184.85	-66.02	155.54	42.43	22.88	-25.18	50.68

Mass case	K = 7				K = 8				K = 9			
	1st peak		2nd peak		1st peak		2nd peak		1st peak		2nd peak	
	FF (%)	SISO (%)										
1	32.26	34.23	-43.24	67.45	37.14	35.24	-5.76	68.46	37.14	35.17	-5.76	68.35
2	42.62	34.53	-28.63	62.31	52.28	34.55	23.91	56.37	52.26	40.28	23.91	57.05
3	39.70	32.36	-28.43	59.65	52.99	32.68	31.09	60.06	52.99	41.31	31.09	61.79
4	58.68	52.57	-16.25	55.90	70.82	50.71	47.68	51.68	70.82	52.13	47.68	51.25
5	52.46	158.03	-3.67	55.66	64.48	92.93	54.83	71.53	64.48	31.73	54.83	78.73
6	49.31	22.09	8.61	69.25	57.05	20.23	68.50	33.28	57.05	21.13	68.50	30.49

Mass case	K = 10			
	1st peak		2nd peak	
	FF (%)	SISO (%)	FF (%)	SISO (%)
1	39.86	31.09	25.14	36.03
2	56.83	28.45	57.12	2.32
3	61.96	20.30	78.70	-70.30
4	63.32	-8.59	70.71	-1.06
5	57.58	-3.26	81.34	7.51
6	46.24	6.58	82.91	134.08

Table B.2Comparison of peak reduction in wing root moment M_x between original aircraft, using feedforward action and feedforward action with SISO controllers.

Mass case	K = 1				K = 2				K = 3			
	1st peak		2nd peak		1st peak		2nd peak		1st peak		2nd peak	
	FF (%)	SISO (%)										
1	13.69	15.87	-393.75	336.02	15.18	30.58	-223.19	24.37	18.08	27.41	-153.37	28.80
2	0.09	31.30	-644.70	22.19	19.13	36.59	-373.68	28.65	25.57	26.79	-238.35	33.95
3	0.00	29.67	17.10	18.11	2.07	28.03	-587.31	43.72	11.81	22.94	464.24	29.53
4	0.00	0.00	-764.34	15.31	-1.32	9.61	-415.59	21.67	14.40	21.22	-176.90	26.75
5	0.00	0.00	-704.76	15.30	2.84	12.63	-378.85	19.88	8.79	17.98	-177.39	25.07
6	0.00	0.00	-787.75	14.06	13.30	15.28	-397.06	20.37	13.22	6.84	-242.87	23.50

Mass case	K = 4				K = 5				K = 6			
	1st peak		2nd peak		1st peak		2nd peak		1st peak		2nd peak	
	FF (%)	SISO (%)										
1	22.19	39.80	-100.89	32.94	28.09	0.00	-72.52	0.00	28.45	46.98	-52.32	60.36
2	31.15	43.19	-35.41	39.29	37.41	46.19	-95.13	47.76	44.36	46.34	-57.45	56.56
3	20.55	36.55	-161.62	37.65	28.99	41.60	-104.24	44.23	38.98	35.75	-63.17	51.92
4	26.31	36.08	-153.61	33.74	36.96	44.09	-93.76	40.68	48.99	52.83	-50.67	48.78
5	22.39	35.09	-132.24	32.28	34.17	43.66	-76.76	39.08	47.24	50.02	-36.74	47.67
6	27.72	34.52	-134.62	29.59	40.13	46.15	-73.24	35.93	53.29	47.91	-29.28	44.78

Mass case	K = 7				K = 8				K = 9			
	1st peak		2nd peak		1st peak		2nd peak		1st peak		2nd peak	
	FF (%)	SISO (%)										
1	35.03	48.71	-34.40	71.70	43.06	47.24	1.34	63.19	43.06	48.10	1.34	59.10
2	47.33	50.27	-25.55	65.23	59.25	50.20	30.12	47.06	59.23	55.36	30.12	44.58
3	41.81	46.50	-28.53	60.86	60.22	46.96	33.59	59.69	60.22	59.72	33.59	54.64
4	56.99	62.62	-14.79	59.76	71.82	51.11	47.48	53.43	71.82	51.95	47.48	48.05
5	57.20	45.05	-3.55	59.41	70.61	29.05	52.48	63.61	70.61	29.64	52.48	57.31
6	64.93	36.55	6.29	59.12	70.89	30.45	62.01	29.21	70.89	31.06	62.01	7.14

Mass case	K = 10			
	1st peak		2nd peak	
	FF (%)	SISO (%)	FF (%)	SISO (%)
1	46.55	29.16	31.09	20.46
2	61.31	11.01	60.16	-21.74
3	68.47	-7.24	75.63	-65.87
4	65.02	-18.48	67.78	13.44
5	61.70	-13.84	69.73	-13.87
6	50.74	1.09	54.51	40.49

Performance improvement using the SISO controller is presented in the 2nd column and it is calculated by

% Improvement using SISO controller

$$= \frac{\text{peak using FF} - \text{peak using SISO}}{\text{peak using FF}} * 100 \quad (\text{B.2})$$

The negative values in the tables mean that there is a rise in the peak than expected, meaning deterioration in the performance. And the positive value tells the percentage improvement in the performance.

Appendix C. Supplementary material

Supplementary material related to this article can be found online at <http://dx.doi.org/10.1016/j.ast.2014.12.020>.

References

- [1] A. Abbas, J.d. Vicente, E. Valero, Aerodynamic technologies to improve aircraft performance, *Aerosp. Sci. Technol.* 28 (1) (2013) 100–132.
- [2] ACFA 2020 Consortium, Active control of flexible 2020 aircraft (ACFA 2020), EU FP7 project No. 213321, URL: <http://www.acfa2020.eu>, last retrieved: Sep. 8th, 2011.
- [3] M. Aikawa, K. Arai, M. Arnould, K. Takahashi, H. Utsunomiya, NACRE update and extension project, in: *Frontiers in Nuclear Structure, Astrophysics, and Reactions – Finustar*, 2006.
- [4] M. Alam, Combined feedforward/feedback gust load alleviation control for highly flexible aircraft, in: *Proceedings of 2014 PEGASUS-AIAA Student Conference*, Prague, 2014.
- [5] N. Aouf, B. Boulet, R. Botez, Robust gust load alleviation for a flexible aircraft, *Can. Aeronaut. Space J.* 46 (3) (2000) 131–139.
- [6] R. Brockhaus, *Flugregelung*, Springer DE, 2001.
- [7] L. Cambier, N. Kroll, MIRACLE – a joint DLR/ONERA effort on harmonization and development, *Aerosp. Sci. Technol.* 12 (7) (2008) 555–566.
- [8] European Commission, CORDIS: Projects and Results: Bringing ‘flying wing’ to the passenger, http://cordis.europa.eu/result/rcn/85652_en.html [accessed 05 11 2014].
- [9] European Commission, CORDIS: Projects and Results: Final Report Summary – ACFA 2020 (Active control for flexible 2020 aircraft), http://cordis.europa.eu/result/rcn/53860_en.html [accessed 05 11 2014].
- [10] J. Frota, NACRE novel aircraft concepts, *Aeronaut. J.* 114 (1156) (2010) 399–404.
- [11] M.U. Guide, *The MathWorks, Inc.*, Natick, MA, 1998, vol. 5.
- [12] T. Hanis, Active control for high capacity flexible aircraft, 2012.
- [13] T. Hanis, V. Kucera, M. Hromcik, Low order H optimal control for ACFA blended wing body aircraft, 2011.
- [14] L. Hansen, W. Heinze, P. Horst, Representation of structural solutions in Blended Wing Body preliminary design, in: *Proc. of the 25th International Congress on Aeronautical Sciences, ICAS2006*, Hamburg, 2006.
- [15] M. Hepperle, *The VELA Project*, 2005.
- [16] D.C. Kammer, Optimal sensor placement for modal identification using system-realization methods, *J. Guid. Control Dyn.* 19 (3) (1996) 729–731.
- [17] R.H. Liebeck, Design of the blended wing body subsonic transport, *J. Aircr.* 41 (1) (2004) 10–25.
- [18] E. Maury, J. Frota, NACRE – New Aircraft Concepts Research, in: *AeroSME FP6-Batch2 Meeting*, 2003.
- [19] D. McLean, *Automatic Flight Control Systems*, 1st edition, Prentice Hall, New York, 1990.

- [20] M. Meheut, R. Grenon, G. Carrier, M. Defos, M. Duffau, Aerodynamic design of transonic flying wing configurations, in: *KATnet II: Conference on Key Aerodynamic Technologies*, Bremen, Germany, 2009.
- [21] B. Mialon, M. Hepperle, Flying wing aerodynamics studies at ONERA and DLR, *MH*, vol. 150, 2005, p. 3.
- [22] R.C. Nelson, *Flight Stability and Automatic Control*, 2nd edition, WCB/McGraw-Hill, 1998.
- [23] N. Qin, A. Vavalle, A.L. Moigne, M. Laban, K. Hackett, P. Weinerfelt, Aerodynamic considerations of blended wing body aircraft, *Prog. Aerosp. Sci.* 40 (6) (2004) 321–343.
- [24] H. Struber, M. Hepperle, Optimization of flying wing transport aircraft configurations in the VELA project, DLR, German Aerospace Center TR-DLR-IB-124-2005/905, Braunschweig, Germany, 2005.
- [25] H. Tomas, M. Hromcik, Information-based sensor placement optimization for BWB aircraft, in: *Proceedings of the 18th IFAC World Congress*, 2011.
- [26] M. Voskuijl, G.L. Rocca, F. Dircken, Controllability of blended wing body aircraft, in: *26th International Congress of the Aeronautical Sciences*, 2008.
- [27] A. Wildschek, An adaptive feed-forward controller for active wing bending vibration alleviation on large transport aircraft, 2009.
- [28] A. Wildschek, Combined feed back control and feedforward control in order to actively reduce oscillations in aircraft, 2009.
- [29] A. Wildschek, T. Hanis, Method and apparatus for minimizing dynamic structural loads of an aircraft, 2013.
- [30] A. Wildschek, T. Hanis, F. Stroscher, E.I. Works, L optimization of an open loop gust load alleviation system for a large blended wing body airliner, 2012.
- [31] A. Wildschek, R. Maier, F. Hoffmann, M. Jeanneau, H. Baier, Active wing load alleviation with an adaptive feedforward control algorithm, in: *AIAA Guidance, Navigation, and Control Conference and Exhibit*, 2006.
- [32] A. Wildschek, R. Maier, M. Hromcik, T. Hanis, A. Schirrer, M. Kozek, C. Westermayer, M. Hemedi, Hybrid controller for gust load alleviation and ride comfort improvement using direct lift control flaps, in: *Proceedings of Third European Conference for Aerospace Sciences, EUCASS*, 2009.
- [33] A. Wildschek, F. Stroscher, T. Klimmek, Z. Šika, T. Vampola, M. Valášek, D. Gangsaas, N. Aversa, A. Berard, A. France, Gust load alleviation on a large blended wing body airliner, in: *Proceedings of ICAS*, 2010.

Section in book

edited by Martin Kozek, Alexander Schirrer; Modeling and Control for a Blended Wing Body Aircraft: A Case Study, Springer, Oct 27, 2014 - Technology & Engineering, ISBN 3319107925, 9783319107929.

Section 6.6 Low-Order Control Law Design

Advances in Industrial Control

Martin Kozek
Alexander Schirrer *Editors*

Modeling and Control for a Blended Wing Body Aircraft

A Case Study

AIC

 Springer

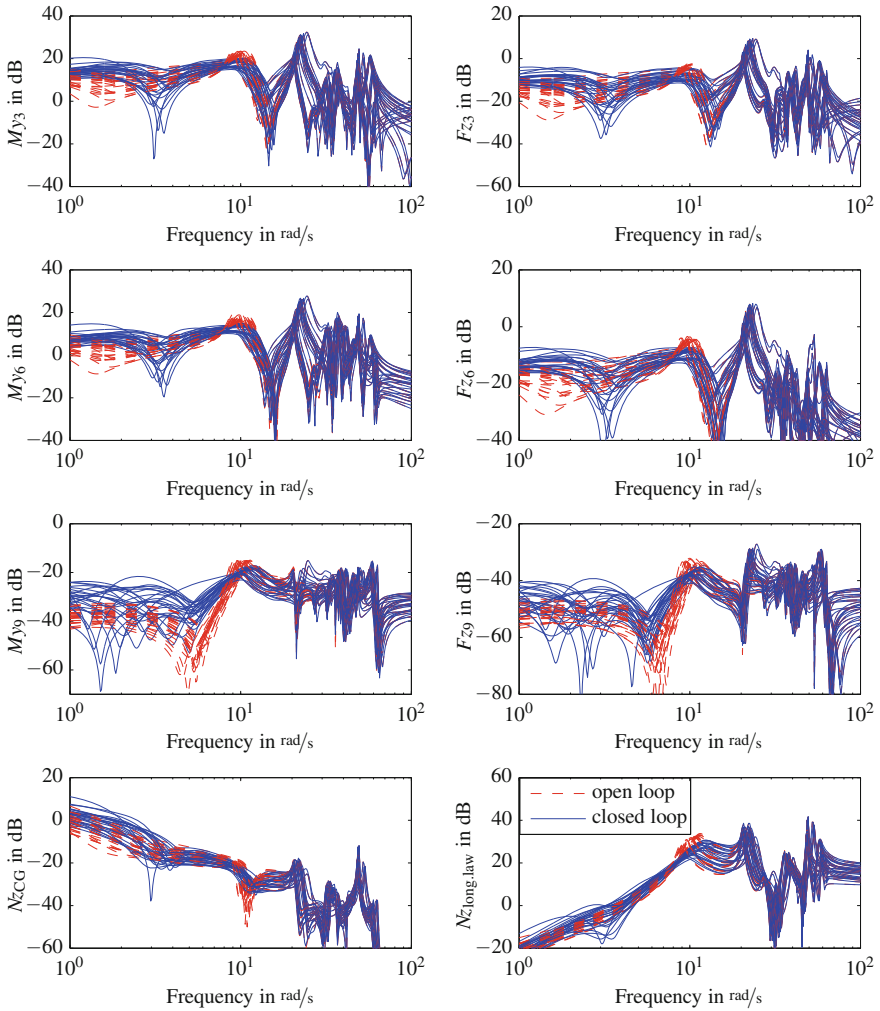


Fig. 6.35 Evaluation of aeroelastic control performance based on singular value analysis plots for several representative outputs

6.6 Low-Order Control Law Design

M. Hromčík and T. Haniš

6.6.1 Lateral \mathcal{H}_∞ -Optimal Control Law

Two different design approaches for design of lateral control augmentation system (CAS) for large BWB aircraft with flexible structure are elaborated and assessed in

this section. The most challenging design issues are related to coupling of rigid-body (RB) mechanics and flexible dynamics. First, a classical approach is employed giving rise to separate flight dynamics controller (\mathcal{H}_2 -optimal, with sufficient roll-off at higher frequencies to avoid spillover) and an active damper for most prominent lateral flexible modes on top of that (mixed-sensitivity \mathcal{H}_∞ design). This approach proves successful and has obvious advantages related to the design process complexity and to implementation/verification/testing. On the other hand, there is always a risk of potentially significant performance loss compared to a fully integrated design. For this reason, a fully integrated design is also presented in the form of a fixed-order multi-input multi-output (MIMO) \mathcal{H}_∞ -optimal flight control system (FCS) controller, obtained by means of direct non-convex non-smooth optimization using the dedicated software package HIFOO. Performance of both approaches is discussed. This design is carried out for the lateral motion of the NACRE BWB 750-passenger aircraft predesign model.

6.6.1.1 Introduction

Large lightweight aircraft structures and novel concepts, such as the BWB aircraft configurations, typically feature low-frequency structural vibrations modes, and their coupling with the flight mechanics modes may occur. Combined with significant dependency of the aircraft dynamics on flight parameters (Mach number/altitude/passengers/fuel volume and its distribution), severe flight control laws design challenges are to be expected.

Traditional methods for flight control design typically use nested single-input single-output (SISO) control loops and strongly structured control architectures [79]. These methods are based on detailed aircraft system analysis and exploit paths with weak coupling to obtain good results for conventional flight control design. However, multivariate methods, such as optimal control and particularly robust control design methods, are state-of-the-art for more complex flight control designs nowadays, especially useful for coupled and/or uncertain system dynamics. Two large groups of control design methodologies are optimal control design methods (for example, LQG control and the Kalman estimator [52]), as well as robust control design methods (see [76, 95] for fundamentals, or [7] for an aerospace-specific overview).

Two different approaches to lateral MIMO feedback CAS for NACRE BWB aircraft are presented in the following sections. They are namely a robust MIMO $\mathcal{H}_2/\mathcal{H}_\infty$ mixed-sensitivity controller and a low-order robust MIMO \mathcal{H}_∞ -optimal controller designed by direct fixed-order control design techniques. All controllers are designed to guarantee the desired closed-loop RB response (namely rise time and no-overshoot behavior to the reference change of the bank angle set point, attenuation of side-slip disturbance, and required damping ratio of the DR mode), and to dampen the first two anti-symmetric wing bending flexible modes. Performance and robustness of all controllers is demonstrated by means of MATLAB/Simulink® simulations, and their advantages and drawbacks are discussed.

6.6.1.2 BWB Aircraft Lateral Mathematical Model

The mathematical model of the BWB aircraft used for control law design consists of the flight mechanics model combined with the models of actuators and sensors. Actuator models are considered as second-order linear models augmented by saturations and rate limiters. Sensors are modeled as second-order Butterworth filters with time delays approximated by second-order Padé approximations. The mathematical model of the aircraft consists of the RB description (modeled as a 12th-order linear system separated into longitudinal and lateral dynamics), flexible modes (for design purposes just four modes are considered, depicted by an eighth-order linear model) and lag states. The overall model used for control law design is of order 52.

6.6.1.3 $\mathcal{H}_2/\mathcal{H}_\infty$ Mixed-Sensitivity Controller

A two-stage control law is devised—a separate CAS taking care of the flight dynamics (robust \mathcal{H}_2 -optimal roll autopilot, with roll-off at higher frequencies), and an active damper for selected flexible modes (\mathcal{H}_∞ -optimal mixed-sensitivity controller tuned to first two anti-symmetric wing bending modes). Such an arrangement has obvious advantages—regarding tuning (both parts are designed/tuned independently), future flight testing (the active damper can be tested after the roll autopilot is implemented and approved, and it can be turned on/off at any time while keeping the aircraft well-controlled), safety (loss of the damper’s functionality, for example, due to sensors failure, does not take the airplane out of control). The drawback is the potential reduction of performance compared to a fully integrated design where both flight dynamics and vibrational issues are handled by a single large MIMO controller.

Design Method

The lateral CAS (roll autopilot) is designed by \mathcal{H}_2 norm minimization of the generalized plant, encompassing the lateral RB dynamics itself (four states/outputs), two integrators (to ensure perfect steady-state tracking of a roll angle set point command and perfect steady-state attenuation of a side-slip disturbance), and two low-pass filters (for the required roll-off at higher frequencies—so that the flexible modes are left untouched and not excited by the controller). As all the RB states are measured, no observer needs to be implemented in fact and the resulting order of this CAS can be kept quite small (six states). Resulting controller features RS/RP for all considered mass cases (three passengers and five fuel cases).

On top of that, a robust MIMO controller is built by minimization of the \mathcal{H}_∞ norm of the frequency-weighted mixed-sensitivity function. The wings’ modal anti-symmetric sensor and anti-symmetric flaps make up the I/O groups. Loosely speaking, the closed-loop sensitivity function is kept small at selected frequency regions (in our case covering the wings’ anti-symmetric modes) to assure for good performance (disturbance attenuation), while the complementary sensitivity function is kept small everywhere else (to ensure robustness—the design model becomes invalid outside the selected frequency region). A simple design model of eighth order was constructed

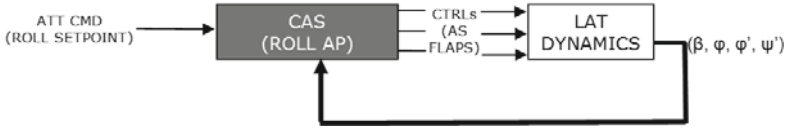


Fig. 6.36 Control augmentation system for \mathcal{H}_2 controller design. Anti-symmetrically operated wings ailerons are considered as control surfaces

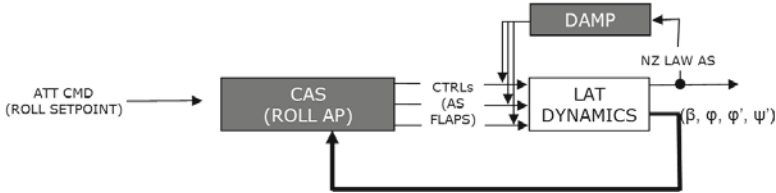


Fig. 6.37 Control augmentation system for $\mathcal{H}_2/\mathcal{H}_\infty$ controller design. Anti-symmetrically operated wings ailerons are considered as control surfaces

(modeling accurately the two modes and close region in the I/O channels). Two resonant weighting filters of second order are tuned to the frequencies and dampings of the anti-symmetric wing bending modes of a selected representative case for this purpose. The resulting \mathcal{H}_∞ controller has 20 states.

The resulting damper (and also the overall CAS/damper combination) provides RS for all mass cases, significant improvement regarding damping of structural vibrations for most mass cases (more than 5 dB attenuation), and no effect on vibration damping for the remaining cases. These findings and the overall performance of the designed controller and its respective parts are visualized in Figs. 6.36 and 6.37.

$\mathcal{H}_2/\mathcal{H}_\infty$ Control Results

Brief assessment of the controller performance is given in the text above (regarding robustness and performance). A set of selected characteristics is now given to document these findings.

Note that very good performance is achieved for those cases that do not vary much in the frequency of the targeted modes (Fig. 6.38 left). However, even for the other cases (Fig. 6.38 right), some performance improvement is achieved, and RS is assured (Figs. 6.39, 6.40, and 6.41).

Required response to bank angle set point is achieved. Note marginal improvement of the response when the damping system is connected (though it was not intended to influence the flight dynamics in fact). As stated above, the flight dynamics part contains integrated yaw damper and side-slip compensator. Gain and phase margins for the complete designed controller have been evaluated. RS of the closed loop for all mass cases is achieved. For simultaneous, independent, worst-case variations in the individual channels the gain margin ranges from 1.9 to 3.7 dB, and the phase margin ranges from 12 to 23°, depending on the mass case.

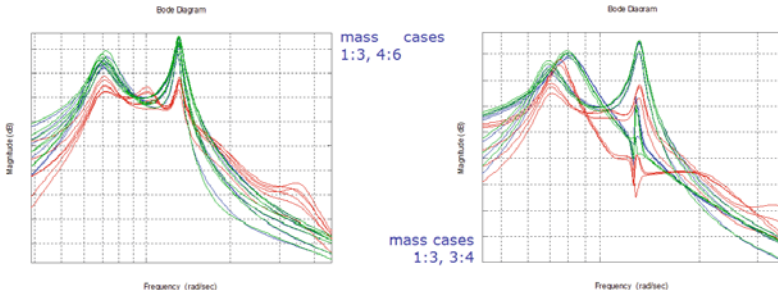


Fig. 6.38 Wing bending modes attenuation. Open loop (green), \mathcal{H}_2 control (blue), and $\mathcal{H}_2/\mathcal{H}_\infty$ control (red)

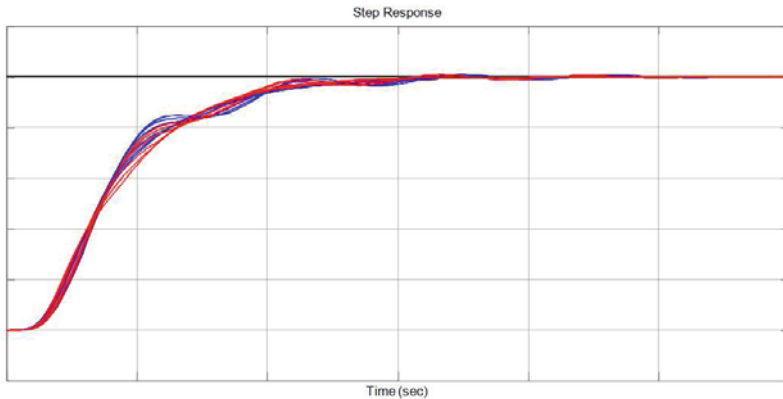


Fig. 6.39 Roll reference tracking. \mathcal{H}_2 control (blue) and $\mathcal{H}_2/\mathcal{H}_\infty$ control (red)

6.6.2 Non-convex Non-smooth Optimization

In recent years, great progress has been made in the challenging area of non-convex non-smooth optimization solvers. In contrast to more traditional setups, such problems are highly non-convex and no differentials or Jacobians can be used to navigate the search for even a local optimum. The solvers rely on a Broyden–Fletcher–Goldfarb–Shanno (BFGS) variable metric (quasi-Newton) method [16, 17, 51], or non-smooth modifications of Virginia Torczon’s multidirectional search (MDS) [2, 81, 82].

Related numerical software has been soon delivered in the form of freeware and commercial package like Hybrid Algorithm for Non-Smooth Optimization (HANSO) based on the BFGS method.

As people from the systems and control community quickly realized, such algorithms and tools can be successfully applied to resolve some control design challenges that are otherwise almost untractable for real-life-size data. Didier Henrion and Mike Overton seem to get furthest, proposing a new methodology for direct design of

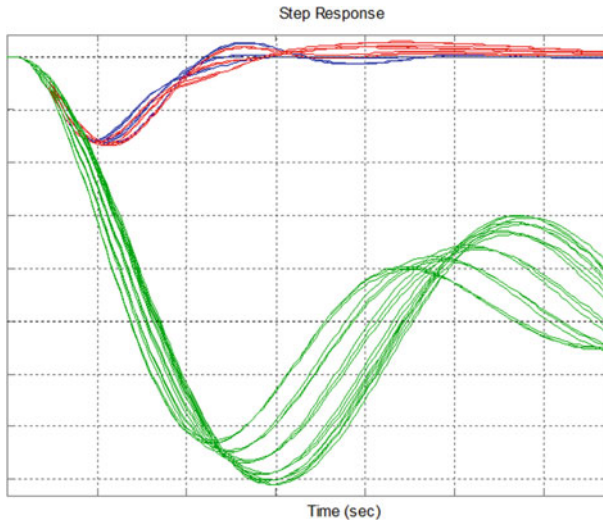


Fig. 6.40 Side-slip disturbance rejection. Open loop (*green*), \mathcal{H}_2 control (*blue*), and $\mathcal{H}_2/\mathcal{H}_\infty$ control (*red*)

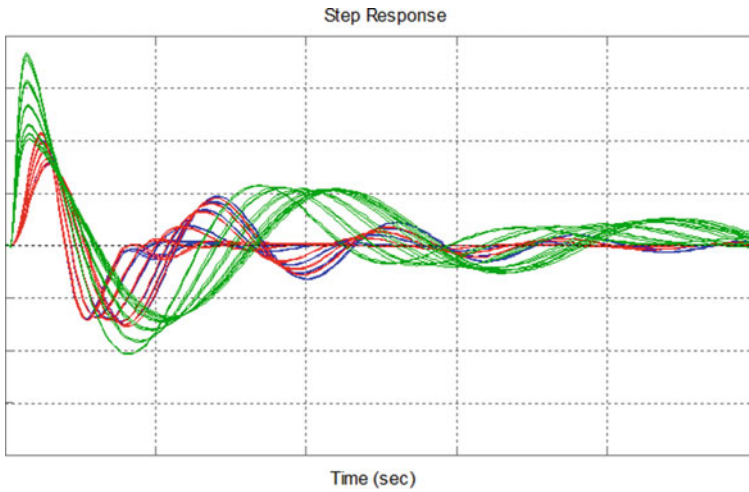


Fig. 6.41 Yaw rate damper. Open loop (*green*), \mathcal{H}_2 control (*blue*) and $\mathcal{H}_2/\mathcal{H}_\infty$ control (*red*)

low-order \mathcal{H}_∞ -optimal controllers in the 2000s [3, 15, 38, 39, 59], and delivering a related freeware package HIFOO.

The HIFOO package has already attracted attention of controls designers in the miscellaneous field [22, 25, 47, 63, 65, 87]. Regarding flight controls design, the first attempt was made in master thesis [59], where the applicability of the package

was approved by a means of a textbook example of a wing-leveler controller for an F-16 aircraft.

In this section, this approach and software will be employed to design, at one-shot, a robust, full-featured, \mathcal{H}_∞ -optimal longitudinal control law for a BWB highly flexible near-future airliner concept, following the recommended and industry-approved structure for this CAS. Performance of the result is assessed by means of high-fidelity simulations and classical, industry-standard robustness analysis results.

6.6.3 Direct Approach to Fixed-Order \mathcal{H}_∞ -Optimal Control Design

For reader's reference, the basic principles of the underlying algorithms used for direct \mathcal{H}_∞ fixed-order control design are summarized in brief in this section, adopted from [38]. Interested readers are advised to consult the original paper for a more detailed and rigorous treatment.

The aim of the HIFOO algorithm is to deliver a stabilizing \mathcal{H}_∞ -optimal controller for given n LTI systems. The criterion for \mathcal{H}_∞ optimization is expressed by the generalized plant setup. The algorithm has two phases. In each phase, the main workhorse is the BFGS optimization algorithm, which is surprisingly effective for non-convex, non-smooth optimization. The user can provide an initial guess for the desired controller; if this is not provided, HIFOO generates randomly generated initial controllers, and even when an initial guess is provided, HIFOO generates some additional randomly generated initial controllers in case they provide better results. The first phase is stabilization: BFGS is used to minimize the maximum of the spectral abscissa of the closed-loop plants. This process terminates as soon as a controller is found that stabilizes these plants, thus providing a starting point for which the objective function for the second phase is finite. The second phase is optimization: BFGS is used to look for a local minimizer of the controllers found in the first phase. The HIFOO control design method searches for locally optimal solutions of a non-smooth optimization problem that is built to incorporate minimization objectives and constraints for multiple plants. The optimization problem is introduced as a set of augmented plants, see Fig. 6.42, commonly used in robust control approaches. First, the controller order is fixed at the start, allowing for low-order controller design. Second, Lyapunov or lifting variables are introduced to deal with the conflicting specifications. The resulting optimization problem is formulated on the controller coefficients only, resulting in a typically small-dimensional non-smooth non-convex optimization problem that does not require the solution of large convex sub-problems, relieving the computational burden typical for Lyapunov LMI techniques. An algorithm that searches only for local minimization is used for the sake of computational time. While no theoretical guarantee can be given on the result's quality, in practice it often yields surprisingly efficient control laws.

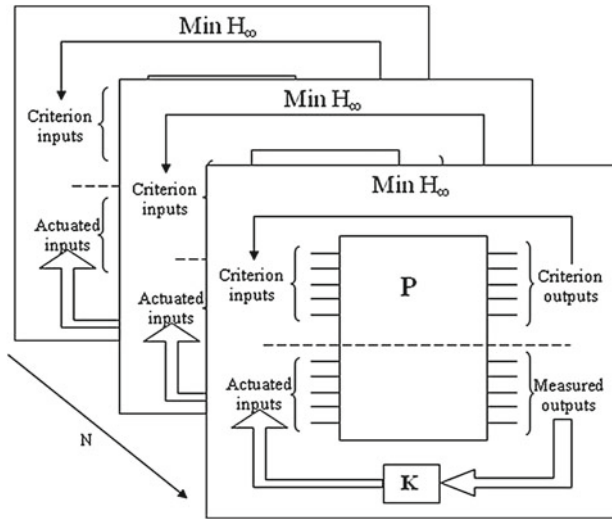


Fig. 6.42 \mathcal{H}_∞ fixed-order optimization setup

6.6.3.1 Lateral Fixed-Order \mathcal{H}_∞ -Optimal MIMO Robust Controller

Similar as in the previous section, the two different control goals are targeted, but this time by one integrated controller. One job of the control law is to provide autopilot functionality. The autopilot consists of a stability augmentation system (SAS) (a DR mode damper) and a CAS (roll and side-slip angle reference tracking). Other roles of the control law are related to vibrations and loads attenuation.

The lateral integrated CAS was designed as a 2DoF architecture using the fixed-order optimization approach to keep control law order low. The resulting, extremely simple controller (in this case, just third-order control law was used) was calculated using the HIFOO toolbox. The overall lateral CAS consists of a RB autopilot (roll and side-slip tracker with DR mode damper) and an active feedback damper for structural modes. The lateral CAS setup can be seen from Fig. 6.43. Two reference signals are used as inputs into the feed-forward part of the controller (roll and side-slip setpoints). The side-slip reference signal is usually set to zero, and then the CAS provides coordinated turn functionality.

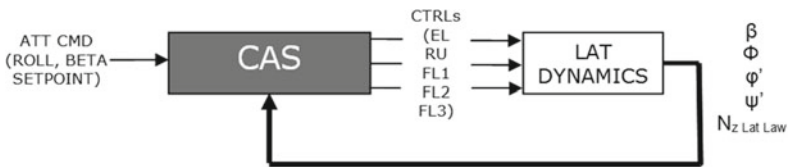


Fig. 6.43 Control augmentation system for HIFOO

The control surfaces used by the CAS are all ailerons (anti-symmetrically actuated FL1–FL3), rudders (RU) and elevators (symmetrically actuated EL). Measured signals are lateral RB variables at CG (side-slip angle, roll angle, roll rate and yaw rate), for structural modes control we have selected a lateral wing bending acceleration modal sensor in an anti-symmetrical setup. The resulting control law (autopilot and structural modes controller) provides RS as well as RP for all 18 cruise condition cases (six fuel and three passenger cases).

6.6.3.2 HIFOO Control Results

The achieved improvement of damping of the first and second wing bending modes can be seen from Fig. 6.44. Simultaneously, the DC gain is preserved for all cases. RP can be approved by the bank angle reference signal tracking response plotted in Fig. 6.45 (left). Responses for a sequence of two steps are shown and one can see sufficiently fast response with acceptably small overshoot.

Side-slip disturbance attenuation functionality is investigated in Fig. 6.46 (left). One can see complete vanishing of side wing influence in a few second and without inducing oscillation for major part of cases. DR mode damping is investigated in Fig. 6.46 (right).

Gain and phase margins for the complete designed controller have been evaluated. RS of the closed loop for all mass cases is achieved. For simultaneous, independent,

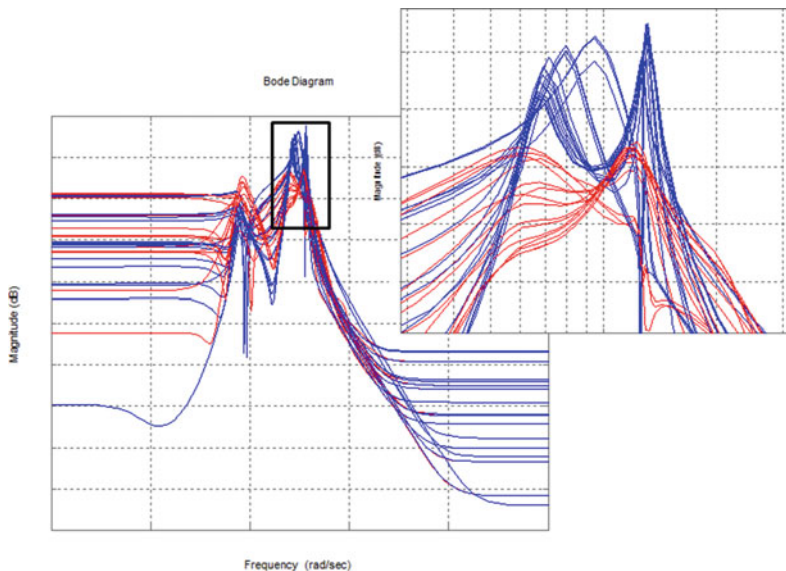


Fig. 6.44 Wing bending mode attenuation. Open loop (blue), closed loop (red)

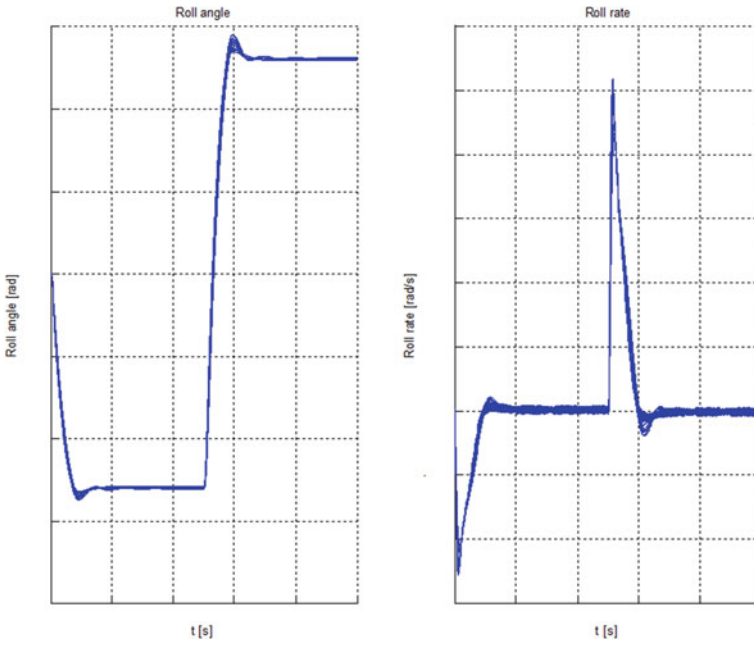


Fig. 6.45 Bank angle and roll rate reference signal tracking

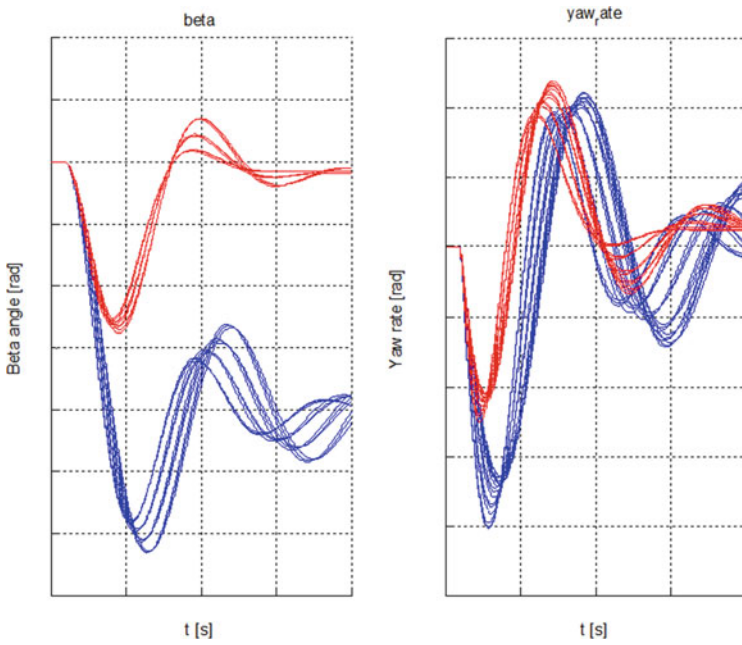


Fig. 6.46 Side-slip angle disturbance attenuation (left) and Yaw rate damping (right). Open loop (blue), closed loop (red)

worst-case variations in the individual channels the gain margin ranges from 0.8 to 2.6 dB, and the phase margin ranges from 5 to 16°, depending on the mass case.

6.6.4 Longitudinal \mathcal{H}_∞ -Optimal Control Law of Prescribed Structure

Advanced non-convex non-smooth optimization techniques for fixed-order \mathcal{H}_∞ robust control are proposed in this part for design of FCSs with prescribed structure. Compared to classical techniques—tuning of and successive closures of particular SISO loops like dampers, attitude stabilizers, etc.—all loops are designed simultaneously by means of quite intuitive weighting-filters selection. In contrast to standard optimization techniques, such as \mathcal{H}_2 or \mathcal{H}_∞ optimization, the resulting controller respects the prescribed structure in terms of engaged channels and orders (for example, P, PI, PID controllers). In addition, robustness with respect to multi-model uncertainty is also addressed which is of most importance for aerospace applications as well. Such a way, robust controllers for various Mach numbers, altitudes, or mass cases can be obtained directly, based only on particular mathematical models for respective combinations of the flight parameters.

6.6.4.1 Introduction

The flight dynamics, exhibiting many oscillatory or unstable modes for a typical aircraft, as well as the automatic or semi-automatic regimes of modern autopilots call for control synthesis methods that can effectively address these issues. Traditionally, classical tools for SISO loops tuning are used successively to deliver a complex FCS composed of a few smartly pre-selected channels, such as pitch, roll, or yaw dampers for suitable dynamics modifications (stability augmentation), subsequent attitude hold autopilots, automatic navigation loops, etc. Typically, a significant number of iterations and “backstepping” is required as the higher-level loops interact partially with the lower-level pre-designed parts. Historically, frequency response methods were developed first in the 1930s and 1940s [11, 32, 56, 58, 60], and they remain arguably the most commonly used methods until today [14].

Since the 1960s, results of optimal control theory have been used extensively for aircraft control design as a powerful alternative to the classical approach. The methods are typically purely multi-input multi-output (MIMO) in nature, delivering all channels of the resulting controller in “one shot”. The design procedure is controlled indirectly by means of selection of some weightings, being it constant matrices for LQ or LQG approach [53, 95], or LTI shaping filters for the \mathcal{H}_2 or \mathcal{H}_∞ -optimal control [7, 76, 95]. Nevertheless, the structure of the FCS is typically very hard or impossible to imprint, and the order (complexity) of the resulting controller can

become unacceptably large as well. In this regard, the classical methods still have quite a lot to offer.

Robustness of the flight controller is of utmost importance. The flight dynamics changes considerably as the aircraft properties vary over time (fuel amount, center of gravity position) and as the flight parameters change (altitude, airspeed, attitude angles). Classical and optimal controllers must fulfill the robustness requirements which is typically acknowledged by means of stability margins analysis (gain margin, phase margin [10, 18, 19, 53, 76, 95]) and extensive simulations for selected important points of the flight envelope. Nevertheless, neither of these methodologies supports incorporating the robustness requirements explicitly into the design procedure. In contrast, the robust control design approach, developed in the 1980s through the 2000s [26, 30, 31, 95] relies on the mathematical formulation of the uncertainty as one of the control design parameters. Most prominent methods are unstructured \mathcal{H}_∞ optimization [7, 76, 95], structured \mathcal{H}_∞ control (μ -synthesis, DK-iterations [6, 27–29, 95], robust loopshaping [55], and others). They all have been naturally accepted by the aerospace controls community, giving rise to significant implementations [9, 35, 44, 62].

One may ask if there is not a way to combine the benefits of the classical, optimal, and robust approaches—the convenient weighting-filters formulation of the optimal control synthesis, hierarchical and comprehensive structure of the classical controllers, and insensitivity to parameters uncertainties of the robust control designs. Indeed, some attempts have been made, based either on linear quadratic optimization (static output feedback design [77–79]), based on mixed-sensitivity \mathcal{H}_∞ optimization with static output constraints [49, 75], or by designing a mixed $\mathcal{H}_2/\mathcal{H}_\infty$ -optimal controller of fixed order based on a homotopy algorithm [91].

In this section, a completely different approach toward this goal is suggested, though. Thanks to the practical availability of computer-aided control systems design (CACSD) tools based on most recent non-convex non-smooth optimization techniques, direct synthesis methods can be employed to deliver a complex FCS that is structured (features pre-selected channels only), of fixed low order (consisting of, for example, P, PI, or lead-lag controllers), optimal in the \mathcal{H}_∞ norm sense (for bandwidth setting, reference tracking, disturbance attenuation requirements), and robust with respect to a multi-model uncertainty (covering a selected number of airspeed, mass, altitude, or other cases).

The rest of this section is structured as follows. In Sect. 6.6.4.2, the method of formulating and solving a structured longitudinal CAS design process with HIFOO is shown. The main result of the paper is the case study presented in Sect. 6.6.4.3 (where advanced case study is presented). The procedure toward a structured, low complexity, and robust lateral FCS is elaborated in detail for a nonlinear model of a BWB-type aircraft, as a proof of practical usefulness of the proposed modern techniques for flight controls design purposes.

6.6.4.2 Longitudinal Structured Control Law with HIFOO

We propose a systematic methodology for a one-shot, robust, full-featured, \mathcal{H}_∞ -optimal longitudinal control design, for a multi-model case covering substantial points of the flight envelope. This methodology literally combines advantages from modern controller design techniques involving \mathcal{H}_∞ or \mathcal{H}_2 optimization with a hierarchical approach for aircraft control system design. The HIFOO toolbox allows to preserve the property of physical meaning of each control system loop (which is one reasonable argument of aircraft control system engineers) and removes disadvantages of loop-by-loop tuning of control systems. On the other hand, the well-known robust control design approach based on the generalized plant setup and a corresponding criterion definition (for example, in the \mathcal{H}_∞ sense) in the frequency domain can be followed also in the HIFOO formulation. Thereby, weighting filters like those used in [70, 71, 89, 90] can be included to produce MIMO controllers. Still, the HIFOO toolbox can be understood as an extension to the classical control design techniques. Due to the local optimization carried out by HIFOO, providing a suitable starting point in terms of an initial controller can significantly save computation time. Standard hierarchical approaches can then be used as a promising initial control law.

Algorithm:

Given:

- Set of systems for control design
- Structure of resulting control law
- Optimization criterion.

Output:

- Robust LTI control law with predefined structure.
- **Step 1:** Specify generalized plant set up (define measurable outputs/actuated inputs and criterion by performance inputs/outputs).
 - **Recommendations:** It is needed to select measurable outputs/actuated inputs in correspondence with structure to be designed.
- **Step 2:** Specify performance requirements by weighting filters.
 - **Recommendations:** Depends on the control problem. Typically, low-pass filters are used for reference signal tracking, and bandpass filters are used for vibration modes attenuation.
- **Step 3:** Specify the control law structure.
 - **Recommendations:** The structure needs to be defined by the controller's Rosenbrock matrix. There can be more than one representation, whereby a minimal realization should be aimed for.
- **Step 4:** Specify the starting control law if any is available, otherwise it will be generated randomly.

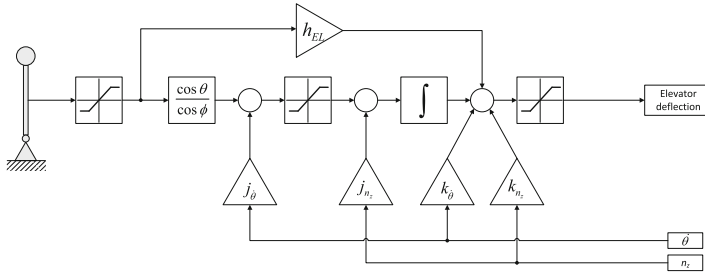
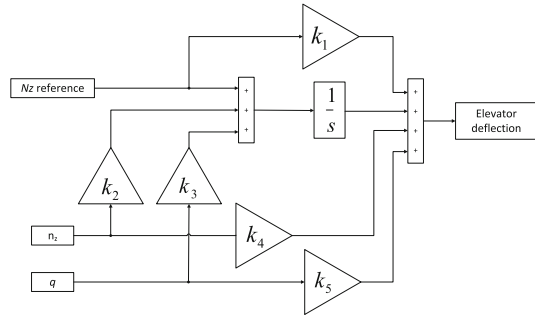


Fig. 6.47 Longitudinal control augmentation system (adopted from [13])

Fig. 6.48 Normal acceleration reference signal tracking control augmentation system with structure



- **Recommendations:** The suitable choice of a starting point is critical to save optimization time. Control laws designed by classical approaches can be a suitable choice.
- **Step 5:** Solve the design problem using the HIFOO toolbox.
 - **Recommendations:** The involved optimization does not guarantee global optimality; therefore, it is usually required to run the optimization several times to reduce the risk of getting caught in mediocre local optima.

A longitudinal CAS of extremely low order (first-order control law) with imprinted structure was designed by the HIFOO toolbox. The structure of the control law is shown in Fig. 6.47, respectively Fig. 6.48 (with mapping of constants (6.54)).

$$\begin{aligned}
 k_1 &= h_\eta \\
 k_2 &= j_{nz} \\
 k_3 &= j_{\dot{\theta}} \\
 k_4 &= k_{nz} \\
 k_5 &= k_{\dot{\theta}}
 \end{aligned}
 \tag{6.54}$$

It is a common hierarchical control law used for an asymptotic tracking of the aircraft normal acceleration reference signal (see [13, 79]). The hierarchical control law design was usually done in an iterative manner, using background knowledge

of the physical meaning of the single loop to reach the required performance. The optimization technique is addressed now to design the overall control law in one shot. \mathcal{H}_∞ -performance criteria can be introduced to design robust control laws with predefined structure and order. The extremely low-order and structural complexity of the overall control law (with preserved robust behavior and control performance of full MIMO high-order control laws) is very important for final on-board implementation. It reduces necessary computational effort and therefore hardware demands for on-board equipment, which is closely connected with reliability and price of implementation. For other possibilities of high-order MIMO CAS designs, see [70, 71, 89, 90]. Control surfaces used by CAS are symmetrically actuated beaver tails (denoted as BT) and elevator (denoted as EL), in our case both flaps are collectively actuated as one. Measured signals are longitudinal RB variables at CG, namely normal acceleration (denoted as Nz_{CG}) and pitch rate (q). Highly valuable feature of \mathcal{H}_∞ optimization is the possibility to introduce the concept of robustness. The HIFOO toolbox will be used, in this particular case, to cover multiple plants, each representing different fueling points in the flight envelope to end up with a longitudinal CAS robust with respect to fueling. The augmented plant used for control law design is shown in Fig. 6.49.

The signals in the augmented plant are divided into exogenous inputs and outputs (which represent control law performance by definition of the optimization criterion), as well as measured outputs and actuated inputs according to Fig. 6.42. The plant G represents aircraft longitudinal dynamics itself and weighting filters W represent the definition of performance criterion in the frequency domain. At this point, the structure of the controller can be introduced into HIFOO by prescribing zero entries in the controller’s Rosenbrock matrix. Let the state-space representation of the controller be $K \cdot a$, $K \cdot b$, $K \cdot c$, and $K \cdot d$, then its Rosenbrock matrix is:

$$K = \begin{bmatrix} K \cdot a & K \cdot b \\ K \cdot c & K \cdot d \end{bmatrix}, \tag{6.55}$$

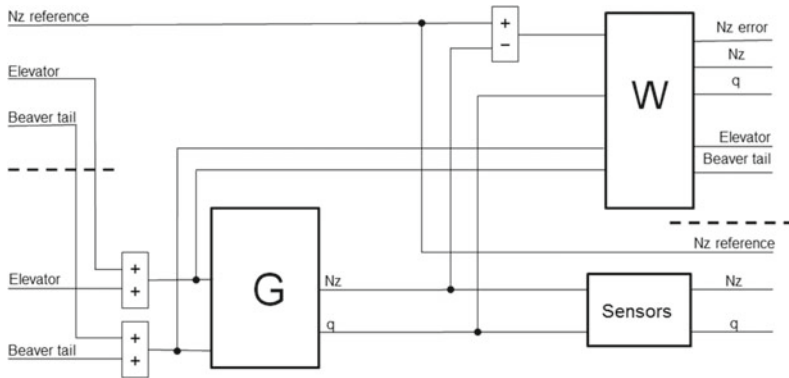


Fig. 6.49 Augmentation plant set up used for longitudinal control law design

with the augmented plant setup shown in Fig. 6.49 and the desired structure of the controller as shown in Figs. 6.47 and 6.48 the controller can be written in the form:

$$A_K = 0 \quad (6.56)$$

$$B_K = [1 \ -k_2 \ k_3] \quad (6.57)$$

$$C_K = [1] \quad (6.58)$$

$$D_K = [k_1 \ k_4 \ k_5]. \quad (6.59)$$

Consequently, the controller's Rosenbrock matrix is

$$K = \begin{bmatrix} 0 & 1 & -k_2 & k_3 \\ 1 & k_1 & k_4 & k_5 \end{bmatrix}. \quad (6.60)$$

The HIFOO toolbox is applied now to carry out the fixed-order optimization with a predefined structure of the controller. The final control law is an integrated first-order multi-input single-output (MISO) controller with predefined structure and can be used as an integrated longitudinal CAS. However, because of the structure it is possible to disassemble it into a hierarchical structure of SISO loops, which can be used one-by-one as a SAS itself (pitch rate damper and normal acceleration damper) as it is known from text books and longitudinal CAS, in this case a normal acceleration reference signal tracker.

6.6.4.3 BWB Case Study

Mathematical Model of Longitudinal Aircraft Dynamics

This longitudinal CAS control design is carried out for the ACFA 2020 BWB aircraft. A variant of the longitudinal ROMs obtained in Sect. 4.1 are utilized in the following. They contain both flight mechanics and aeroelastic effects as well as their coupling. A set of linearized state-space systems for various parameter values of fuel and payload mass (at fixed cruise altitude and airspeed) is available:

$$\begin{aligned} \dot{\mathbf{x}} &= \mathbf{A} \cdot \mathbf{x} + \mathbf{B} \cdot \mathbf{u} \\ \mathbf{y} &= \mathbf{C} \cdot \mathbf{x} + \mathbf{D} \cdot \mathbf{u}, \end{aligned} \quad (6.61)$$

where the state vector \mathbf{x} is composed of the six flight mechanic states (x -position X , body forward speed u , altitude Z , body down speed w (it is proportional to angle of attack α), pitch angle θ and pitch rate q), 12 elastic states (six symmetrical structural

modes), as well as seven aerodynamic lag states. The states X (x -position) and Z (altitude) are neglected in this study. Utilized inputs u for control design are:

- Symmetric Extended Elevator deflection δ_{EEL} (in rad) and deflection rate $\dot{\delta}_{EEL}$ (in rad/s).
- Symmetric Elevator deflection δ_{EL} (in rad) and deflection rate $\dot{\delta}_{EL}$ (in rad/s).

The Extended Elevator and Elevator control surfaces are coupled and actuated simultaneously (will be notated as δ_{EL}) in case of longitudinal control law. The actuator dynamics are modeled via second-order low-pass filters.

Utilized outputs for control design are:

- Pitch rate q (in rad/s)
- Normal acceleration N_{zCG} (in m/s^2)

where in both sensor signals 160 ms time delay (due to signal processing latency, modeled via a second-order Padé approximation) and low-pass Butterworth filters of second order were considered.

Simulations

The resulting longitudinal control law performance is presented in this section. First are presented linear model simulation in MATLAB[®] and than nonlinear MATLAB/Simulink[®] model is involved to demonstrate longitudinal control law capabilities. Position of the closed-loop poles is constrained by required relative damping of 0.5 for all RB poles, the only exception is for the phugoid mode, which can have even one real unstable pole with time period less than 0.1. The closed-loop pole locations can be seen in Fig. 6.50.

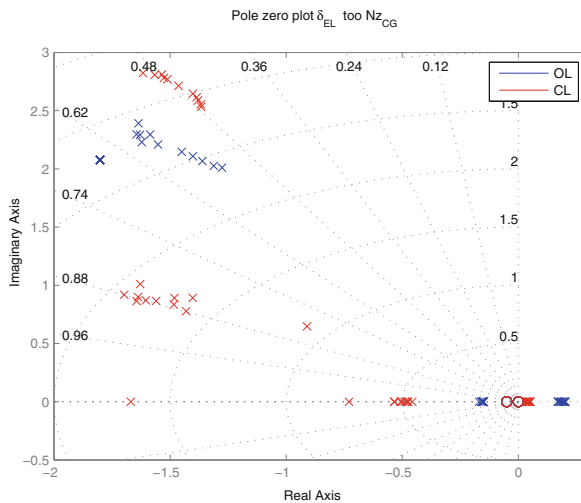


Fig. 6.50 Poles and zeros of N_{zCG} reference signal to N_{zCG} output signal channel (10 fueling cases are plotted)

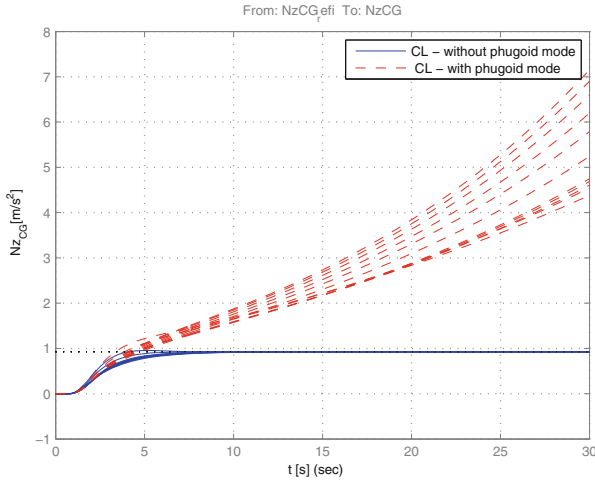


Fig. 6.51 Normal acceleration step response—linear simulation (10 fueling cases are plotted)

The aircraft normal acceleration step response can be seen in Fig. 6.51, where the design plant (without phugoid mode) response as well as the validation plant (with phugoid mode) responses are plotted for all fuel cases (which is one of the robust behavior requirements).

The robustness of control law with respect to unmodeled uncertainty is presented. The uncertainty is here illustrated by diamonds in a Nichols charts, as standard margins or robustness evaluation measures among aircraft controls designers for decades. Uncertainty in this case should be understood as a phase lag and gain variance insensitiveness. One Nichols chart is used for each opened loop (closed loop is disconnected at controller inputs or its output) of the multiple inputs and single-output control law to validate controller robustness. There are different robustness requirements for predefined frequency regions of control law, bounded by phugoid mode frequency (solid line diamond), short-period frequency (dot and dash line diamond) and the first wing bending mode frequency (dotted line diamond). First, the robustness is investigated with respect to unmodeled uncertainty at system input, represented by diamonds in a Nichols chart of open-loop transfer function from system δ_{EL} input to controller δ_{EL} output, see Fig. 6.52 and its zoom in Fig. 6.53. One can see that all curves are outside of the prescribed diamonds which guarantees the required robustness.

Similarly, robustness with respect to output unmodeled uncertainty is investigated. The open-loop system has two inputs pitch rate q and normal acceleration Nz (controller inputs) and two measurements of the same notations (plant outputs). Nichols charts of open-loop transfer functions are plotted in Fig. 6.54, and its zoom for Nichols diamonds are plotted in Fig. 6.55.

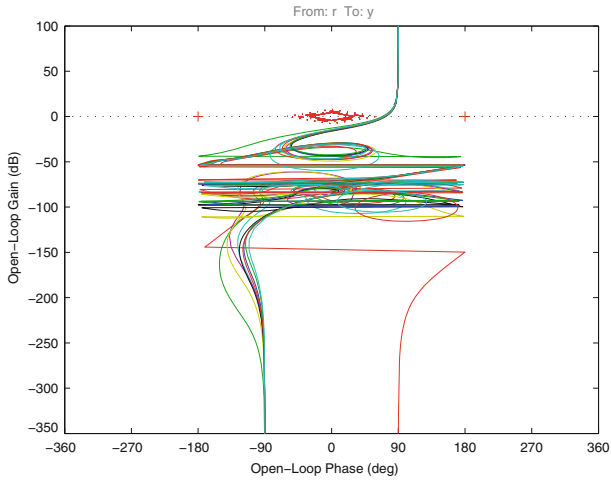


Fig. 6.52 Nichols charts of the closed loops (disconnected at actuators). Ten fueling cases are depicted

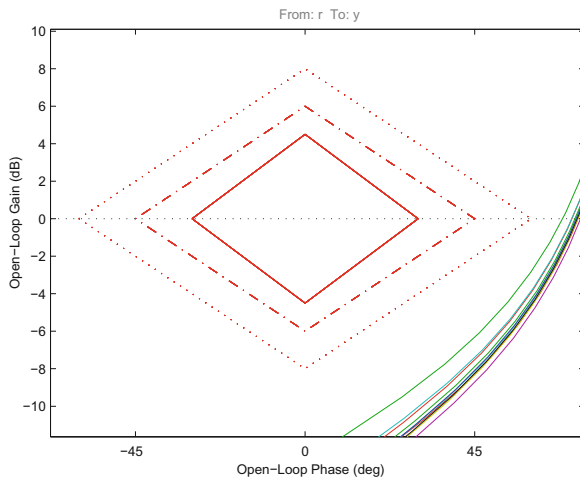


Fig. 6.53 Nichols charts of the closed loops (disconnected at actuators). Ten fueling cases are depicted. Zoomed in for Nichols diamonds

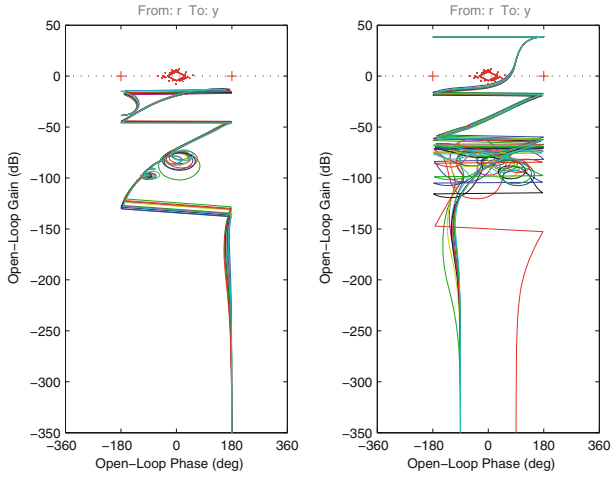


Fig. 6.54 Nichols charts of closed loop disconnected at sensors, pitch rate (*left*) and Nz_{CG} (*right*) (10 fueling cases are plotted)

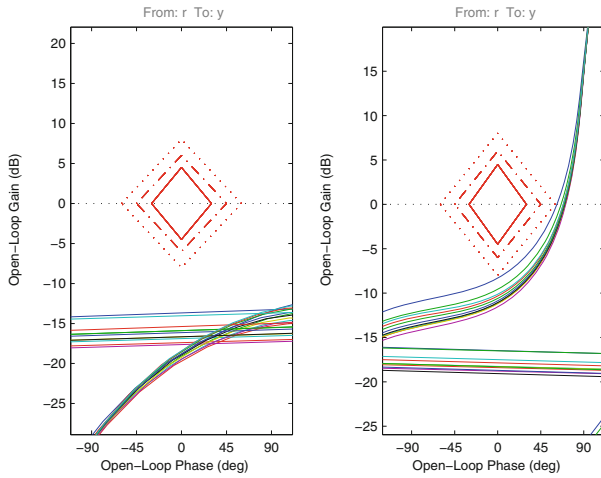


Fig. 6.55 Nichols charts of closed loop disconnected at sensors, pitch rate (*left*) and Nz_{CG} (*right*), zoomed for Nichols diamonds (10 fueling cases are plotted)

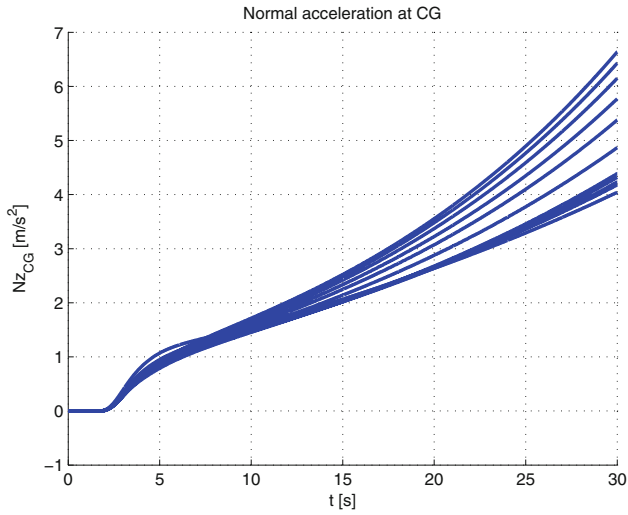


Fig. 6.56 Normal acceleration step response (10 fueling cases are plotted)

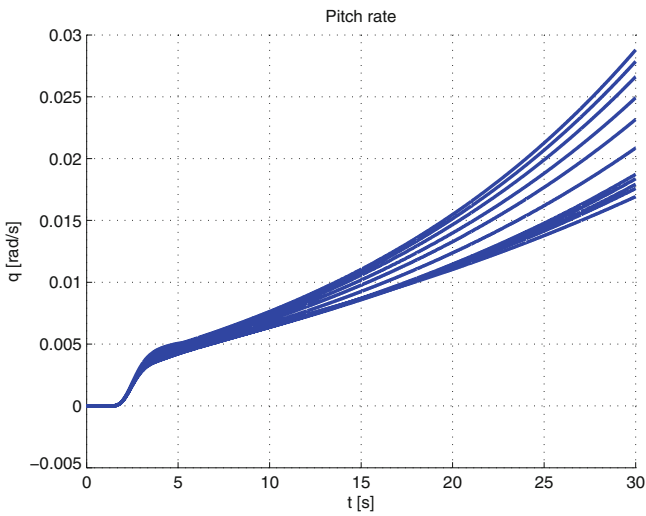


Fig. 6.57 Pitch rate response to step in normal acceleration reference signal (10 fueling cases are plotted)

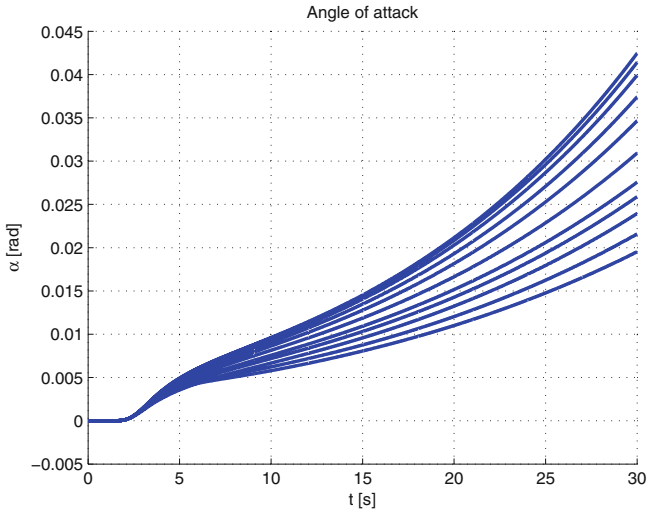


Fig. 6.58 Angle of attack response to step change in normal acceleration reference signal (10 fueling cases are plotted)

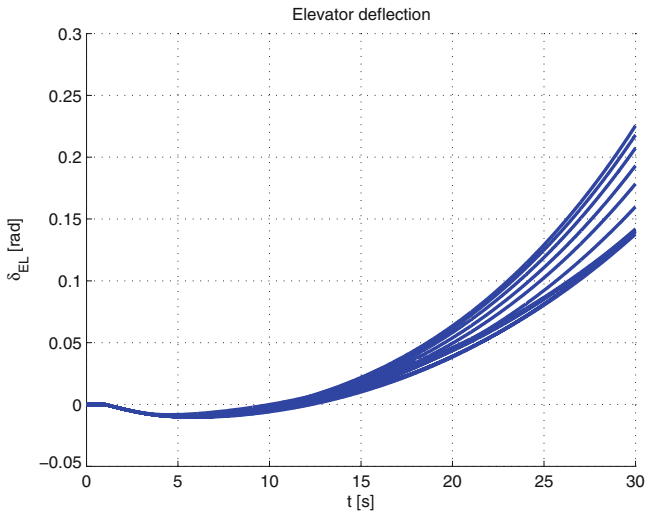


Fig. 6.59 Elevator command induced by step change in normal acceleration reference signal tracking (10 fueling cases are plotted)

Eventually, a MATLAB/Simulink[®] nonlinear model has been involved. Main sources of nonlinearity come from a fully nonlinear model of actuators, which considers control surface maximal deflections, maximal deflection rates, and aerodynamic effects. All nonlinear simulations are influenced by the unstable phugoid mode, but with a time constant of instability of less than 0.1 s it does not violate control constraints or requirements. Time responses of the aircraft's normal acceleration for all considered aircraft fuel cases are plotted in Fig. 6.56. The pitch rate and angle of attack responses are plotted in Figs. 6.57 and 6.58, again plotted for all considered cases. Finally, control law effort needed for such a maneuver, for all fuel cases, is plotted in Fig. 6.59.

References

1. Alazard D, Apkarian P (1999) Observer-based structures of arbitrary compensators. *Int J Robust Nonlinear Control* 9(2):101–118
2. Apkarian P, Noll D (2006) Controller design via nonsmooth multidirectional search. *SIAM J Control Optim* 44:1923–1949
3. Arzelier D, Deaconu G, Gumussoy S, Henrion D (2011) H_2 for HIFOO. In: IFAC world congress on automatic control
4. Balas GJ (2002) Linear, parameter-varying control and its application to a turbofan engine. *Int J Robust Nonlinear Control* 12:763–796
5. Balas G, Chiang R, Packard A, Safonov M (2010) MATLAB robust control toolbox 3, user's guide. MathWorks
6. Balas G, Doyle JC, Glover A (1991) The mu analysis and synthesis toolbox, Math Works and MUSYN
7. Bates D, Postlethwaite I (2002) Robust multivariable control of aerospace systems. DUP Science, Ios Pr Inc
8. Benatzky C (2006) Theoretical and experimental investigation of an active vibration damping concept for metro vehicles. Dissertation, Vienna University of Technology, Vienna
9. Bennami S, Looye G (1998) Design of flight control laws for a civil aircraft using mu synthesis. In: Proceedings of the AIAA conference on guidance, navigation and control
10. Bing-Fei Wu, Perng Jau-Woei (2004) Gain and phase margin analysis of pilot-induced oscillations for limit-cycle prediction. *J Guidance Control Dyn* 27:59–65
11. Blakelock JH (1965) Automatic control of aircraft and missiles. Wiley, New York
12. Boyd S, Barrat C (1990) Linear controller design: limits of performance. Prentice Hall, Englewood Cliffs
13. Brockhaus R (2001) Flugregelung (English: Flight control). Springer, Berlin
14. Bryson AE (1994) Control of spacecraft and aircraft. Princeton University Press, Princeton
15. Burke JV, Henrion D, Lewis AS, Overton ML (2006) HIFOO—a MATLAB package for fixed-order controller design and \mathcal{H}_∞ optimization. In: IFAC symposium on robust control design, 2006
16. Burke JV, Lewis AS, Overton ML (2005) A robust gradient sampling algorithm for nonsmooth, nonconvex optimization. *SIAM J Optim*
17. Burke JV, Lewis AS, Overton ML (2006) Stabilization via nonsmooth, nonconvex optimization. *IEEE Trans Autom Control* 51:1760–1769
18. Chang Che-Hsu, Hant Kuang-Wei (1990) Gain margins and phase margins for control systems with adjustable parameters. *J Guidance Control Dyn* 13:404–408
19. Chopra I, Ballardf J (1981) A method for measuring the stability of a full-scale rotor control system. *J Guidance Control Dyn*

20. Dardenne I (1999) Développement de méthodologies pour la synthèse de lois de commande d'un avion de transport souple. Ph.D. thesis, Ecole Nationale Supérieure de l'Aéronautique et de l'Espace (SUPAERO), France, 1999. (English: Development of methodologies for control law synthesis for a flexible transport aircraft)
21. Dehkordi VR, Boulet B (2009) Robust controller order reduction. In: Proceedings of the american control conference, pp 3083–3088
22. Delwiche T (2009) Contribution to the design of control laws for bilateral teleoperation with a view to applications in minimally invasive surgery. PhD thesis, Free University of Brussels
23. Demourant F, Ferreres G (2002) A frequency domain identification-control approach for a flexible aircraft. In: IEEE CCA'02
24. Demourant F, Ferreres G (2013) A linear parameter-varying multiobjective control law design based on Youla parametrization for a flexible blended wing body aircraft. In: Progress in flight dynamics, guidance, navigation, control, fault detection, and avionics, vol 6. EDP Sciences, pp 729–748
25. Dotta D, Silva AS, Decker IC (2009) Design of power systems controllers by nonsmooth, nonconvex optimization. In: IEEE power and energy society general meeting
26. Doyle JC (1979) Robustness of multiloop linear feedback systems. In: Proceedings of the 17th IEEE conference decision and control
27. Doyle JC, Mall J, Stein G (1982) Performance and robustness analysis for structured uncertainty. In: IEEE conference on decision and control
28. Doyle JC, Packard A (1987) Uncertain multivariable systems from a state space perspective. In: Proceedings of American control conference, Minneapolis
29. Doyle JC, Packard A, Zhou K (1987) Review of LFT's LMIs and mu. In: Proceedings of 30th IEEE conference on decision and control
30. Doyle JC (1982) Analysis of feedback systems with structured uncertainties. IEE Proc Part D 129(6):242–250
31. Doyle JC, Glover K, Khargonekar PP, Francis BA (1989) State-space solutions to standard \mathcal{H}_2 and \mathcal{H}_∞ control problems. IEEE Trans Autom Control 34(8):831–847
32. Evans WR (1948) Graphical analysis of control systems. Trans AIEE 67:547–551
33. Ferreres G, Puyou G (2006) Flight control law design for a flexible aircraft: limits of performance. J Guidance Control Dyn 29(4):870–878
34. Ferreres G, Biannic JM (1998) A μ analysis technique without frequency gridding. In: American control conference. Proceedings of the 1998, vol 4. IEEE, pp 2294–2298
35. Fialho I, Balas G, Packard A, Renfrow J, Mullaney C (1997) Linear fractional transformation control of the F-14 aircraft lateral-direction axis during powered approach landing. In: Proceedings of the American control conference
36. Gawronski W (2004) Advanced structural dynamics and active control of structures. Springer, New York
37. Gu DW, Petkov PH, Konstantinov MM (2005) Robust control design with MATLAB, vol 1. Springer, London
38. Gumussoy S, Henrion D, Millstone M, Overton M (2009) Multiobjective robust control with HIFOO 2.0. In: IFAC symposium on robust control design
39. Gumussoy S, Millstone M, Overton ML (2008) \mathcal{H}_∞ strong stabilization via HIFOO, a package for fixed-order controller design. In: Proceedings of CDC
40. Haddad WM, Chellaboina V (2008) Nonlinear dynamical systems and control: a Lyapunov-based approach. Princeton University Press, Princeton
41. Hanel M (2001) Robust integrated flight and aeroelastic control system design for a large transport aircraft. Number 866 in 8. VDI-Verlag, Düsseldorf
42. Haniš T, Kučera V, Hromčík M (2013) Low order \mathcal{H}_∞ optimal control for ACFA blended wing body aircraft. In: Progress in flight dynamics, guidance, navigation, control, fault detection, and avionics, vol 6. EDP Sciences, pp 671–684
43. Hecker S (2006) Generation of low order LFT representations for robust control applications. PhD thesis, Technische Universität München, Lehrstuhl für Steuerungs- und Regelungstechnik
44. Hyde RA (1995) \mathcal{H}_∞ aerospace control design: a VSTOL flight application. Springer, Berlin

45. Ito H, Ohmori H, Sano A (1993) Design of stable controllers attaining low \mathcal{H}_∞ weighted sensitivity. *IEEE Trans Autom Control* 38(3):485–488
46. Jeanneau M, Lamolie J, Puyou G, Aversa N (2005) AWIATOR's design of multi-objectives control laws. *IFAC*
47. Knittel D, Henrion D, Millstone M, Vedrines M (2007) Fixed-order and structure \mathcal{H}_∞ control with model based feedforward for elastic web winding systems. In: *Proceedings of the IFAC/IFORS/IMACS/IFIP symposium on large scale systems*
48. Kron A, de Lafontaine J, Alazard D (2003) Robust 2-DOF H-infinity controller for highly flexible aircraft: design methodology and numerical results. *Can Aeronaut Space J* 49:19–29
49. Kureemun R, Bates DG (2001) Aircraft flight controls design using constrained output feedback—a \mathcal{H}_∞ loopshaping approach. In: *AIAA guidance, navigation, and control conference*
50. Kwakernaak H (2002) Mixed sensitivity design. In: *Proceedings of the 15th IFAC world congress, Barcelona*
51. Lewis AS, Overton ML (2009) Nonsmooth optimization via BFGS. *SIAM J Optim*
52. Lewis F (1986) *Optimal estimation*. Wiley, New York
53. Lewis FL, Vrabie D, Syrmos VL (2012) *Optimal control*. Wiley, New York
54. Magni J-F (2002) *Robust modal control with a toolbox for use with MATLAB*. Kluwer Academic Publishers, New York
55. McFarlane D, Glover K, Khargonekar PP, Francis BA (1992) A loop-shaping design procedure using \mathcal{H}_∞ synthesis. In: *IEEE transactions on automatic control*
56. McRuer D, Ashkenas I, Graha D (1973) *Aircraft dynamics and automatic control*. Princeton University Press, Princeton
57. Mialon B, Hepperle M (2005) Flying wing aerodynamics studies at ONERA and DLR. In: *CEAS Katnet conference on key aerodynamic technologies, Braunschweig*
58. Miller JE (1966) Space navigation, guidance and control. *AGARDograph*
59. Millstone M (2006) HIFOO 1.5: structured control of linear systems with a non-trivial feedthrough. Master's thesis, Department of Mathematics, Courant Institute of Mathematical Sciences—New York University
60. Perkins CD (1970) Development of airplane stability and control. *J Aircr* 7:290–301
61. Pfifer H, Hecker S (2010) LPV controller synthesis for a generic missile model. In: *IEEE international conference on control applications, Yokohama*, pp 1838–1843
62. Postlethwaite I, Smerlas A, Walker A, Gubbels AW, Baillie S, Strange ME, Howitt J (1999) \mathcal{H}_∞ control of the NRC Bell 205 fly-by-wire helicopter. *J Am Helicopter Soc* 44:276–284
63. Pouly G, Lauffenburger J-P, Basset M (2010) Reduced order \mathcal{H}_∞ control design of a nose landing gear steering system. In: *12th IFAC symposium on control in transportation systems*
64. Puyou G, Ferreres G, Chiappa C, Menard P (2004) A multiobjective method for flight control law design. In: *AIAA guidance, navigation, and control conference, Providence*
65. Robu B, Budinger V, Baudouin L, Prieur C, Arzelier D (2010) Simultaneous \mathcal{H}_∞ vibration control of fluid/plate system via reduced-order controller. In: *Proceedings of CDC*
66. Rugh WJ, Shamma JS (2000) Survey paper: research on gain scheduling. *Automatica* 36:1401–1425
67. Safonov MG, Chiang RY (1988) Model reduction for robust control: a Schur relative error method. *Int J Adapt Control Signal Process* 2(4):259–272
68. Scherer C, Weiland S (2004) *Linear matrix inequalities in control*. Lecture notes. <http://www.dsc.tudelft.nl/cscherer/lmi.html>, Accessed 16 May 2014
69. Schirrer A, Westermayer C, Hemedi M, Kozek M (2010) A comprehensive robust control design and optimization methodology for complex flexible-structure systems. In: *Proceedings of the 18th mediterranean conference on control and automation, Marrakech*
70. Schirrer A, Westermayer C, Hemedi M, Kozek M (2010) LQ-based design of the inner loop lateral control for a large flexible BWB-type aircraft. In: *2010 IEEE multi-conference on systems and control, Yokohama*
71. Schirrer A, Westermayer C, Hemedi M, Kozek M (2010) Robust \mathcal{H}_∞ control design parameter optimization via genetic algorithm for lateral control of a BWB type aircraft. In: *IFAC workshop on intelligent control systems, Sinaia*

72. Schirrer A, Westermayer C, Hemedi M, Kozek M (2011) Multi-model convex design of a scheduled lateral feedforward control law for a large flexible BWB aircraft. In: Preprints of the 18th IFAC world congress, Milano, pp 2126–2131
73. Schirrer A, Westermayer C, Hemedi M, Kozek M (2011) Robust convex lateral feedback control synthesis for a BWB aircraft. In: Preprints of the 18th IFAC world congress, Milano, pp 7262–7267
74. Schirrer A, Westermayer C, Hemedi M, Kozek M (2013) Robust lateral blended-wing-body aircraft feedback control design using a parameterized LFR model and DGK-iteration. In: Progress in flight dynamics, guidance, navigation, control, fault detection, and avionics, vol 6. EDP Sciences, pp 749–766
75. Skelton RE, Stoustrup J, Iwasaki T (2007) The hinf control problem using static output feedback. *Int J Robust Nonlinear Control* 4:449–455
76. Skogestad S, Postlethwaite I (2005) *Multivariable feedback control: analysis and design*, 2nd edn. Wiley, New York
77. Stevens BL, Vesty P, Heck BS, Lewis FL (1983) Loop shaping with output feedback. In: American control conference
78. Stevens BL, Lewis FL, Al-Sunni F (1992) Aircraft flight controls design using output feedback. *J Guidance Control Dyn* 15:238–246
79. Stevens BL, Lewis FL (2003) *Aircraft control and simulation*. Wiley, New York
80. Tobie HN, Elliot EM, Malcolm LG (1966) A new longitudinal handling qualities criterion. In: Proceedings of the annual national aerospace electronics conference, pp 93–99
81. Torczon V (1991) On the convergence of the multidirectional search algorithm. *SIAM J Optim*
82. Torczon V (1997) On the convergence of pattern search algorithms. *SIAM J Optim*
83. Torralba J, Demourant F, Puyou G, Ferreres G (2009) A method for flexible aircraft LFT modelling. In: Proceedings of the European control conference
84. Torralba J, Puyou G, Demourant F (2009) Self-scheduling multiobjective control law design for a flexible aircraft. In: AIAA guidance, navigation, and control conference, Chicago
85. Vanek B (2008) Control methods for high-speed supercavitating vehicles. PhD thesis, Graduate School of the University of Minnesota
86. Vidyasagar M (1988) *Control system synthesis: a coprime factorization approach*. MIT, Cambridge
87. Wang FC, Chen HT (2009) Design and implementation of fixed-order robust controllers for a proton exchange membrane fuel cell system. *Int J Hydrogen Energy* 34:2705–2717
88. Westermayer C (2011) 2DOF parameter-dependent longitudinal control of a blended wing body flexible aircraft. PhD thesis, Vienna University of Technology
89. Westermayer C, Schirrer A, Hemedi M, Kozek M (2010) Linear parameter-varying control of a large blended wing body flexible aircraft. In: 18th IFAC symposium on automatic control in aerospace, Nara
90. Westermayer C, Schirrer A, Hemedi M, Kozek M, Wildschek A, Robust \mathcal{H}_∞ flight and load control of a flexible aircraft using a 2DOF multi-objective design. In: Proceedings of 2009 CACS international automatic control conference, Taipei
91. Whorton M, Buschek H, Calise AJ (1996) Homotopy algorithm for fixed order mixed $\mathcal{H}_2/\mathcal{H}_\infty$ design. *J Guidance Control Dyn* 19:1262–1269
92. Wildschek A, Maier R, Hromčík M, Haniš T, Schirrer A, Kozek M, Westermayer C, Hemedi M (2009) Hybrid controller for gust load alleviation and ride comfort improvement using direct lift control flaps. In: Proceedings of the 3rd EuCASS
93. Wu F (1995) Control of linear parameter varying systems. PhD thesis, University of California, Berkeley
94. Youla DC, Jabr HA, Bongiorno JJ (1976) Modern Wiener-Hopf design of optimal controllers. II. The multivariable case. *IEEE Trans Autom Control* 21(3):319–338
95. Zhou K, Doyle JC, Glover K (1996) *Robust and optimal control*. Prentice Hall, Upper Saddle River

Paper 4

Vosahlik D., Hanis T. and Hromcik H.; Vehicle longitudinal dynamics control based on LQ, 22nd International Conference on Process Control, June 11–14, 2019, Štrbské Pleso, Slovakia

Vehicle longitudinal dynamics control based on LQ

David Vošahlík

Department of Control Engineering,
Faculty of Electrical Engineering,
Czech Technical University in Prague
Email: vosahda1@fel.cvut.cz

Tomáš Haniš

Department of Control Engineering,
Faculty of Electrical Engineering,
Czech Technical University in Prague
Email: hanistom@fel.cvut.cz

Martin Hromčík

Department of Control Engineering,
Faculty of Electrical Engineering,
Czech Technical University in Prague
Email: xhromcik@fel.cvut.cz

Abstract—Trend of autonomous vehicles and e-mobility is in favor of an advanced control system development and deployment. Vehicle dynamics level control systems providing safety limits and high performance response, especially during high dynamics maneuvers, are necessary. This work provides solution for vehicle longitudinal dynamics (vehicle acceleration) considering physical limits given by road, tire and vehicle dynamics respectively. The goal is to maximize vehicle longitudinal acceleration by controlling each wheel longitudinal slip ratio. Considered mathematical model is non-linear single track model incorporating non-linear Pacejka magic formula as a tire model. Design model for control system is derived as a linearized state-space model at constant acceleration operation point. Therefore, the common linearization approach, at system equilibrium, is not possible and the linearization along system trajectory is used. Such solution results in involvement of LPV techniques, as vehicle velocity is state variable. Finally, the LQ optimal control framework is employed to deliver control algorithms providing constant vehicle acceleration trajectory tracing. This is accomplished by longitudinal slip ratio control for each wheel.

Index Terms—Vehicle longitudinal control, Traction control, Linearization along trajectory, Linear-Quadratic controller, Longitudinal slip ration control, Single track model, Pacejka magic formula

I. INTRODUCTION

Electrical vehicle development needs to be build upon the advanced control systems. This work deals with development of full time full authority (FTFA) system which is novel approach. The system controls the longitudinal dynamics using the LQ framework for such vehicle. The nonlinear model which was adopted from [1] is suited for the purpose of the electromobility. Usage of the FTFA system also allows to use nonconventional mechanical architectures which wouldn't be controllable directly by human. These are described later in the model section. The contribution of this work is mainly in LPV technique used for linearization and control laws deployment, which is necessary for linearization along trajectory (constant acceleration). The results and ideas from [2], [3], [5] and [6] were taken into consideration and as inspiration when this work was created.

Goal of this work is to propose a LQ based control law for longitudinal slip ratio control of the single track vehicle model.

II. MODEL

The dynamical model used for control laws development will be discussed in this section.

Due to the fact that only longitudinal dynamics was considered the single track model was chosen. In future the torque vectoring is to be studied so the quarter-car model is not suitable. If there should be in future extension also for lateral dynamics control, the twin track model would be more suitable, but for this work the single track model is sufficient. Both of these models considered were developed by my colleagues from the department of control engineering. In next section the single track model will be introduced.

A. Single track model

The Non-linear single track model was adopted from [1].

The Non-linear model is used to describe planar motion of a vehicle (car) with electrical traction. Also rotational rear wheel is considered in this model. There are some simplifications and assumptions which were used during model derivation. These are:

- Lifting, rolling and pitching motion is neglected.
- All the mass is concentrated in center of gravity (CG).
- Both front wheels are represented as single wheel, this is also applied for both rear wheels.
- Pneumatic trail and aligning torque caused by side-slip angle of a tire is neglected.
- Electrical powertrain dynamics is neglected

Vehicle coordinate system used is conventional right hand oriented cartesian coordinate system with x axis in direction of travel and z axis pointing upwards.

The Single track model with all simplifications and assumptions mentioned above is presented on the figure 1.

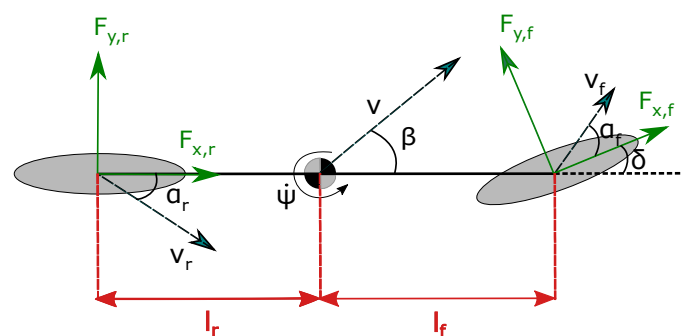


Fig. 1. Single track non-linear model. The picture was adopted from [1]

The equations of motion can be rewritten into the state space description in following manner

$$\dot{\beta} = -\dot{\psi} + \frac{1}{mv}(\cos(\beta)F_y - \sin(\beta)F_x) \quad (1)$$

$$\dot{v} = \frac{1}{m}(\sin(\beta)F_y + \cos(\beta)F_x) \quad (2)$$

$$\dot{\psi} = \frac{1}{I_z}M_z \quad (3)$$

where m [kg] stands for mass at center of gravity (CG), v [$m s^{-1}$] is the vehicle's CG velocity, β is side-slip angle of vehicle, ψ is yaw rate around CG. F_x and F_y respectively is force acting at the vehicle's CG in x and y direction.

I_z is moment of inertia and M_z is cornering torque acting on the vehicle around z axis.

The forces acting on the vehicle are

$$F_x = \cos\delta_f F_{xf} - \sin\delta_f F_{yf} + \cos\delta_r F_{xr} - \sin\delta_r F_{yr} \quad (4)$$

$$F_y = \sin\delta_f F_{xf} + \cos\delta_f F_{yf} + \sin\delta_r F_{xr} + \cos\delta_r F_{yr} \quad (5)$$

$$M_z = l_f \sin\delta_f F_{xf} + l_f \cos\delta_f F_{yf} + l_r \sin\delta_r F_{xr} - l_r \cos\delta_r F_{yr} \quad (6)$$

Here F_{xf} and F_{yf} are forces acting on the front wheel in x and y direction. F_{xr} and F_{yr} are forces acting on the rear wheel. δ_f and δ_r are inputs to the system, these are steering angles of the front and rear wheel respectively.

B. Wheel models

Wheel coordinate system is used for the wheel dynamics description. This coordinate system is depicted on figure 2.

The wheel dynamics are described with the equations

$$\dot{\rho}_f = \frac{1}{J_f}(\tau_f - R_f F_{xf} - \text{sign}(\dot{\rho}_f)\tau_{Bf} - k_f v_{xf}) \quad (7)$$

$$\dot{\rho}_r = \frac{1}{J_r}(\tau_r - R_r F_{xr} - \text{sign}(\dot{\rho}_r)\tau_{Br} - k_r v_{xr}) \quad (8)$$

where J_i is moment of inertia of the i -th wheel around its y axis; τ_i is drive torque applied by a motor on the i -th wheel; R_i is a radius of the i -th wheel; F_{xi} is the force acting on the center of the i -th wheel along its x -axis; $\dot{\rho}_i$ is angular velocity of the i -th wheel; τ_{Bi} is braking torque applied by brakes on the i -th wheel; k_i is a coefficient of the road drag for the i -th wheel; v_{xi} is the velocity vector projection of the i -th wheel's center on its x -axis.

The model has overall 5 states and 6 inputs. These are velocity v , side-slip angle β , yaw rate $\dot{\psi}$ and angular velocity of both wheels $\dot{\rho}_f$ and $\dot{\rho}_r$. Inputs are engine torques τ_i , braking torques τ_{Bi} and wheel steerings δ_i .

C. Longitudinal slip ratio

Pacejka magic formula is used for computation of the longitudinal force. This formula requires the longitudinal slip ratio from which the force is determined. Longitudinal slip ratio is evolved based on $\dot{\rho}_i$ and wheel travel velocity v_{xi} .

The i -th wheel travel velocity v_{xi} is computed using vehicle side-slip angle β , the vehicle's center of mass velocity v , yaw

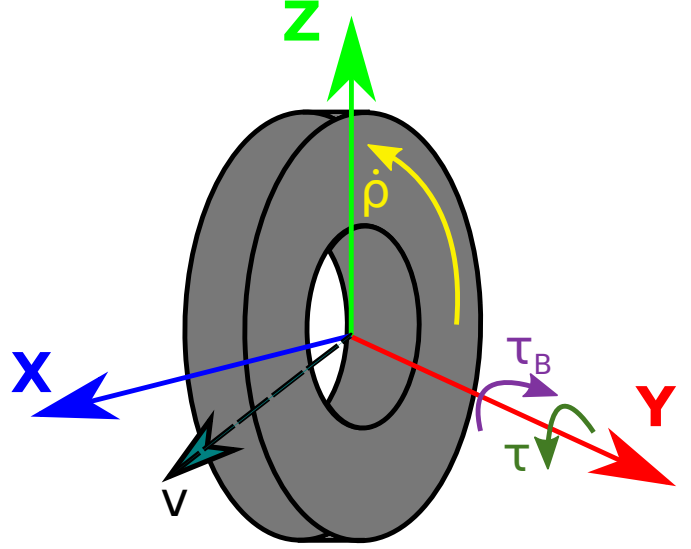


Fig. 2. Wheel coordinate system.

rate of the vehicle $\dot{\psi}$ and steering angle δ_i . It is computed using following formula

$$v_{xf} = v \cos\beta \cos\delta_f - \sin(\delta_f)(v \sin\beta + l_f \dot{\psi}) \quad (9)$$

$$v_{xr} = v \cos\beta \cos\delta_r - \sin(\delta_r)(v \sin\beta + l_r \dot{\psi}) . \quad (10)$$

Then the longitudinal slip ratio for i -th wheel is

$$\lambda_i = \frac{v_{ci} - v_{xi}}{\max(v_{ci}, |v_{xi}|)} , \quad (11)$$

where v_{ci} is circumferential velocity of i -th wheel which is computed as

$$v_{ci} = R_i \dot{\rho}_i , \quad (12)$$

where R_i is radius of i -th wheel.

D. Pacejka magic formula

The tires are modeled using Pacejka magic formula. The formula is

$$F_{xi}(\lambda_i) = D F_{zi} \sin(C \arctan(B \lambda_i - E(B \lambda_i - \arctan(B \lambda_i)))) , \quad (13)$$

where D , C , B and E are shaping coefficients, F_{zi} is normal load for i -th wheel and λ_i is slip ratio for i -th wheel. Pacejka configuration used for front wheel can be seen on the figure 3.

III. LINEARIZATION

In this section a brief discussion of linearization will be held.

The problem statement is quite clear. The goal is to track longitudinal acceleration. This leads to the control of constant slip ratio. The desired operating region of the closed-loop system on the Pacejka model (can be seen on the figure 3) is in the almost linear region. For the configuration used in this work it is approximately till $\lambda_i = 0.2$.

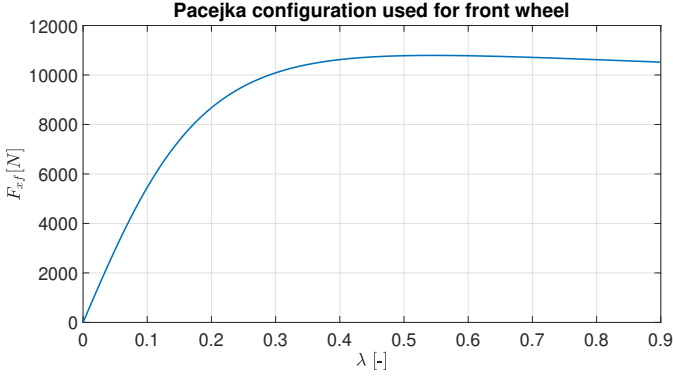


Fig. 3. Front wheel Pacejka model used.

Trajectory along which the model was linearized is constant acceleration and constant wheel angular acceleration for both wheels. The linearization along trajectory creates set of linear models, which are switched based on the velocity of vehicle. This scheme leads to LPV (linear parameter varying) model usage. The switching of the models will be discussed later on. In the following subsection LPV model and algorithm used for linearization of the non-linear model will be described.

A. LPV model

A linear parameter-varying (LPV) system is a linear state-space model with dynamics changing as a function of parameters p , called scheduling parameters. It has mathematical equations

$$\frac{dx}{dt}(t) = A(p)x(t) + B(p)u(t) \quad (14)$$

$$y(t) = C(p)x(t) + D(p)u(t) \quad (15)$$

where A , B , C and D are system matrices. In the scope of this work the scheduling parameter is only velocity v of the vehicle. The states, inputs and outputs are those described in section II.

B. Linearization algorithm

In this section the linearization algorithm used to derive linearized model will be described.

The input parameters of this algorithm are velocity range, slip ratio used and linearization error tolerance. The linearization error tolerance is euclidean norm of error between non-linear and linearized model's derivatives. The actual error is computed as

$$ERR = \|\dot{x}_{non-lin} - \dot{x}_{lin}\|_2. \quad (16)$$

The output of the algorithm is grid of state space models that are then switched depending on the velocity. The switching is described later. If linearization error tolerance parameter is smaller than ERR new linearization operation point is created. The acceleration is computed from the longitudinal force applied to the vehicle and using it's mass. The longitudinal force is derived from the slip ratio using the Pacejka magic formula.

The linearization algorithm takes initially the lowest velocity from the velocity range that has to be linearized. From the velocity and slip ratio, which is specified as parameter, the wheel angular velocity and angular acceleration is concluded. With these information the trim point search can be launched.

1) *Trimming*: The trim point is found using numerical methods. The cost function $L(x, \dot{x}, u, \dot{x}_{desired})$ is introduced where the non-linear equations from the model are used to compute the derivatives depending upon the state and inputs. $L(x, \dot{x}, u, \dot{x}_{desired})$ equals to weighted square of difference between the desired derivatives and computed ones:

$$\dot{x}_{diff} = \dot{x}_{desired} - \dot{x}_{non-lin}(x_{OP}, \dot{x}_{OP}, u_{OP}) \quad (17)$$

$$L(x, \dot{x}, u, \dot{x}_{desired}) = \dot{x}_{diff}^T \cdot weight \cdot \dot{x}_{diff} \quad (18)$$

, where x_{OP} , \dot{x}_{OP} and u_{OP} are operating point values. $weight$ is identity matrix. $\dot{x}_{desired}$ are the derivatives of the trajectory along which the system is linearized. Fixed states and input values are loosely fixed (there is $\pm 1\%$ tolerance in the specified values) in order to trim feasible operating point. These fixed states are velocity and wheel angular velocity for both wheels. Then the algorithm performs minimization (using MATLAB's command *fmincon*) of the cost function.

2) *Linearization*: At this moment the trim has been already found. The actual linearization is done using MATLAB's *linmod* command and simulink implementation of non-linear model which was described in the section II.

This way the state space representation is derived. The algorithm adds to the current working velocity increment (described in (16)) and checks if the ERR value is sufficiently small. If so, the increment is iteratively added and the ERR value is checked until either the ERR value is higher than the specified tolerance or the velocity exceeds the velocity range specified. In the latter case the algorithm is terminated. In the first case, the algorithm repeats the trimming step (noted in section III-B1).

C. Linearized model

The linearization was created in a grid of longitudinal velocity from 3 m/s to 40 m/s. Using longitudinal slip ratio 0.15 and Error tolerance equal to 3.

With these parameters array of 53 state space models was derived. These state space describe only behavior of incremental model

$$\frac{d\Delta x}{dt} = A(p)\Delta x + B(p)\Delta u \quad (19)$$

$$\Delta y = C(p)\Delta x + D(p)\Delta u. \quad (20)$$

The algorithm's output are also offsets. Namely offsets of states derivatives dx_0 , inputs u_0 and states x_0 . The input to the system u is then $u = u_0 + \Delta u$.

As the system is linearized along trajectory the output of the incremental model must be added to the trajectory. The trajectory is being reconstructed using the $dx_0(p)$ values obtained from the linearization algorithm. These values being integrated will provide the trajectory which is then added to the system output.

The whole model can be described by incremental model (equations (19) and (20)) and by equations

$$u = u_0(p) + \Delta u \quad (21)$$

$$y = \Delta y + trajectory \quad (22)$$

D. Switching of the models

The switching of the models is quite straightforward. Out of the grid of trimmed velocities the weighted average of two nearest models is used (convex combination). The weight is computed as

$$w = \frac{v - grid(i)}{grid(j) - grid(i)} \quad (23)$$

where $j = i + 1$, i is the index in the grid of velocities of the closest smaller velocity to the current velocity v ($v > grid(i)$). Then the values for the variables dependent on the switching variable v are computed as

$$A(p) = (1 - w) \cdot a(i) + w \cdot a(j) , \quad (24)$$

where w is the weight from (23), a stands for generic switched variable (it is sampled on a grid of velocities) and $A(p)$ stands for that variable used in the LPV model (eg. state space matrix $B(p)$).

Due to inaccurate trim of the non-linear model, the switching wouldn't be bump-less if the system would be switched as it stands. So the generated system matrices' and operating points' values were fitted with polynomial curve. The eight order polynomial was used. The robust bisquare method was used for fitting. Using the fitted curves' values in the velocity grid points new system matrices and operating points' values were generated. These values are then used in switching as described by equation (24).

E. Linearization results

For illustrational purposes comparison of some variables has been made. On the figure 4 can be seen the comparison of non-linear and linear model velocity. Finally on the figure 5 can be seen the difference between non-linear and linear derivatives.

All the figures mentioned above are for operating point inputs $u_0(p)$ derived during the linearization - due to this fact the linearized model derivatives are constant.

IV. LQ BASED CONTROL

The LQ (linear quadratic) control is based on minimization of the cost function

$$J(u) = \int_0^T (x^T Q x + u^T R u + 2x^T N u) dt \quad (25)$$

on time horizon T . The solution leads to input $u = -Kx$, where $K = R^{-1}(B^T P + N^T)$ is computed using the Riccati equation. In this work infinite time horizon $T = \infty$ was chosen, so the Riccati equation is reduced to the algebraic Riccati equation

$$0 = A^T P + P A - (P B + N) R^{-1} (B^T P + N^T) + Q \quad (26)$$

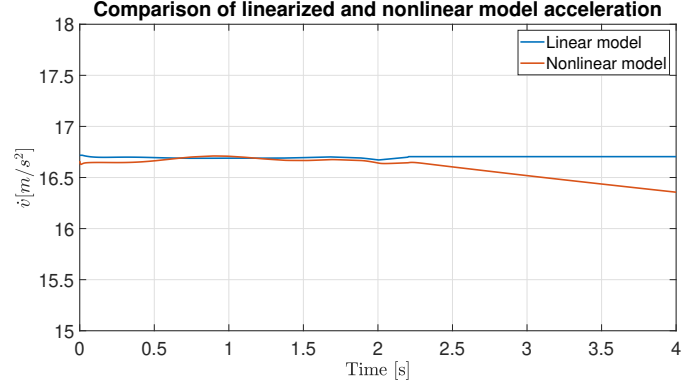


Fig. 4. Comparison of non-linear and linearized model acceleration.

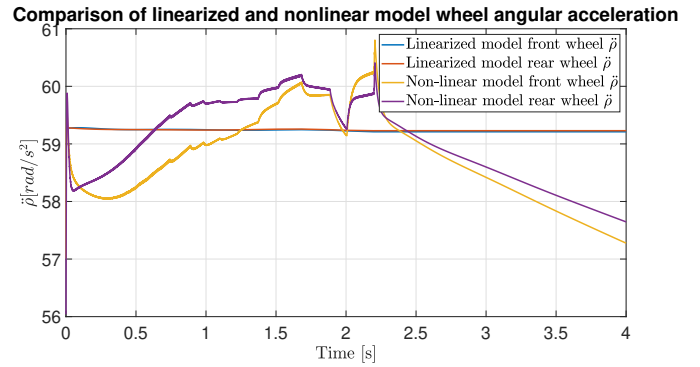


Fig. 5. Comparison of non-linear and linearized model wheels' angular acceleration.

for the solution of this equation the MATLAB's *lqr* function was used. The Q and R were tuned so that the integral of error signal is with reasonable input values (τ_i and τ_{Bi}) regulated. The weights were tuned experimentally. For the grid of state space models also a grid of gains was computed. This grid of gains is switched similarly as in the case of state space switching described in section III-D.

The control architecture is depicted on the figure 6. Because of the requirement of zero error signal $e = \lambda_i - r$, where λ_i is i -th slip ratio, the extra integrals have been added to the system. The Q and R matrices are diagonal and are tuned so, that the state of the integrated error goes to zero. Elements of R corresponding to the δ_i inputs are set to zero. This is achieved simply by extending the system in following way

$$\begin{bmatrix} \dot{x} \\ \dot{x}_i \end{bmatrix} = \begin{bmatrix} A & 0 \\ C & 0 \end{bmatrix} \begin{bmatrix} x \\ x_i \end{bmatrix} + \begin{bmatrix} B \\ 0 \end{bmatrix} \begin{bmatrix} u \\ 0 \end{bmatrix} + \begin{bmatrix} 0 \\ r \end{bmatrix} \quad (27)$$

$$\dot{x}_{aug1} = A_{aug1} \cdot x_{aug1} + B_{aug1} \cdot u_{aug1} , \quad (28)$$

where r is reference and from the control design point of view it is taken as disturbance and is not considered in the design of LQ controller. The x is state of the LPV system and x_i is state of the added integral. Input of this integral is the error signal e . Second thing, that is done in the architecture and can also be seen on the block diagram are input filters.

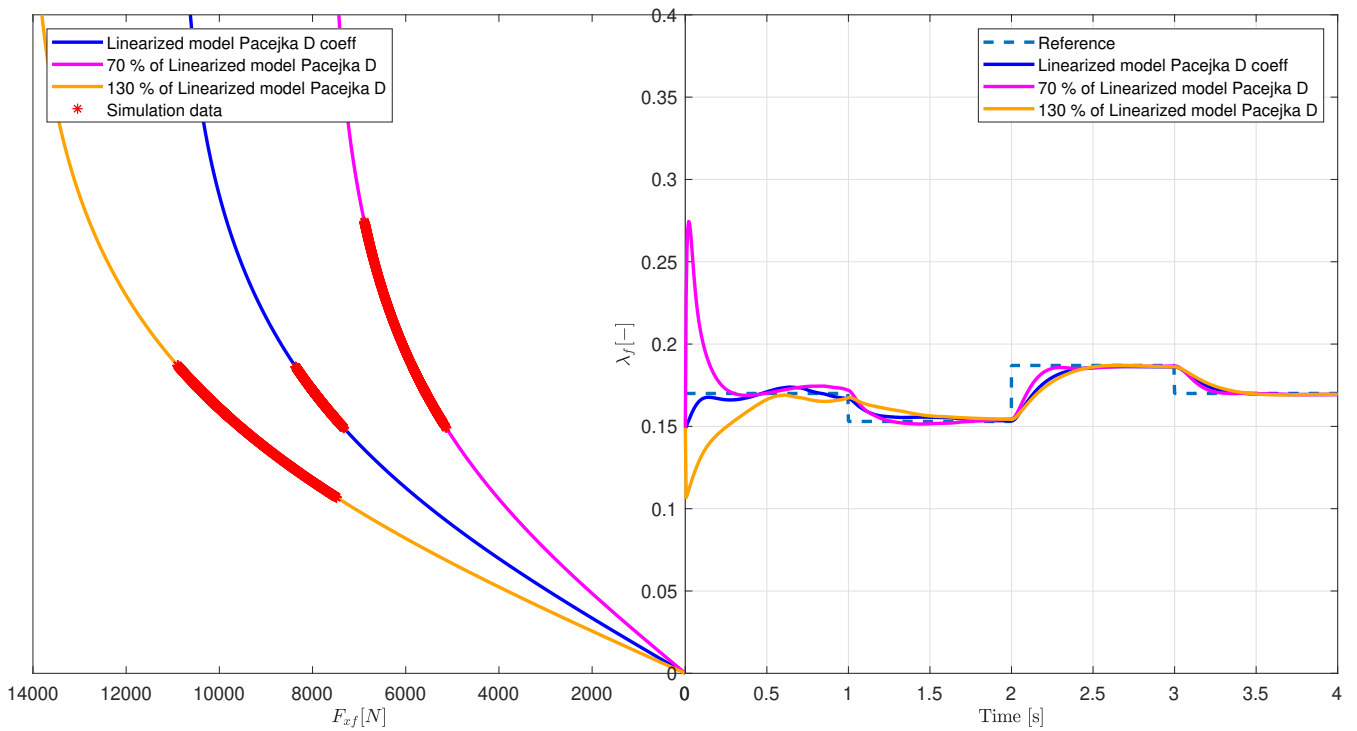


Fig. 9. Comparison of the designed regulator for different Pacejka model of tires/road. On this figure is slip ratio of front wheel. On the left part of the figure are different Pacejka models. The simulation data points shows the operating range of the slip ratio respectively longitudinal force. On the right part of the figure the corresponding time response is shown.

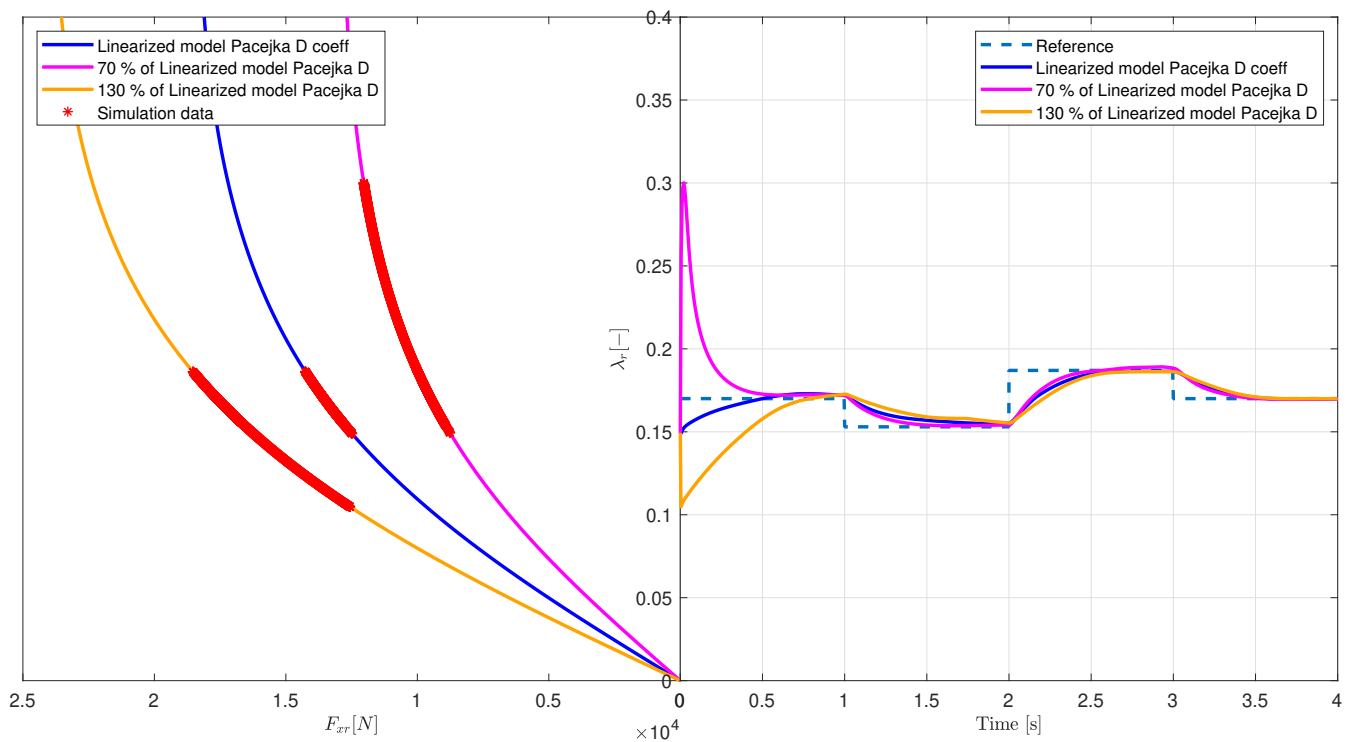


Fig. 10. Comparison of the designed regulator for different Pacejka model of tires/road. On this figure is slip ratio of rear wheel. On the left part of the figure are different Pacejka models. The simulation data points shows the operating range of the slip ratio respectively longitudinal force. On the right part of the figure the corresponding time response is shown.

Paper 5

Efremov D., Hanis T. and Hromcik H.; Introduction of Driving Envelope and Full-Time-Full-Authority Control for Vehicle Stabilization Systems, 22nd International Conference on Process Control, June 11–14, 2019, Štrbské Pleso, Slovakia

Introduction of Driving Envelope and Full-Time-Full-Authority Control for Vehicle Stabilization Systems

Denis Efremov*, Tomáš Haniš[†] and Martin Hromčík[‡]

Department of Control Engineering, Faculty of Electrical Engineering, Czech Technical University in Prague
Email: *efremov.denis@fel.cvut.cz [†]hanis.tomas@fel.cvut.cz [‡]hromcik.martin@fel.cvut.cz

Abstract—This paper introduces the idea of the full-time-full-authority control, known from the flight control field, for the automotive industry. Also, it provides a derivation of a non-linear single-track vehicle model for an over-actuated car and introduces the vehicle states feasibility set, called here driving envelope, inspired by aircraft flight envelope, providing safe operation zone limits for a vehicle. As an addition, authors show proof based on vehicle dynamic physics, what practical pros can bring the usage of the steered rear axle together with the front axle.

Index Terms—Driver assistance, full-time and full-authority vehicle control, envelop control, over-actuated cars, driving envelope, vehicle stability, vehicle safety, vehicle dynamics, a single-track model

I. INTRODUCTION

The flight control systems show beneficial results of using over-actuated aircraft together with full-time-full-authority control which is abused firstly to keep aircraft into so-called flight envelope, secondly to make the plane easy to fly, being the layer between the cabin actuators used by the pilot and thrusts and control surfaces on the aircraft.

This paper is trying to summarize steps done in the field of flight control and map this idea on the nowadays automotive industry. Also in this paper, a driving envelope, analog of the flight envelope is introduced and analyzed.

The key idea of a full-time-full-authority control in aircraft is more in-depth described in [1]. The concept of control of over-actuated cars are described in [2], model predictive envelope control based on handling envelope is discussed in [3].

This paper is organized as follows: the second section shows basic concepts of flight controls, and automotive control systems, and key idea of a technology transfer possibilities; the third introduces non-linear single-track model; the fourth introduces a driving envelope and provides its analysis; the last section summaries this paper and defines a future work.

II. VEHICLE DYNAMICS CONTROLS: AEROSPACE VS. AUTOMOTIVE

A. Flight controls

Safety was always one of the primary goals for all human beings. But this is not the only thing, what is trying to be reached in the transportation field. However, there are things,

almost as crucial as safety, which are wanted to be improved in every step, in every paper, in every innovation; such as performance and usability.

In the field of flight control, these parameters were heavily studied and improved during the last few decades. The first upgrade, from the control point of view, was the introduction of the fly-by-wire system, where the actuators in an airplane are not connected mechanically to the stick in a pilot cabin but through a control computer. This upgrade opens a possibility to add control signals to a pilot's action, which helps a pilot in the handling of the aircraft.

The introduction of the fly-by-wire system enabled the next step of airplane improvements - an over-actuated aircraft. If a pilot does not handle every control surface directly, why not to add more actuators, in some cases to improve maneuverability (such as separated ailerons, elevators, or nozzle flaps on jet engines), in some cases to improve power, for example, by increasing of the number of jet engines? Over-actuation here means having significantly more inputs than you need to have a system controllable. This step opened the possibility to reach the same system state in the state-space applying different control strategies. For example, if you want to make an airplane changing its heading (yaw angle), you can do it in three different ways: use ailerons, use rudder, or use thrust-vectoring (if you have two engines, you can generate different forces on each to create an angular momentum around aircraft's z -axis). Thanks to the fly-by-wire technology, all of these strategies can be combined to improve performance without any extra load on a pilot. Moreover, this augmentation is also used for redundancy; for instance, in case of failure of ailerons the thrust-vectoring can be used instead; that strategy would be impossible without over-actuation.

The next step, to increased an aircraft's stability, was the result of the research in domain so-called flight envelope - a reasonably large subset of the state variables of the vehicle dynamical model with guaranteed safety and performance margins. The envelopes and limitations must be calculated individually for each loading and configuration of an aircraft. There is a batch of envelopes such as angle of attack versus side-slip angle, airspeed versus altitude, airspeed versus load factors, etc. These envelopes must be investigated to establish the limits in which an aircraft's handling qualities, engine behavior, structural loads, and many other different aspects

remain acceptable [4].

The final step, for now, is an introduction of full-time-full-authority control in aircraft. That means that a pilot is not an ultimate authority and he/she can be overridden by some autopilot restrictions. The main reason for this is safety. People tend to make mistakes; a human can fail due to overload or another health problem - electronics cannot. Nowadays, pilots set control references such as altitude, airspeed, an angle of heading, etc. Electronics and sophisticated control algorithms decide, what actuators must be used and how; what are the restrictions and how these requirements must be handled.

B. Automotive control systems

The automotive industry today can offer different simple control techniques which have not higher authority (excluding critical cases) than a driver. This systems usually increase driver's and passenger's safety or merely reduce the driver's effort needed during driving a vehicle [5]:

- Anti-lock Braking System (ABS) - helps mainly during the critical weather conditions such as wet or icy road, or during other dangerous situations such as registered obstacles in front of the car. This system prevents the wheel blocking and decreases skid or crash probability.
- Electronic Stability Program (ESP) - uses vehicle's braking system for vehicle stabilization, mainly breaks one wheel to increase or decrease vehicle's heading rate (yaw rate) dependently on vehicle understeer or oversteer behavior.
- Traction Control - extends ESP, helps to keep traction during the start of vehicle's acceleration.
- Torque-Vectoring (TV) - analogously to the thrust-vectoring uses differential torque produced on an axle to generate an additional momentum to increase or decrease vehicle's yaw rate.
- Adaptive Cruise Control (ACC) is an automatic system, which controls the longitudinal vehicle velocity. Usually, it is used with additional sensors, which provide necessary information about the situation in front of the vehicle, adjusts speed or requests emergency braking by overriding the driver's actions.
- Advanced Driver-Assistance Systems (ADAS) - a family of systems which uses state-of-the-art sensors and algorithms such as LiDAR, radar, image processing, and computer vision. Those systems help to steer a vehicle during drive mostly in every-day use-cases such as driving a car in the city or in a traffic flow on a highway. ADAS's primary goals are to provide collision avoidance, pedestrian crash, avoidance mitigation, comfort (ACC, Line Keeping Assistance (LKA), Parking system, etc.)

C. Technology transfer possibilities

Let us compare the progress done in aerospace and project it on the nowadays vehicles which can be seen on the market:

- Fly-by-wire systems in flight control: nowadays there are state-of-the-art concepts on the market about using so-called drive-by-wire vehicle sub-systems, where actuators

are not connected mechanically to the steering wheel [6] and pedals [7]. From a control systems point of view, it means, that additional control signals can be adjusted to control actions, what is done the same way as in aircraft.

- Over-actuation of an aircraft: on the market, there are different solutions which augment the list of control inputs, such as four-wheel steering (4WS); four-wheel drive (4WD); and four-wheel braking (4WB). But there is one flaw, from a control systems point of view, done by car producers: they are not using this augmentation effectively. For example, 4WS systems are used only within mapping tables dependently on a vehicle's velocity to increase or decrease artificial vehicle length or changing of an instant center of a car as it is done in [8]. 4WD means that you have just a differential to distribute torques on wheels, but it has its limitations in static torque difference. 4WB systems nowadays use gain maps to distribute proportional braking torques applied on wheels with some augmentation made by ESP and ABS. Today's technology can offer in-wheel drive, in-wheel braking and entirely independent steering of each wheel. But this leads to enormously increased controllers' number (steering wheels and pedals), what have to be handled by the control system as it is done in the field of flight control.

Moreover, this idea is not completely new. Stanford University had already started working on a prototype of the over-actuated ground vehicle [2]. Also, there are already different commercial solutions such as RIMAC [9] and NIO [10] available.

- Flight envelope and its protection by full-time-full-authority control algorithm: the analogy of flight envelope, **driving envelope**, is the primary subject of this paper. The second idea presented in this paper is the definition of a layer between the control strategies which are commanded by a driver (or algorithms for autonomous cars) and primary actuators (wheels, brakes, and engines). This layer should inherit the functionality of all nowadays assistance systems and additionally incorporate a better understanding of vehicle's dynamics related to the driving envelope, namely the reasonable ranges of state variables to guarantee vehicle's safety and stability systematically. Moreover, such layer must handle and keep the car in a safe envelope by restricting the driver's actions and thus preventing critical situations persistently (not act only in case of a dangerous situation as it is mostly done in the today's assistance systems), which leads to the usage of naming **full-time-full-authority** control.

III. NON-LINEAR SINGLE-TRACK MODEL

In comparison with the flight control field, the automotive area has no proven vehicle model suitable for benchmarking. There are different modeling approaches including kinematic, single-track and twin-track models. Those models are described by Schramm in [12]. As a basis model, we are using the single-track model which was tested and compared with

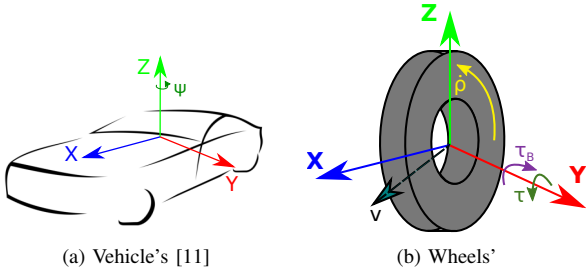


Fig. 1: Used coordinate systems

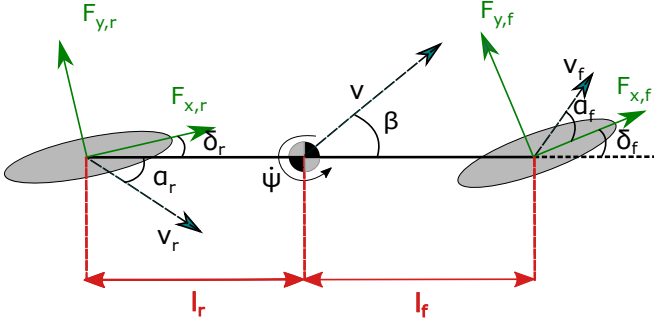


Fig. 2: The single-track model [11]

the high-fidelity twin-track model on a laboratory simulator, validated by means of virtual ride tests.

A. Assumptions and simplifications

The derivation of the non-linear single-track model presented here is an augmentation of the model used in [11].

This model is derived using the following simplifications:

- All lifting, rolling, and pitching motions of a vehicle body are neglected.
- Vehicle mass is assumed to be concentrated at the center of gravity.
- Front and rear tires are represented as one single tire for each axle. Imaginary contact points of tires with a surface are assumed to lie on the center of axles.
- Pneumatic trail and aligning torque resulting from a side-slip angle of a tire are neglected.
- Mass distribution on the axles is assumed to be constant.

B. Dynamics of the rigid-body and a steering angle projection

Used vehicle coordinate system is shown in Fig. 1a. It is the conventional right-hand Cartesian coordinate system. The x -axis direction is from the center of gravity to the front of the vehicle. The y -axis points towards the left side of the car, and z -axis points from the center of gravity to the top of the vehicle. Vehicle's yaw has positive angle increment while turning to the left.

The single-track model following the assumptions above is presented in Fig. 2. The three degrees of freedom are considered: longitudinal, lateral, and yaw motions.

The dynamics of the rigid-body together with a steering angle projection can be described using the following set of differential equations:

$$\begin{pmatrix} \dot{\beta} \\ \dot{v} \\ \dot{\psi} \end{pmatrix} = \begin{pmatrix} -\dot{\psi} \\ 0 \\ 0 \end{pmatrix} + \begin{pmatrix} \frac{1}{mv} & 0 & 0 \\ 0 & \frac{1}{m} & 0 \\ 0 & 0 & \frac{1}{I_z} \end{pmatrix} \begin{pmatrix} -\sin \beta & \cos \beta & 0 \\ \cos \beta & \sin \beta & 0 \\ 0 & 0 & 1 \end{pmatrix} \begin{pmatrix} F_{xf} \\ F_{yf} \\ F_{xr} \\ F_{yr} \end{pmatrix}, \quad (1)$$

where system states are: the side-slip angle β , the velocity of the center of gravity of the vehicle v , the yaw rate angle $\dot{\psi}$; parameters of the model are: the vehicle's mass m , the moment of inertia of the vehicle around its z -axis I_z , the distance from the vehicle's center of gravity to the front axle (the front wheel) l_f , the distance from the vehicle's center of gravity to the rear axle (the rear wheel) l_r ; inputs are: steering angles of the front and the rear wheel respectively δ_f and δ_r (next four inputs, wheel torques, will be added in one of the following subsections). Forces F_{yf} , F_{yr} , F_{xf} , and F_{xr} are forces acting on tires and are described in one of the following subsections.

C. Kinematics

The kinematics of the single-track vehicle model includes calculation of the tires' side-slip angles. Those angles are used in Pacejka Magic formula for calculation of the side tires' forces F_{yr} and F_{yf} . The calculation of tires' slip angle takes into account the steering angles δ_f and δ_r , vehicle states, and parameters described above as:

$$\alpha_f = -\arctan \frac{(v \sin \beta + l_f \dot{\psi}) \cos \delta_f - v \cos \beta \sin \delta_f}{|(v \sin \beta + l_f \dot{\psi}) \sin \delta_f + v \cos \beta \cos \delta_f|}, \quad (2)$$

$$\alpha_r = -\arctan \frac{(v \sin \beta - l_r \dot{\psi}) \cos \delta_r - v \cos \beta \sin \delta_r}{|(v \sin \beta - l_r \dot{\psi}) \sin \delta_r + v \cos \beta \cos \delta_r|}, \quad (3)$$

where α_f and α_r are the tire's side-slip angles of the front and rear tires in wheel's coordinate systems.

Attentive reader can see that the equations provided in this paper are not commonly used in other of kinematics in implementations of a single-track model. As an example, we are introducing here equations used in [11]:

$$\alpha_f = \delta_f - \arctan \left(\frac{v \sin \beta + l_f \dot{\psi}}{v \cos \beta} \right), \quad (4)$$

$$\alpha_r = \delta_r - \arctan \left(\frac{v \sin \beta - l_r \dot{\psi}}{v \cos \beta} \right), \quad (5)$$

The equations (4) and (5) have a singularity in points, where $\beta = \frac{\pi}{2} + \pi k, k \in \mathbb{Z}$, what is solved in the proposed definitions here ((2) and (3)). Because here the singularity, dependent on the state β , exists only in a case when $\beta = \frac{\pi}{2} + \pi k, k \in$

\mathbb{Z} & $\delta_i = 0$. Shifting the state singularity points is done due to our research interests. Singularities of the eq. (4) and (5) commonly are not reachable for the conventional car. However, we want to test our future algorithms on the different ride test scenarios, where a car can get a spin and simulation or reference model can hit a singularity.

D. Wheel dynamics

Fig. 1b shows the wheel coordinate system which is used during the model derivation.

Each wheel model has an internal state that describes its rotation acceleration using the following formulas adopted from [12]:

$$\ddot{\rho}_f = \frac{1}{J_f}(\tau_f - R_f F_{xf} - \text{sign}(\dot{\rho}_f)\tau_{Bf} - k_f v_{xf}), \quad (6)$$

$$\ddot{\rho}_r = \frac{1}{J_r}(\tau_r - R_r F_{xr} - \text{sign}(\dot{\rho}_r)\tau_{Br} - k_r v_{xr}), \quad (7)$$

where J_i is moment of inertia of the i -th wheel around its y -axis; τ_i is drive torque applied by a motor on the i -th wheel; R_i is a radius of the i -th wheel; F_{xi} is the force acting on the center of the i -th wheel along its x -axis; $\dot{\rho}_i$ is angular speed of the i -th wheel; τ_{Bi} is braking torque applied by brakes on the i -th wheel; k_i is a coefficient of the road drag for the i -th wheel; v_{xi} is the velocity vector projection of the i -th wheel's center on its x -axis (also travel velocity (9)).

E. Longitudinal slip ratio

Most tire models define the longitudinal tire force dependent on the tire slip ratio. The most commonly used longitudinal slip is defined with the circumferential velocity v_c in case of accelerating and longitudinal component of the wheel travel velocity v_x in case of braking as the reference velocity [13].

Circumferential velocity is defined as:

$$v_{ci} = \dot{\rho}_i R_i. \quad (8)$$

Travel velocity v_{xi} for the i -th wheel is calculated from the rigid-body's states, and steering angle projection δ_i applied on that wheel:

$$v_{xf} = v \cos(\beta) \cos(\delta_f) + (v \sin(\beta) + l_f \dot{\psi}) \sin(\delta_f), \quad (9)$$

$$v_{xr} = v \cos(\beta) \cos(\delta_r) + (v \sin(\beta) - l_r \dot{\psi}) \sin(\delta_r). \quad (10)$$

Longitudinal slip ratio for the i -th wheel can be computed in the following manner:

$$\lambda_i = \frac{v_{ci} - v_{xi}}{\max(v_{ci}, |v_{xi}|)}, \quad -1 \leq \lambda_i \leq 1. \quad (11)$$

Resulted slip ratios λ_f and λ_r are used in Pacejka Magic Formula to calculate longitudinal forces F_{xf} and F_{xr} acting on the front and rear tire respectively.

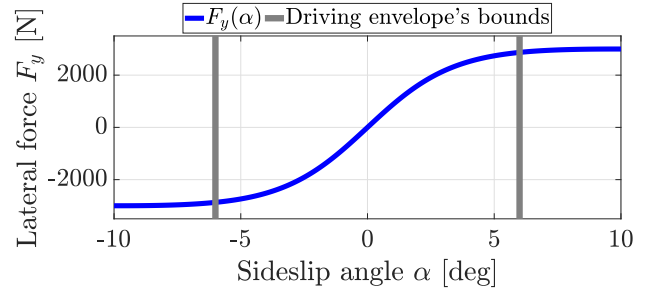


Fig. 3: A lateral force acting on a tire and the driving envelope's definition

F. Pacejka Magic formula

As a tire model, we are using Simplified Pacejka Magic formula [14], which can be used for estimation not only the lateral and longitudinal forces' acting on a tire, but also all the torques acting on a wheel around all axis. It has a straightforward calculation, and the same formula is used to estimate all the forces and torques using different sets of coefficients.

The general Simplified Pacejka Magic formula has the following equation:

$$F(\alpha_i) = DF_{zi} \sin(C \arctan(B\alpha_i - E(B\alpha_i - \arctan(B\alpha_i)))), \quad (12)$$

where D , C , B , and E is the set of shaping coefficients, F_{zi} is a wheel-load force for the i -th wheel, α_i is a tire's side-slip angle of the i -th wheel. In case of calculating of longitudinal force F_x , the slip ratio λ_i instead of side-slip angle is used, together with a different set of shaping coefficients D_x , C_x , B_x , and E_x .

An example of the lateral force F_y produced by tires is shown in the Fig. 3.

G. Friction ellipse

A tire cannot generate combined force (lateral and longitudinal together) higher than the vertical force μF_z acting on the wheel by the vehicle (excluding the cases, where friction coefficient of the tire/road contact zone μ is greater than 1, e.g., in case of high-performance cars). Combined slip occurs when the vehicle is accelerating or braking in a cornering maneuver. That restriction is guaranteed by the friction ellipse (also traction ellipse or Kamm's circle [13]):

$$F_{combined} = \sqrt{\frac{F_x^2}{D_x^2} + \frac{F_y^2}{D_y^2}} \leq \mu F_z, \quad (13)$$

where μ is a friction coefficient of a road; D_x and D_y are parameters from Pacejka (in general, they are friction coefficients of the road in different directions).

The implementation of the friction ellipse in our model is adopted from [15]. Let's call the forces calculated using Pacejka Magic formula as $F_{x,max}$ and $F_{y,max}$. Then the

following algorithm (14) - (18) is applied to scale the resulting forces (if it is needed):

$$\beta_c = \arccos\left(\frac{|\lambda|}{\sqrt{\lambda^2 + \sin^2(\alpha)}}\right), \quad (14)$$

$$\mu_{x,act} = \frac{F_{x,max}}{F_z}, \quad \mu_{y,act} = \frac{F_{y,max}}{F_z}, \quad (15)$$

$$\mu_{x,max} = D_x, \quad \mu_{y,max} = D_y, \quad (16)$$

$$\mu_x = \frac{1}{\sqrt{\left(\frac{1}{\mu_{x,act}}\right)^2 + \left(\frac{\tan(\beta_c)}{\mu_{y,max}}\right)^2}}, \quad F_x = \left|\frac{\mu_x}{\mu_{x,act}}\right| F_{x,max}, \quad (17)$$

$$\mu_y = \frac{\tan(\beta_c)}{\sqrt{\left(\frac{1}{\mu_{x,max}}\right)^2 + \left(\frac{\tan(\beta_c)}{\mu_{y,act}}\right)^2}}, \quad F_y = \left|\frac{\mu_y}{\mu_{y,act}}\right| F_{y,max}, \quad (18)$$

IV. DRIVING ENVELOPE

A. Definition of the driving envelope

The relation between tire's side-slip angle and generated force (12) can be divided into three parts (Fig. 3): almost linear dependency between two peaks (maximum and minimum generated force), and two nearly saturated parts. When tire's side-slip angle goes after the peak, we reach the state, when a tire is slipping, and it cannot generate more force. If the car has all tires slipping, it starts slip too (namely, side-slip angle diverges). It may lead to an uncontrollable spin, which is a hazardous situation not only for the driver and passengers of the car but for other traffic members as well. Then we had decided to restrict minimum and maximum possible tires' slip angles using envelope control. The driving envelope's bounds in an example are chosen a bit after the peaks, as it is done in [3]. An example of bounds is shown in Fig. 3.

To implement envelope control, that restriction has to be translated into the variables of the state-space representation. As can be seen from (2) and (3), it is impossible to analytically express states and inputs using the definition of side-slip angles. Thus, all possible combinations of the inputs and states, where both side-slip angles α_f and α_r are in the defined bounds, had decided to be numerically calculated. It can be seen in the figures below, that the envelope is a convex 3D set in case of constant velocity, and this envelope can be approximated by linear functions. The linear approximation can be easily used, e.g., in MPC control as constraints.

B. Analysis of the driving envelope

Fig. 4 shows a dependency of the driving envelope on the velocity state v . With the higher velocity, maximum and minimum possible side-slip angle β remains the same (see the flat area around the origin), but the maximum and minimum possible yaw rate $\dot{\psi}$ grows, what changes the volume of the driving envelope and rotates the envelope around the yaw rate axis.

Fig. 5 shows a dependency of the driving envelope on the position of the center of gravity inside the vehicle. Changing

this parameter, we rotate the envelope around the steering angle axis.

The volume of the envelope is linearly dependent on the maximum and minimum possible steering angle δ_f and cubically dependent on the maximum and minimum possible side-slip angles of tires α_f and α_r (Fig. 6).

Fig. 7 is an excellent proof based on vehicle dynamic physics, why cars shall be over-actuated. There is a comparison between three cars: 2WS, 4WS with a half-steered rear axel (compare to the front axle), and 4WS with the fully-steered rear axle. Addition of the rear axle steering independent system change the set of stable vehicle states and dramatically expands a driving envelope, what can be very useful not only in sports cars but in commonly used city cars as well.

V. CONCLUSION AND FUTURE WORKS

Firstly, this paper introduces the idea of using flight control experience, such as flight envelope, over-actuation and full-time-full-authority control in the field of automotive.

Secondly, this paper introduces driving envelope prepared for yaw stabilization of 2WS and 4WS vehicles. The limits are numerically calculated bounds of the single-track model states. These bounds are convex and can be easily linearized, which means, that it can be useful for yaw stabilization using model predictive envelope control of a vehicle.

The third contribution is a proof based on vehicle dynamic physics, why over-actuation in cars and vehicle control systems may be useful, namely, how independently steered rear axle can expand a driving envelope.

The next step of this research is to develop model predictive control for yaw stabilization based on the presented envelope as for 2WS vehicle, so for an over-actuated 4WS car, which would be one of the first steps to introducing of full-time-full-authority control approach for ground vehicles.

ACKNOWLEDGMENT

This research was supported by the Czech Science Foundation (GACR) under contract No. 19-18424S. The first author was also supported by the Grant Agency of the Czech Technical University in Prague, grant No. SGS19/174/OHK3/3T/13.

REFERENCES

- [1] R. W. Pratt, *Flight control systems*. American Institute of Aeronautics and Astronautics, 2000.
- [2] H. Park, "Optimal tire force allocation for autonomous trajectory tracking," Ph.D. dissertation, STANFORD UNIVERSITY, 2017.
- [3] C. E. Beal and J. C. Gerdes, "Model predictive control for vehicle stabilization at the limits of handling," *IEEE Transactions on Control Systems Technology*, vol. 21, no. 4, pp. 1258–1269, 2013.
- [4] H. Walgemoed, "Flight envelope," *Introduction to Flight Test Engineering*, 1995.
- [5] M. Mondek, "Active torque vectoring systems for electric drive vehicles," Master's thesis, Czech Technical University in Prague, 2018.
- [6] B. J. Andonian, B. Zheng, G. J. Stout, M. Husain, and M. Radamis, "Steer-by-wire system with steering feedback," Patent US 6,655,490, 2003.
- [7] K. Togai, Y. Danno, M. Yoshida, M. Shimada, and K. Ueda, "Drive-by-wire vehicle engine output control system," Patent US 5,625,558, 1997.

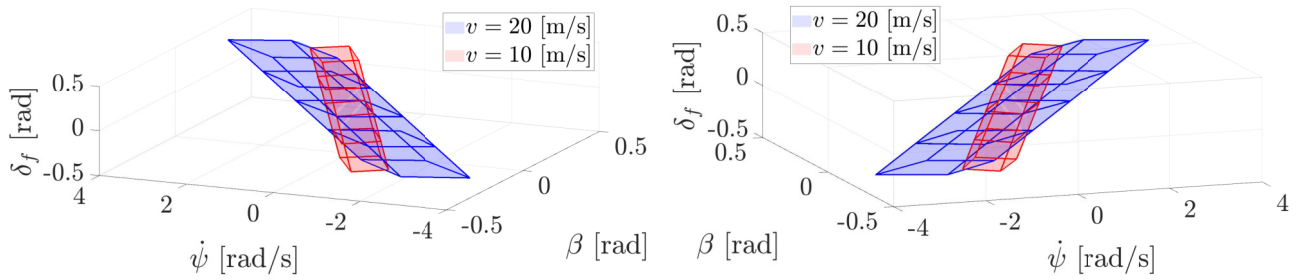


Fig. 4: Dependence of the driving envelope on velocity for the vehicle model with $-20^\circ \leq \delta_f \leq 20^\circ$, $\delta_r = 0^\circ$, $l_f = 1$ m, $l_r = 2$ m, $-6^\circ \leq \alpha_i \leq 6^\circ$.

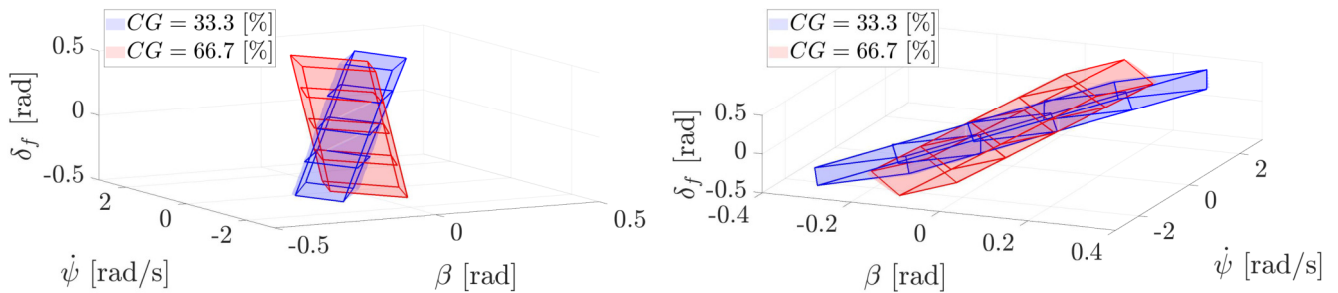
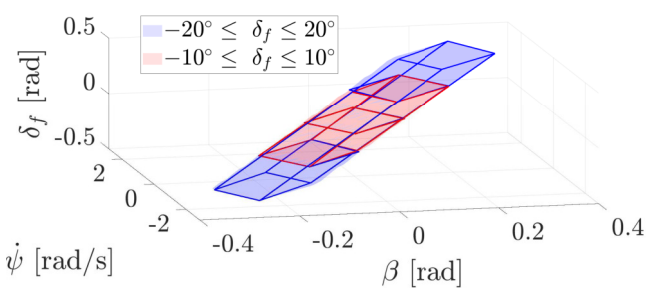
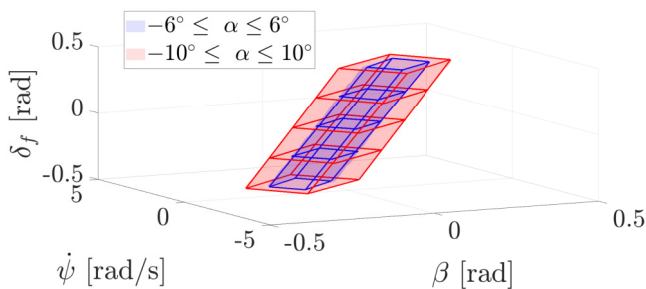


Fig. 5: Driving envelope for cars with different center of gravity positions (from the front wheel (0 %) to the rear (100 %) model with $-20^\circ \leq \delta_f \leq 20^\circ$, $\delta_r = 0^\circ$, $v = 15$ m/s, $-6^\circ \leq \alpha_i \leq 6^\circ$.



(a) Dependence on the steering angle δ_f , $-6^\circ \leq \alpha_i \leq 6^\circ$.



(b) Dependence on the tires' side-slip angle α , $-20^\circ \leq \delta_f \leq 20^\circ$.

Fig. 6: Dependence of the driving envelope on steering angle and tires' side-slip angle for the vehicle model with $l_f = 1$ m, $l_r = 2$ m, $\delta_r = 0^\circ$, $v = 15$ m/s.

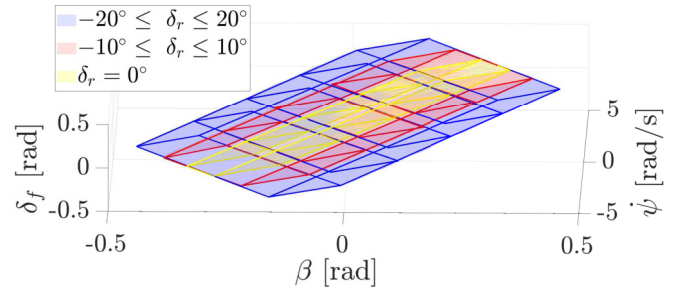


Fig. 7: Comparison of the driving envelope for 2WS and 4WS vehicles with $-20^\circ \leq \delta_f \leq 20^\circ$, $l_f = 1$ m, $l_r = 2$ m, $v = 15$ m/s, $-6^\circ \leq \alpha_i \leq 6^\circ$.

- [8] K. Mori and N. Irie, "Rear wheel steer angle control system for vehicle," Patent US 4,947,326, 1990.
- [9] R. Automobili. (2019) Rimac automobili, rimac official website. [Online]. Available: <http://www.rimac-automobili.com/en>
- [10] N. Inc. (2019) Nio official website. [Online]. Available: <https://www.nio.io/>
- [11] D. Efmov, "Unstable ground vehicles and artificial stability systems," Master's thesis, Czech Technical University in Prague, 2018.
- [12] D. Schramm, M. Hiller, and R. Bardini, *Vehicle dynamics, Modeling and Simulation*. Springer, 2014.
- [13] L. Haffner, "Real-time tire models for lateral vehicle state estimation," Ph.D. dissertation, Vienna University of Technology, 2008.
- [14] H. Pacejka, *Tire and vehicle dynamics*. Elsevier, 2005.
- [15] MSC.Software. (2008) Adams/tyre: Using the pac2002tire model. [Online]. Available: http://mech.unibg.it/~lorenzi/VD&S/Matlab/Tire/tire_models_pac2002.pdf

Paper 6

M. A. Eder, F. Belloni, A. Tesauro, T. Hanis; A multi-frequency fatigue testing method for wind turbine rotor blades; Journal of Sound and Vibration, Available online 2nd November 2016.



A multi-frequency fatigue testing method for wind turbine rotor blades



M.A. Eder ^{a,*}, F. Belloni ^a, A. Tesauro ^b, T. Hanis ^a

^a DTU Wind Energy, Frederiksborgvej 399, 4000 Roskilde, Denmark

^b Siemens Wind Power A/S, Assensvej 11, 9220 Aalborg, Denmark

ARTICLE INFO

Article history:

Received 8 March 2016

Received in revised form

19 September 2016

Accepted 21 October 2016

Handling Editor: I. Trendafilova

Available online 2 November 2016

Keywords:

Wind turbine rotor blade

Fatigue testing

Fatigue damage

Resonance testing

Multi-frequency approach

Exciter

ABSTRACT

Rotor blades are among the most delicate components of modern wind turbines. Reliability is a crucial aspect, since blades shall ideally remain free of failure under ultra-high cycle loading conditions throughout their designated lifetime of 20–25 years. Full-scale blade tests are the most accurate means to experimentally simulate damage evolution under operating conditions, and are therefore used to demonstrate that a blade type fulfils the reliability requirements to an acceptable degree of confidence. The state-of-the-art testing method for rotor blades in industry is based on resonance excitation where typically a rotating mass excites the blade close to its first natural frequency. During operation the blade response due to external forcing is governed by a weighted combination of its eigenmodes. Current test methodologies which only utilise the lowest eigenfrequency induce a fictitious damage where additional tuning masses are required to recover the desired damage distribution. Even with the commonly adopted amplitude upscaling technique fatigue tests remain a time-consuming and costly endeavour. The application of tuning masses increases the complexity of the problem by lowering the natural frequency of the blade and therefore increasing the testing time. The novel method presented in this paper aims at shortening the duration of the state-of-the-art fatigue testing method by simultaneously exciting the blade with a combination of two or more eigenfrequencies. Taking advantage of the different shapes of the excited eigenmodes, the actual spatial damage distribution can be more realistically simulated in the tests by tuning the excitation force amplitudes rather than adding tuning masses. This implies that in portions of the blade the lowest mode is governing the damage whereas in others higher modes contribute more significantly due to their higher cycle count. A numerical feasibility study based on a publicly available large utility rotor blade is used to demonstrate the ability of the proposed approach to outperform the state-of-the-art testing method without compromising fatigue test requirements. It will be shown that the novel method shortens the testing time and renders the damage evolution with a higher degree of fidelity.

© 2016 Elsevier Ltd. All rights reserved.

1. Introduction

Wind turbine rotor blades are thin-walled, multicellular composite beam type structures subject to highly dynamic multi-directional loading conditions. During their designated life span of 20–25 years, blades accumulate a vast number of load reversals. Not surprisingly, proprietary inspection reports suggest that a substantial number of damages are attributed

* Corresponding author.

E-mail address: maed@dtu.dk (M.A. Eder).

Nomenclature

δ_{ij}	Kronecker delta (1)	\mathbf{M}	total mass matrix (kg)
Δz	equispaced distance between neighbouring nodes (m)	$\hat{\mathbf{M}}$	base mass matrix (kg)
ϵ	strain value in time history (1)	\hat{M}_{ij}	element of base mass matrix (kg)
$\bar{\epsilon}$	root mean square (RMS) strain value of the time history (1)	\mathbf{M}_k	k -th additional tuning and or exciter mass matrix (kg)
ϵ_{UC}	uniaxial failure strain in compression (1)	\bar{M}_{ij}^k	element of k -th tuning and or exciter mass matrix (kg)
ϵ_{UT}	uniaxial failure strain in tension (1)	$M_{eq}(z)$	equivalent bending moment (N m)
ρ	air density at ambient room temperature and mean sea level (kg/m ³)	$M_m(z)$	mean bending moment per bin (N m)
Φ_i	n -dimensional eigenmode vector of the i th mode (1)	$M_a(z)$	average bending moment amplitude per bin (N m)
ψ	dual excitation mode mixity (1)	$M_m^*(z)$	mean (static) bending moment (N m)
ω_i	angular natural eigenfrequency of the i th mode (rad/s)	$M_s(z)$	self-weight induced flapwise bending moment (N m)
\mathbf{A}	aerodynamic damping matrix (kg/m)	$M_t(z)$	tuning mass induced bending moment (N m)
A_{ij}	element of aerodynamic damping matrix (kg/m)	$M_{rs,(DLC,WS)}^*$	element of matrix containing M_a and M_m of the time history (N m)
a, b	Rayleigh damping coefficients (1/s, s)	$M_{UC}(z)$	ultimate bending moment capacity (fibre in compression) (N m)
DLC	design load case (1)	$M_{UT}(z)$	ultimate bending moment capacity (fibre in tension) (N m)
$c(z)$	chord length (m)	n	total number of nodes (1)
C_d	aerodynamic drag coefficient for 90° angle of attack (1)	\bar{n}	number of load cycles (1)
\mathbf{D}	Rayleigh damping matrix (N s/m)	n_b	number of bins (1)
D	actual damage index (fatigue failure attained when $D=1$) (1)	n_c	number of cases (1)
D_t	target damage index (1)	N_{eff}	number of cycles at a pre-defined constant moment amplitude (1)
$\hat{\mathbf{e}}_i$	i th n -dimensional orthonormal basis vector (1)	n_l	number of cycles in bin l (1)
E_{aer}	aerodynamic energy dissipation (J)	N_{rs}, N_{rs}^*	number of cycles in the bin rs (1)
E_{str}	structural energy dissipation (J)	n_t	number of tuning masses (1)
E_{tot}	total energy dissipation (J)	$N_{F,rs}$	number of cycles to cause failure for bin rs (1)
$El(z)$	flapwise bending stiffness (N m ²)	\mathbf{q}	design variable vector (–)
$F_{1,2}$	excitation force amplitude where index indicates mode (N)	r	index of mean moment bin (1)
$\mathbf{f}_{1,2}$	nodal excitation force amplitude vector (N)	s	index of mean amplitude bin (1)
f_{up}, f_{low}	upper and lower excitation frequency limit (Hz)	\mathbf{S}	compliance matrix (m/N)
g	gravitational acceleration (m/s ²)	S_{ij}	element of compliance matrix (m/N)
i, j	node number indices $i=1,2,3,\dots,n$ and $j=1,2,3,\dots,n$; (1)	t	time variable (s)
k	tuning mass index (1)	T_{tot}	total testing time (s)
l	bin index (1)	$T_{1,2}$	time instant (s)
\mathbf{K}	stiffness matrix (N/m)	w	scaling factor (1)
L	blade length (m)	w_{WS}	probability of occurrence of each wind speed WS (1)
m	number of turbulence seeds used in the aeroelastic simulations (1)	w_{DLC}	probability of occurrence for each load-case DLC (1)
$m(z)$	blade mass per unit length (kg/m)	\mathbf{x}	nodal deflection vector (downward positive) (m)
\bar{m}_k	k -th tuning and or exciter mass (kg)	x_c	distance between extreme fibre and bending axis (m)
m_{SN}	slope of double logarithmic SN-diagram (N/m ²)	z	spanwise coordinate starting from the root (m)
		\bar{z}_k	spanwise coordinate of k -th additional mass (m)

to ultra-high cycle fatigue. According to a damage assessment report by Sheng [1], the contribution of wind turbine rotor issues to the total downtime ranges between 8% and 20%. The cost impact due to poor blade reliability creates a strong research demand on mitigation of fatigue damage in order to lower the cost of energy by decreasing downtime and repair intervals. The challenge of accurate fatigue lifetime predictions of blades is posed by a complex interplay of several aspects

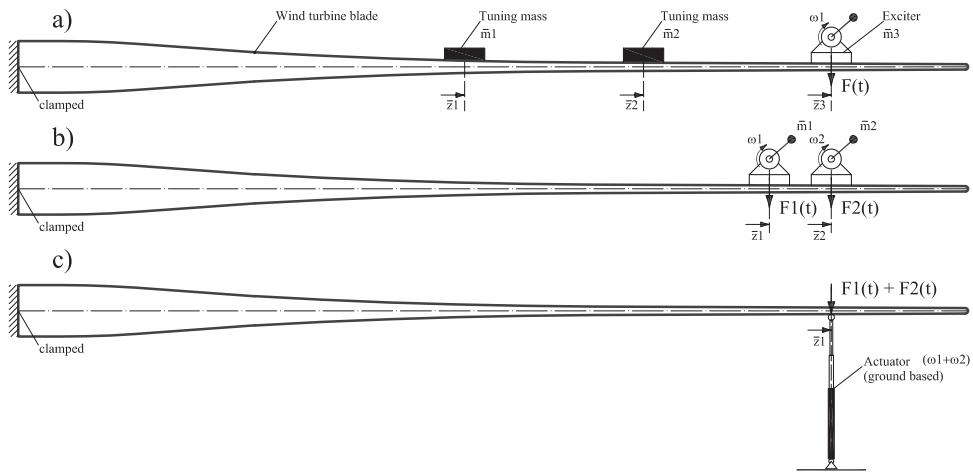


Fig. 1. (a) Fatigue test setup following the mono-frequency approach and (b) setup for the multi-frequency approach using rotating mass excitation and (c) ground based actuation which can be used for both mono- and multi-frequency excitation.

such as taper, twist, size effects, curing-induced residual stresses, manufacturing flaws, geometrical imperfections, material mismatch, geometrical nonlinearity and aeroelastic loads, to name a few. Under such circumstances, empirical data obtained from full-scale fatigue tests represent an indispensable part of blade research, also for the validation and development of accurate numerical analysis methods and design processes. Full-scale tests give the most realistic representation of fatigue failure that occurs under operating conditions when compared to sub-component tests on medium scale or coupon tests on small scale. Therefore, over the past 30 years the development of ever more realistic and efficient testing methods has been the focus of extensive international research efforts. A review of state-of-the-art testing methods appears in Malhotra et al. [2].

In a fatigue test, one or more concentrated cyclic forces are applied to the blade. During a *resonance* test these excitation forces are applied at the natural frequencies of the blade in order to minimise the required excitation energy. Conversely, non-resonant excitation is referred to as *forced* approach. Excitation forces can be simultaneously applied in one or two directions, where the first approach is referred to as *uniaxial* testing and the second one as *biaxial* or *dual-axis* testing. This article focuses solely on uniaxial testing. Figs. 1(a)–(c) show different excitation methods used for wind turbine blades. Fig. 1 (a) depicts until now the most common testing method used in industry, hereafter referred to as the *mono-frequency* approach. In the depicted setup, a rotating mass exciter is externally mounted on the outer part of the span thereby exciting the blade near its first natural frequency. Additional tuning masses serve the purpose of adjusting the dynamic section forces and hence the lengthwise spatial damage distribution. The simplicity of this technique lowers equipment and maintenance costs. Furthermore, resonance testing is an energy-efficient method compared to forced approaches.

The blade certification process regulated by the IEC 61400 standard [3] requires to demonstrate that a blade type endures at least the same fatigue damage that it will experience during the operational life. Such a damage can be specified as a number N_{eff} of cycles at a pre-defined constant bending moment amplitude M_{eq} – which is aptly called the *equivalent moment*. Assuming the applicability of Miner’s rule and the Wöhler [4] based Basquin relation [5] for modeling high cycle fatigue, M_{eq} and N_{eff} can be related, in its most basic form (omitting mean correction), by Eq. (1) – as explained by Sutherland and Herbert [6], where M_{al} and n_l result from the binning of the moment time history for the entire lifetime of the turbine:

$$M_{eq} = \left(\sum_{l=1}^{n_b} \frac{n_l M_{al}^{m_{SN}}}{N_{eff}} \right)^{1/m_{SN}} \tag{1}$$

Eq. (1) is used to compute the equivalent moment in several cross sections along the blade, given the lifetime long load time history. Additional tuning masses as depicted in Fig. 1(a) are employed to match the dynamic bending moment amplitudes with the required M_{eq} amplitudes in the individual cross-sections.

During their lifespan, modern wind turbine rotor blades can accumulate a vast number of load cycles in excess of 1×10^8 . A testing campaign aiming to reproduce such an amount of cycles would require unacceptably long testing times. Consequently, *amplitude scaling* is used to reduce the testing time by assigning a lower N_{eff} in the range of 1×10^6 – 5×10^6 cycles to Eq. (1). However, even with amplitude scaling the testing time remains in the order of several months which remains a costly endeavour. One needs to bear in mind that the application of tuning masses increases the complexity of the problem by decreasing the natural frequency. In fact there is no other means in the paradigm of mono-frequency excitation to further decrease the testing time without decreasing the cycle number and hence compromise the level of confidence.

Figs. 1(b) and (c) show two applications of the proposed testing method – here referred to as *multi-frequency* approach – which aims at addressing the main issue of the mono-frequency approach. In the new setup at least two excitation forces

are employed to simultaneously excite two or more natural frequencies of the blade. At this point, it is noteworthy to mention that the upscaling of blade sizes – driven by maximising power production – has decreased the lower natural frequencies, so that their excitation has become feasible in terms of controllable adiabatic heating. Such a process can however have a detrimental effect on the fatigue life of glass-fibre composites, as investigated by Kim and Ebert [7].

The shift in paradigm evoked by the multi-frequency method could render the equivalent force approach obsolete inasmuch the dynamic bending moment response is no longer constrained to constant amplitudes. Moreover, it must be stressed that the practical approach to fit an equivalent bending moment amplitude gives rise to considerable deviations from the desired damage distribution. In order to shed light on this issue, Miner's damage accumulation rule, which defines the damage index as $D = \tilde{n}/N_{eff}$ and Basquin's law, $M_{eq} = M_{UT} N_{eff}^{-1/m_{SN}}$, can be combined to express the damage index as a function of M_{eq} :

$$D = \frac{\tilde{n}}{\left(\frac{M_{UT}}{M_{eq}}\right)^{m_{SN}}} \quad (2)$$

The error of the equivalent moment amplitude ϵ_{eq} and the error of the damage index ϵ_D are shown in Eqs. (3) and (4) respectively. Substitution of Eqs. (2) and (3) into (4) shows that the damage error is a power function of the moment amplitude error:

$$\epsilon_{eq} = \frac{\overline{M}_{eq}}{M_{eq}} \quad (3)$$

$$\epsilon_D = \frac{\overline{D}}{D} = \epsilon_{eq}^{m_{SN}} \quad (4)$$

where the overline indicates experimentally obtained values.

Eq. (4) elucidates that for a typical glass-fibre composite material fatigue exponent of $m_{SN}=10$, a deviation of only 1% from M_{eq} causes an intensified deviation of 10% from the target damage D . From a practical point of view, areas which deviate from the equivalent force by a seemingly small portion can lead to damage distributions which are significantly at variance with the target damage. For compelling reasons of applicability and accuracy, the objective of the simulations performed in this paper was therefore to directly match the desired target damage distribution.

In the multi-frequency approach, the spatial damage distribution is obtained by superposition of different eigenmodes, by means of optimisation-based selection of the associated excitation force amplitudes. The spatial damage distribution and the required precision of its reproduction in a test can be understood as the criterion for the selection of particular modes. It is not a priori clear which modes need to be excited in order to minimise the deviation of spatial damage distribution of the blade from reference distribution, therefore optimisation techniques are involved to determine the proper mode-shapes and their optimal combination i.e. the design of excitation signals.

The dynamic system is in principle non-linear because of aerodynamic damping and geometric non-linearity but can reasonably be assumed to be linear within the framework of the proposed testing method. Therefore, a decoupling of the response in different mode shapes is possible, where the spatial distribution of mass and stiffness of modern wind turbine blades ensures that the frequencies are sufficiently separated. The mechanical inertia of the rotating mass induces a clean harmonic excitation force signal with only one frequency which e.g. in contrast to an impulse makes it possible to excite modes separately. Moreover, at steady state resonance the excitation input energy is small in comparison to the kinetic/strain energy stored in the system. Therefore, spatial deviation of the applied exciter force from the ideal mode shape based distribution was found to have an insignificant effect on spurious mode excitation. That is, blade tests performed in industry at the lowest frequency empirically show no undesired higher mode excitation.

A well-known property of modal decomposition is the fact that the contribution of higher modes to the total response decays with the inverse square of the angular frequency. This renders the contribution of spurious modes insignificant for practical purposes.

In this paper, a simplified dynamic model is used to study and demonstrate the feasibility of this novel approach in terms of its ability to meet the demands of a full-scale fatigue test and to outperform the state-of-the-art method.

2. Aeroelastic simulations and fatigue-damage prediction

The DTU-owned aero-servo-elastic analysis software package Horizontal Axis Wind Turbine Code HAWC2 11.9 [8,9] was used to perform the aeroelastic load simulations of the DTU 10 MW Reference Wind Turbine (RWT). The purpose of this simulation was to compute a realistic target damage distribution in order to compare the performance of the different testing approaches.

The code is based on a multibody formulation and was used to calculate the section force histories of the 10 MW RWT blade. Controller algorithm [10], airfoil characteristics as well as mass and stiffness distributions are taken from the publicly

available report by Bak et al. [11]. The Design Load Basis for onshore turbines treated by Hansen et al. [12] which is based on the IEC 61400-1 standard [3,13] and which covers typical extreme- and fatigue load situations was used for the analysis.

The standard prescribes at least 21 Design Load Cases, DLCs. The 17 of them are used to assess the severity of the response of the turbine to extreme deterministic inputs, which have a very low occurrence rate. The remaining DLCs, namely DLC1.2, DLC2.4, DLC1.3, DLC1.4 and DLC6.4, are used to evaluate the response of the turbine and of the blade as a subsystem to stochastic inputs, induced by the atmospheric turbulence. These are relevant for the calculation of the fatigue damage and are therefore analysed in the present study.

For each DLC several wind speeds (WS) were considered and n WS bins were defined between the cut-in (defined as the minimal speed at which the net power output of the turbine becomes positive) and cut-out speed (defined as the speed at which the turbine brakes are activated to avoid structural damage). A Weibull distribution was used to describe the frequency of occurrence of each WS, w_{WS} . HAWC2 simulation was performed for each design situation, defined by the triplet (DLC, WS, atmospheric turbulence conditions), repeated for m stochastic wind conditions, called “turbulence seeds” (TS). The fatigue damage was computed using the time history output of the HAWC2 simulation, along the lines of Fossum et al. [14]. Only one of the six section forces – the flapwise bending moment M – was considered in the present study, as the damage on the caps of the blade beam is dominated by the flapwise bending moment. A matrix containing the amplitudes M_a and mean M_m of the set of bending moment histories for the specific design situation was defined, $M_{rs,(DLC,WS)}^* = (M_a, M_m)$. For a given DLC, the number of cycles occurring at a specific WS was stored in the matrix $N_{rs,(DLC,WS)}^*$. The total number of cycles in each bin (M_a, M_m) occurring in the specified DLC during 20 years of operation was obtained by weighting each $N_{rs,(DLC,WS)}^*$ with its frequency of occurrence w_{WS} , in the following way.

$$N_{rs,(DLC)}^* = 20 \cdot 24 \cdot 365 \cdot \sum_{WS} w_{WS} \cdot N_{rs,(DLC,WS)}^* \quad (5)$$

where $20 \cdot 24 \cdot 365$ is the scaling factor from 60 min simulation to 20 years. The procedure was repeated for each DLC and the total number of cycles in each bin, n , N_{rs}^* was derived by weighting $N_{rs}^*(DLC)$ with the expected frequency of occurrence, w_{DLC} , according to Eq. (6):

$$N_{rs}^* = \sum_{DLC} w_{DLC} \cdot N_{rs,(DLC)}^* \quad (6)$$

Accepting the applicability of the well-known linear Palmgren–Miner [15,16] high-cycle fatigue-damage accumulation law for composite materials [17], the target damage index $D_t(z)$ can be obtained by summing the partial damages for each bin (M_a, M_m) as follows:

$$D_t(z) = \sum_r \sum_s \frac{N_{rs}^*(z)}{N_{F,rs}(z)} = \sum_{DLC} w_{DLC} \sum_r \sum_s \frac{N_{rs,(DLC)}^*(z)}{N_{F,rs}(z)} \quad (7)$$

Exploiting the linear relationship between stress and section forces; the numbers of cycles to failure can directly be obtained on the basis of bending moments according to Eq. (8). The latter is used to obtain fatigue lifetimes for a given amplitude as a function of the mean fibre strain state. Eq. (8) is based on linear extrapolation between three different bending moment ratios i.e., $M_a = 0, M_m = M_{UT}$; $M_a = M_{UT}, M_m = 0$; $M_a = 0, M_m = M_{UC}$. They define a *linear constant life diagram* (CLD) as e.g. discussed by Hahn [18] and Nijssen [19] and depicted in Fig. 2:

$$N_{F,rs}(z) = \begin{cases} \left[\frac{M_{UT}(z)}{M_a(z)} \left(1 - \frac{M_m(z)}{M_{UC}(z)} \right) \right]^{mSN}, & \text{for } M_{UC}(z) \leq M_m(z) < 0 \\ \left[\frac{M_{UT}(z)}{M_a(z)} \left(1 - \frac{M_m(z)}{M_{UT}(z)} \right) \right]^{mSN}, & \text{for } 0 \leq M_m(z) \leq M_{UT}(z) \end{cases} \quad (8)$$

The ultimate bending moment capacities given by Eqs. (9) and (10) are defined as those magnitudes at which failure is induced after one single tension–compression load reversal. For the sake of simplicity, those were evaluated only for the critical fibre indicated in Fig. 3, using the flapwise bending stiffness together with the ultimate strains $\epsilon_{UT} = 6.892 \times 10^{-3}$ and $\epsilon_{UC} = -6.462 \times 10^{-3}$. The adopted strain limits are taken from [11] for uniaxial glass-fibre composite materials (i.e. UD) in fibre direction including partial material safety factors according to [20].

$$M_{UC}(z) = \frac{\epsilon_{UC} EI(z)}{\chi_c(z)} \quad (9)$$

$$M_{UT}(z) = \frac{\epsilon_{UT} EI(z)}{\chi_c(z)} \quad (10)$$

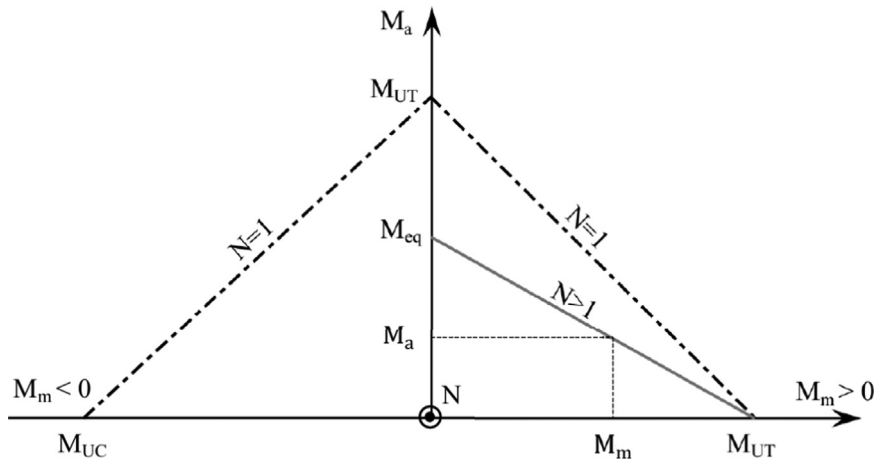


Fig. 2. The CLD represents a contour plot of equal fatigue life where the linear CLD or classical *linear Goodman diagram* without peak shift is most commonly used to obtain $N_{f,rs}$ for a specific mean bending moment and bending moment amplitude.

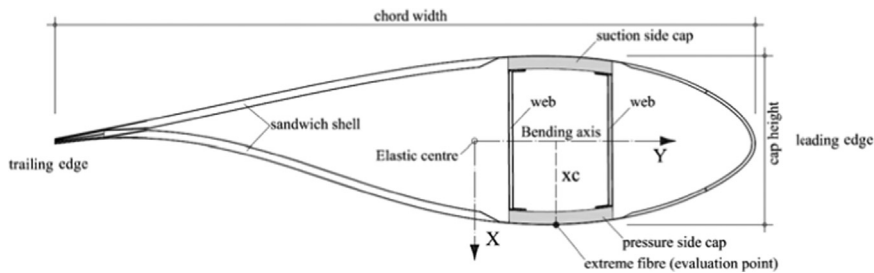


Fig. 3. Typical cross section of the 10 MW RWT rotor blade showing the damage evaluation line along the extreme fibre of the pressure side cap. Owing to the high demand on bending stiffness and strength, the caps (grey hatch) are made of unidirectional composite material. Flapwise bending is stipulated as bending around the y -axis.

3. Fatigue-test simulation methodologies

3.1. Lumped mass blade model

The DTU Wind Energy 10 MW RWT blade is designed for off-shore operation whose design specifications are publicly available in [11]. The overall length of the blade is $L=86.366$ m. The blade is made of glass-fibre composite material where balsa wood is used as sandwich core. Fig. 3 depicts a typical cross-section which follows a classic design approach where a load-carrying box girder is composed of two shear webs and two caps. The aerodynamic shell is formed by a pair of trailing panels and a pair of leading panels – both attached to the box girder.

For the feasibility study presented in this paper, the 10 MW RWT blade was discretised by a 2D lumped mass model shown in Fig. 4. It shows that the model was fully restrained on the left-hand side such that $x=0$ and $dx/dz=0$ at $z=0$. The model was generated in the multi-paradigm numerical computing environment *Matlab v.15a* [21]. It consisted of $n=100$ nodes, equally spaced at $\Delta z=L/n$, with one translational degree of freedom per node in the x -direction.

The moment of deviation of the blade cross section causes a rotation of the principal axes which reflects in a coupling between the flap and edgewise response due to pure flapwise excitation. This implies that the bending axis is not aligned with the global y -axis. This strictly speaking causes the extreme fibre to be different from the one identified in Fig. 3. However, the rotation of the principal axis in a typical cross section is mild implying a small effect on the extreme fibre strain.

The locus of the elastic centres describes a space curve which is not aligned with the z -axis and the elastic centres do not coincide with the shear centres. These features induce a torsional moment – albeit – the significant torsional stiffness of the thin-walled multicellular cross section renders torsional dof negligible for the present case.

In addition, neglecting the aforementioned effects does not alter the validity of the comparison between mono- and multi-frequency approach, as they are both modeled in the same simplified way. Other features, such as geometric non-linearity as well as damage-induced stiffness degradation, are disregarded as they are considered to be beyond the scope of this work.

The dynamic response of the lumped mass system depicted in Fig. 4(c) subject to mono- and dual-frequency excitations can be described by a non-linear second-order differential equation in dot-notation as follows:

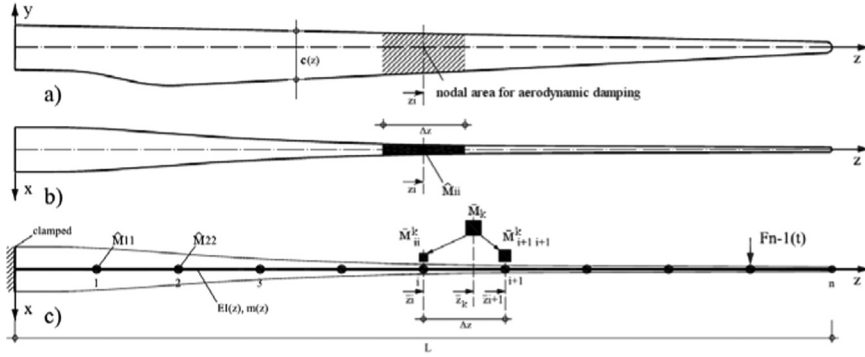


Fig. 4. (a) The associated nodal planform area used for aerodynamic damping, (b) the associated nodal blade mass and (c) discretisation of the blade by a lumped mass model used for numerical feasibility study showing terminology and distribution of the individual tuning mass to its neighbouring nodes.

$$\mathbf{M} \ddot{\mathbf{x}} + \mathbf{D} \dot{\mathbf{x}} + \mathbf{A} \dot{\mathbf{x}}|\dot{\mathbf{x}}| + \mathbf{K} \mathbf{x} = \mathbf{f}_1 \sin \omega_1 t + \mathbf{f}_2 \sin \omega_2 t \tag{11}$$

where $|\dot{\mathbf{x}}| = \{ |\dot{x}_1|, |\dot{x}_2|, |\dot{x}_3|, \dots, |\dot{x}_n| \}^T$ is the component-wise absolute value velocity vector.

The number of excitation forces was limited to two for reasons of practicality. Eq. (11) can be re-written as a set of first-order differential equations and subsequently solved numerically. The most efficient solver for this hard problem was found to be Matlab type *ode15s*. The latter is a 1st-order to 5th-order accuracy solver based on implicit backward differences which variably adjusts the subsequent time-step size according to an error estimate of the previous time step [21,22]. The initial conditions used for the initial time step were $\mathbf{x}|_{t=0} = 0$ and $\dot{\mathbf{x}}|_{t=0} = 0$.

The structural input parameters for the dynamic model were taken from the 10 MW RWT documentation report [11]. Fig. 5 shows the chord width and the distance between the bending axis and the extreme fibre as a function of the z -coordinate (see also Fig. 3). Fig. 6 likewise shows the mass and flapwise bending stiffness distribution.

Each element of the upper triangle of the symmetric compliance matrix ($z_i < z_j$) was computed semi-analytically according to Eq. (12) using first-order *Euler–Bernoulli* beam theory. Eq. (12) expresses the deformation of node i induced by a unit load applied at node j using the principle of virtual work, as for instance described in [23]. Eq. (12) was obtained by numerical integration using *Simpson's rule*. The inverse of the compliance matrix yields the stiffness matrix given by Eq. (13):

$$S_{ij} = \int_0^{z_i} \frac{1}{EI(z)} (z_i - z)(z_j - z) dz \tag{12}$$

$$\mathbf{K} = \mathbf{S}^{-1} \tag{13}$$

The elements of the base mass matrix of the blade itself can be obtained as follows:

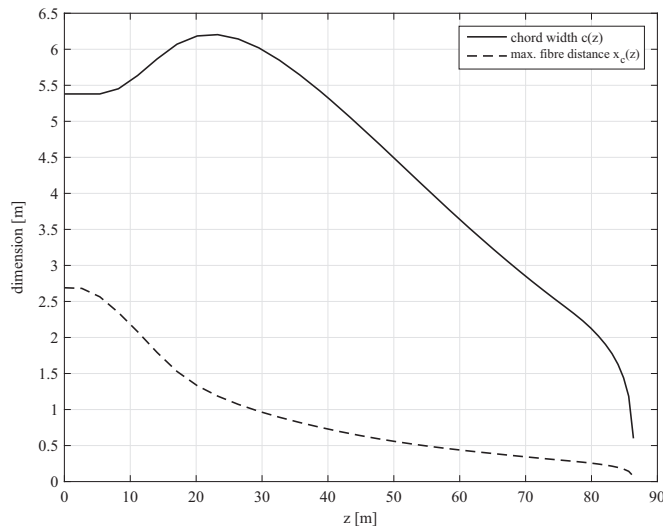


Fig. 5. Chord width and maximum distance between bending axis and extreme fibre of the pressure side cap along blade length.

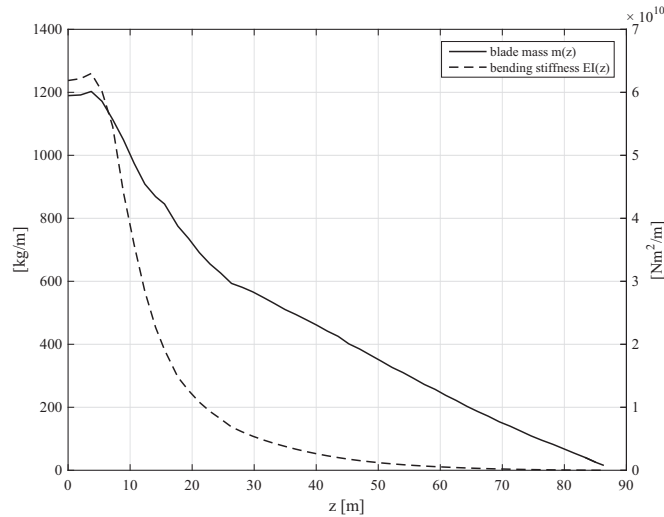


Fig. 6. Blade mass and flapwise bending stiffness distribution per meter along blade length.

$$\hat{\mathbf{M}}_{ij} = \begin{cases} \delta_{ij} \int_{(i-1/2)\Delta z}^{(i+1/2)\Delta z} m(z) dz, & \text{if } i < n \\ \delta_{ij} \int_{(i-1/2)\Delta z}^{i\Delta z} m(z) dz, & \text{if } i = n \end{cases} \quad (14)$$

The lumped mass model formulation demands the additional (tuning or exciting) masses to be discretely assigned to its nodes. The optimisation algorithm described in Section 3.3, on the other hand, demands masses to be placed continuously along the blade. Eq. (15) was used to resolve the dilemma by distributing the k -th additional mass, \bar{m}_k , between its two neighbouring nodes, i and $i + 1$, where $i = \lfloor z_k/\Delta z \rfloor$ for $\Delta z \leq z_k \leq L$ as depicted in Fig. 4(c):

$$\bar{\mathbf{M}}_{ij}^k = \bar{m}_k \left(1 - \frac{z_k}{\Delta z} + i \right) \hat{\mathbf{e}}_i \hat{\mathbf{e}}_i^T + \bar{m}_k \left(\frac{z_k}{\Delta z} - i \right) \hat{\mathbf{e}}_{i+1} \hat{\mathbf{e}}_{i+1}^T \quad (15)$$

To this end the total mass matrix can be obtained as follows

$$\mathbf{M} = \hat{\mathbf{M}} + \sum_{k=1}^{n_t} \bar{\mathbf{M}}_k \quad (16)$$

Rayleigh damping [24] was used in its most common form as follows

$$\mathbf{D} = a \mathbf{M} + b \mathbf{K} \quad (17)$$

where $a=0$ and $b=0.0156$ were assumed. The associated modal damping ratios are listed in Table 4 to be found in the Appendix.

Aerodynamic damping was considered by the drag equation as described in [25] with the diagonal matrix containing the associated nodal planform areas as indicated by the hatched region in Fig. 4(a). The elements of the aerodynamic damping matrix can be obtained by Eq. (18) where $C_d = 2$ for a flat plate perpendicular to the flow was deemed to represent a conservative approximation of a complex aerodynamic situation:

$$\mathbf{A}_{ij} = \begin{cases} \frac{\rho C_d}{2} \delta_{ij} \int_{(i-1/2)\Delta z}^{(i+1/2)\Delta z} c(z) dz, & \text{if } i < n \\ \frac{\rho C_d}{2} \delta_{ij} \int_{(i-1/2)\Delta z}^{i\Delta z} c(z) dz, & \text{if } i = n \end{cases} \quad (18)$$

By solving the well-known generalised eigenvalue problem posed by Eq. (19) the corresponding eigenvectors defining the mode shapes were obtained by Eq. (20)

$$|\mathbf{K} - \omega_i^2 \mathbf{M}| = 0 \quad (19)$$

$$(\mathbf{K} - \omega_i^2 \mathbf{M}) \Phi_i = 0 \quad (20)$$

3.2. Additional parameters

The static bending-moment distribution induced by the self-weight of the blade is calculated with a two step procedure. First the shear force is computed using Eq. (21) and the boundary condition $Q(L) = 0$ at the tip:

$$Q(z) = Q(L) + g \int_L^z m(s) ds \quad (21)$$

Subsequently the moment distribution is obtained using Eq. (22), with the boundary condition $M_s(L) = 0$:

$$M_s(z) = M_s(L) + \int_L^z Q(s) ds \quad (22)$$

The static bending-moment distribution induced by the self-weight of external masses can be obtained by Eq. (23). Using the superposition principle, the resulting static bending moment can be obtained by Eq. (24):

$$M_t(z) = \begin{cases} g \sum_{k=1}^{n_t} \bar{m}_k (\bar{z}_k - z), & \text{if } \bar{z}_k \geq z \\ 0, & \text{if } \bar{z}_k \leq z \end{cases} \quad (23)$$

$$M_m^*(z) = M_s(z) + M_t(z) \quad (24)$$

The nodal bending moment history used for damage calculation is expressed by Eq. (25), where the nodal curvature was numerically obtained by the central difference approximation of the second derivative of the nodal displacement history $x(z, t)$:

$$M(z, t) = M_m^*(z) + \frac{\partial^2 x(z, t)}{\partial z^2} EI(z) \quad (25)$$

Strain measurements are a crucial part of fatigue testing where the lifespan of the strain sensors affects the testing time due to test interruptions and equipment replacement. It is therefore, common practice to limit the peak strain amplitude to an empirical sensor type specific threshold. Nonetheless, strain signals exhibiting varying amplitudes – as is the case of multi-frequency excitation – render the commonly adopted peak strain limit in fatigue tests inapplicable. Therefore, the root of the mean square strain threshold given by Eq. (26) was instead used as a constraint in the subsequently discussed optimisation procedure:

$$\bar{\epsilon}(z) = \sqrt{\frac{1}{(T_2 - T_1)} \int_{T_1}^{T_2} \epsilon(z, t)^2 dt} \quad (26)$$

where the time span $T_2 - T_1$ corresponds to the steady-state part of the time history and the strain history for the extreme fibre of the flange, $\epsilon(z, t)$ was obtained by means of the strain-moment relation for the first-order Euler–Bernouli beam, presented in Eq. (27):

$$\epsilon(z, t) = \frac{M(z, t) x_c(z)}{EI(z)} \quad (27)$$

The ratio between the two force amplitudes in a dual-frequency excitation case is measured by the mode mixity, here defined as

$$\psi = \frac{2}{\pi} \arctan\left(\frac{F_1}{F_2}\right) \quad (28)$$

where $\psi = 1$ refers to pure Mode-1 excitation and $\psi = 0$ refers to pure Mode-2 excitation.

3.3. Optimisation

As pointed out previously, a fatigue test must satisfy four general constraints which can be grossly summarised as minimum number of cycles, maximum strain threshold, spatial damage distribution and limits on adiabatic heating. The considerable amount of free parameters involved in the dynamic system described yields a multi-dimensional solution space that is held by the design-variable vector. A numerical optimisation algorithm is required in order to find solutions which satisfy the aforementioned constraints to a sufficient degree of accuracy and efficiency. The aim of the optimisation process was to find optimal solution sets as a prerequisite for objective comparison between the mono-frequency and the multi-frequency approaches. For the present problem, the readily implemented Matlab optimiser *fmincon* [21] was used for nonlinearly constrained optimisation. By default *fmincon* computes the *Hessian* matrix by finite differences which is justified assuming the presence of small finite difference errors due to the semi-analytical formulation of the model.

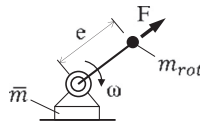


Fig. 7. Additional rotating mass added to the mass matrix according to the prevailing excitation force amplitude.

3.3.1. Optimisation of the mono-frequency approach

In the mono-frequency approach the design variable vector given by Eq. (29) consists of two tuning masses $\bar{m}_{1,2}$, the exciter mass \bar{m}_3 , their respective positions, the excitation force amplitude and a linear scaling factor:

$$\mathbf{q} = (\bar{m}_1 \bar{m}_2 \bar{m}_3 \bar{z}_1 \bar{z}_2 \bar{z}_3 F_1 w) \quad (29)$$

The total exciter mass was consequently updated according to the additional rotating mass defined by the excitation force magnitude with an assumed eccentricity of $e=1.2$ m (see Fig. 7) as follows

$$\bar{m}_{,3} = \bar{m}_3 + m_{rot} = \bar{m}_3 + \frac{F_1}{e \omega_1^2} \quad (30)$$

During every iteration the mass matrix was updated by substituting Eq. (30) into (15) before solving Eq. (11). The simulation time was adjusted such that a 60 s steady-state signal could be obtained upon which the optimisation procedure was based. The transient was discarded. The 60 s time span was deemed to give a satisfactory stochastic representation of the long-term signals involved. Rainflow counting [26] was used to compute the nodal damage vector given by Eq. (31) using Eqs. (24), (25) and (8):

$$D(z) = w \sum_r \sum_s \frac{N_{rs}(z)}{N_{F,rs}(z)} \quad (31)$$

Eq. (8) degenerates in (31), as the test condition can be seen as a single *DLC*, defined by the steady excitation from the rotating mass. Therefore, the factor w (design variable) was used to scale the damage obtained within the simulation time to fit the target damage distribution. The total nodal cycle number vector and the total testing time as well as the total dissipated energies can be computed by scaling the required steady state entities of the simulation using the same scaling factor, as follows

$$n_{tot}(z) = w \sum_r \sum_s N_{rs}(z) \quad (32)$$

$$T_{tot} = w(T_2 - T_1) \quad (33)$$

$$E_{tot} = w \int_{T_1}^{T_2} (\mathbf{f}_1 \sin \omega_1 t + \mathbf{f}_2 \sin \omega_2 t) \cdot \dot{\mathbf{x}} dt \quad (34)$$

$$E_{str} = w \int_{T_1}^{T_2} \mathbf{D} \dot{\mathbf{x}} \cdot \dot{\mathbf{x}} dt \quad (35)$$

$$E_{aer} = w \int_{T_1}^{T_2} \mathbf{A} \dot{\mathbf{x}} \circ |\dot{\mathbf{x}}| \cdot \dot{\mathbf{x}} dt \quad (36)$$

where the dissipated energy must satisfy the condition $E_{tot} = E_{str} + E_{aer}$.

The objective function is given by Eq. (37) where the optimisation problem including constraints is expressed in Eq. (38):

$$f(\mathbf{q}) = \sqrt{\sum_{i=1}^n (D_t(z_i) - D(z_i))^2} \quad (37)$$

$$\text{minimise}_{\mathbf{q}} f(\mathbf{q})$$

$$\text{subject to } 3 \times 10^6 - n_{tot}(\mathbf{q}) = 0$$

$$\bar{\epsilon}(\mathbf{q}) - \frac{0.003}{\sqrt{2}} \leq 0$$

$$\max(x_{100}(\mathbf{q})) - \frac{L}{10} \leq 0 \quad (38)$$

The optimisation problem posed above is non-convex since the optimiser usually converged to local minima of the solution space in the vicinity of the initial design variables. In order to overcome this issue, the optimisation procedure was repeated for 5×10^2 randomly selected starting variables. In the constraint set stipulated in Eq. (38), the number of cycles was arbitrarily specified as 3×10^6 cycles. The peak strain value of 3000 microstrain used for $\bar{\epsilon}$ reflects an empirical fatigue threshold for a standard electrical resistance strain gauge suitable for composite materials. The last constraint in Eq. (38) limits the tip deformation to 10% of the span in order to anticipate the deviation from first-order beam theory.

3.3.2. Optimisation of the multi-frequency approach

In the dual-frequency case, the blade was simultaneously excited by two excitation forces. In the case denoted as *dual rot.* the blade was excited by two rotational masses whereas in the case denoted as *dual grd.* a ground-based actuator was used. In the latter case both excitation forces were applied at a single identical node. Except of the exciter self-weights the application of additional tuning masses was omitted. In the dual-frequency approach, the design variable vector given by Eq. (39) consists of two excitation force magnitudes; the exciter positions and a scaling factor:

$$\mathbf{q} = (F_1 F_2 \bar{z}_1 \bar{z}_2 w) \quad (39)$$

In the case of rotating mass excitation, the mass matrix was updated at every iteration with the individual exciter masses according to Eq. (30). A base exciter mass of 200 kg was assumed. The total nodal cycle number vector and the total testing time as well as the total dissipated energies were obtained by Eq. (32) through (36). The objective function of the multi-frequency approach conforms to Eq. (37). However, in contrast to the mono-frequency case, the nodal cycle number in a multi-frequency case varies along the blade. Therefore, the non-linear constraint in Eq. (40) required the minimum nodal cycle number to be equal to or greater than the 3×10^6 cycle benchmark:

$$\begin{aligned} & \underset{\mathbf{q}}{\text{minimise}} && f(\mathbf{q}) \\ & \text{subject to} && 3 \times 10^6 - \min(n_{tot}(\mathbf{q})) \leq 0 \\ & && \bar{\epsilon}(\mathbf{q}) - \frac{0.003}{\sqrt{2}} \leq 0 \\ & && \max(x_{100}(\mathbf{q})) - \frac{L}{10} \leq 0 \end{aligned} \quad (40)$$

4. Results

4.1. Proof of principle

The proof of principle aims at a general performance comparison between mono- and dual-frequency excitations. For the sake of better comparability, all evaluations in this subsection are based on a single cross section located at $z=55$ m which corresponds to the peak of the target damage distribution D_r . The model was excited at the tip node in pure Mode-1, pure Mode-2 and mixed mode excitation; the application of tuning masses was disregarded in all three cases.

Fig. 8 shows a mode-mixity plot in which Eq. (28) is plotted against the mean frequency, defined as the total number of cycles over the steady-state simulation time. The black dots represent individual simulation runs for three different Mode-1 excitation force amplitudes. The solid lines are third-order polynomial curve fits of the transition regions. Fig. 8 shows that the frequency and therefore the cycle content of the bending moment history remains constant for small Mode-2 excitation force amplitudes. Further increasing the Mode-2 amplitude progressively increases the cycle content until the second natural frequency plateau is reached, whereupon any further increase of the Mode-2 excitation-force amplitude naturally cannot increase the cycle content. The intersections of the solid lines with the Mode-2 plateau are denoted as saturation points in this paper. Fig. 8 also shows that the saturation mode mixity is a function of the Mode-1 excitation force amplitude.

Fig. 9 is denoted as a *Time-Energy-Damage* (TED) contour plot depicted in a triple logarithmic scale. In the TED diagram, T_{tot} obtained from Eq. (33) is plotted along the abscissa whereas E_{tot} obtained from Eq. (34) is plotted along the ordinate. The contours represent the inverse of n_{tot} obtained from Eq. (32). The scale factor w was obtained by the reciprocal of the damage based on a 60 s steady-state bending moment signal. It appears that the results in a triple-log-plot are located on two planes, whose intersection represents the saturation line produced by interconnecting the individual saturation points. The dashed lines along the external borders of the planes indicate solutions for pure Mode-1 and pure Mode-2 excitations. The following considerations are based on an arbitrarily assumed threshold of 1×10^7 cycles. The intersection of the line denoted as pure Mode-1 with the 1×10^7 cycles contour shows that the testing time cannot be reduced below 190 d. The intersection of the dashed line denoted as *pure Mode-2* with the same contour shows that Mode-2 excitation reduces the testing time down to 70 d but exhibits a greater energy demand. It is obvious that an optimum can be found through mixed-mode excitation at the intersection of saturation lines. The kink in the 1×10^7 cycle contour marked by a circle indicates an optimum obtained by mixed-mode excitation. In fact, all optima of the single contours appear to be located along the saturation line.

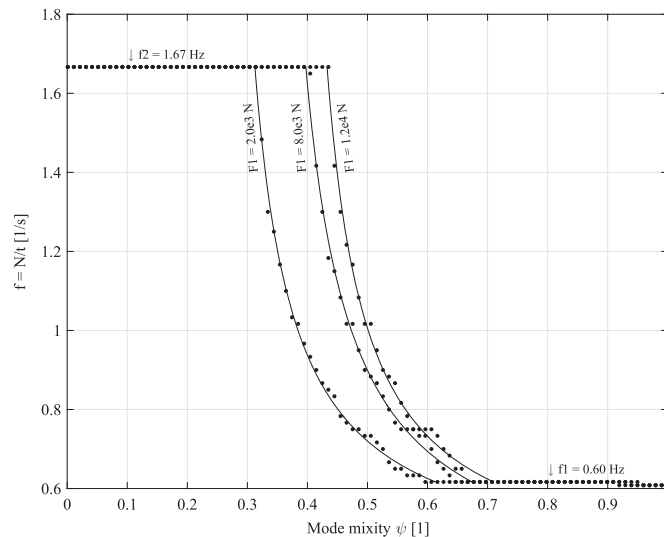


Fig. 8. Cycle number content as a function of capitalised Mode-1 excitation force amplitude and mode mixity ψ with three saturation points. It can be noted that the plateau lie at frequencies f_1 and f_2 , which are slightly lower than ω_1 and ω_2 , the natural frequencies of the sole blade, listed in Table 4. This is due to the presence of the exciters, which add concentrated masses, lowering the eigenvalues of the system. Secondly, the results represent the damped eigenfrequencies, which progressively decrease with increasing mode number.

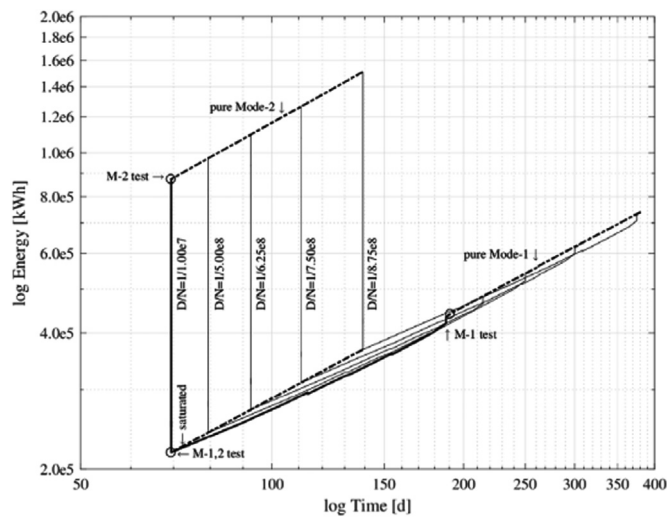


Fig. 9. Damage velocity contour plot as a function of total testing time and total excitation energy demand.

Table 1 lists the three excitation cases marked as circles in Fig. 9. In this table, the total testing time is compared with the associated energy dissipation portions for a total number of 1×10^7 cycles. Fig. 10 shows the CLD at the $z = 55$ m cross section with the turning points of the steady-state bending-moment signal for the three cases listed in Table 1. It shows that the two single-mode cases are located on the $N = 1 \times 10^7$ contour as required where the constant mean is induced by the static bending moment. The mixed mode data shows that as expected, amplitudes are over- and undershooting the single mode amplitude. The horseshoe-like distribution of small amplitude cycles shows that mixed-mode excitation can lead to higher mean values when these occur close to the underlying Mode-1 amplitudes, as can be deduced from the strain history signal section depicted in Fig. 11. Fig. 12 shows a plot of the steady-state excitation force history versus the excitation node displacement history for the three cases. The area enclosed by the Mode-2 hysteresis loop is greater than that enclosed by the Mode-1 hysteresis loop. The grey graph shows that the mixed-mode case does not produce a closed hysteresis loop eventually leading to lower energy dissipation when compared to the single mode excitations.

4.2. Optimised performance evaluation

The optimisation takes the feasibility study a step further by including the spatial damage distribution instead of one single cross-section. Fig. 13 compares the three best optimisation results with the normalised target damage distribution. It

Table 1
Performance comparison of different excitation methods leading to damage of the extreme fibre in the pressure-side cap at z=55 m.

Mode (-)	F ₁ (N)	F ₂ (N)	N _{tot} (1)	T _{tot} (d)	ε̄ (μs)	E _{str} (kW h)	E _{aer} (kW h)	E _{tot} (kW h)
1	1.204 × 10 ⁴	–	1.0 × 10 ⁷	1.9 × 10 ²	980	1.98 × 10 ⁵	2.43 × 10 ⁵	4.42 × 10 ⁵
2	–	4.148 × 10 ⁴	1.0 × 10 ⁷	6.9 × 10 ¹	980	7.54 × 10 ⁵	1.29 × 10 ⁵	8.83 × 10 ⁵
1+2	9.274 × 10 ³	1.715 × 10 ⁴	1.0 × 10 ⁷	7.1 × 10 ¹	870	2.00 × 10 ⁵	8.17 × 10 ⁴	2.82 × 10 ⁵

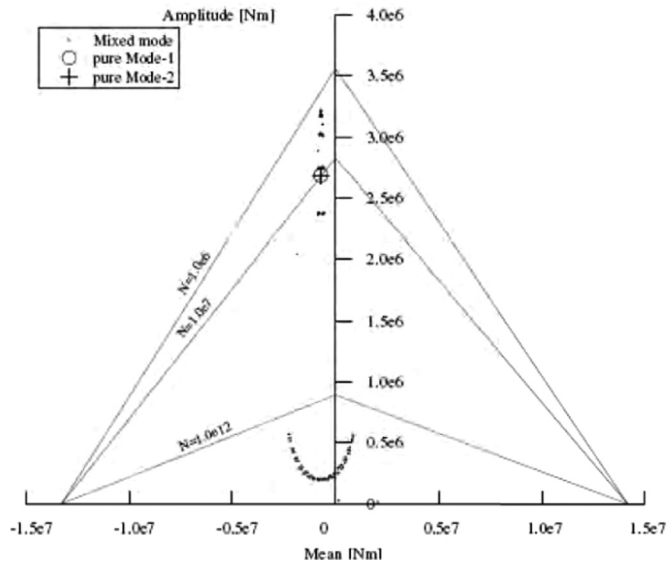


Fig. 10. Linear CLD used throughout the study with pure Mode-1, pure Mode-2 and optimal mixed-mode results as indicated by circles in Fig. 9.

shows that the damage peaks agree well, whereas good overall agreement was achieved by the ground-based excitation case. Reasonable agreement was achieved with the two remaining excitation methods. Fig. 14 shows that all equivalent strain maxima remained well below the specified threshold. The position of the strain peaks do not directly correspond to the damage peaks reflecting the influence of the CLD on the damage evolution. Table 2 lists the optimal parameters of the three different excitation cases, showing that the mono-frequency approach involves a considerable amount of additional mass distributed along the blade. The mass involved in the dual-frequency case is mainly required to provide the required first-frequency excitation-force amplitude. Eq. (30) shows that the excitation mass decreases with the inverse square of the angular speed which explains the lower mass for the second frequency excitation-force amplitude. Furthermore, the force

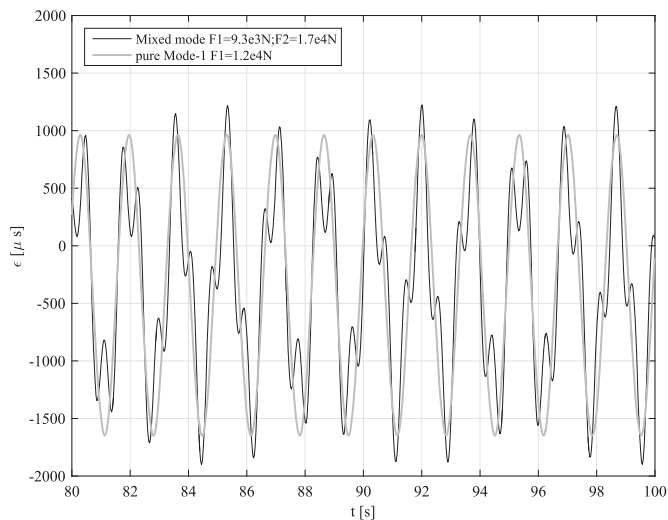


Fig. 11. Cap strain history section in evaluation point at z=55 m for pure Mode-1 and optimal mixed mode excitation.

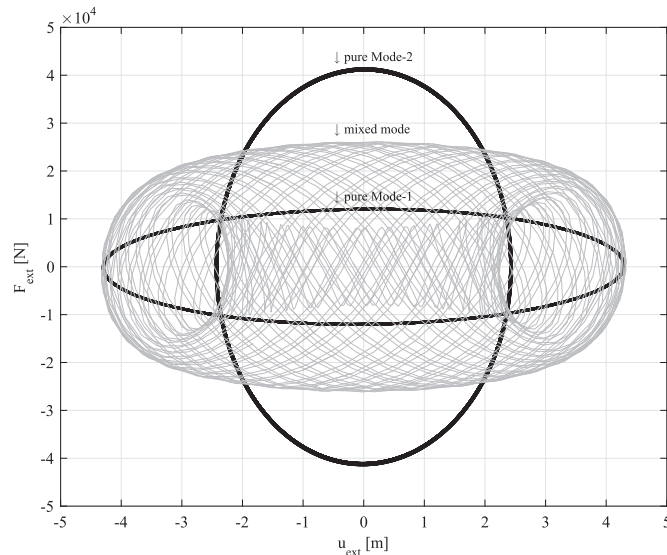


Fig. 12. Hysteresis loops of excitation node for three different excitation modes.

amplitudes are considerably higher under rotating mass excitation compared to the ground-based excitation. In the latter case, see Fig. 15 in the Appendix, the actuator is most efficiently placed in the outer part of the blade in the region of high eigenmode values. Table 3 shows that dual excitation decreases the testing time, whereas it increases the energy demand. The maximum tip deformations remain well below the threshold and are slightly higher under dual excitation.

5. Discussion

The results of the single cross-section evaluation summarised in Table 1 show that an optimal mixed-mode excitation exists in which both testing time and energy demand are lower than under pure Mode-1 excitation. The reduced testing time can straightforwardly be explained by the higher cycle content of mixed-mode excitation. In this case the structurally dissipated energy appears to be the same, but the dissipation rate under mixed-mode excitation is approximately three times as high. A prevalent portion of structurally dissipated energy is changed by transfer as heat. The detrimental effect of adiabatic heating on the fatigue life of composite materials as investigated by Kim [7] suggests that temperatures in the laminates should be measured (e.g. thermal imaging) and controlled.

Damage accumulation in wind turbine rotor blades is induced by the stochastic dynamic response which can be interpreted as a weighted combination of all eigenmodes together. The mono-frequency approach compromises the physics of

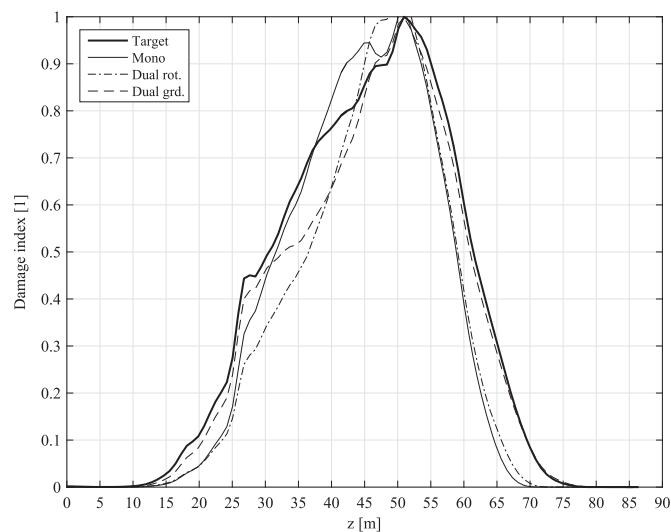


Fig. 13. Comparison of spatial damage distribution against target distribution for different excitation methods.

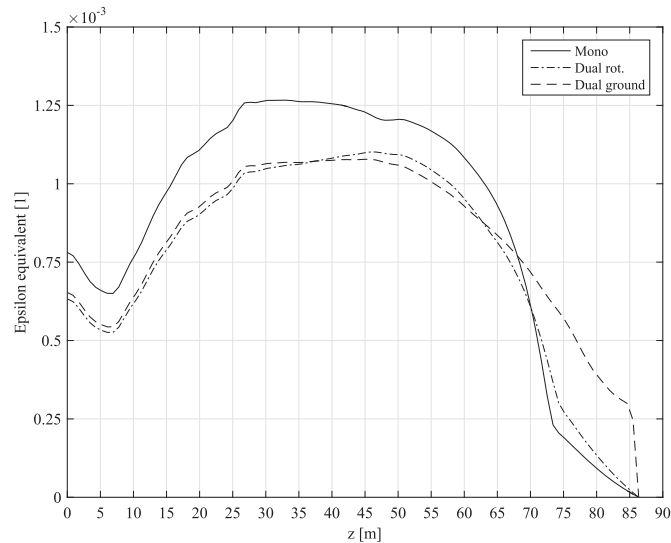


Fig. 14. Comparison of equivalent strain distribution for different excitation methods. The strain plateau in the mid-section of the span is a deliberate blade design feature. The maximum strain peaks are well below the defined threshold of $0.003/\sqrt{2} = 0.0021$, which satisfies the constraints.

Table 2

Design variables of the mono- and the two dual-frequency excitation cases. The mass in the *dual rot.* case reflects that of the exciters.

Case (-)	\bar{m}_1 (kg)	\bar{m}_2 (kg)	\bar{m}_3 (kg)	\bar{z}_1 (m)	\bar{z}_2 (m)	\bar{z}_3 (m)	F_1 (N)	F_2 (N)
Mono	4910	68	3390	47	61	73	1.142×10^4	–
Dual rot.	1340	636	–	74	64	–	1.524×10^4	1.949×10^4
Dual grd.	–	–	–	80	80	–	1.628×10^4	9.200×10^3

Table 3

Performance parameters of the mono- and the two dual-frequency excitation cases where R^2 represents the coefficient of determination.

Case (-)	$\min(n)$ (1)	T_{tot} (d)	E_{str} (kW h)	E_{aer} (kW h)	E_{tot} (kW h)	$\bar{\epsilon}_{max}$ (μ S)	χ_{tip}^{max} (m)	R^2 (1)
Mono	3×10^6	80	4.455×10^4	3.967×10^4	8.422×10^4	1300	4.4	0.93
Dual rot.	3×10^6	64	5.805×10^4	6.081×10^4	1.189×10^5	1100	4.8	0.91
Dual grd.	3×10^6	56	7.821×10^4	9.332×10^4	1.715×10^5	1150	5.1	0.98

the damage mechanism inasmuch all eigenmodes except the first are discarded. As a matter of compensation for the eigenmode deprivation, the mono-frequency approach requires the introduction of tuning masses. These considerably alter the original mass-to-stiffness ratio of the blade. In this respect the ground-based excitation outperforms the mono-frequency approach by better preserving the original state. That is, the real damage mechanism is closely replicated through consideration of several eigenmodes.

The results presented in Section 4.2 show that optimisation over the spatial domain only partially utilises the advantages reflected in the TED diagram on a single cross-section. The shorter testing times offered by multi-frequency excitation were mainly attributed to the deployment of reduced mass. The utilisation of a higher cycle content could not be achieved in the mid-section of the span without compromising the damage distribution. However, in the state-of-the-art approach due to deviations from the desired damage distribution, it is often necessary to test the blade in several stages by rearranging the entire test setup. Therefore, the time savings accumulated over different stages using the dual-frequency rotating mass approach can be substantial.

It has to be noticed, however, that the dual-frequency method always outperforms the mono-frequency one with respect to the testing time (cf. Table 3), which is reduced by at least 20%. The downside is a higher energy demand (30% at least). On the fidelity side, the solution with two rotating exciters proves to be slightly less efficient than the classical approach, $R^2 = 0.91$ compared to 0.93. On the other hand, the ground based dual excitation method better reproduces the damage distribution from real operating conditions ($R^2 = 0.98$ vs $R^2 = 0.93$ for the mono-frequency).

6. Conclusions

The following conclusions are drawn:

- (i) The equivalent force concept deprives fatigue testing methods of their opportunity to use a broader palette of the frequency spectrum. In other words, the stochastic nature of real load histories is more realistically recovered by a combination of several frequencies rather than by one single frequency.
- (ii) The multi-frequency approach has the potential to significantly reduce the testing time by increasing the cycle content in the time history and by avoiding the application of tuning masses.
- (iii) Rotating- or translating mass excitation is less suitable than ground-based excitation. In the first case the testing time can be shortened by 20% and in the latter case by 30%, compared to the state-of-the-art method.
- (iv) The multi-frequency approach fulfills all requirements of a state-of-the-art full-scale fatigue test.

Acknowledgements

The work was supported by the DTU Wind Energy *Advanced Materials* project and realised within the Micro-to-Macro task, whose support is gratefully acknowledged. Moreover, the authors are very grateful for the support of Dr. Robert D. Bitsche from DTU-VIM for his scientific input. The authors are grateful for the support of Christian Pavese from DTU-AED regarding the aeroelastic simulations.

Appendix A

Table 4 compares the first three flapwise natural frequencies of the 10 MW RWT blade between the 3D finite element model reported in [11, Table 6.4, p. 68] and the lumped mass model. The frequencies agree well where the deviation increases with increasing mode number. This deviation is caused by a stiffness overestimation owing to the negligence of shear deformation in the 2D model. The latter becomes increasingly apparent with decreasing effective length defined between the nodes of the mode shapes.

Fig. 15 shows the normalised first three eigenmodes of the lumped mass model obtained from Eq. (20). The wip-like flapwise deformation modes caused by the taper induced stiffness decrease towards the tip are characteristic for long

Table 4

Comparison of natural flapwise frequencies of the 3D 10 MW RWT blade model and the 2D lumped mass model; modal structural damping.

Mode	3D Model (Hz)	2D Model (Hz)	Error (%)	$\xi = b\omega/2$ (%)
1	0.61	0.62	1.45	3
2	1.74	1.78	2.42	8
3	3.57	3.73	4.21	17

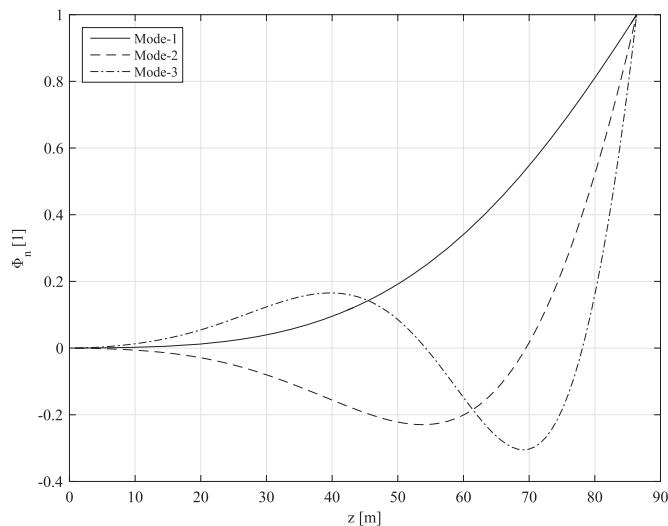


Fig. 15. First three mode shapes normalised against the tip displacement.

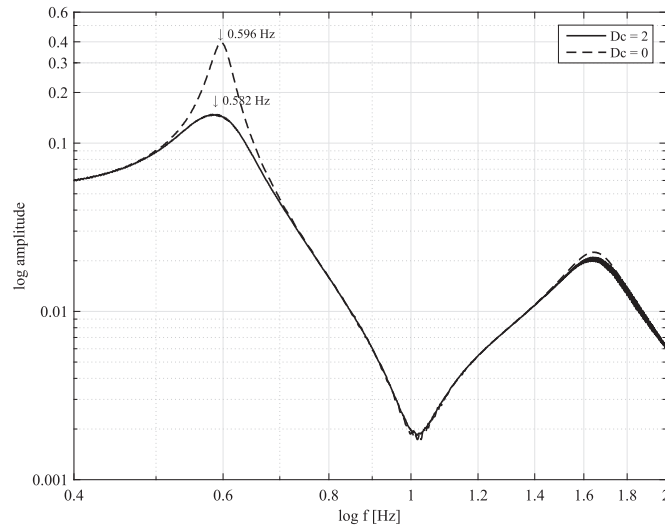


Fig. 16. Sine sweep amplitude spectrum obtained with and without aerodynamic damping.

blades. It shows that excitation forces are most efficiently placed in the outer part of the blade.

In order to investigate the effect of aerodynamic damping on the resonance frequencies a sine-sweep procedure was performed by solving Eq. (11) with the excitation force given by Eqs. (41) and (42) as e.g. discussed by Tuma [27]:

$$R = \frac{\ln(f_{up}/f_{low})}{(T_2 - T_1)\ln(2)} \quad (41)$$

$$F(t) = F \sin\left(2\pi\left(\frac{f_{low}(2^{Rt} - 1)}{R \ln(2)}\right)\right) \quad (42)$$

The resonance frequencies were obtained by a fast Fourier transform (FFT) of the excitation node displacement history between the sweep range of $f_{low} = 0.4$ Hz to $f_{up} = 2.0$ Hz for a simulation time of 300 s.

Fig. 16 shows the tip node displacement amplitude spectrum obtained from a sine-sweep excitation. The two peaks represent the first two damped natural frequencies of the model. It can be seen from Fig. 16 that aerodynamic damping mainly affects the first frequency but the frequency shift can in general be neglected in practice.

References

- [1] S. Sheng, Report on Wind Turbine Subsystem Reliability - A survey of Various Databases, Technical Report, NREL/PR-5000-59111, accessed: 2015-04-24, 2013.
- [2] P. Malhotra, J. Hyers, J.M. Manwell, A review and design study of blade testing systems for utility-scale wind turbines, *Renew. Sustain. Energy Rev.* 16 (2012) 284–292.
- [3] IEC 61400-1: Wind Turbines – Part 1: Design Requirements, 2005.
- [4] A. Wöhler, Wöhler's experiments on the strength of metals, *Engineering* 4 (1867) 160.
- [5] O.H. Basquin, The exponential law of endurance tests, *Proc. ASTM* 10 (2) (1910) 625–630.
- [6] H.J. Sutherland, SAND99-0089 Fatigue Analysis of Wind Turbines, Technical Report, Sandia National Laboratories, accessed: 2015-04-24, 1999.
- [7] H.C. Kim, L.J. Ebert, Fatigue life-limiting parameters in fibreglass composites, *J. Mater. Sci.* 14 (1979) 2616–2624, <http://dx.doi.org/10.1007/BF00610630>.
- [8] T.J. Larsen, A.M. Hansen, How 2 hawc2, the User's Manual, Technical Report Risø-R-1576(ver.4-5)(EN), RisøDTU, National Laboratory for Sustainable Energy, 2011.
- [9] HAWC2 – horizontal axis wind turbine simulation code 2nd generation, (<http://www.hawc2.dk>), accessed: 2015-04-24.
- [10] A.M. Hansen, L.C. Henriksen, Basic DTU Wind Energy Controller, Technical Report DTU Wind Energy-E-0018(EN), Technical University of Denmark, 2013.
- [11] C. Bak, R.D. Bitsche, A. Yde, T. Kim, H. Morten, F. Zahle, M. Gaunaa, J.P.A. Blasques, M. Døssing, H. Wedel, J. Jens, T. Behrens, The 10-MW reference wind turbine, in: Proceedings of EWEA 2012 European Wind Energy Conference & Exhibition, 2012, European Wind Energy Association (EWEA), Copenhagen, Denmark.
- [12] M.H. Hansen, K. Thomsen, A. Natarajan, A. Barlas, Design load basis for onshore turbines – revision 00, Technical Report DTU Wind Energy-E-0074(EN), Technical University of Denmark, 2015.
- [13] IEC 61400-1: Wind turbines – Part 1: Design requirements amend 1, 2005.
- [14] P. Fossum, L. Frøyd, O. Dahlhaug, Design and fatigue performance of large utility-scale wind turbine blades, *J. Sol. Energy Eng.* 135 (2013) 11.
- [15] A. Palmgren, Die Lebensdauer von Kugellagern, *Z. Vereines Dtsch. Ing.* 68 (14) (1924) 339–341.
- [16] M. Miner, Cumulative damage in fatigue, *J. Appl. Mech.* 12 (1945) 159.
- [17] A. Echtermeyer, C. Kenschke, P. Bach, M. Poppen, H. Lilholt, S. Andersen, P. Brøndsted, *Method to Predict Fatigue Lifetimes of GRP Wind Turbine Blades and Comparison with Experiments*, H.S. Stephens & Associates, Sweden, 1996, 907–913.
- [18] H. Hahn, Fatigue of Composites, Technomic, Lancaster, 1989, pp. 73–130.

- [19] R. Nijssen, Fatigue Life Prediction and strength degradation of wind turbine rotor blade composites (Ph.D. thesis), Technische Universiteit Delft, 2006.
- [20] Guideline for the certification of wind turbines, 2010.
- [21] The MathWorks, Inc., Natick, Massachusetts, United States, MATLAB and Statistics Toolbox Release 2015a, 2014.
- [22] A. Ryuichi, N. Michihiro, V. Rémi, Behind and Beyond the MATLAB ODE Suite, Technical Report CRM-2651, Osaka Kyoiku University, Japan, 2000.
- [23] H. Mang, G. Hofstetter, *Festigkeitslehre*, Springer, Vienna-New York, 2000.
- [24] M. Liu, D.G. Gorman, Formulation of Rayleigh damping and its extensions, *Comput. Struct.* 57 (1995) 277–285.
- [25] G.K. Batchelor, An Introduction to Fluid Dynamics, 2002, Reprint; Cambridge University Press.
- [26] A. Nieslony, Rainflow Counting Algorithm - Very fast rainflow cycle counting for MATLAB, (<http://www.mathworks.com/matlabcentral/fileexchange>), accessed: 2015-11-25.
- [27] J. Tuma, *Engineering Mathematics Handbook*, McGraw-Hill, New York, 1979.